

# CMS Draft Analysis Note

*The content of this note is intended for CMS internal use and distribution only*

2020/06/09

Archive Hash: e95bb68-D

Archive Date: 2020/06/08

## Measurement of differential $t\bar{t}$ production cross sections in the full kinematic range using lepton+jets events from pp collisions at $\sqrt{s} = 13$ TeV

Otto Heinz Hindrichs  
University of Rochester (US)

### Abstract

Measurements of differential and double-differential cross sections of the production of top quark pairs ( $t\bar{t}$ ) are presented in the lepton+jets channels with a single electron or muon and jets in the final state. The analysis combines signatures of top quarks with low transverse momentum  $p_T$ , where the top decay products can be identified as separated jets and isolated leptons, and with high  $p_T$ , where the decay products are collimated and overlap. With this combination implicit selections of the top quark  $p_T$  are avoided and the full  $p_T$  range is probed. The measurements are based on data collected by the CMS experiment at the LHC between 2016 and 2018 corresponding to an integrated luminosity of  $137\text{ fb}^{-1}$ . The cross sections are presented at parton and particle level, where the later minimizes extrapolations based on theoretical assumptions. Both results are compared to various kinds of standard model calculation using different combinations of matrix elements and parton shower models. In general, decent agreements between the measurements and the predictions are observed. The next-to-next-to-leading order quantum chromodynamics (QCD) calculation with its reduced uncertainty provides an improved description of the measurements compared to next-to-leading order QCD calculations. From the integration of the differential cross sections an inclusive  $t\bar{t}$  production cross section of  $\sigma_{\text{tot}} = 815 \pm 25\text{ pb}$  is obtained.

This box is only visible in draft mode. Please make sure the values below make sense.

PDFAuthor:

O. Hindrichs

PDFTitle:

Measurement of differential cross sections for the production of top quark pairs in lepton+jets events from pp collisions at  $\sqrt{s} = 13$  TeV

PDFSubject:

CMS

PDFKeywords:

CMS, top quark pairs, differential cross section

Please also verify that the abstract does not use any user defined symbols



## 1 Introduction

We present measurements of differential top quark pair ( $t\bar{t}$ ) production cross sections in the  $e/\mu+jets$  channels, i.e., with a single electron or muon and jets in the final state. Precision measurements of  $t\bar{t}$  production are important tests of the standard model (SM), since the top quark with its high mass and its property of being the only quark that can be observed before hadronization, plays an exceptional role. With its strong coupling to the Higgs boson it might be involved in beyond SM scenarios of electroweak symmetry breaking. These could become visible in altered kinematic distributions of  $t\bar{t}$  production. A detailed understanding of  $t\bar{t}$  production is also important for many searches for beyond SM phenomena, where it often forms an important background. In addition, it is shown in TODO that differential  $t\bar{t}$  production can contribute significantly to the measurement of parton distribution functions (PDF).

At the CERN LHC measurements of differential cross sections have been performed in various  $t\bar{t}$  decay channels at pp collision energies of 7 TeV [1, 2], 8 TeV [3–9], and 13 TeV [10–17].

This analysis is based on  $137 \text{ fb}^{-1}$  recorded in LHC Run 2, where  $35.9 \text{ fb}^{-1}$  were recorded in 2016,  $41.5 \text{ fb}^{-1}$  in 2017, and  $59.7 \text{ fb}^{-1}$  in 2018. Since the running conditions and the CMS detector changed with the years, performance and calibration measurements are performed separately for each year.

We use techniques of resolved  $t\bar{t}$  reconstruction introduced in previous CMS analyses [13, 14]. These are applicable if all  $t\bar{t}$  decay products can be reconstructed as separated leptons and jet in the detector typically for top quarks with  $p_T < 500 \text{ GeV}$ . These results are extended adding the information of boosted top quarks, whose decay products are collimated and overlap. Reconstruction techniques for both, the hadronically ( $t_h$ ) and the leptonically ( $t_\ell$ ) decaying boosted top quarks, are developed and combined with the resolved reconstruction. Finally, the differential cross sections are extracted performing a combined likelihood fit to several categories of different reconstruction methods and lepton flavors in the three years of data taking. The combinations of the different categories allow for constraints of systematic uncertainties and result in an improved precision with respect to previous measurements.

The differential cross sections are presented at parton and particle levels. The parton level is represented by a  $t\bar{t}$  pair before their decays and the cross sections are presented in the full phase space of the top quarks. This means for the parton-level measurements all effects related to top quark decays, hadronization, and limited detector acceptance are corrected based on theoretical assumptions. These extrapolations can be reduced in the particle-level measurements, where the  $t\bar{t}$  pair is defined based on jets and leptons that can be observed in the detector. All details about the particle-level top quarks are given in Section 13.1.

At the parton level we measure the differential cross sections as a function of the following variables:  $p_T(t_h)$ ,  $p_T(t_\ell)$ , their scalar sum  $S_T$ , the transverse momentum of leading  $p_T(t_{\text{hard}})$  and trailing  $p_T(t_{\text{soft}})$  of top quarks,  $|y(t_h)|$ ,  $|y(t_\ell)|$ , rapidity differences  $\Delta|y_{t/\bar{t}}| = |y(t)| - |y(\bar{t})|$ ,  $|\Delta y_{t/\bar{t}}| = |y(t) - y(\bar{t})|$ , the angle between the top quarks in the transverse plane  $\Delta\phi_{t/\bar{t}}$ ;  $|y(t\bar{t})|$ , the mass  $M(t\bar{t})$ , and  $p_T(t\bar{t})$ ;  $\cos(\theta^*)$ , where  $\theta^*$  is the angle between the  $t$  and the direction of flight of the  $t\bar{t}$  system calculated in the  $t\bar{t}$  rest-frame. Double differential cross sections are measured as functions of several combinations of these variables:  $p_T(t_h)$  vs.  $|y(t_h)|$ ,  $M(t\bar{t})$  vs.  $|y(t\bar{t})|$ ,  $M(t\bar{t})$  vs.  $\cos(\theta^*)$ ,  $M(t\bar{t})$  vs.  $p_T(t_h)$ ,  $M(t\bar{t})$  vs.  $\Delta|y_{t/\bar{t}}|$ ,  $|\Delta y_{t/\bar{t}}|$  vs.  $M(t\bar{t})$ , and  $|y(t)|$  vs.  $|y(\bar{t})|$ . From the integration of the differential cross sections a precise measurement of the inclusive  $t\bar{t}$  production cross section is obtained. In addition, at particle level the cross sections of jet multiplicities and differential cross section as function of  $p_T(t_h)$ ,  $M(t\bar{t})$ , and  $p_T(t\bar{t})$  in bins of jet multiplicity are determined. Finally, the differential cross section as function of the scalar sum

<sup>47</sup> of the  $p_T$  of additional jets  $H_T$ , the invariant mass of the top quarks and all additional jets  $M_{\text{evt}}$ ,  
<sup>48</sup> and the  $p_T$  of the electron and muons  $p_T(\ell)$  are presented.

<sup>49</sup> The methods used in the parton- and particle-level measurements are the same. In this doc-  
<sup>50</sup> ument we will concentrate mainly on the parton level in Section 13 details of the definition of  
<sup>51</sup> particle-level object, the differences with respect to the parton-level analysis, and the results at  
<sup>52</sup> particle-level are discussed.

DRAFT

## 53 2 Simulation and Data

54 Events are selected from the SingleMuon and SingleElectron/EGamma data streams in the  
 55 MINIAOD format as shown in Tab. 1 if they pass single lepton triggers. For the muon channel  
 56 HLT\_IsoMu24/27/24 is used in 2016/2017/2018 for  $p_T < 50 \text{ GeV}$  while for higher  $p_T$  the com-  
 57 bination HLT\_IsoMu24/27 OR HLT\_Mu50 is required. The later allows for the selection of non  
 58 isolated muons used in the reconstruction of boosted  $t_\ell$ .

59 Electrons are selected with the combination

60 HLT\_Ele27\_WPTight\_Gsf OR HLT\_Ele32\_WPTight\_Gsf. To avoid a double counting of events all  
 61 events selected by the muon triggers described above are rejected in the SingleElectron/EGamma  
 62 data stream. Events with at least one AK4CHS jet with  $p_T > 165 \text{ GeV}$  and an electron with  
 63  $p_T > 50 \text{ GeV}$  can also be selected by the HLT\_Ele50\_CaloIdVT\_GsfTrkIdT\_PFJet165 trigger. This  
 64 trigger is available for the full Run2, except for the first 11.6% of the 2017 dataset. This is taken  
 65 into account by applying an event weight of 0.884 for all events in the simulation that are se-  
 66 lected only by the nonisolated electron trigger.

67 The JetHT data stream is used for the extraction of background templates for the separation of  
 68  $t_h$  and other jets.

69 Simulations using reprocessing version

70 RunIISummer16MiniAODv3-PUMoriond17\_94X\_mcRun2\_asymptotic\_v3 (2016),

71 RunIIFall17MiniAODv2-PU2017\_12Apr2018\_94X\_mc2017\_realistic\_v14 (2017), and

72 RunIIAutumn18MiniAOD-102X\_upgrade2018\_realistic\_v15 (2018) are used. A list of simula-  
 73 tions together with their sum of weights and the cross sections are given in Tabs. 7–9 in Ap-  
 74 pendix C.

## 75 3 Object selection

### 76 3.1 Muons

77 For muons  $p_T > 30 \text{ GeV}$  is required. This ensures that the offline selection is well above the  
 78 maximum trigger threshold of 27 GeV. The pseudo-rapidity is restricted to the silicon tracker  
 79 coverage of  $|\eta| < 2.4$ . The tight selection is applied. Muons are categorized as isolated if the  
 80 particle-flow (PF) isolation  $I_{\text{PF}}/p_T(\mu) < 0.15$ , where  $I_{\text{PF}} = I_{\text{CH}} + \max(0, I_{\text{N}} + I_{\text{PH}} - 0.5I_{\text{CH,pu}})$   
 81 and  $I_X$  if the  $p_T$ -sum of charged (CH), neutral (N), and photon-like (PH) particle-flow candi-  
 82 dates within  $\Delta R = 0.4$  around the muon. The last term  $I_{\text{CH,pu}}$  is the sum over charged particles  
 83 not originating from the main primary vertex and compensates for contributions from pileup.

84 Since the minimum  $p_T$  threshold for nonisolated muons is 50 GeV, this threshold is also used as  
 85 offline selection for muons not passing the isolation requirement. However, they have to fulfill  
 86 all other requirements of the tight selection. Efficiencies for reconstruction, identification and  
 87 the trigger have been studied and scale factors are applied to the simulation. Details can be  
 88 found in Appendices A and A.3.

### 89 3.2 Electrons

90 In 2016 and 2017 the trigger threshold for isolated electrons is 27 GeV with some exceptions in  
 91 2017 where the L1 seed was pre-scaled below 32 GeV. However, for both years an offline se-  
 92 lection of  $p_T > 30 \text{ GeV}$  is used and the pre-scales in 2017 are treated as additional inefficiency.  
 93 In 2018 the trigger threshold was raised to 32 GeV and an offline selection of  $p_T > 34 \text{ GeV}$  is  
 94 used. The pseudo-rapidity is restricted to the silicon tracker coverage of  $|\eta| < 2.4$ . Electrons

Table 1: Data streams.

**2016**

```
/SingleElectron/Run2016B-17Jul2018.ver2-v2/MINIAOD
/SingleElectron/Run2016C-17Jul2018-v1/MINIAOD
/SingleElectron/Run2016D-17Jul2018-v1/MINIAOD
/SingleElectron/Run2016E-17Jul2018-v1/MINIAOD
/SingleElectron/Run2016F-17Jul2018-v1/MINIAOD
/SingleElectron/Run2016G-17Jul2018-v1/MINIAOD
/SingleElectron/Run2016H-17Jul2018-v1/MINIAOD
/SingleMuon/Run2016B-17Jul2018.ver2-v1/MINIAOD
/SingleMuon/Run2016C-17Jul2018-v1/MINIAOD
/SingleMuon/Run2016D-17Jul2018-v1/MINIAOD
/SingleMuon/Run2016E-17Jul2018-v1/MINIAOD
/SingleMuon/Run2016F-17Jul2018-v1/MINIAOD
/SingleMuon/Run2016G-17Jul2018-v1/MINIAOD
/SingleMuon/Run2016H-17Jul2018-v1/MINIAOD
/JetHT/Run2016B-17Jul2018.ver2-v1/MINIAOD
/JetHT/Run2016C-17Jul2018-v1/MINIAOD
/JetHT/Run2016D-17Jul2018-v1/MINIAOD
/JetHT/Run2016E-17Jul2018-v1/MINIAOD
/JetHT/Run2016F-17Jul2018-v1/MINIAOD
/JetHT/Run2016G-17Jul2018-v1/MINIAOD
/JetHT/Run2016H-17Jul2018-v1/MINIAOD
```

**2017**

```
/SingleMuon/Run2017B-31Mar2018-v1/MINIAOD
/SingleMuon/Run2017C-31Mar2018-v1/MINIAOD
/SingleMuon/Run2017D-31Mar2018-v1/MINIAOD
/SingleMuon/Run2017E-31Mar2018-v1/MINIAOD
/SingleMuon/Run2017F-31Mar2018-v1/MINIAOD
/SingleElectron/Run2017B-31Mar2018-v1/MINIAOD
/SingleElectron/Run2017C-31Mar2018-v1/MINIAOD
/SingleElectron/Run2017D-31Mar2018-v1/MINIAOD
/SingleElectron/Run2017E-31Mar2018-v1/MINIAOD
/SingleElectron/Run2017F-31Mar2018-v1/MINIAOD
/JetHT/Run2017B-31Mar2018-v1/MINIAOD
/JetHT/Run2017C-31Mar2018-v1/MINIAOD
/JetHT/Run2017D-31Mar2018-v1/MINIAOD
/JetHT/Run2017E-31Mar2018-v1/MINIAOD
/JetHT/Run2017F-31Mar2018-v1/MINIAOD
```

**2018**

```
/SingleMuon/Run2018A-17Sep2018-v2/MINIAOD
/SingleMuon/Run2018B-17Sep2018-v1/MINIAOD
/SingleMuon/Run2018C-17Sep2018-v1/MINIAOD
/SingleMuon/Run2018D-22Jan2019-v2/MINIAOD
/EGamma/Run2018A-17Sep2018-v2/MINIAOD
/EGamma/Run2018B-17Sep2018-v1/MINIAOD
/EGamma/Run2018C-17Sep2018-v1/MINIAOD
/EGamma/Run2018D-22Jan2019-v2/MINIAOD
/JetHT/Run2018A-17Sep2018-v1/MINIAOD
/JetHT/Run2018B-17Sep2018-v1/MINIAOD
/JetHT/Run2018C-17Sep2018-v1/MINIAOD
/JetHT/Run2018D-PromptReco-v2/MINIAOD
```

95 with an ECal cluster in the gap between the barrel and the endcap,  $1.4442 < |\eta(SC)| < 1.566$ ,  
 96 are rejected. The tight electron ID (V2) is used. In addition, a selection on the transverse impact  
 97 parameter  $|d_0| < 0.05(0.10)$  cm and the longitudinal impact parameter  $|d_z| < 0.1(0.2)$  cm is  
 98 applied in the barrel(endcap) regions. For the identification of nonisolated leptons the tight ID  
 99 without the isolation requirement is used. However, a suitable trigger for these events requires  
 100  $p_T > 50$  GeV and an additional jet with  $p_T > 165$  GeV. Since the threshold behavior of the jet  
 101 in the trigger (Appendix A.3 Fig. 92) is not well modeled and we want to avoid an implicit de-  
 102 pendence of the trigger on the multiplicity and kinematics of additional jets, the corresponding  
 103 trigger object has to belong to a jet (AK4) with  $p_T > 250$  GeV that is consistent with the direction  
 104 of a boosted  $t_h$  candidate (Section 6). Efficiencies for reconstruction, identification and the trig-  
 105 gers are measured in data and correction factors are applied to the simulation. Details can be  
 106 found in Appendices A and A.3. In about 65% of the 2018 data a failure of HEM 15/16 causes  
 107 problems with the identification of electrons between  $-1.5 < \phi < -0.9$  in the minus endcap  
 108 region. Especially, a large number of nonisolated electron are faked in this region. Therefore,  
 109 all electrons in the affected region and runs are rejected. In the simulation events with electrons  
 110 in this region are weighted down accordingly.

### 111 3.3 Jets and b-jet identification

112 The default jets are clustered from PF objects using the anti- $k_T$  jet algorithm with a distance pa-  
 113 rameter of 0.4. Charged particles originating from a pileup interaction vertex are excluded. Jet  
 114 energy/resolution corrections are applied: Summer16\_07Aug2017\_V11 / Summer16\_25nsV1  
 115 for 2016, Fall17\_17Nov2017\_V32 / Fall17\_V3 for 2017, and  
 116 Autumn18\_RunX\_V19 / Autumn18\_Run (ABC | D) \_V7 for 2018. The minimum  $p_T$  for jets is  
 117 30 GeV and  $|\eta| < 2.4$  is required. The tight jet ID as recommended by the JME POG is required.

118 The same versions of corrections are also applied to the large cone PUPPI-jets with a distance  
 119 parameter of 0.8 that are used in the reconstruction of boosted  $t_h$ . PUPPI-jets with  $p_T > 400$  GeV  
 120 and  $|\eta| < 1.6$  are selected.

121 A jet within  $\Delta R < 0.4$  with respect to an isolated electron or muon is assumed to be dominated  
 122 by the isolated lepton and not considered as real jet for further analysis.

123 The DeepCSV b-tagging algorithm is used for the identification of b jets. In events with a  
 124 boosted  $t_h$  candidate and a resolved(boosted) leptonically decaying top quark one b-jet can-  
 125 didate passing the medium(loose) working point criterion is required, while events with a  
 126 resolved reconstruction of the  $t_h$  are categorized in events with two b-jet candidates passing  
 127 the medium working point criterion and events with one medium- and one loose-tagged b-jet  
 128 candidate. Scale factors calculated from efficiency measurements in data are used to correct the  
 129 tagging and mistagging efficiencies of the individual working points in the simulation.

130 Due to a timing issue with the EGamma triggers in the endcap regions in 2016 and 2017, events  
 131 that should be selected by these triggers are rejected. A detailed description how this ineffi-  
 132 ciency is taken into account can be found in Appendix B.

### 133 3.4 Missing transverse momentum

134 The missing transverse momentum  $\vec{p}_T^{\text{miss}}$  is reconstructed as negative  $\vec{p}_T$  sum of all PF objects.  
 135 Events that do not pass the recommended  $p_T^{\text{miss}}$  filters are rejected. Due to the large noise level  
 136 in the ECal forward regions in 2017 all PF candidates with  $2.65 < |\eta| < 3.139$  are not considered  
 137 in the calculation of  $\vec{p}_T^{\text{miss}}$ , unless they are constituents of a jet with  $p_T > 50$  GeV.

## 138 4 Resolved reconstruction of the top quark-antiquark system

139 The requirements for an event to fall into the resolved reconstruction categories are exactly one  
 140 isolated electron or muon and at least four jets. If at least two of the jets pass the medium b-  
 141 tagging criterion the event is categorizes as “2m”. If there is one jet passing the medium and  
 142 another jet passing the loose b-tagging criteria the event falls into the “1m1l” category.

143 The reconstruction of the  $t\bar{t}$  system in the resolved case follows closely the methods used in  
 144 Ref. [13]. The goal is the correct identification of detector-level objects as top quark decay  
 145 products. In the simulation, a quark or lepton at the generator level can be spatially matched  
 146 to the corresponding detector-level object. If no one-to-one assignment to a corresponding  
 147 detector-level object is possible for any of the objects in the generator-level  $t\bar{t}$  system, the event  
 148 is considered as “nonreconstructable”.

149 For the reconstruction all possible permutations of assigning detector-level jets to the corre-  
 150 sponding  $t\bar{t}$  decay products are tested and a likelihood that a certain permutation is correct  
 151 is evaluated. Permutations are considered only if the two jets with the highest b identifica-  
 152 tion probabilities are the two b jet candidates. In each event, the permutation with the highest  
 153 likelihood is selected.

154 For each tested permutation the neutrino four-momentum  $p_\nu$  is reconstructed using the algo-  
 155 rithm of Ref. [18]. The idea is to find all possible solutions for the three components of the  
 156 neutrino momentum vector using the two mass constraints  $(p_\nu + p_\ell)^2 = m_W^2$  and  $(p_\nu + p_\ell +$   
 157  $p_{b_\ell})^2 = m_t^2$ . Each equation describes an ellipsoid in the three-dimensional momentum space of  
 158 the neutrino. The intersection of these two ellipsoids is usually an ellipse. We select  $p_\nu$  as the  
 159 point on the ellipse for which the distance  $D_{\nu,\min}$  between the ellipse projection onto the trans-  
 160 verse plane and  $\vec{p}_T^{\text{miss}}$  is minimal. This algorithm leads to a unique solution for the longitudinal  
 161 neutrino momentum and an improved resolution of its transverse component. For the cases  
 162 where the invariant mass of the lepton and  $b_\ell$  candidate is above  $m_t$  no solution can be found  
 163 and the corresponding permutation is discarded. The minimum distance  $D_{\nu,\min}$  is also used to  
 164 identify the correct  $b_\ell$ , as described below. This algorithm is also used in the reconstruction of  
 165 events with boosted top quark candidates and is referred to as “Neutrino-Solver”.

The value of  $D_{\nu,\min}$  from the neutrino reconstruction and the mass constraints on the hadroni-  
 cally decaying top quark are combined in a likelihood function  $\lambda$ , given by

$$-\log[\lambda] = -\log[P_m(m_2, m_3)] - \log[P_\nu(D_{\nu,\min})], \quad (1)$$

166 where  $P_m$  is the two-dimensional probability density of the invariant masses of W bosons and  
 167 top quarks that are correctly reconstructed, based on the matching criteria described above.  
 168 The value of  $\lambda$  is maximized to select the permutation of jets. The probability density  $P_m$  is  
 169 calculated as a function of the invariant mass of the two jets,  $m_2$ , tested as the W boson de-  
 170 cay products, and the invariant mass of the three jets,  $m_3$ , tested as the decay products of the  
 171 hadronically decaying top quark. The distributions for the correct jet assignments, taken from  
 172 the POWHEG+PYTHIA8 simulation and normalized to unit area, are shown in Fig. 1. This part  
 173 of the likelihood function is sensitive to the correct reconstruction of the hadronically decaying  
 174 top quark. For the 2m(1m1l) category  $-\log[P_m(m_2, m_3)] < 11(9)$  is required. This selection  
 175 removes more than 50% of multijet/W and single top backgrounds. For higher values almost  
 176 all  $t\bar{t}$  events are reconstructed incorrectly and are considered for a boosted reconstruction.

177 The probability density  $P_\nu$  describes the distribution of  $D_{\nu,\min}$  for a correctly selected  $b_\ell$ . In  
 178 Fig. 1 (lower), the normalized distributions of  $D_{\nu,\min}$  for  $b_\ell$  and for other jets are shown. On  
 179 average, the distance  $D_{\nu,\min}$  for a correctly selected  $b_\ell$  is smaller and has a smaller tail compared

180 to the distance obtained for other jets. Permutations with values of  $D_{\nu,\min} > 150 \text{ GeV}$  are  
 181 rejected since they are very unlikely to originate from a correct  $b_\ell$  association. This part of  
 182 the likelihood function is sensitive to the correct reconstruction of the leptonically decaying  
 183 top quark.

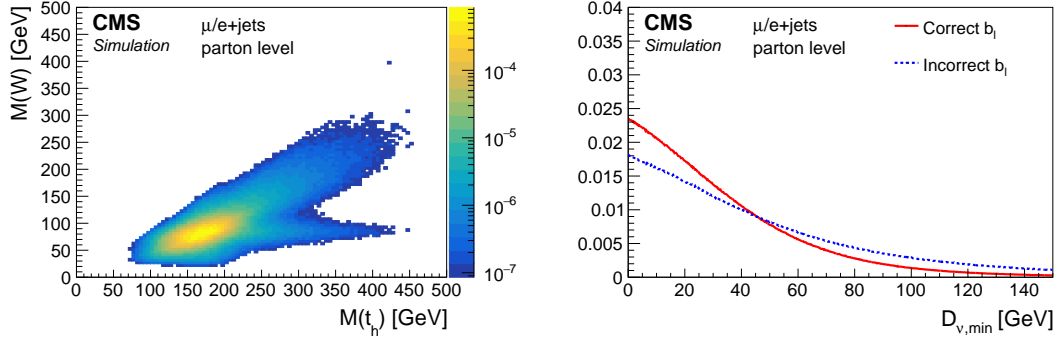


Figure 1: Normalized two-dimensional mass distribution of the correctly reconstructed hadronically decaying W bosons  $M(W)$  and the correctly reconstructed top quarks  $M(t_h)$  (left). Normalized distributions of the distance  $D_{\nu,\min}$  for correctly and incorrectly selected  $b$  jets from the leptonically decaying top quarks (right). The distributions are taken from the POWHEG+PYTHIA8 $t\bar{t}$  simulation.

184 A comparison of data to the simulation of variables related to the reconstruction of the resolved  
 185  $t\bar{t}$  system are shown in Figs. 2 and 3 for the 2m and 1m1l categories, respectively.

## 186 5 Identification and reconstruction of boosted leptonically decay- 187 ing top quarks

188 For  $p_T(t_\ell) > 400 \text{ GeV}$  the separation between the lepton and the  $b$  jet becomes increasingly  
 189 small and the isolation cone of the lepton starts overlapping with constituents of the  $b$  jet.  
 190 In this case the leptons do not fulfill the standard isolation criterion. Therefore, we remove  
 191 the isolation criteria from the lepton selection requirements. These nonisolated leptons are  
 192 selected with  $p_T > 50 \text{ GeV}$  and  $|\eta| < 2.4$ . We look for a loose-tagged  $b$  jet within  $\Delta R = 0.6$   
 193 around such a lepton. If the lepton is a constituent of the jet, its momentum is subtracted  
 194 from the jet momentum to avoid a double counting. Afterwards, the neutrino momentum is  
 195 determined using the Neutrino-Solver. This uses the W boson and top quark mass constraints  
 196 to calculate the  $p_z$  of the neutrino and to improve its  $p_T$  resolution compared to the  $p_T^{\text{miss}}$ . If the  
 197 resulting  $p_T$  sum of the lepton, the  $b$  jet, and the neutrino is  $> 400 \text{ GeV}$ , we consider this as a  
 198 boosted  $t_\ell$  candidate. Candidates that are incompatible with the mass constraints imposed by  
 199 the neutrino solver are removed with the requirement of  $D_\nu < 150 \text{ GeV}$  (Fig. 4), where  $D_\nu$  is  
 200 the distance in the transverse momentum plane between the  $p_T^{\text{miss}}$  and the closest point on the  
 201 ellipse that represents possible solutions.

202 In Fig. 5 the distributions of  $\Delta R(t_{\text{rec}}, t_{\text{gen}})$  is shown and a good reconstruction of the direction  
 203 and the momentum is observed. In addition, the scales and resolutions of  $p_T$  and  $p_z$  are shown.  
 204 The momentum resolution is about 10% for the whole  $p_T$  range. The reconstructed momenta  
 205 are in good agreement with the momenta of the parton-level top quarks. The momentum scales  
 206 are flat as a function of  $p_T$ .

207 The reconstructed candidates might be jets containing a lepton from a hadron decay or from  
 208 a leptonically decaying W boson produced within the jet. Based on the following variables

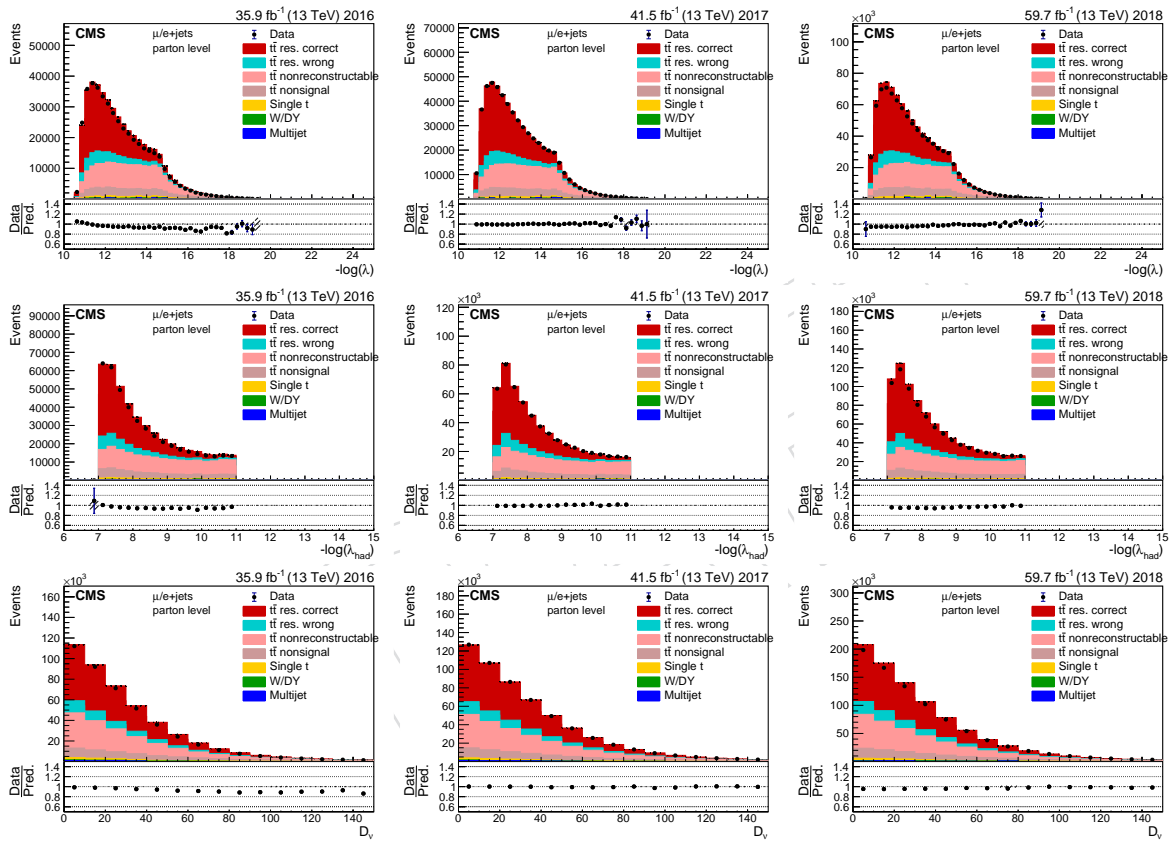


Figure 2: Comparison of data and simulation of variables related to the resolved reconstruction in the 2m category. The hatched uncertainty shows the statistical uncertainties in the prediction.

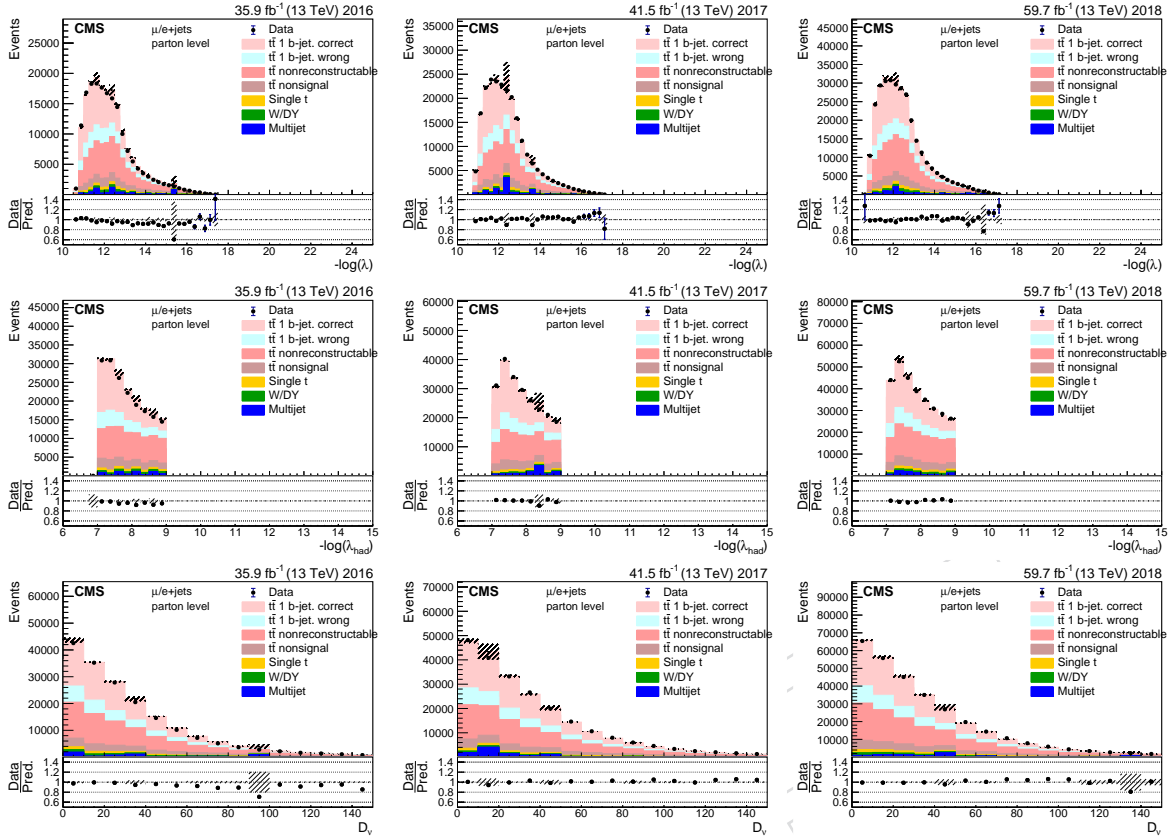


Figure 3: Comparison of data and simulation of variables related to the resolved reconstruction in the 1m1l category. The hatched uncertainty shows the statistical uncertainties in the prediction.

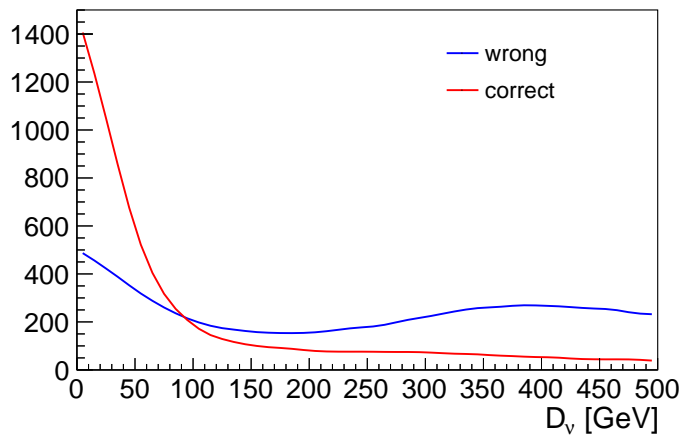


Figure 4: Distribution of  $D_\nu$ . A cut of  $D_\nu < 150$  GeV is used to reduce wrongly reconstructed  $t_\ell$ .

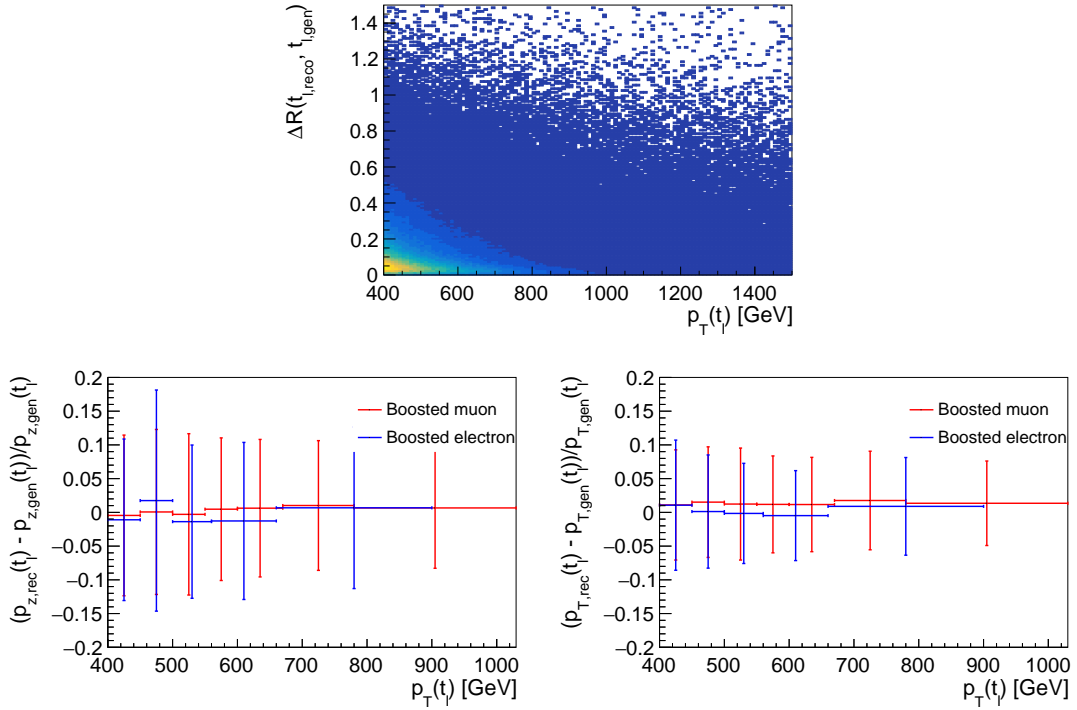


Figure 5: Distribution of  $\Delta R(t_{\text{rec}}, t_{\text{gen}})$  (top). And the  $p_T$  and  $p_z$  scales and their resolutions (error bars) for the boosted leptonically decaying top quarks (bottom).

209 we use an artificial neural network (NN) to discriminate between top quark and background  
 210 candidates:

- 211     •  $M(\ell, j)$
- 212     •  $p_T(\ell)/p_T(\ell + j)$
- 213     •  $M(j)/M(\ell, j)$
- 214     •  $I_{\text{far}}/I_0$
- 215     •  $I_{\text{near}}/I_0$

216 with the isolation variables  $I = \sum_{\text{PF objects}} p_T(\text{PF obj.}) \Delta R^q(\ell, \text{PF obj.})$  with  $q = -2, 0, 2$  for  $I_{\text{near}}$ ,  
 217  $I_0$ , and  $I_{\text{far}}$ , respectively. The variables are shown in Fig. 6. Two NNs are used: one for  
 218  $400 < p_T(\ell) < 650 \text{ GeV}$  and one for  $p_T(\ell) > 650 \text{ GeV}$ . The muon and electron channels  
 219 are combined. The NNs consist of a 5 node input layer, three fully connected hidden layers  
 220 with 20, 10, and 5 nodes, and single output node. The activation function is tanh in all layers.  
 221 The logistic loss function is minimized using stochastic gradient descent with the Adam  
 222 algorithm. A training sample of 2000  $t\bar{t}$  and 2000 QCD/W background events is used. During  
 223 the training we verify that the loss function for a statistically independent validation sample is  
 224 falling to protect against overtraining.

225 The selected variables are very powerful in reducing the multijet background, while W bosons  
 226 produced within a b jet are hard to distinguish from the boosted  $t_\ell$ . On the neural network  
 227 output variable we apply the requirement  $L_{\text{NN}} > 0.7$ . This selection has a signal efficiency  
 228 of 87% at  $p_T = 500 \text{ GeV}$  decreasing slightly toward higher  $p_T$ , with about 80% efficiency at  
 229  $p_T = 1000 \text{ GeV}$ .

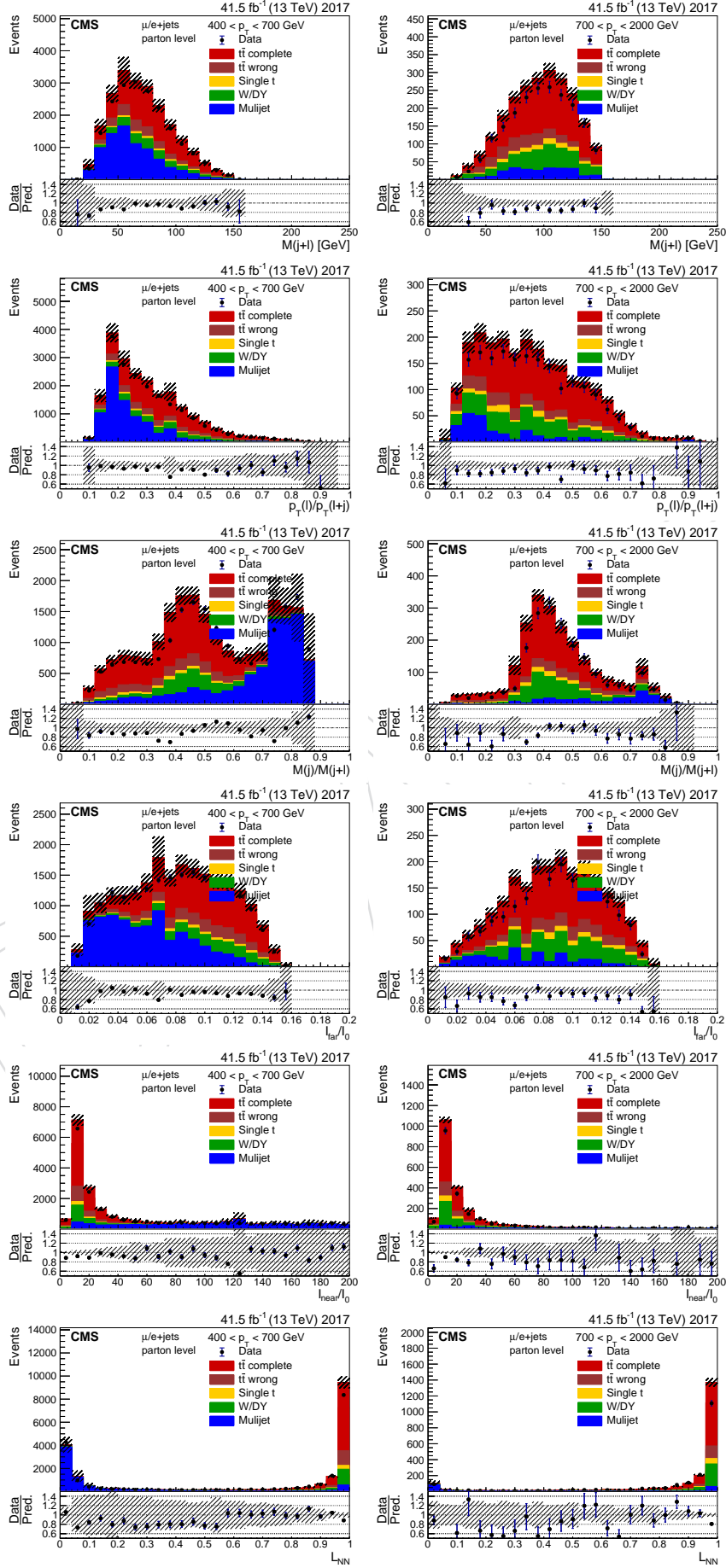


Figure 6: Distribution of variables used as input to the NN for the identification of a boosted  $t_\ell$  for 2017 (the other years can be found in Appendix H).

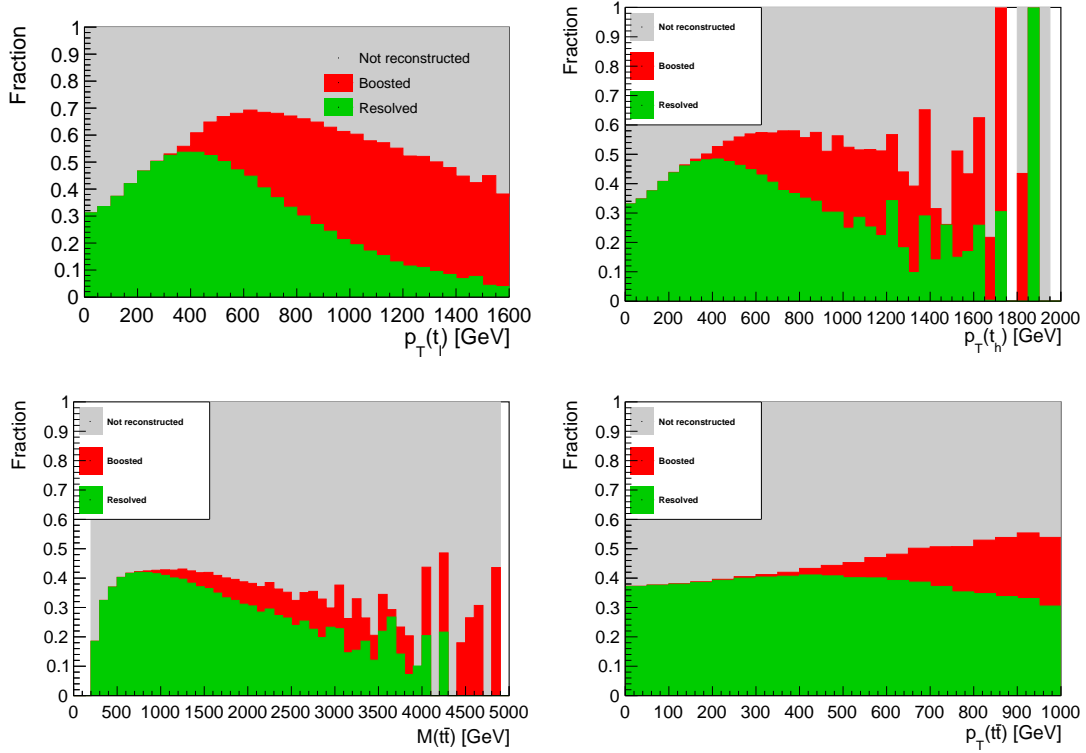


Figure 7: Fraction of the  $t_\ell$  reconstruction mode as function of various kinematic variables.

In Fig. 7 the fractions of resolved and boosted reconstructed  $t_\ell$  as a function of various kinematic variables are shown. As expected,  $p_T(t_\ell)$  profit most from the boosted reconstruction mode, but also the measured phase space  $M(t\bar{t})$  and  $p_T(t\bar{t})$  are extended.

## 6 Identification and reconstruction of boosted hadronically decaying top quarks

Boosted  $t_h$  candidates are identified as jets with a size parameter of 0.8,  $p_T > 400$  GeV,  $|\eta| < 1.6$ , and a jet mass  $M_{jet} > 120$  GeV. The jets are based on the PUPPI algorithm for pileup subtraction and the  $p_T$  of all PF constituents are rescaled according to theirs PUPPI weights before clustering. The momentum scale and resolution of the jets are corrected using the corresponding jet energy and resolution corrections.

To discriminate candidates containing top decay products from other jets, several properties of the candidates are used as input variables of a NN. Most of these quantities are calculated after boosting the jet constituents into their center-of-mass system and clustering them with the anti- $k_T$  jet algorithm with a size parameter of 0.5 to obtain a couple of sub-jets. Since these sub-jets are clustered in the center-of-mass frame and not in the laboratory frame, the special treatment of longitudinal and transverse components of the momentum is not meaningful. Therefore, instead of the longitudinal boost invariant variables  $p_T$  and  $\Delta R$ , the energy and the angle between objects are used in the jet-definition. We use the following input variables:

- From all combinations of two sub-jets calculate the invariant mass and use the three highest as input variables ( $M_{2,a-c}$ ).
- The number of combinations of two sub-jets whose invariant masses exceed 40 GeV

(pairs).

- From all combinations of three sub-jets calculate the invariant mass and use the two highest as input variables ( $M_{3,a-b}$ ).
- The ratio of the highest invariant mass of three sub-jets over the mass of all constituents ( $M_{3,a} / M_{\text{jet}}$ ).
- The ratios of n-jettiness  $\tau_2/\tau_1, \tau_3/\tau_2, \tau_4/\tau_3$ , and  $\tau_5/\tau_4$  with  $\tau_N = c \sum_k \min(q_1 \cdot p_k, q_2 \cdot p_k, \dots, q_N \cdot p_k)$ , where  $q_i$  with  $1 \leq i \leq N$  are the momenta of the  $N$  leading jets and  $p_k$  are the momenta of all constituent in the rest-frame.
- The energy of the four highest energetic sub-jets ( $E(j_{a-d})$ ).
- The triple-product  $a \cdot (b \times c)$  of the three leading normalized sub-jets.
- The sphericity of all sub-jets. The sphericity  $s = \frac{3}{2}(\lambda_2 + \lambda_3)$  with  $\lambda_2$  and  $\lambda_3$  the second and third highest eigenvalues of the tensor  $S^{\alpha\beta} = \frac{\sum_i p_i^\alpha p_i^\beta / |p_i|}{\sum_i |p_i|}$ , where  $p_i$  are the momenta of the sub-jets in the rest-frame.
- Reboost the three leading sub-jets in the laboratory frame and calculate their momentum fractions of the whole jet ( $f_{a-c}$ ).

We always find at least three sub-jets (isolated leptons are removed from the jet collection). Some of the variables rely on at least four sub-jets. Those are set to zero in the very rare cases where a fourth sub-jet is missing. In Figs. 8–13, we show the distributions of all input variables and in Fig. 14 the output of the NN  $H_{NN}$  for two ranges of  $p_T(t_h)$ . The various components of the simulation are normalized according to the results of the template fit described in Section 9.

In fact, we use four NNs in different  $p_T(t_h)$  regions: 400–500 GeV, 500–700 GeV, 700–1000 GeV, and  $>1000$  GeV. The NNs consist of a 21 node input layer, four fully connected hidden layers with 63, 42, 42, and 21 nodes, and single output node. The activation function is tanh in all layers. The logistic loss function is minimized using stochastic gradient descent with the Adam algorithm. A training sample of 100000  $t\bar{t}$  signal and 100000  $t\bar{t}$  background events is used. During the training we verify that the loss function for a statistically independent validation sample is falling to protect against overtraining.

We consider two types of top candidates, “complete” and “broken”. Complete means that the AK8 jet used to define the top jet candidate is the closest jet (with  $\Delta R(\text{quark}, \text{jet}) < 0.8$ ) to the three quarks from the top quark decay. For a broken top candidate two quarks must point towards the AK8 jet. Broken top candidates present a significant contribution at intermediate transverse momentum ( $p_T < 600$  GeV). They are in general more difficult to distinguish from background. However, as shown in Fig. 15 the momentum response and resolution for the broken candidates is not much worse than for complete candidates. Therefore, we consider the identification of the broken top candidates as useful. The distribution of  $H_{NN}$  is also very stable as function of pileup interactions (Fig. 15 right).

In Fig. 16 the fractions of available reconstruction methods are shown as a function of  $p_T(t_h)$ ,  $M(t\bar{t})$ , and  $p_T(t\bar{t})$ . In certain ranges of the three quantities the boosted reconstruction provides an important contribution.

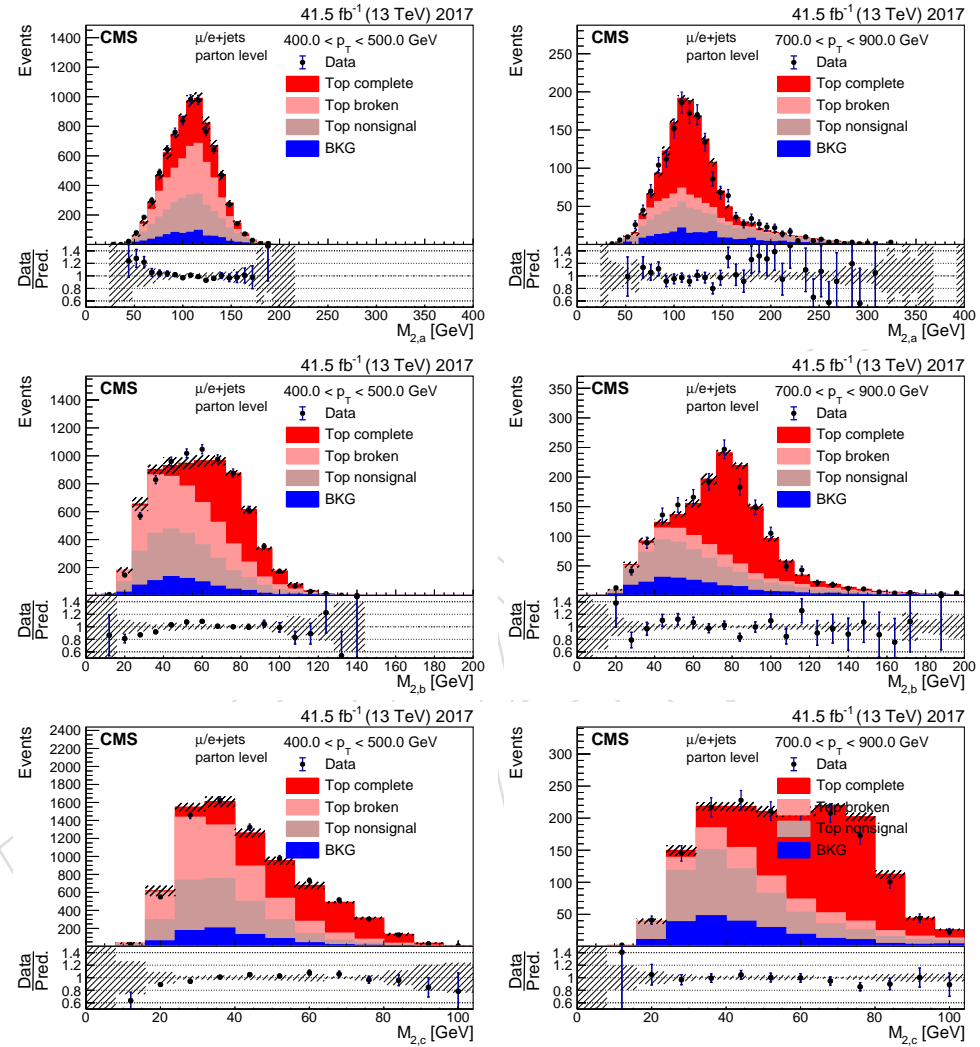


Figure 8: Variables used in the identification of boosted top quarks. The plots are shown for events with a reconstructed  $t_\ell$ . The normalization of the various components is obtained from a fit of  $H_{NN}$  used to extract the signal contributions (complete and broken top candidates) in 2017 (the other years can be found in Appendix H).

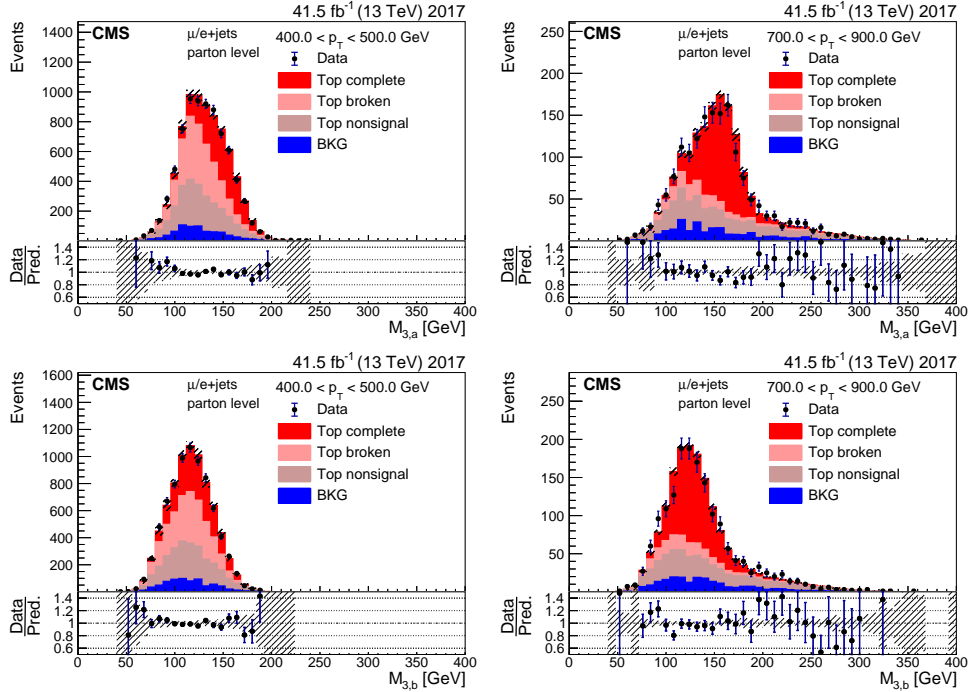


Figure 9: Variables used in the identification of boosted top quarks. The plots are shown for events with an reconstructed  $t_\ell$ . The normalization of the various components is obtained from a fit of  $H_{NN}$  used to extract the signal contribution (complete and broken top candidates) in 2017 (the other years can be found in Appendix H).

## 290 7 Event reconstruction and categorization

291 The first attempt for all events is the resolved reconstruction described in Section 4. If an event  
 292 passes the required selection criteria of the 2m category, no further attempt of a different recon-  
 293 struction is made. The same is true for 1m1l, but in these events no boosted  $t_h$  candidate must  
 294 exist.

295 If the event is not categorized as 2m or 1m1l but an isolated lepton, at least one b jet (medium  
 296 WP), and at least one boosted  $t_h$  candidate is found the event falls into the category BHRL  
 297 (resolved  $t_\ell$ , boosted  $t_h$ ). The  $t_\ell$  is reconstructed using the lepton and the closest b jet (minimum  
 298  $\Delta R(\ell, \text{bjet})$ ) for which the Neutrino-Solver finds a solution with  $D_\nu < 150 \text{ GeV}$ . If a  $t_\ell$  can be  
 299 reconstructed,  $t_h$  candidates with  $\Delta R(t_h, \ell) > 1.2$  and  $\Delta R(t_h, \text{bjet}) > 1.2$ , are considered. The  
 300 event is filled into histograms once for each available  $t_h$  candidate. Later a fit of the  $H_{NN}$  output  
 301 distribution is performed to estimate the fraction correct  $t_h$  candidates.

302 If no isolated lepton exists, but a boosted  $t_\ell$  with  $L_{NN} > 0.7$  is found, the event is filled into  
 303 histograms once for each boosted  $t_h$  candidate with  $\Delta R(t_\ell, t_h) > 1.2$ . We refer to this category  
 304 as BHBL (boosted  $t_\ell$ , boosted  $t_h$ ). As for the BHRL category the fraction of correct  $t_h$  candidates  
 305 is extracted with a fit of the  $H_{NN}$  output distribution. A brief overview of the various categories  
 306 and how they are used in the analysis is shown in Fig. 17.

307 The category with a boosted  $t_\ell$  and a resolved  $t_h$  is not used, since a boosted reconstruc-  
 308 tion for  $t_h$  is more often needed than for  $t_\ell$  and the fraction of these events is small. In addition, we  
 309 find a low fraction of correctly reconstructed  $t\bar{t}$  events. Since the nonisolated electron trigger re-  
 310 quires an additional jet above 165 GeV, it is not guarantied that these events are accepted by the  
 311 trigger. Therefore, we do not use this category, but consider these events as nonreconstructable.

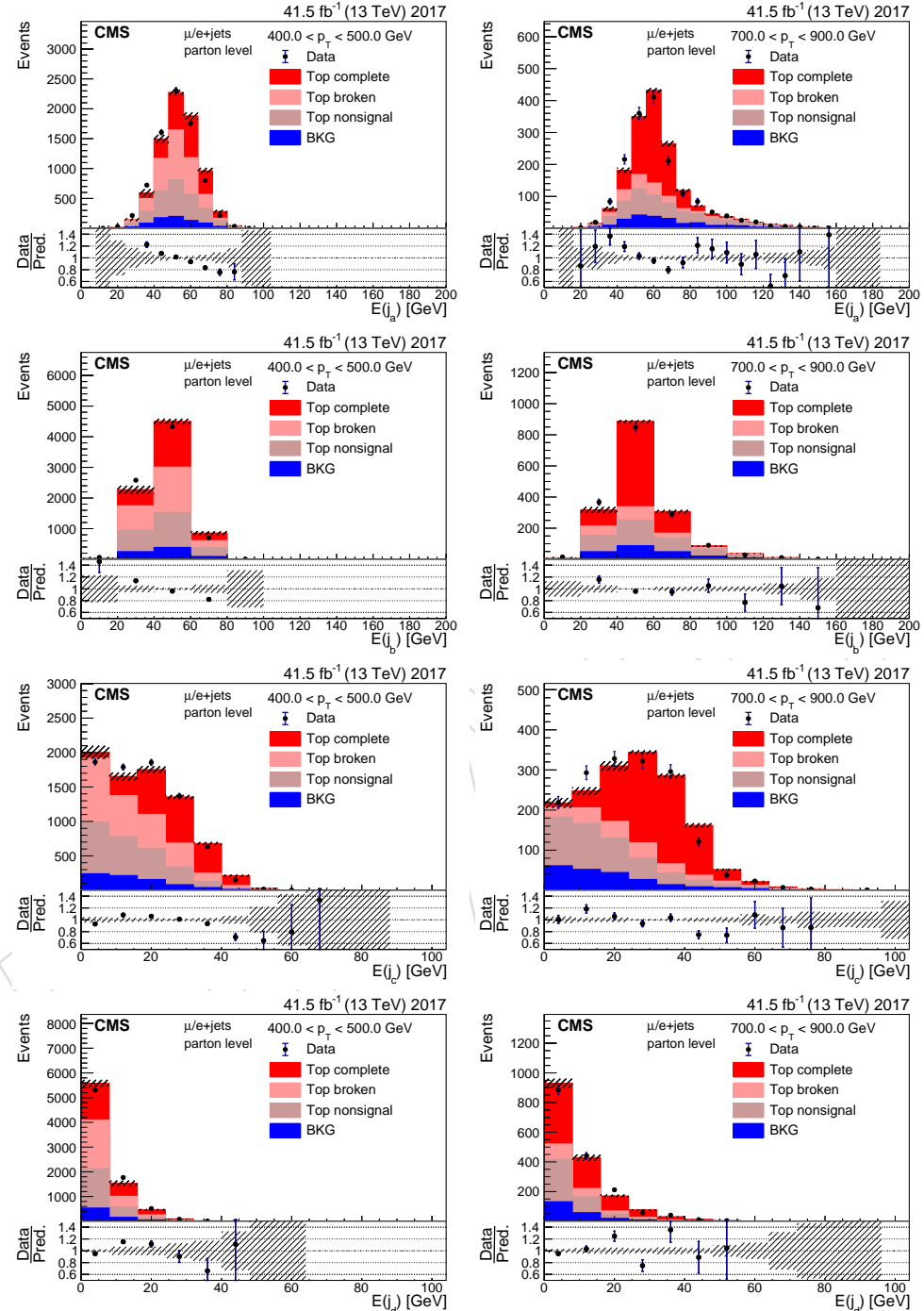


Figure 10: Variables used in the identification of boosted top quarks. The plots are shown for events with an reconstructed  $t_\ell$ . The normalization of the various components is obtained from a fit of  $H_{NN}$  used to extract the signal contribution (complete and broken top candidates) in 2017 (the other years can be found in Appendix H).

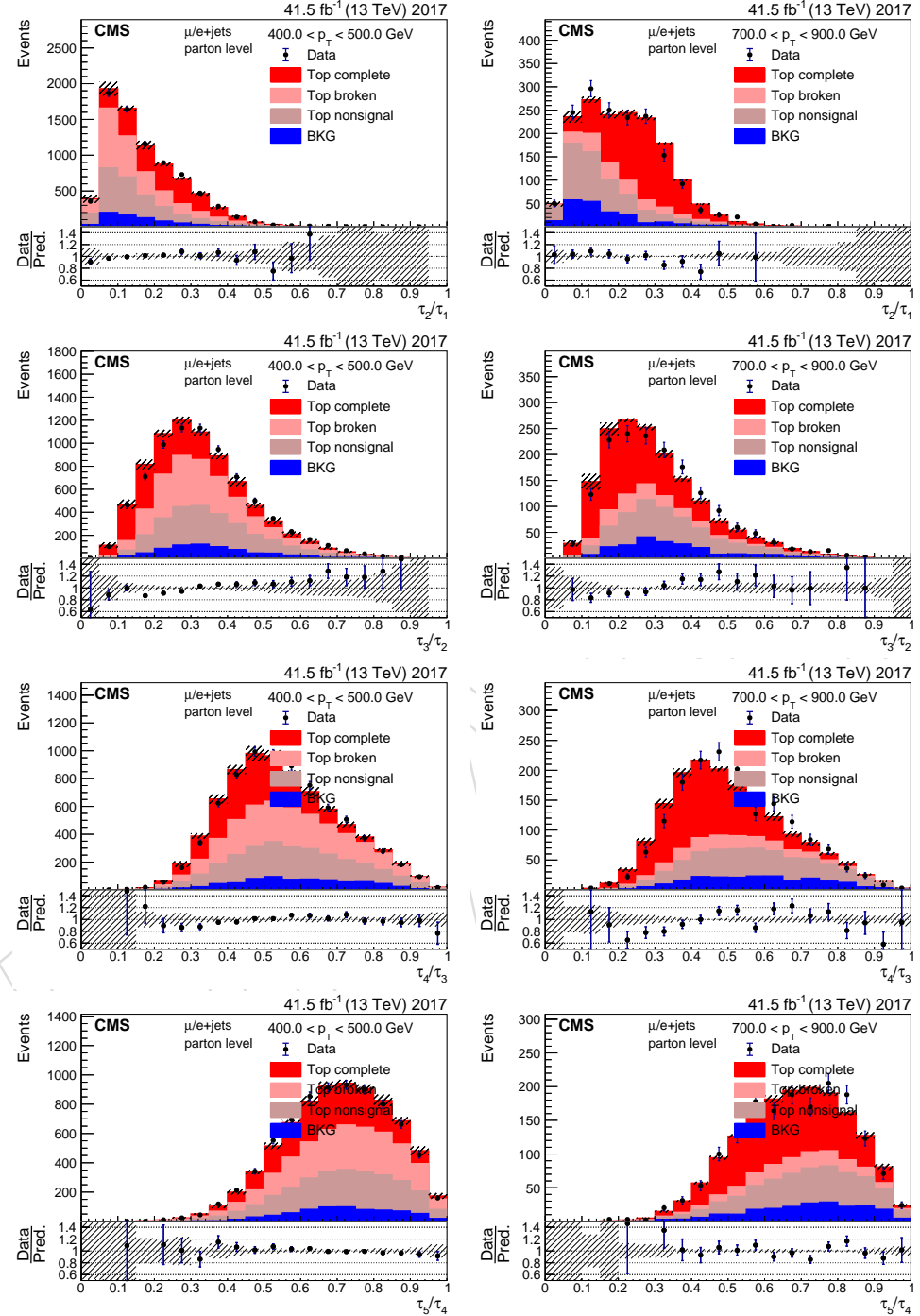


Figure 11: Variables used in the identification of boosted top quarks. The plots are shown for events with an reconstructed  $t_\ell$ . The normalization of the various components is obtained from a fit of  $H_{NN}$  used to extract the signal contribution (complete and broken top candidates) in 2017 (the other years can be found in Appendix H).

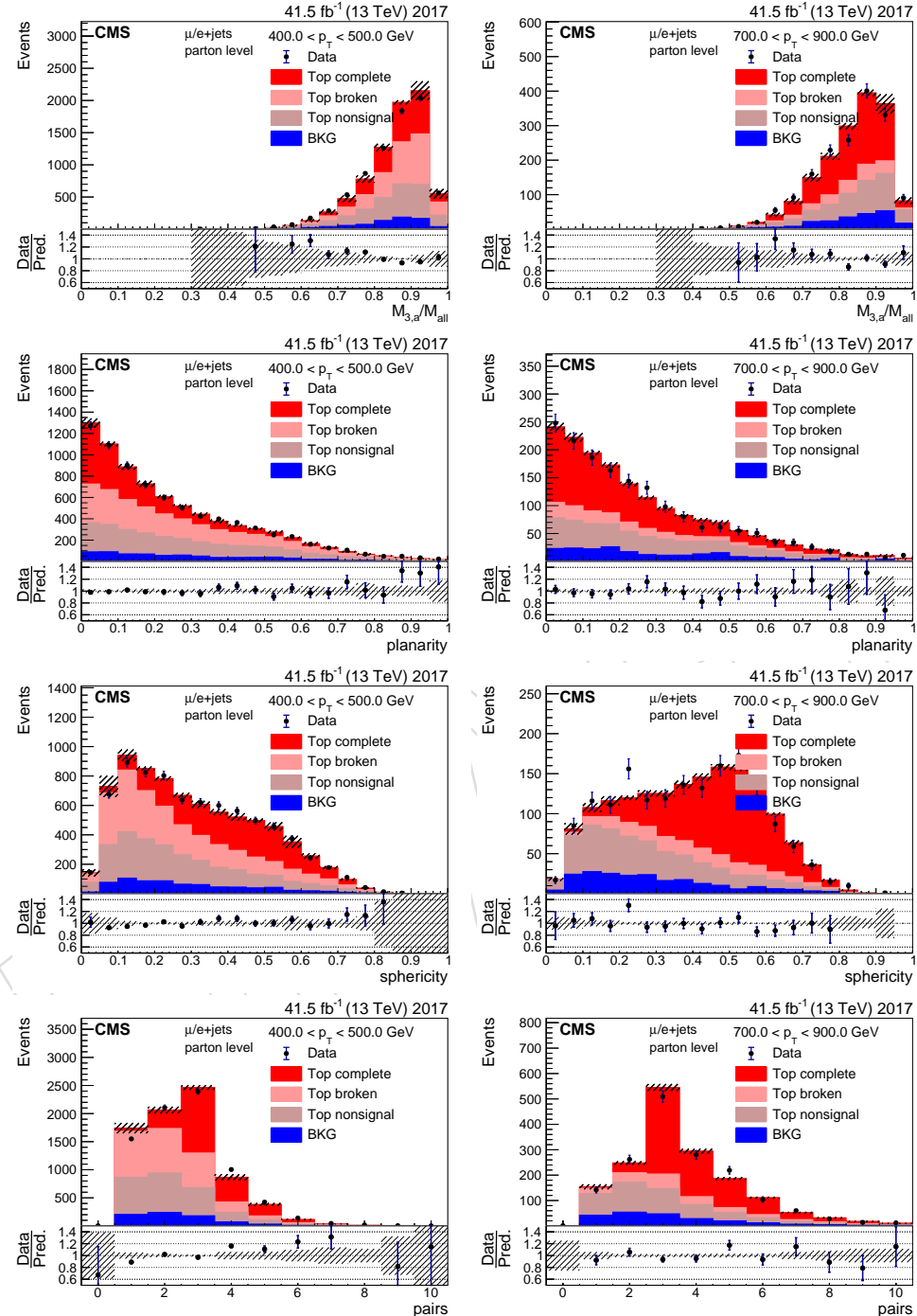


Figure 12: Variables used in the identification of boosted top quarks. The plots are shown for events with an reconstructed  $t_\ell$ . The normalization of the various components is obtained from a fit of  $H_{NN}$  used to extract the signal contribution (complete and broken top candidates) in 2017 (the other years can be found in Appendix H).

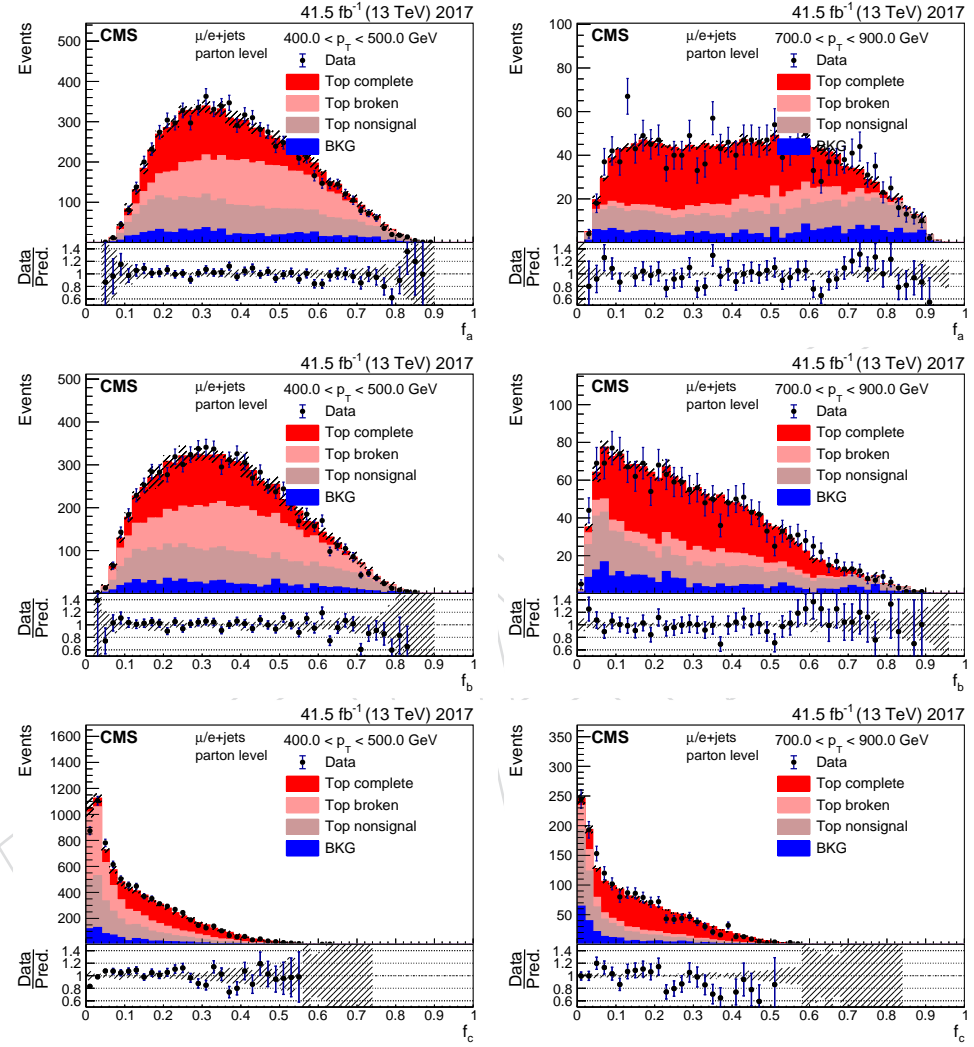


Figure 13: Variables used in the identification of boosted top quarks. The plots are shown for events with an reconstructed  $t_\ell$ . The normalization of the various components is obtained from a fit of  $H_{NN}$  used to extract the signal contribution (complete and broken top candidates) in 2017 (the other years can be found in Appendix H).

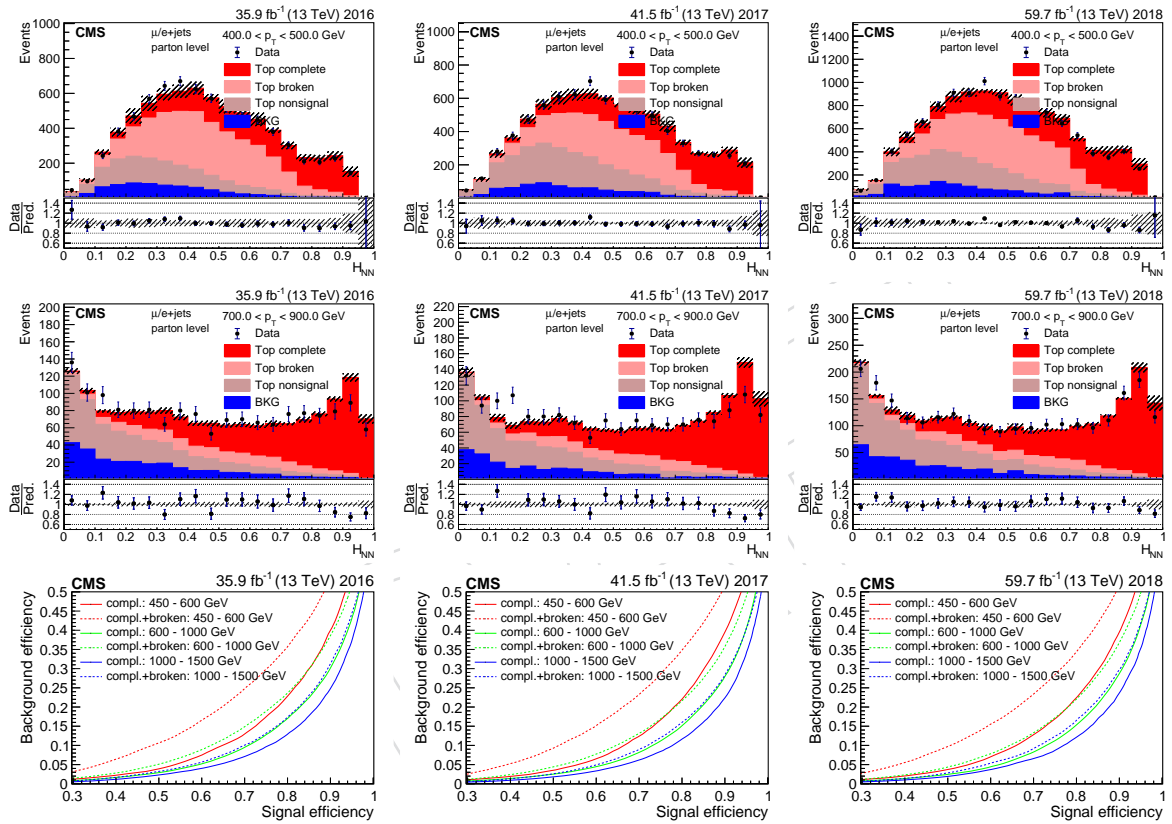


Figure 14: Output of the NN  $H_{NN}$ . The plots are shown for events with an reconstructed  $t_\ell$ . The normalization of the various components is obtained from a fit of  $H_{NN}$  used to extract the signal contribution (complete and broken top candidates.). The bottom plots show the background selection efficiency as function of the signal selection efficiency in various  $p_T$  regions.

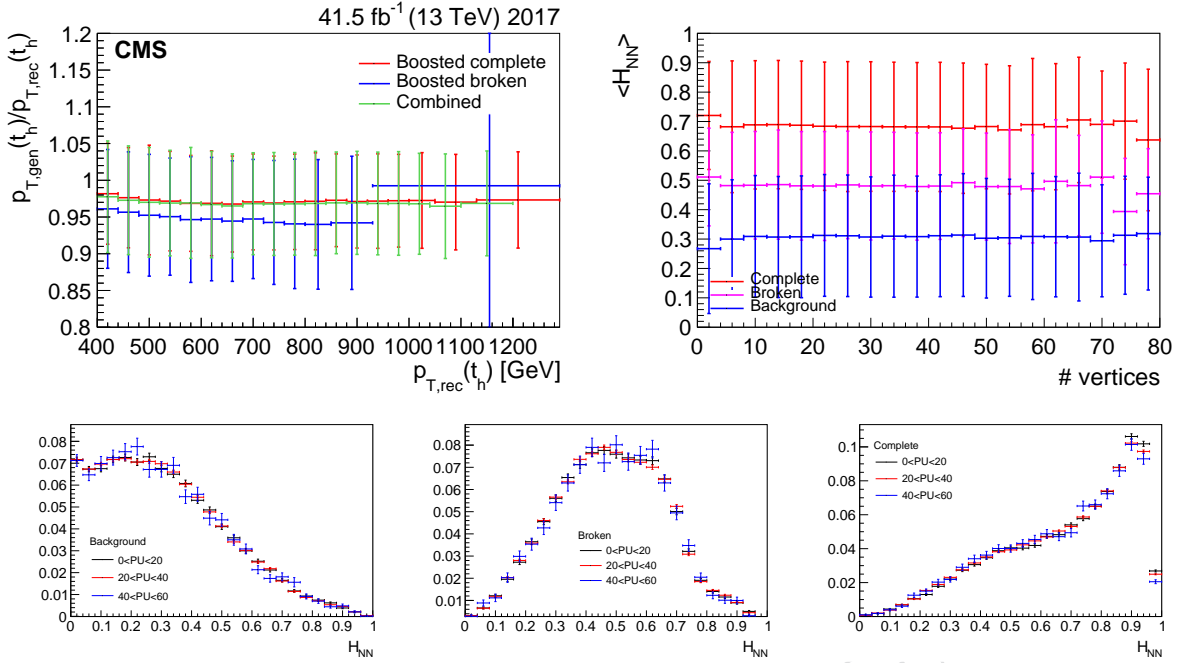


Figure 15: Energy scale and resolution (as uncertainty) of reconstructed complete and broken top quarks as a function of  $p_T$  (left). Mean and standard deviation of  $H_{NN}$  as function of the number of primary vertices (right). The lower row shows the template shapes for low, medium, and high pileup.

<sup>312</sup> In Figs. 18–22 comparisons of data and simulation are shown for the various categories.

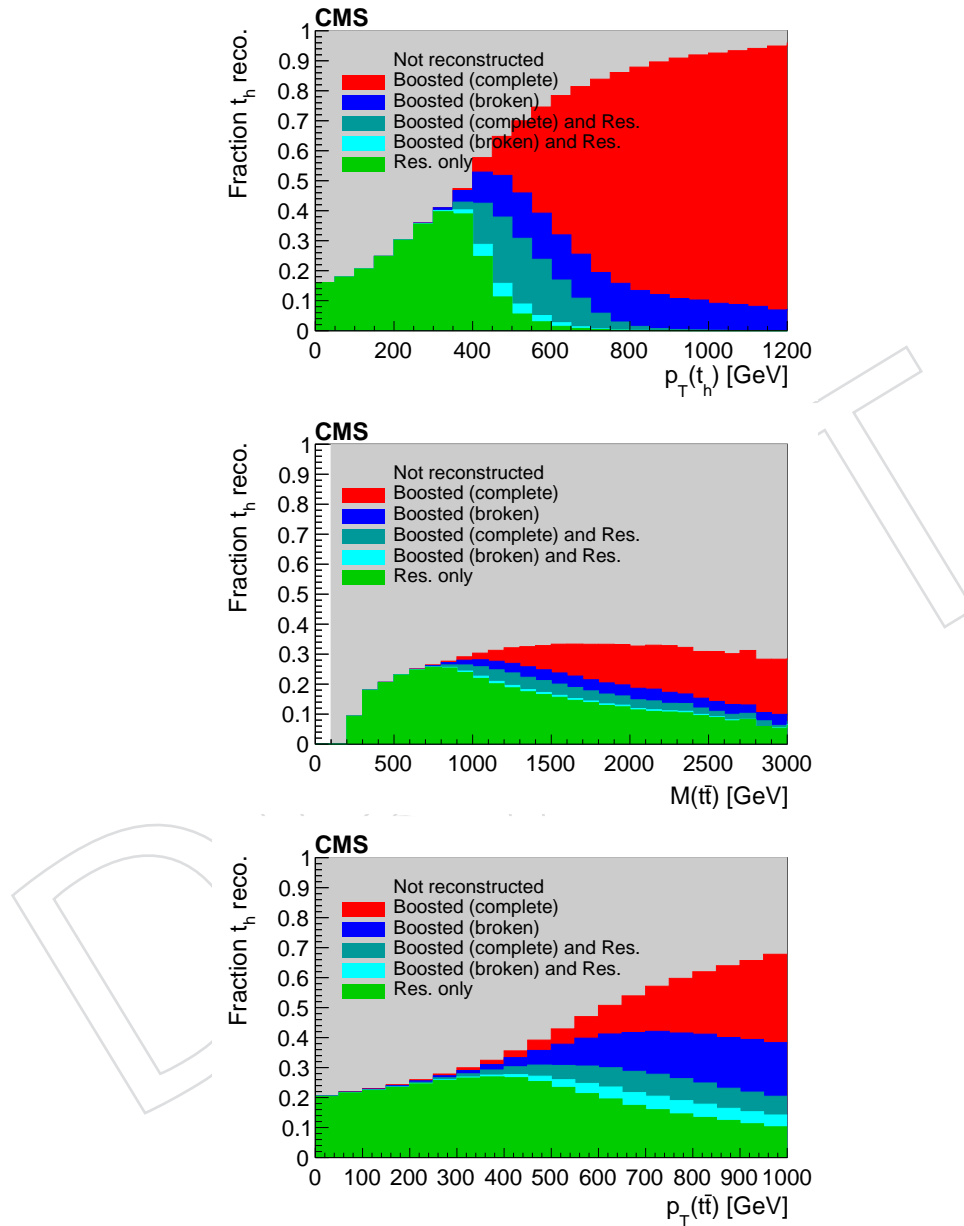


Figure 16: Fractions of possible reconstruction methods of the hadronically decaying top quarks as function of various kinematic variables.

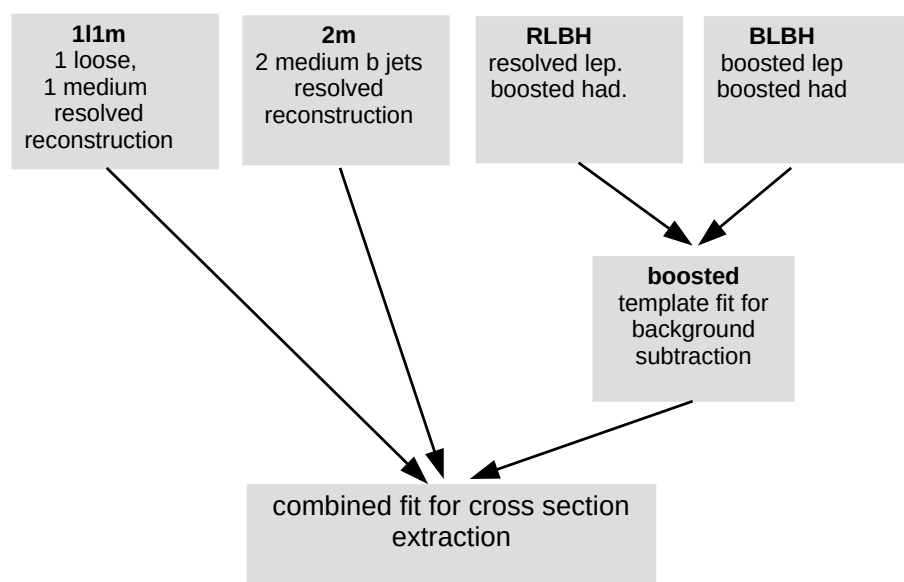


Figure 17: Overview of categories and the analysis workflow.

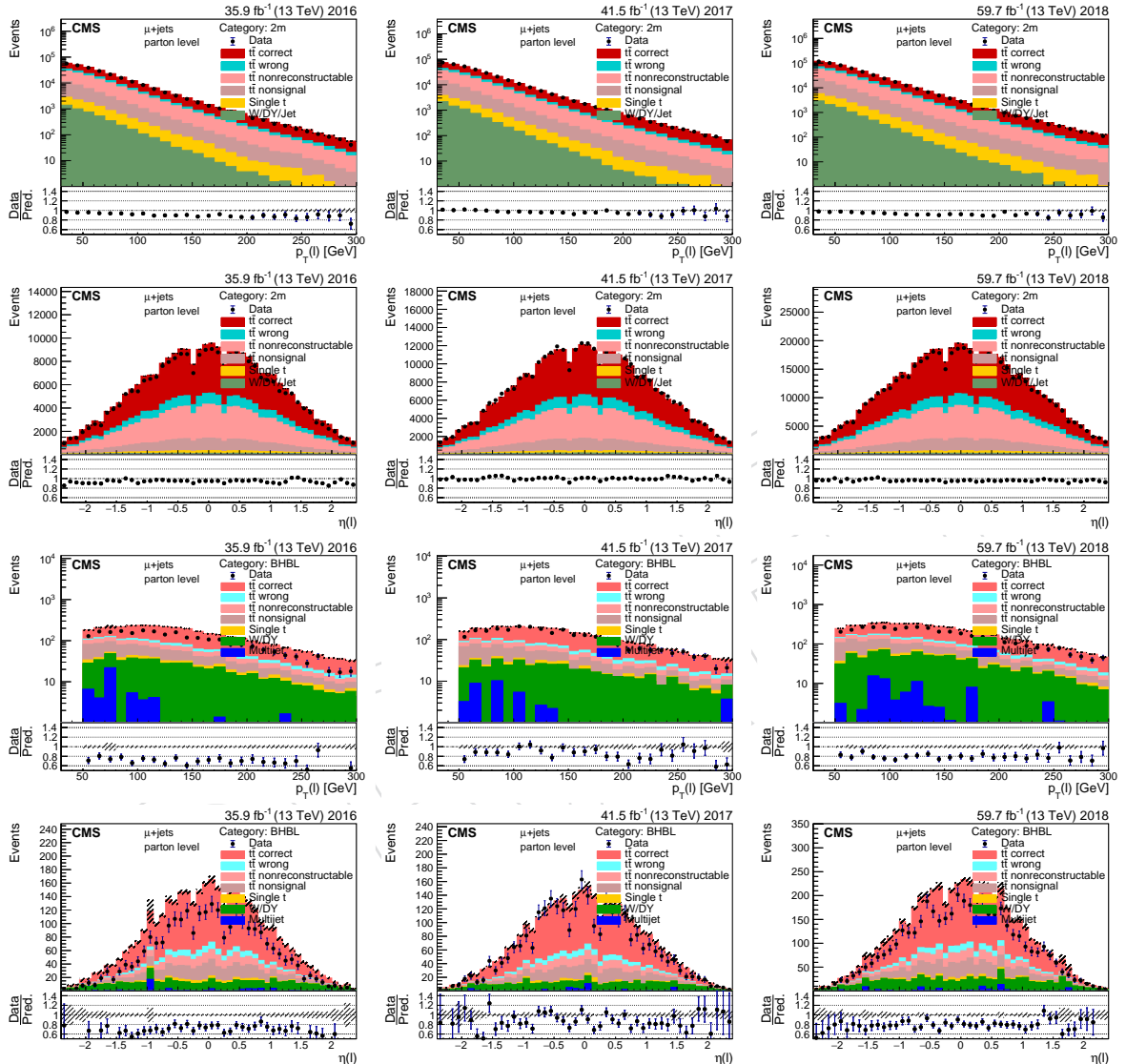


Figure 18: Data to simulation comparisons of the muon  $p_T$  and  $\eta$  for the three years. The upper two rows show the 2m category with isolated muons the lower two rows show the BHBL category with nonisolated muons. The hatched uncertainty shows the statistical uncertainties in the prediction.

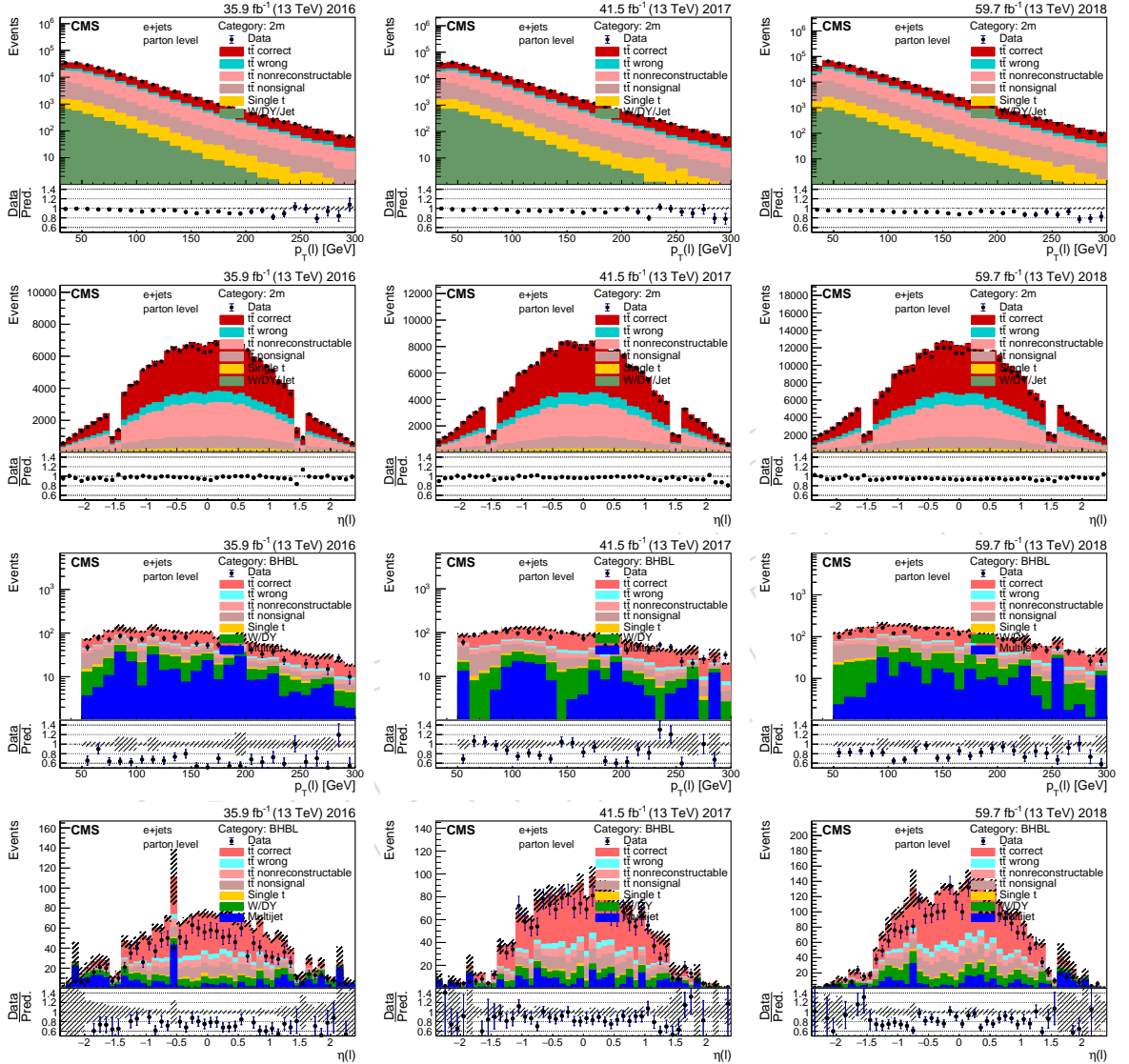


Figure 19: Data to simulation comparisons of the electron  $p_T$  and  $\eta$  for the three years. The upper two rows show the 2m category with isolated electrons the lower two rows show the BHBL category with nonisolated electrons. The hatched uncertainty shows the statistical uncertainty in the prediction.

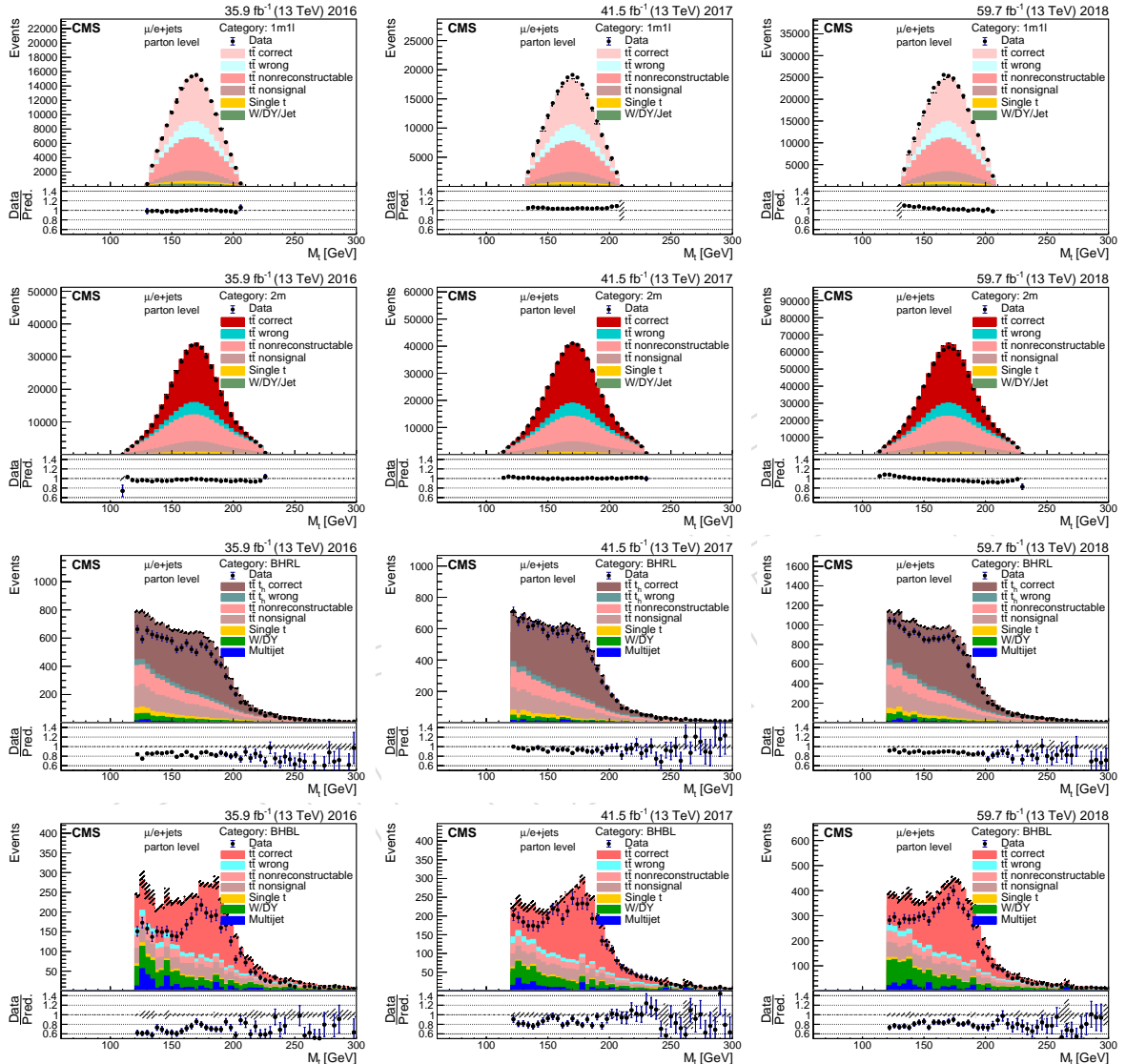


Figure 20: Data to simulation comparisons of the reconstructed  $m_t$  of the  $t_h$  for the three years. From top to bottom these are the categories: 1m1l, 1m, BHRL, BHBL. The hatched uncertainty shows the statistical uncertainties in the prediction.

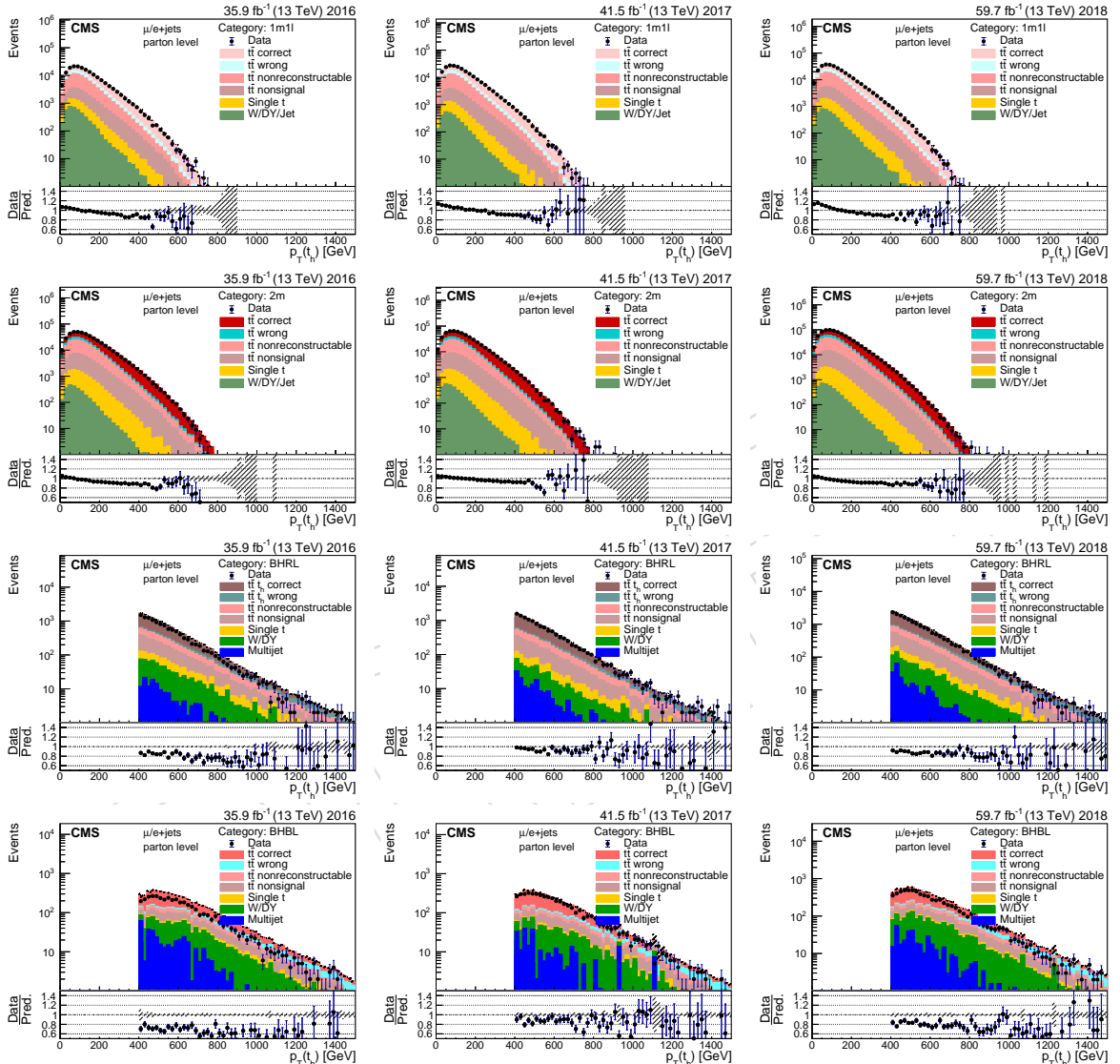


Figure 21: Data to simulation comparisons of the reconstructed  $p_T(t_h)$  for the three years. From top to bottom these are the categories: 1m1l, 1m, BHRL, BHBL. The hatched uncertainty shows the statistical uncertainties in the prediction.

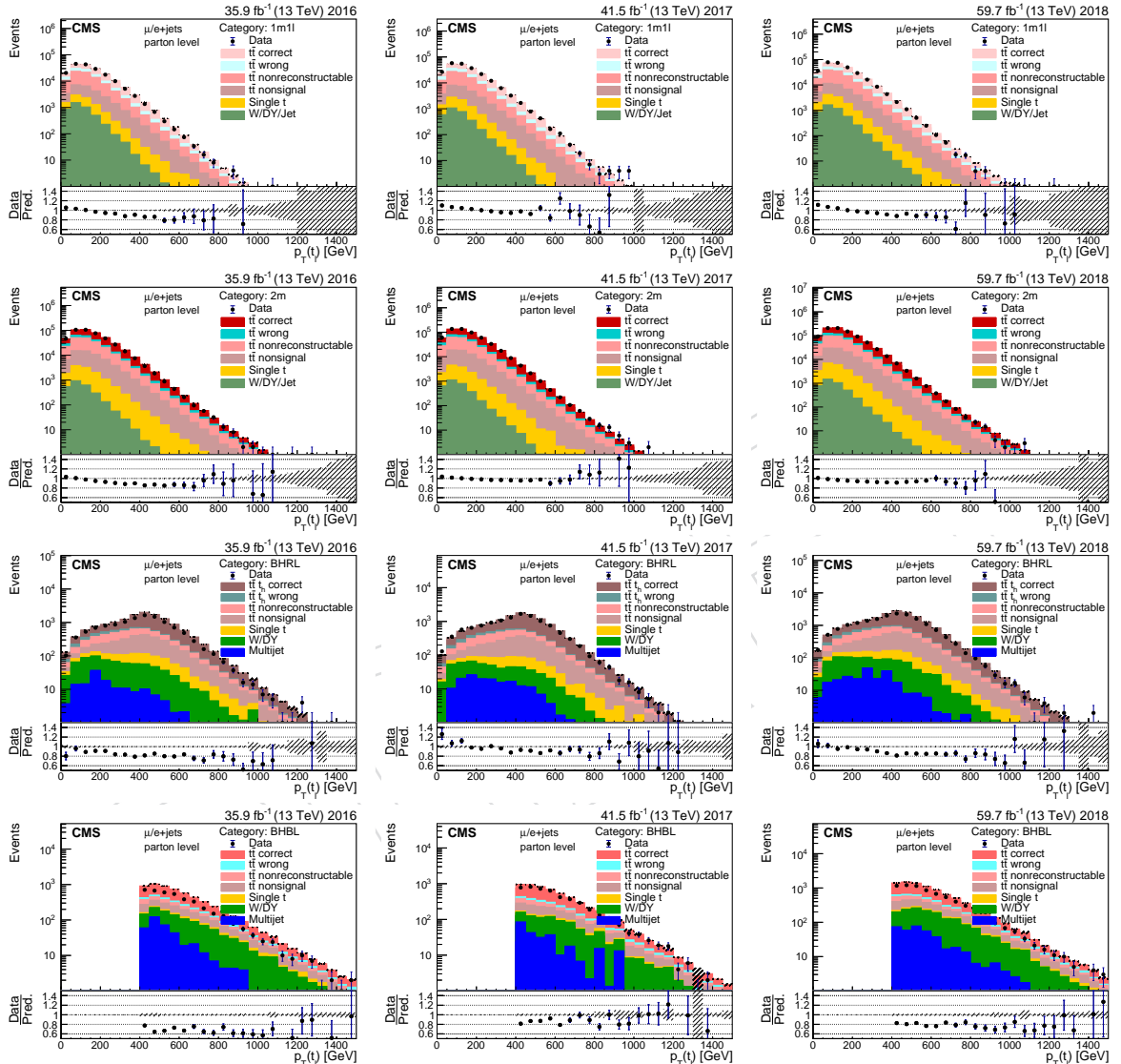


Figure 22: Data to simulation comparisons of the reconstructed  $p_T(t_\ell)$  for the three years. From top to bottom these are the categories: 1m1l, 1m, BHRL, BHBL. The hatched uncertainty shows the statistical uncertainties in the prediction.

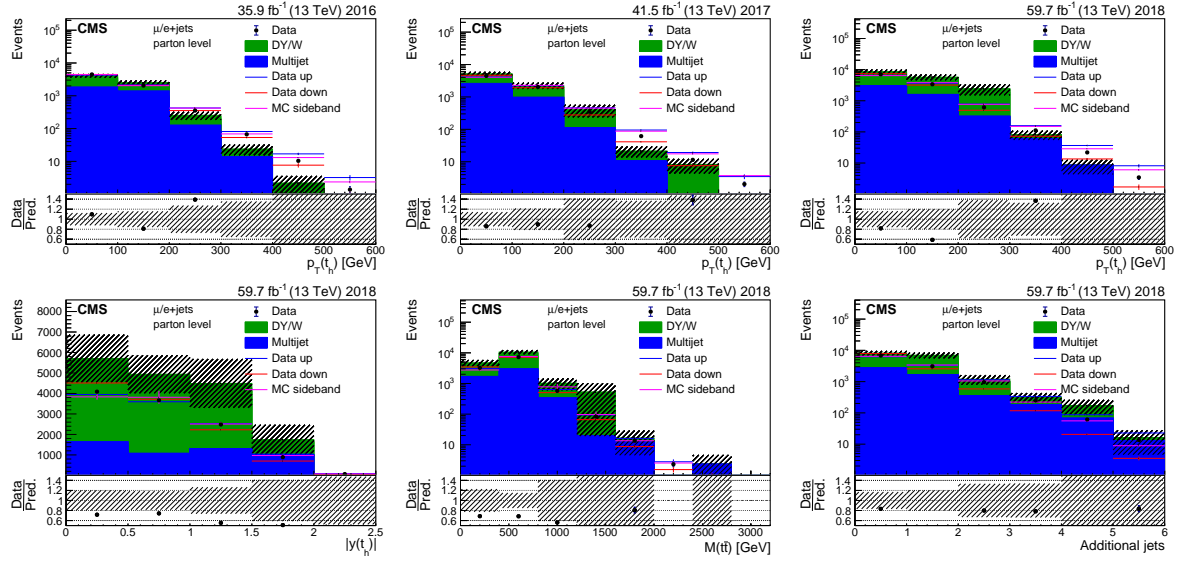


Figure 23: Comparison of the background shapes from the control region and the simulation in the signal region in the 2m category. The red and blue lines show the shape uncertainties obtained by varying the selection of the control region. The hatched uncertainty shows the statistical uncertainties in the prediction.

## 8 Background subtraction in the resolved categories

In the resolved categories (2m, 1m1l) the multijet and DY/W backgrounds are subtracted using a combined template of the two backgrounds that is obtained from a b-jet reduced control region. The simulation of these backgrounds suffer from large statistical uncertainties. In the 2m and 1m1l categories these backgrounds form a fraction of 1.5% and 5.5%, respectively. We repeat exactly the reconstruction algorithms but for events with the highest value of the b-tagging discriminant between 0.1 and 0.2. The range of the discriminant was selected to reach a good agreement between the distributions in the control region and the simulated prediction of the background in the signal region this is verified using a coarse binning shown in Figs. 23 and 24. Deviations between the simulated backgrounds and the distributions in the control region are covered by variations obtained with the different ranges between 0–0.1 (down) and 0.1–0.3 (up) of the b-tagging discriminant.

The normalization of this backgrounds is obtained from the comparison of data and simulation in the control region as shown in Fig. 25. After subtracting the predicted yield of  $t\bar{t}$  events the ratio of the observed and simulated yields is used to scale the predicted event yield in the signal region. The difference from one and the statistical uncertainty in the simulations are taken as uncertainties in the normalization of these backgrounds. This results in a normalization uncertainty of about 50%.

The obtained background predictions with their shape and normalization uncertainties are included in the fitting procedure for the cross section extraction as described in Section 10. Since statistical uncertainties in the simulations contribute mostly, the background normalization is considered as uncorrelated among the years. However, since the same method is used to derive the shape of the distribution, this uncertainty is expected to be correlated among the year.

The contribution of single top quark production is about 2.5% in the 2m and 1m1l categories. Templates according to their SM expectation are taken from the simulation. We evaluate the dominant uncertainties in these templates: matrix elements scales ( $\mu_r$ ,  $\mu_f$ ), jet energy scales, and b-tagging efficiency and include them in the fit. The scale uncertainty are treated inde-

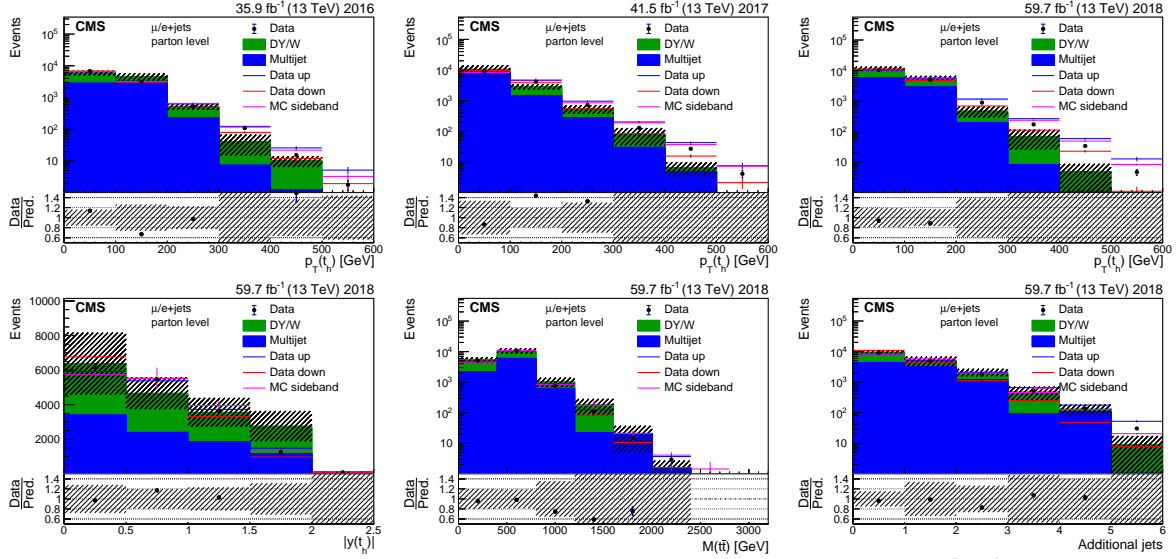


Figure 24: Comparison of the background shapes from the control region and the simulation in the signal region in the 1m1l category. The red and blue lines show the shape uncertainties obtained by varying the selection of the control region. The hatched uncertainty shows the statistical uncertainties in the prediction.

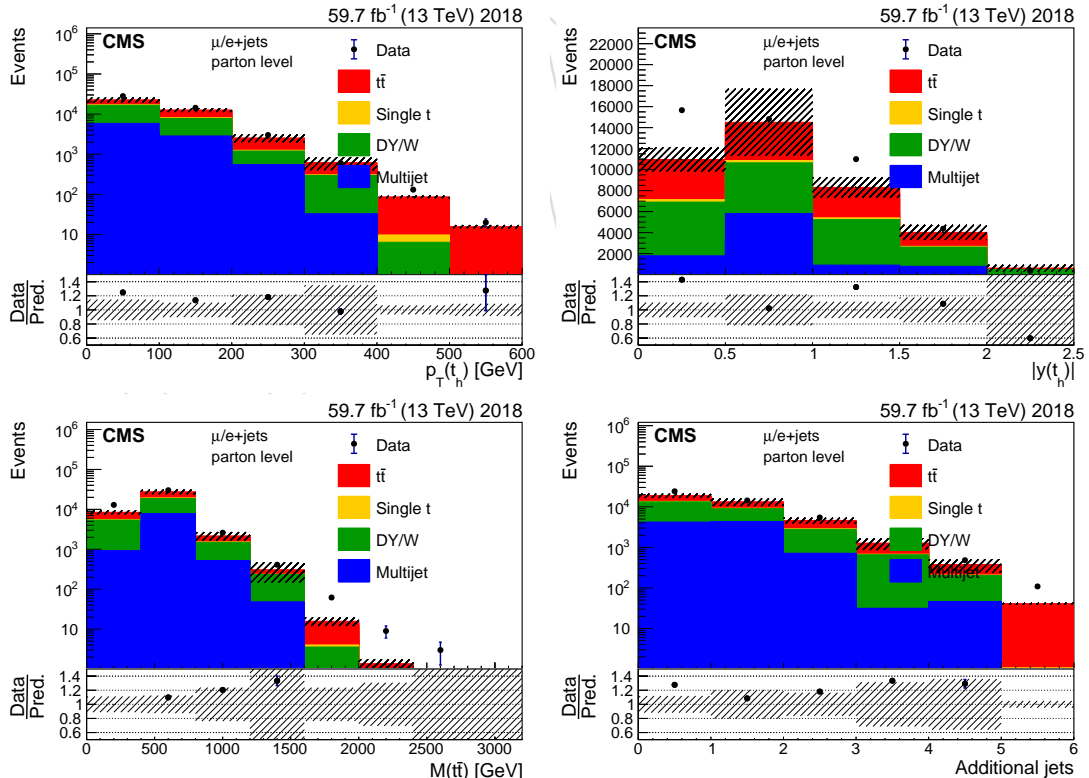


Figure 25: Comparison of data and prediction in the control region. The hatched uncertainty shows the statistical uncertainties in the prediction.

---

<sup>340</sup> pendently from the corresponding variations of the  $t\bar{t}$  simulation. However, the experimental  
<sup>341</sup> uncertainties are fully correlated.

DRAFT

## 342 9 Background subtraction in categories with boosted hadronically 343 decaying top quarks

344 Events with boosted  $t_h$ , categories BHRL and BHBL, are added and template fits based on the  
 345 distribution of  $H_{NN}$  are used to extract the signal yields. Since the shape of  $H_{NN}$  is changing  
 346 with  $p_T(t_h)$ , the template fit is always performed in the following bins of  $p_T(t_h)$ : 400, 450, 500,  
 347 550, 600, 700, 800, 900, 1000, 1500. This means in each bin of a variable under consideration we  
 348 fit 9  $p_T$  bins (not all bins have to be populated, or are populated only with a few events). The  $t\bar{t}$   
 349 templates are taken from the simulation after applying the full event selections. Separate tem-  
 350 plates for the contribution of complete and broken  $t_h$  are used. The  $t\bar{t}$  background templates  
 351 contain all other selected candidates, i.e., either with a single quark pointing towards it or a jet  
 352 not related to a  $t_h$  decay. No prior is used for the normalization of the  $t\bar{t}$  templates. Single top  
 353 background templates are taken from the Simulation and normalized to their SM expectation  
 354 with a Gaussian prior representing normalization uncertainty. The two background templates  
 355 of W/Z boson and multijet production are determined from a control region in the data. The  
 356 two backgrounds have slightly different shapes due to different compositions of quark and  
 357 gluon jets. The templates are normalized to the SM prediction and a Gaussian prior corre-  
 358 sponding to an uncertainty of 50% is used for the W/Z boson and multijet templates. These  
 359 50% uncertainties are meant to guide the fit to a minimum similar to the expectations. Since  
 360 the background shapes are very similar, the obtained fraction of the background components  
 361 becomes rather arbitrary if the constraints are removed. However, this does not affect the ex-  
 362 tracted signal fraction significantly.

363 The shapes of the templates are only varied as function of  $p_T(t_h)$ . However, we split the tem-  
 364 plates into two regions with  $|\eta(t_h)| < 0.8$  and  $0.8 < |\eta(t_h)| < 1.6$ . For each fitted bin the  
 365 fractions in the lower and upper region are obtained from data and the template is composed  
 366 accordingly. Fig. 26 shows that the dependence of the templates on  $\eta(t_h)$ , but also on other  
 367 kinematic variables of the  $t_\ell$  and the  $t\bar{t}$  system, is very small.

### 368 9.1 Background templates

369 The background templates are extracted from the JetHT data stream selected by the HLT\_AK8PFJet(320,  
 370 400, 450, 500) triggers. These jet triggers were prescaled for  $p_T < 500$  GeV. In data this is cor-  
 371 rected by applying a weight  $\omega_p$  per event, where  $\omega_p$  is the prescale of the selecting trigger with  
 372 the highest  $p_T$ -threshold. This correction is important, since the prescale depends on the in-  
 373 stantaneous luminosity (higher prescales to reduce the rate at higher instantaneous luminosity  
 374 usually at beginning of the LHC fill) and the pileup profile would not agree with the overall  
 375 pileup profile during data-taking.

376 Events with an isolated electron or muon (tight WP) with  $p_T > 15$  GeV are vetoed. In addition,  
 377 there must be no boosted  $t_\ell$  candidate with  $L_{NN} > 0.8$  in the event.

- 378 • For the W/Z boson template: a quark jet enhanced region is needed. Therefore, we  
 379 require a photon (medium WP) with  $p_T > 35$  GeV and  $|\eta| < 2.4$  in the event. The  
 380 additional requirement, that the photon has to be separated from all selected PFAK4  
 381 jets with  $p_T > 30$  GeV and  $|\eta| < 2.4$  by  $\Delta R(j, \gamma) > 0.5$ , increases the fraction of  
 382 prompt photons that couple to quarks but not to gluons. In such events we select  
 383 for the template all  $t_h$  candidates that do not overlap with the photon and if there is  
 384 no other  $t_h$  candidate with  $H_{NN} > 0.4$ . The later condition suppresses contributions  
 385 from  $t\bar{t}$  all-hadronic decays.
- 386 • For the multijet template: we require at least a medium b-tagged PFAK4 jet with

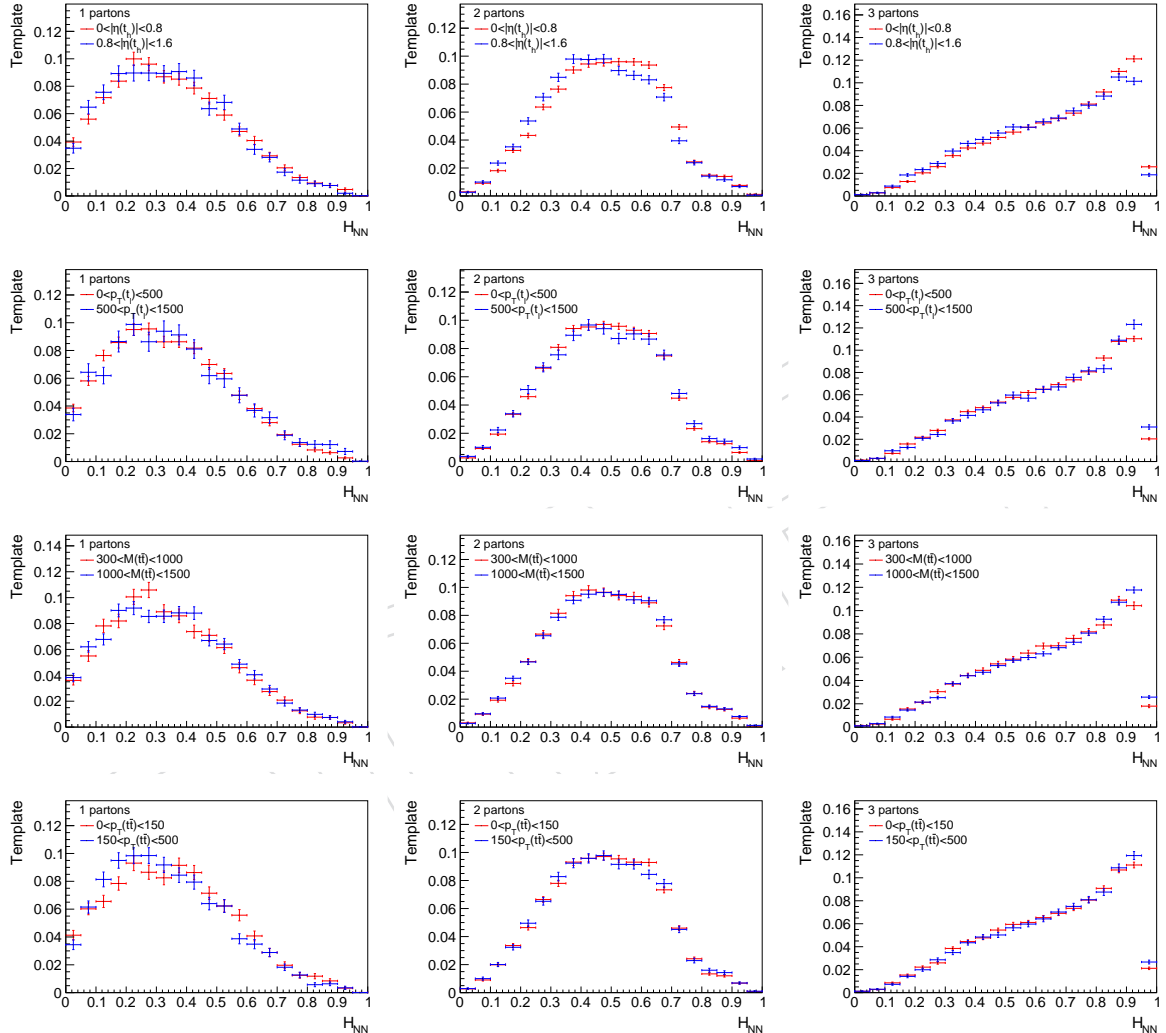


Figure 26: Distribution of  $H_{NN}$  for  $450 < p_T(t_h) < 550$  GeV in various kinematics regions for the different number of partons pointing towards the jet.

Table 2: Additional MC samples used to describe the control region.

MC	$\sigma$ [pb]	weights	$L \text{ fb}^{-1}$
GJetsHT-100To200.TuneCUETP8M1_13TeV-madgraphMLM-pythia8	9.25e+03	10104155	1.09
GJetsHT-200To400.TuneCUETP8M1_13TeV-madgraphMLM-pythia8	2.32e+03	20527506	8.84
GJetsHT-400To600.TuneCUETP8M1_13TeV-madgraphMLM-pythia8	275	5060070	18.4
GJetsHT-600ToInf.TuneCUETP8M1_13TeV-madgraphMLM-pythia8	93.2	5080857	54.5
QCDHT200to300.TuneCUETP8M1_13TeV-madgraphMLM-pythia8	1.71e+06	57580393	0.0337
QCDHT300to500.TuneCUETP8M1_13TeV-madgraphMLM-pythia8	3.48e+05	54552852	0.157
QCDHT500to700.TuneCUETP8M1_13TeV-madgraphMLM-pythia8	3.21e+04	62622029	1.95
QCDHT700to1000.TuneCUETP8M1_13TeV-madgraphMLM-pythia8	6.83e+03	15629253	2.29
QCDHT1000to1500.TuneCUETP8M1_13TeV-madgraphMLM-pythia8	1.21e+03	15210939	12.6
QCDHT1500to2000.TuneCUETP8M1_13TeV-madgraphMLM-pythia8	120	11839357	98.7
QCDHT2000toInf.TuneCUETP8M1_13TeV-madgraphMLM-pythia8	25.2	6019541	238

387  $p_T > 30 \text{ GeV}$  and  $|\eta| < 2.4$  in the event. In such events we select for the template all  
 388  $t_h$  candidates that do not overlap with at least one of the  $b$  jets, if there is not other  
 389  $t_h$  candidate with  $H_{NN} > 0.4$ .

390 In order to verify that the selected  $t_h$  candidates from the control regions provide sufficient  
 391 background templates, we compare the templates obtained from the simulation in the signal  
 392 region to the templates obtained from the simulation in the control region — the two should  
 393 agree with each other. The agreements are demonstrated in Fig. 27 and 28 for the  $W/Z$  boson  
 394 and multijet template, respectively, where the comparisons are shown for various  $p_T$  regions.  
 395 We also observe a reasonable agreement between data and simulation in the control region.  
 396 Though at medium and high  $p_T$  a deviations in the shapes of the QCD templates are observed.  
 397 The additional MC samples used in the description of the control region are listed in Tab. 2.  
 398 Events with prompt photons ( $p_T > 30 \text{ GeV}$ ) are rejected in the QCD sample to avoid a double  
 399 counting of those events with the photon+jets (GJets) sample.

## 400 9.2 Fit results

Systematic uncertainties that affect the distribution of  $H_{NN}$  in the simulation are included in the fit in the form of additional nuisance parameters. These are the uncertainties in the FSR scale,  $m_t$ , PS tune, pileup, and energy scale and resolution of the  $t_h$  jets. These are the only sources that are expected and found to affect the substructure of jets and hence the distribution of  $H_{NN}$ . In Figs. 29 – 31 the effects of the modeling and experimental uncertainties on the templates are shown. Especially, in the low  $p_T$  bins where we cannot use the high stat. simulation of boosted top quarks the templates have large statistical fluctuation. A LOWEES algorithm is used to smooth the templates. In addition, the up and down variations are symmetrized in the fit if they are bins with one-sided effects after smoothing. Especially, for  $m_t$  and PS tune, which are obtained from statistically independent simulations no systematic effect on the shape can be extracted. However, using the available statistics by combining all bins and templates, we can show that the effect of these uncertainties on the template is below 1% (Fig. 30 bottom row). Therefore, the statistical uncertainty in data is much higher and  $m_t$  and PS tune are negligible. A single nuisance for each uncertainty affects the fit in all bins. The shape of a template takes the following form as function of the nuisance parameters  $\lambda$ :

$$T_b = N(\lambda) C_b \prod_u \left( \frac{U_{bu}}{C_b} \frac{1}{1 + e^{-a\lambda_u}} + \frac{C_b}{D_{bu}} \frac{1}{1 + e^{a\lambda_u}} \right)^{\lambda_u}. \quad (2)$$

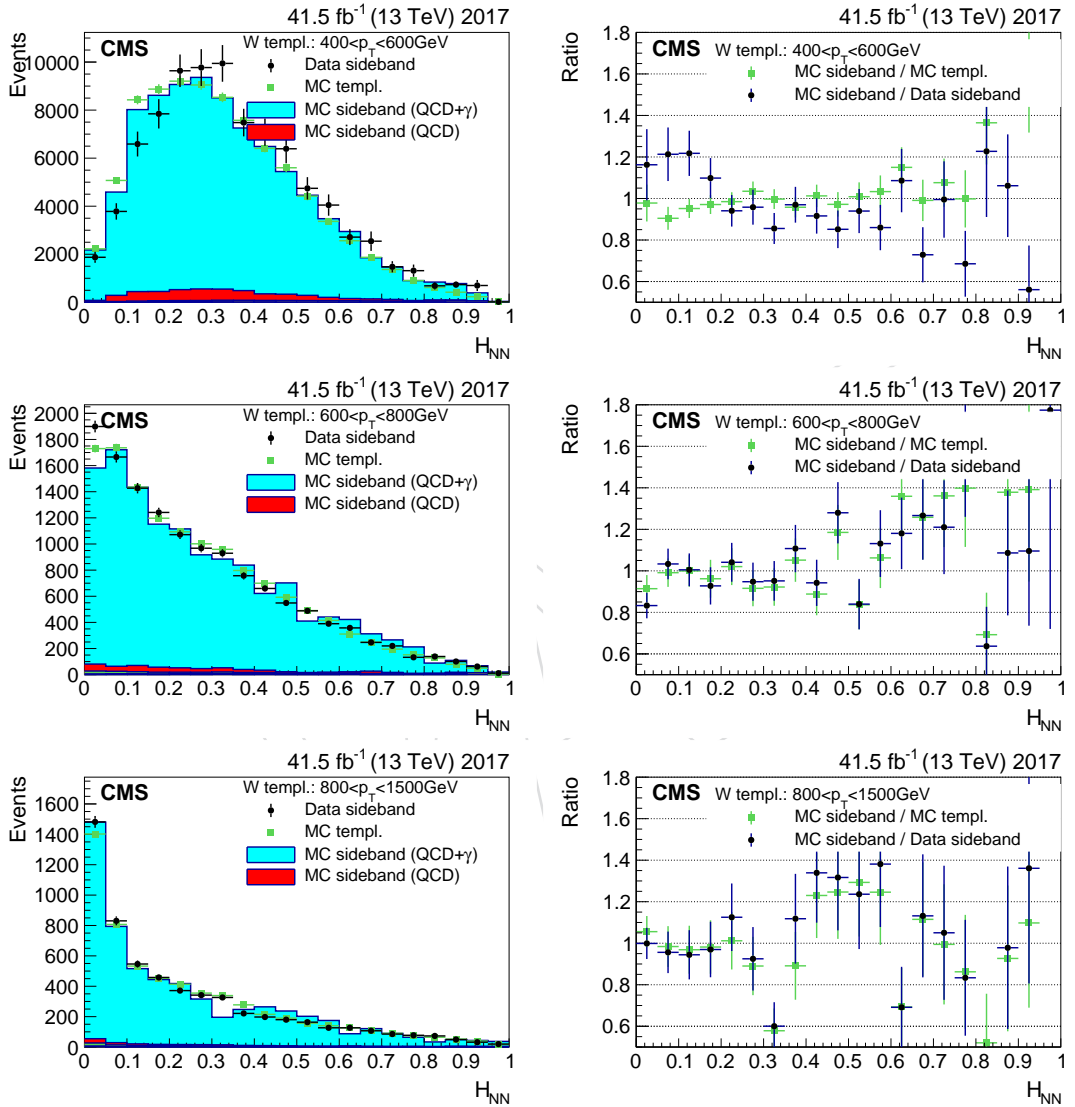


Figure 27: Comparison the background templates extracted from the simulation in the signal and control regions. In addition, the template obtained from the data in the control regions is shown.

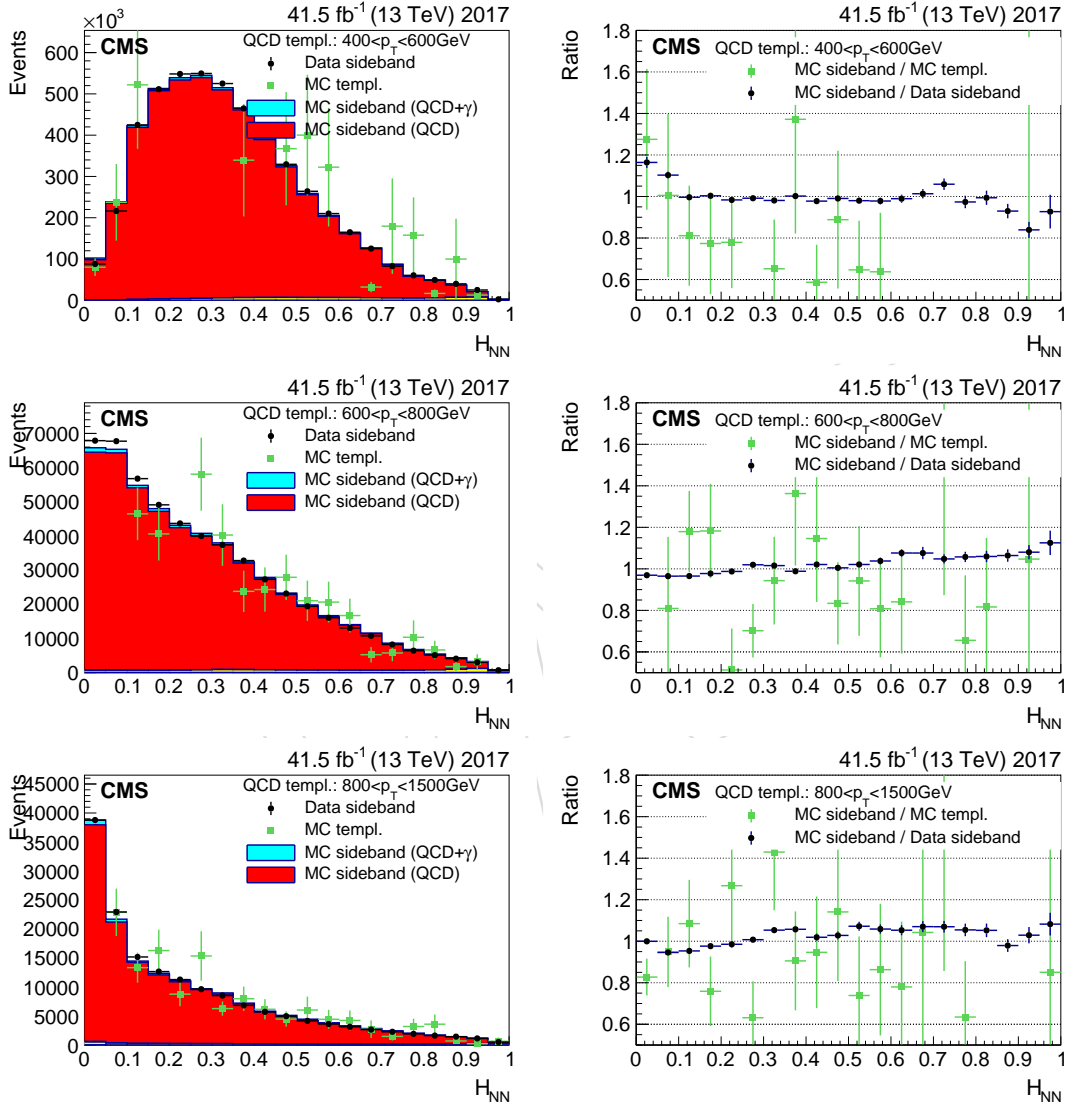


Figure 28: Comparison the background templates extracted from the simulation in the signal and control regions. In addition, the template obtained from the data in the control regions is shown.

401 where  $C_b$  is the prediction of the default simulation in bin  $b$  and  $U_{bu}$  and  $D_{bu}$  the prediction  
 402 of the up and down variations for uncertainty  $u$ . The factor  $N$  normalizes the template to  
 403 unity. The Sigmoid functions are used interpolate smoothly between asymmetric up and down  
 404 variations. With  $a = 5$  the effect of the interpolation is below 1% for  $\lambda = 1$  and provides a  
 405 continuously differentiable function. A multiplicative error model is used where the effect of  
 406 an uncertainty is expressed in terms of  $CE^\lambda$ , where  $E$  is the relative uncertainty. This error  
 407 model has the advantage of respecting the lower boundary at zero for event yields.

408 Binned maximum likelihood fits taking into account empty bins are performed. As examples,  
 409 the 2017 template fits for  $p_T(t_h)$  are shown in Fig. 32 and 33 for the muon and electron channels,  
 410 respectively. The corresponding plots for 2016 and 2018 can be found in Appendix J. The  $\chi^2$   
 411 values are calculated separately for each bin and provide an additional test, but are not used in  
 412 the fit and are not reliable in low populated bins. Nevertheless, they provide a rough estimate  
 413 of the goodness of the fit in the higher populated bins. The covariance matrix is calculated  
 414 from the second derivatives of the likelihood at the minimum. There is no other technically  
 415 applicable method available for fits with such a large number of parameters (about 1000). Since  
 416 this approximation might not be reliable for low populated bins ( $N < 10$  events), we set the  
 417 uncertainty  $\sqrt{N}$  regardless the fitted fraction. These low populated bins have not impact on  
 418 the final result, since their contribution to the integrated yield (sum over  $p_T(t_h)$ -bins) per bin  
 419 of the measurement is negligible.

420 To obtain the signal yields as a function of the variable of interest we integrate the extracted  
 421 number of complete plus broken events over the  $p_T(t_h)$ -bins. When the sums are calculated the  
 422 correlations among the event yields as obtained from the fit are taken into account. In Fig. 34  
 423 the extracted yields are compared to the simulation. For comparison these plots also show the  
 424 yields in the 2m and 1m1l categories that use the resolved reconstruction. The backgrounds  
 425 are not subtracted in these categories. The ratio of data to the prediction as a function of  $p_T(t_h)$   
 426 shows a smooth transition between the boosted and resolved reconstruction. Some examples  
 427 of correlation matrices are shown in Fig. 35. In Fig. 36 the pull distributions of the various  
 428 nuisance parameters are shown.

429 To verify that the setup of the fit is self-consistent and no bias is introduced due to the selection  
 430 of templates we perform a closure test by fitting the simulation. This pseudo dataset consists  
 431 of all relevant processes scaled to the luminosity of a single year (as an example we use 2018  
 432 here). The ratio of the fitted over the injected signal yields are shown in Fig. 37 as function of  
 433 several kinematic variables. These tests confirm that the fit is able to extract the injected signal  
 434 yields correctly.

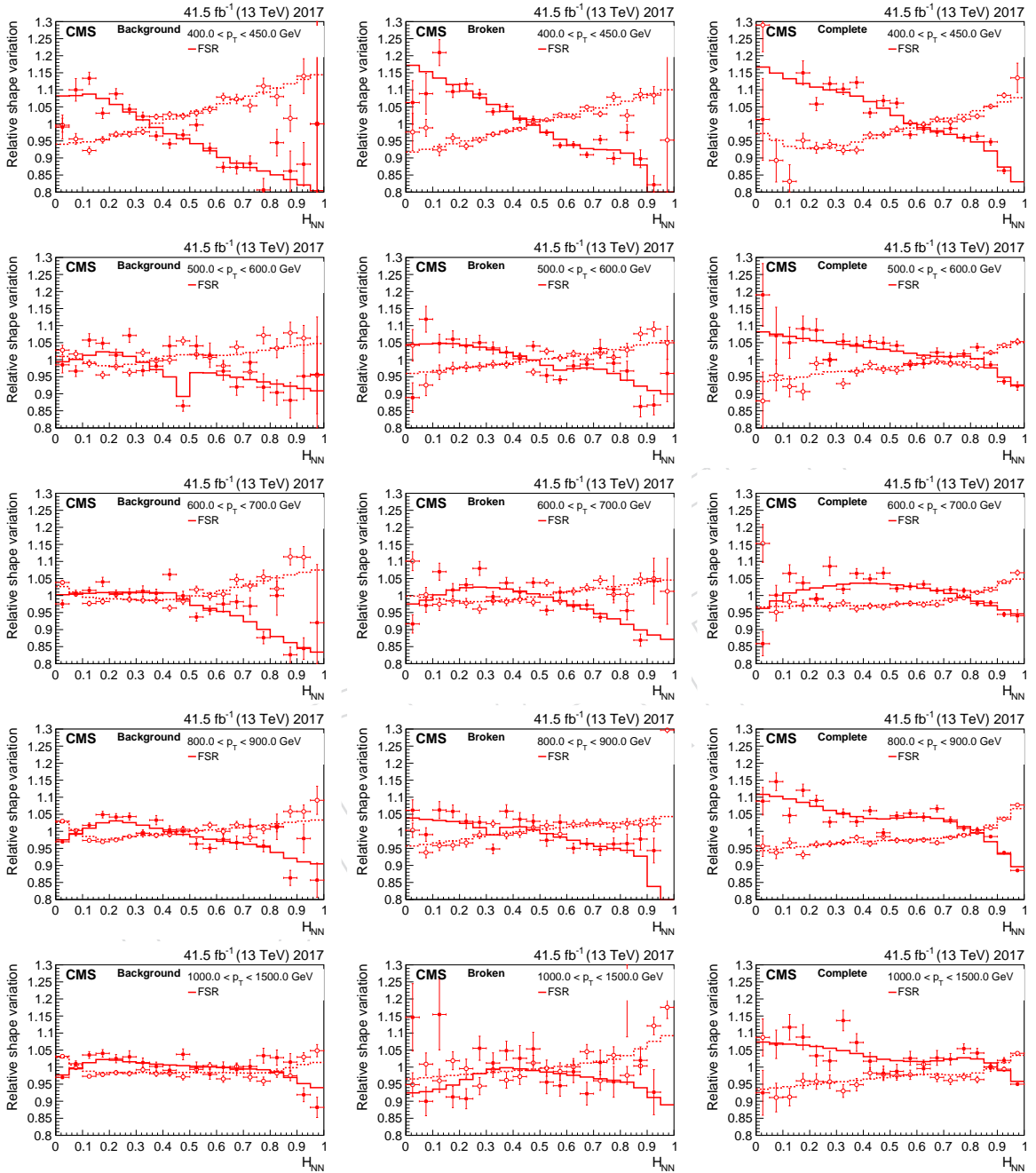


Figure 29: Modeling uncertainties of the Complete, Broken, and Background templates. The solid and dashed lines show the smoothed up and down variations. The markers are the original distributions.

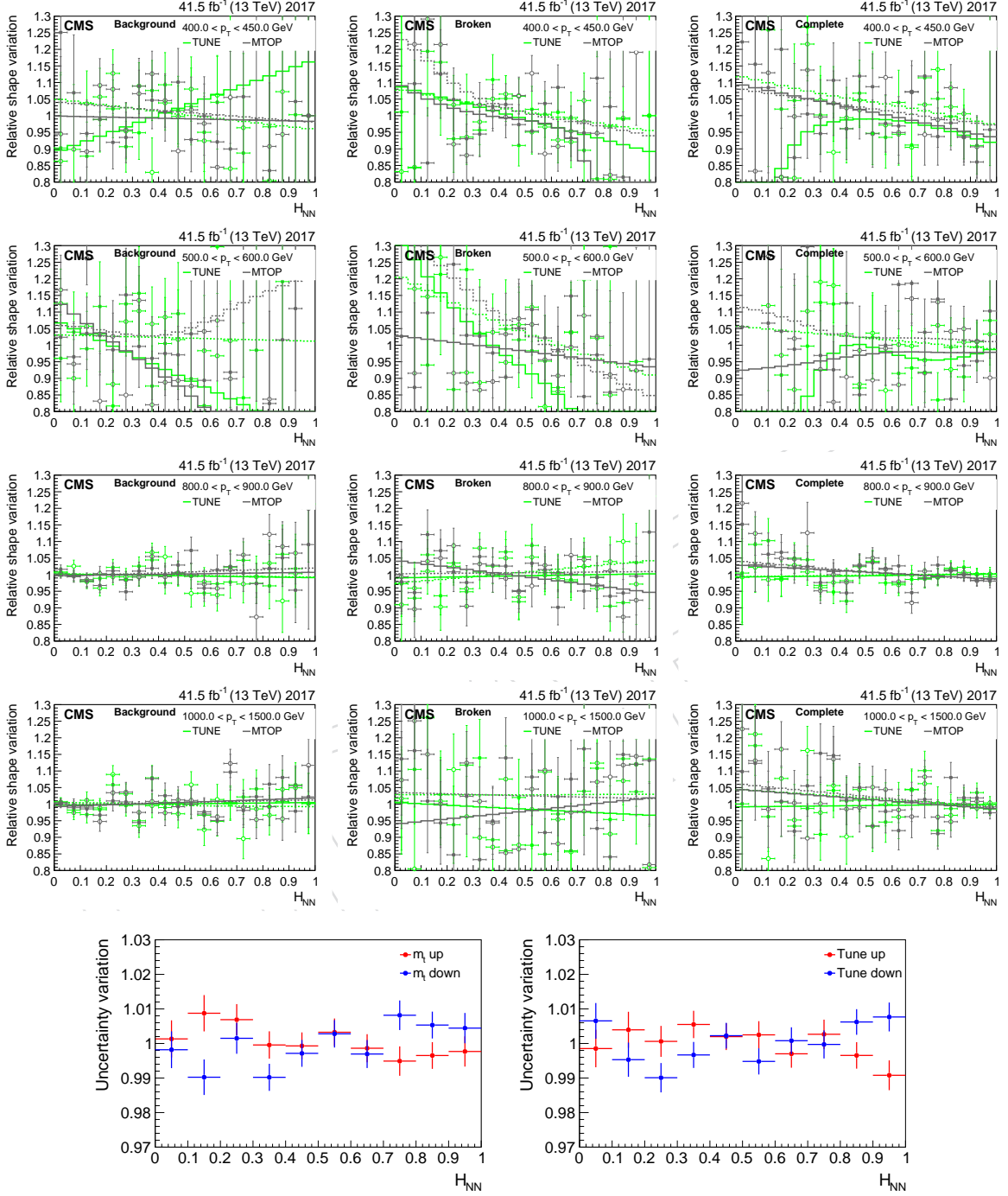


Figure 30:  $m_t$  and PS tune uncertainties of the Complete, Broken, and Background templates. The solid and dashed lines show the smoothed up and down variations. The markers are the original distributions. An estimate of these uncertainties suffers from large statistical uncertainties in the templates. However, the bottom row shows that the uncertainties on the combined templates is below 1%.

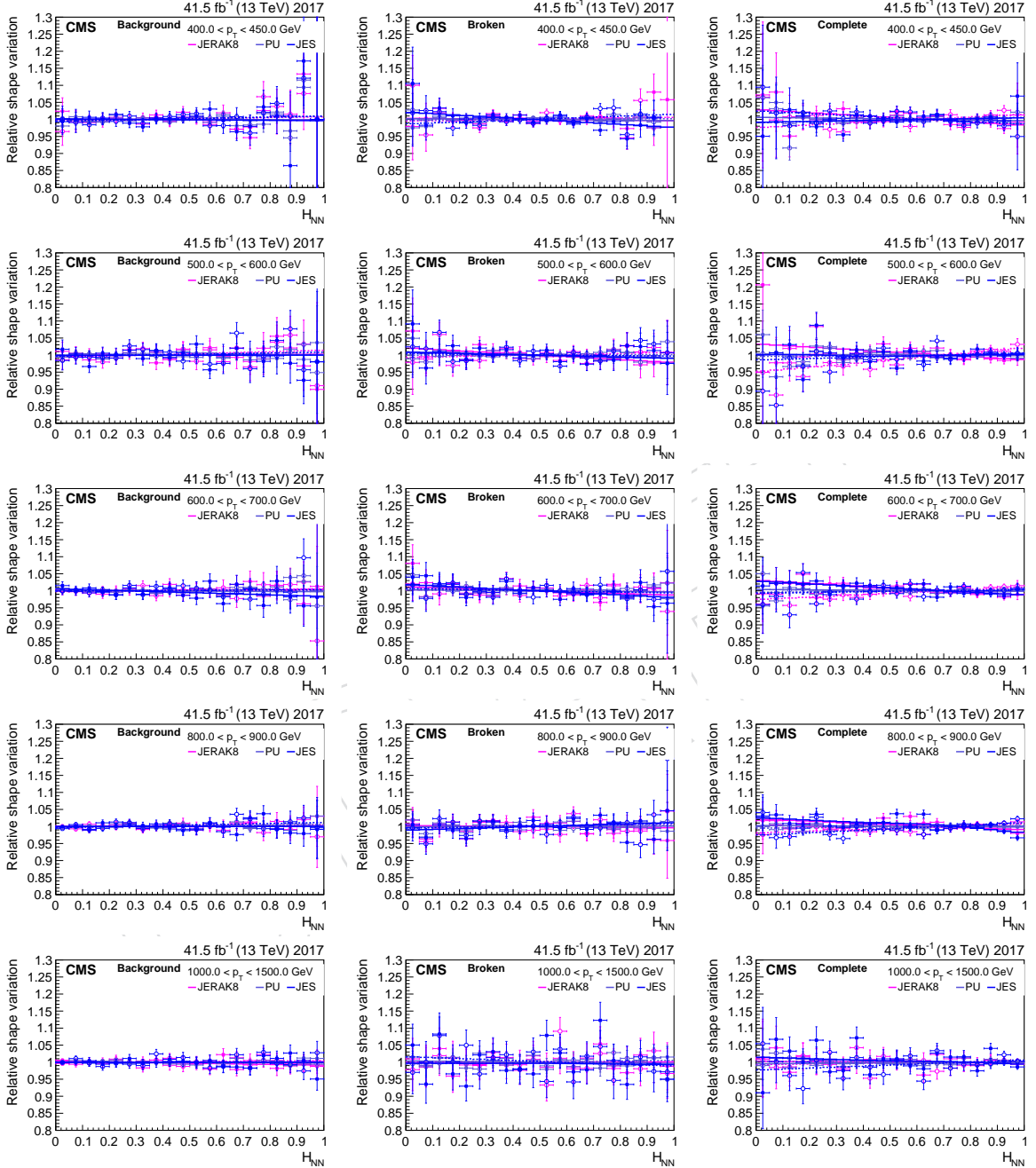


Figure 31: Experimental uncertainties of the Complete, Broken, and Background templates. The solid and dashed lines show the smoothed up and down variations. The markers are the original distributions.

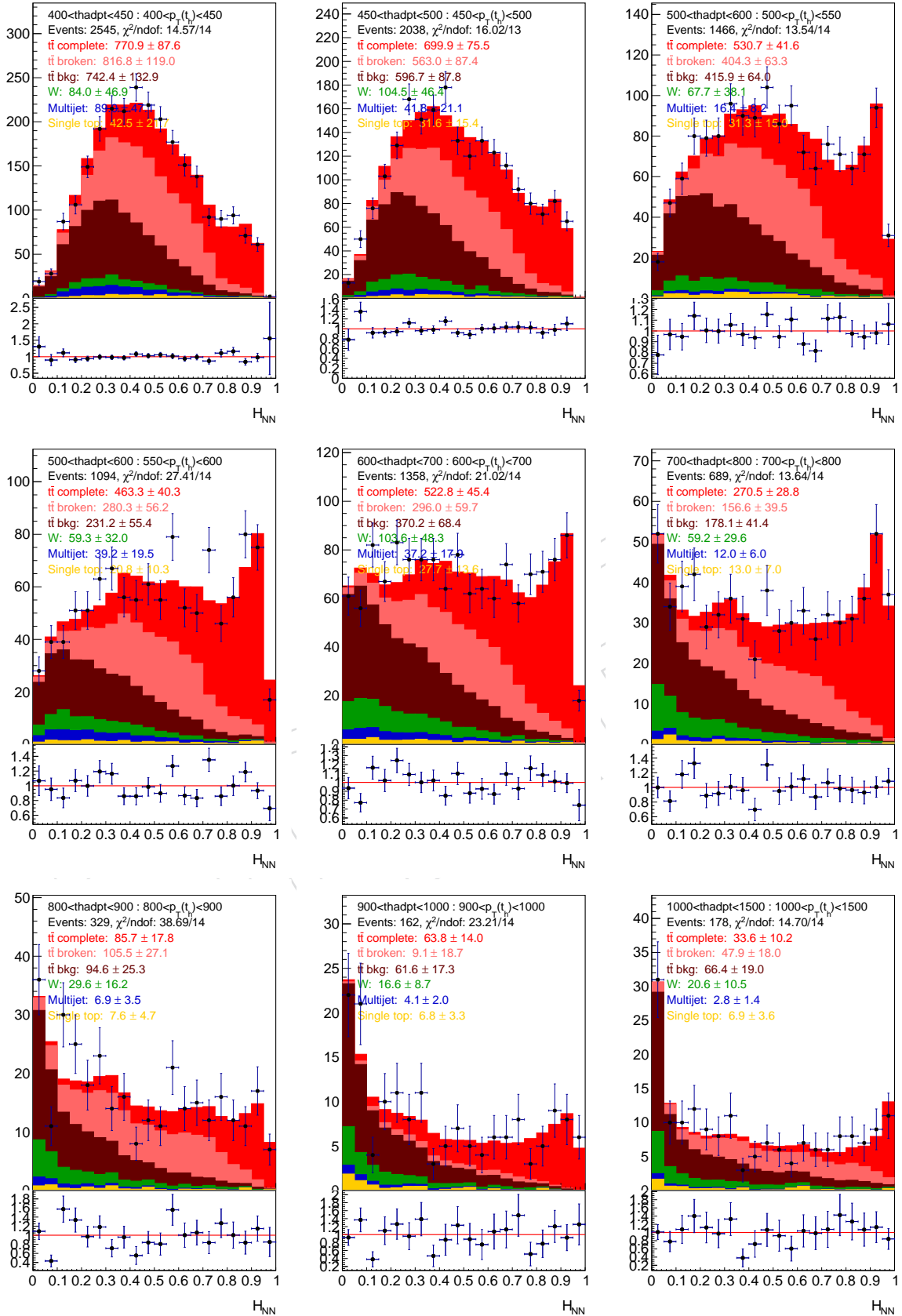


Figure 32: Fit in bins of  $p_T(t_h)$  in the muon channel for 2017 data. Signal  $t\bar{t}$  complete/broken (red/light red), background  $t\bar{t}$  (brown),  $W/Z$  boson (green), multijet (green), single top (yellow).

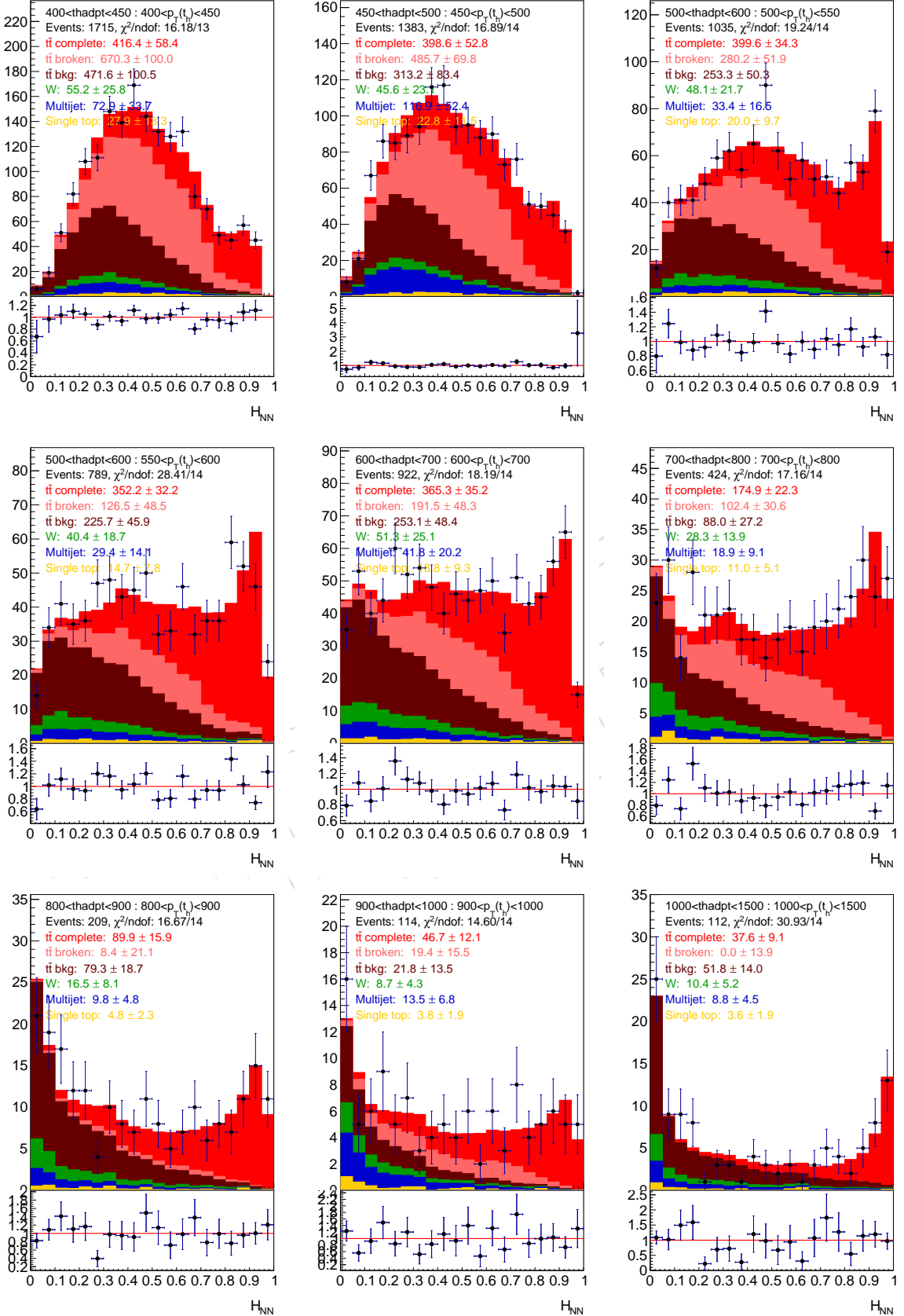


Figure 33: Fit in bins of  $p_T(t_h)$  in the electron channel for 2017 data. Signal  $t\bar{t}$  complete/broken (red/light red), background  $t\bar{t}$  (brown), W/Z boson (green), multijet (green), single top (yellow).

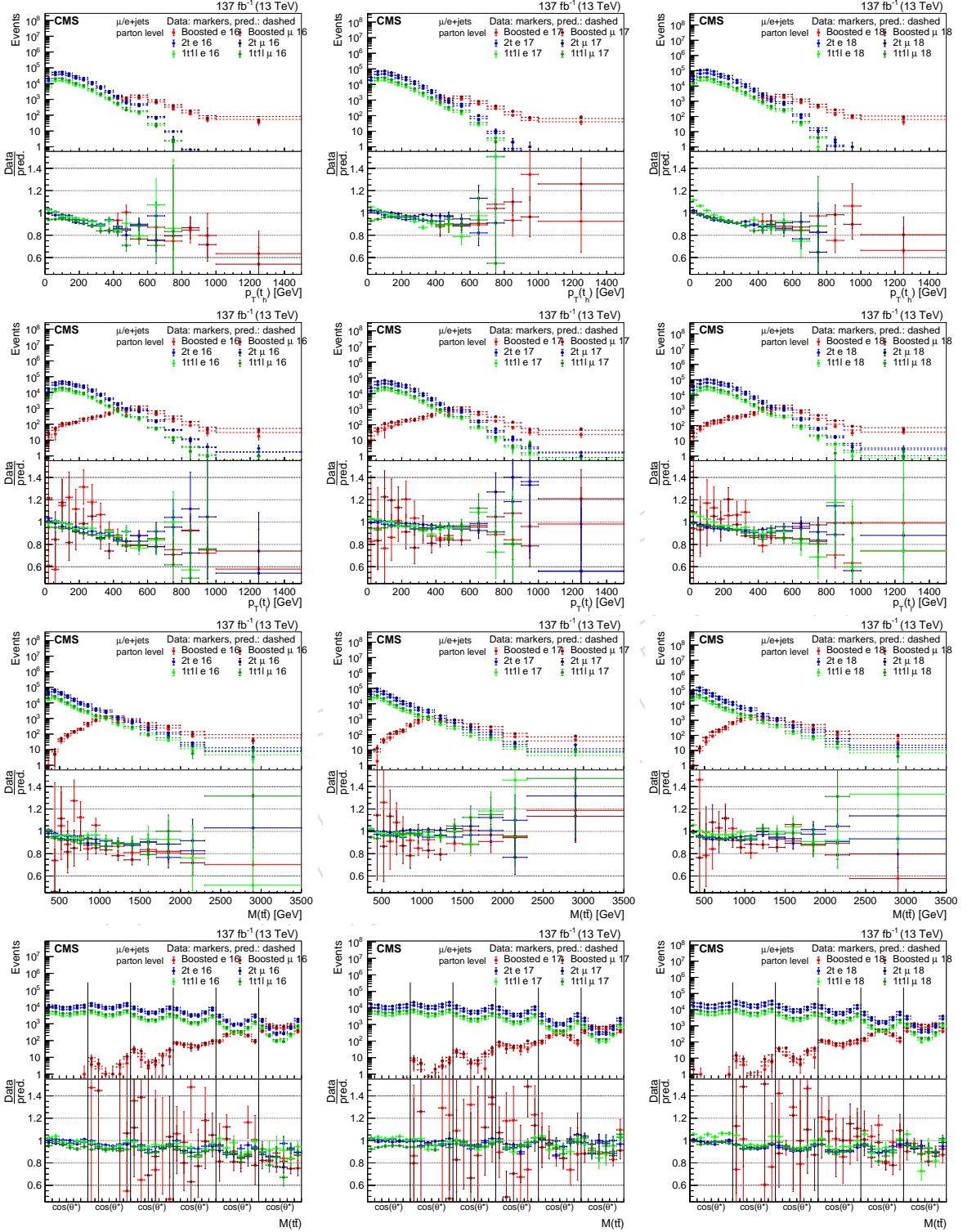


Figure 34: Signal yields in the various categories. Only the boosted category is background subtracted. The background in the 2m and 1m1l categories are not subtracted but will be fitted in the combination in Section 10.

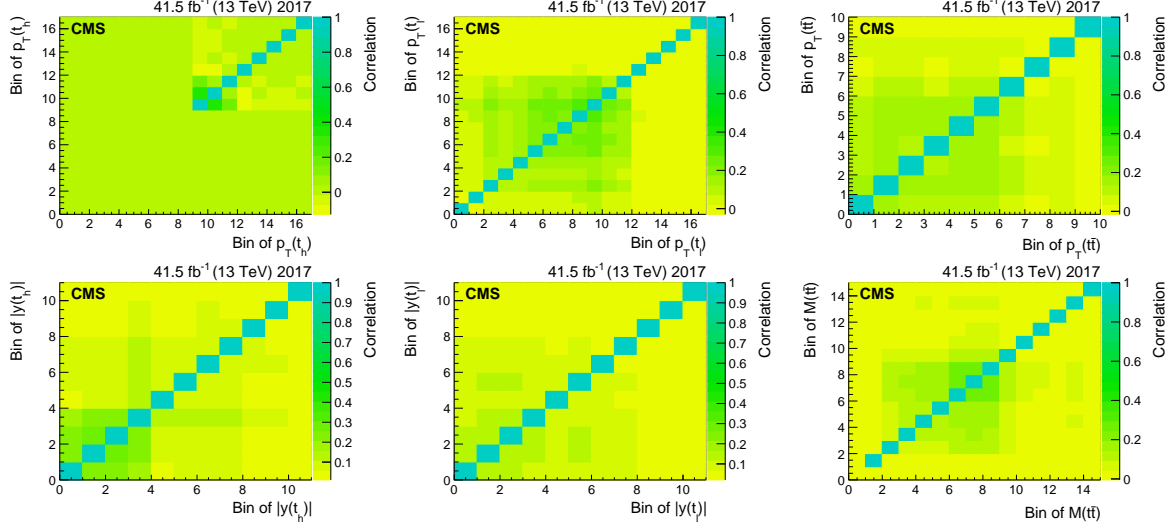


Figure 35: Bin-by-bin correlation after the fit for background subtraction in the boosted categories.

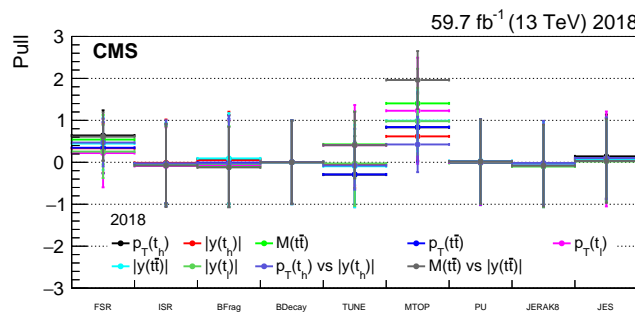
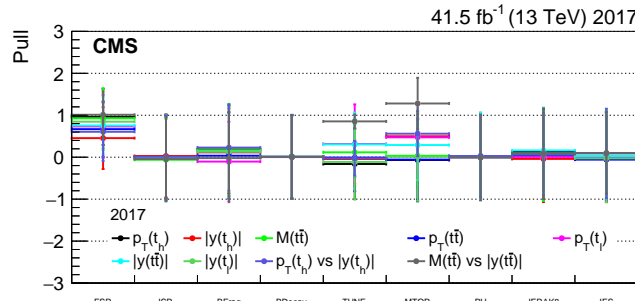
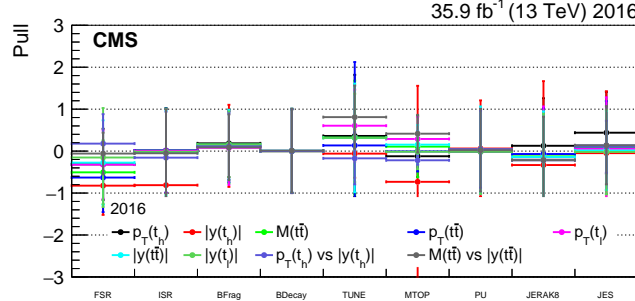


Figure 36: Pull distributions of nuisances affecting the shape of the simulated templates.

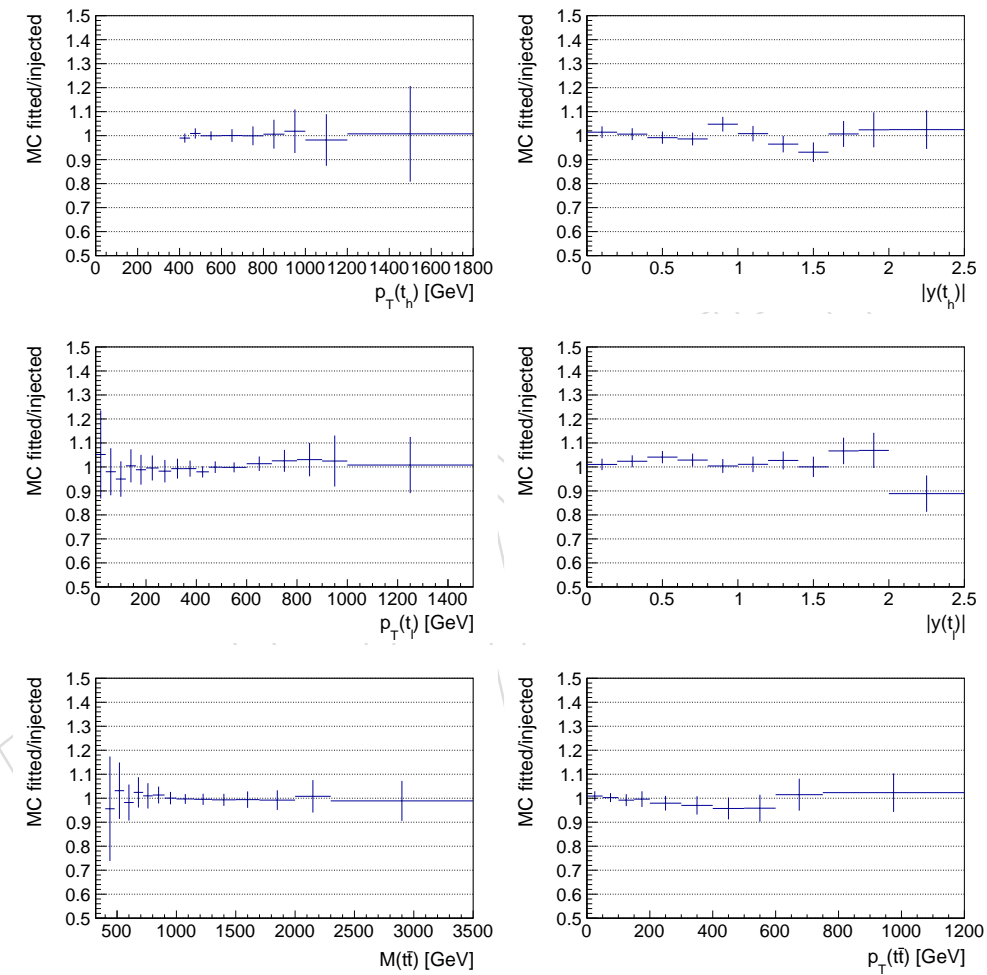


Figure 37: Results of the closure test. The fits are able to extract the injected signal yields.

## 435 10 Extraction of inclusive and differential cross sections

436 As explained in the Section 9 the BHRL and BHBL categories are combined in the “boosted”  
 437 category for the fit of  $H_{\text{NN}}$  in the background subtraction. The distributions in the boosted, the  
 438 2m, and the 1m1l categories are used in a fit for the extraction the differential cross sections.  
 439 These three categories are further split into the electron and muon channels and are obtained  
 440 for the three years. This results in 18 categories entering the fit.

441 The main ingredient to the extraction of the cross sections are the response matrices  $R$ . These  
 442 map a vector of cross sections  $\sigma$  into the corresponding event yield at detector level. After  
 443 adding a vector of non-t̄ background events  $b$ , a prediction of events at detector level is ob-  
 444 tained that can be compared to the measured event yields

$$s = R\sigma + b. \quad (3)$$

445 Since non-t̄ backgrounds are already subtracted in the boosted category there is no  $b$ . How-  
 446 ever, t̄ background events exist in all categories. Since this should scale with the t̄ cross  
 447 section, its contribution is encoded in the response matrix, which can be calculated from the  
 448 simulated t̄ events,

$$R_{ij} = \sum_m \sum_n \frac{\delta_{ni}(r_n + M_{n:})}{M_{n:}} M_{nm} \frac{\delta_{mj}}{t_m + M_{:m}} L \quad (4)$$

449 where  $M_{n,m}$  is the 2D distribution the unfolded vs folded quantity. The first index corresponds  
 450 to a bin at folded, the second index to a bin at unfolded level. This distribution can only be filled  
 451 if the quantity can be calculated at both levels. In addition, we define the quantities  $M_{j:}$  and  $M_{:j}$   
 452 as the sum of entries in row and column  $j$ , respectively. Events that can be reconstructed, but  
 453 there is no t̄ pair considered as signal, are t̄ background events and filled into distribution  $r$ .  
 454 The first fraction in Eq. 4 corrects for these non-signal t̄ events. Events with a signal t̄ pair at  
 455 unfolded level, but no reconstructed t̄ pair, are filled into distribution  $t$ . The second fraction in  
 456 Eq. 4 represents the losses due to inefficiencies and acceptance. To obtain an actual event yield  
 457 from the cross section it has to be multiplied by the luminosity  $L$ . In this analysis the same  
 458 binning is used at folded and unfolded level. In Fig. 38 we show the response matrix of the  
 459  $p_T(t_h)$  measurement together with its purity (fraction of correctly reconstructed events per bin  
 460 at detector level) and stability (fraction of correctly reconstructed events per bin at unfolded  
 461 level). The plotted matrices show the sum of the matrices in the individual categories. Very  
 462 similar reconstruction performances are expected for the three years.

463 With the measured event yields  $m$  we define the likelihood

$$\chi^2(\sigma, \nu) = \sum_y \sum_c \sum_\ell (\mathbf{m}_{ycl} - \mathbf{s}_{ycl}((\sigma, \nu)))^T C_{ycl}^{-1} (\mathbf{m}_{ycl} - \mathbf{s}_{ycl}(\sigma, \nu)) + \nu^T Q^{-1} \nu, \quad (5)$$

464 where we sum over the years ( $y = 2016, 2017, 2018$ ), the reconstruction categories ( $c = \text{boosted},$   
 465 2m, 1m1l), and the lepton channels ( $\ell = e, \mu$ ). In the resolved categories the covariance matrix  
 466  $C$  is a diagonal matrix with the numbers of observed events per bin, while in the boosted  
 467 categories, since the background was already subtracted, the covariance matrix is obtained  
 468 from the fits as described in Section 9. In each category only bins with at least four events are  
 469 used, i.e., very low and unpopulated bins are not taken into account for the fit. For such bins  
 470 the  $\chi^2$  fit is not well defined. Since the combined event yields of all categories is at least several

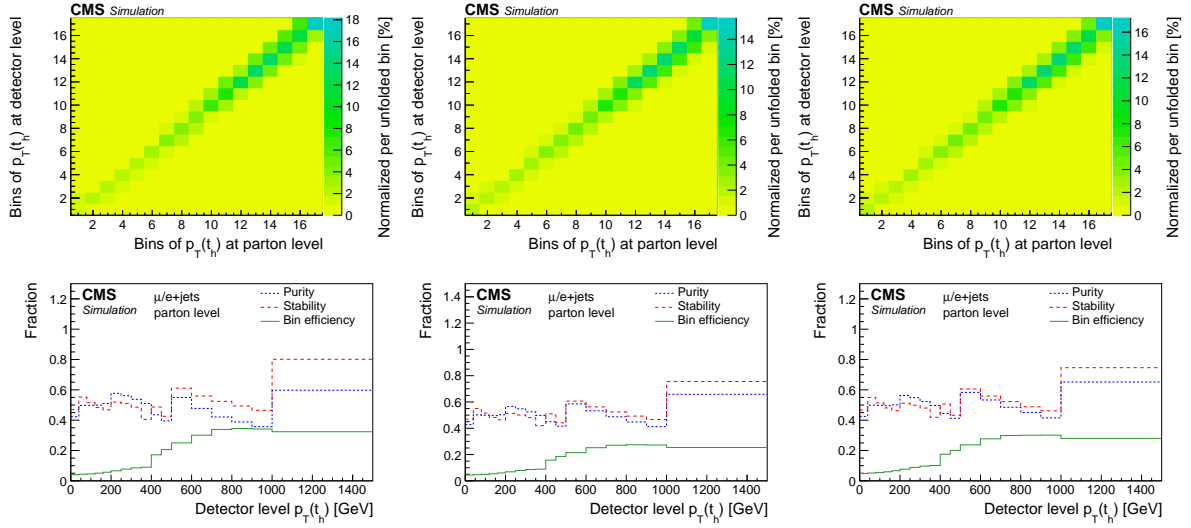


Figure 38: Sum of response matrices of the  $p_T(t_h)$  measurement together with its purity, stability, and the efficiency per bin, from left to right the matrices for 2016–2018 are shown.

471 100–1000 events per bin, neglecting such a few events cannot affect the results. The number  
 472 of degrees of freedom of the fit is given by the number of bins taken into account minus the  
 473 number of bins in  $\sigma$ .

474 The predicted event yields depends on the differential cross section and the systematic uncer-  
 475 tainties parameterized as function of nuisances  $\nu$ . The later are constrained by the last term,  
 476 where the matrix  $Q$  is the correlations matrix of the nuisances. Especially, the correlations of  
 477 the uncertainty sources between the years is important and listed together with a description  
 478 in Tabs. 3 and 4 for the modeling and experimental uncertainties, respectively. In Fig. 39, as an  
 479 example, the effect of modelling uncertainties on the distributions of  $p_T(t_h)$  at generator and  
 480 detector levels are shown for the three years. In Fig. 40 the effect of experimental uncertainties  
 481 is shown for various distributions. In Fig. 41 the normalized distributions at detector level for  
 482 some selected bins at generator level are shown. These demonstrates the bin migrations in the  
 483 response matrix. Since a bin-by-bin interpolation is used to model the systematic uncertainties  
 484 as function of a nuisance parameter, it is important to verify that there are no significant shifts  
 485 in the peak positions, which could not be described by this interpolation. Indeed, we find the  
 486 largest uncertainties in the order of a few per cent. Therefore, a bin-by-bin interpolation is  
 487 valid.

488 The pulls of the nuisance parameters after minimizing  $\chi^2$  are shown in Figs. 42 and 43, where  
 489 the latter includes the pulls of the PDF uncertainties. In Fig. 45 the postfit model is compared  
 490 to the data at detector level. Good agreement is observed in all categories. The corresponding  
 491 p-values, shown in Fig. 44, confirm a good agreement between data and the fitted model. In  
 492 addition, the total cross sections of the  $e/\mu$ +jets channel obtained by integrating the differential  
 493 distributions are consistent. The integral of most distributions covers to the whole phase space.  
 494 Only for rapidity related distributions an overflow of up to 3% is estimated from the simulation.  
 495 This is corrected in Fig. 44. The most precise measurement,  $M(t\bar{t})$  vs.  $p_T(t_h)$ , yields a value of

$$\sigma_{e/\mu+\text{jets}} = 235 \pm 7.0 \text{ pb.} \quad (6)$$

496 With a branching fraction of  $28.77 \pm 0.32\%$  to  $e/\mu$ +jets the total cross section becomes

Table 3: List of modeling uncertainties and their correlations among years.

Source	16/17	16/18	17/18	comments
ME scales $\mu_r, \mu_f$	100	100	100	Fully correlated among years, since the same ME are used. Separate variation of $\mu_r, \mu_f$ , and their simultaneous variation by a factor of 2.
MATRIX/POWHEG	100	100	100	$p_T(t)$ reweighting to NNLO QCD calculation with difference as uncertainty
PDF	0	0	100	Different PDFs in T4 (NNPDF30_nlo_as_0118) and CP5 (NNPDF31_nnlo_hessian_pdfas). In general, there are correlations between the PDF sets, but the parameterizations of PDF uncertainties cannot be directly compared. $100 + 1 \alpha_s$ variations.
ISR shower scale	100	100	100	similar $\alpha_s$ 0.1108/0.118 for T4/CP5. Variation by a factor of 2. Using weights in all years.
FSR shower scale	0	0	100	different $\alpha_s$ 0.1365/0.118 for T4/CP5. Variation by a factor of 2. Using weight in all years.
$h_{\text{damp}}$	50	50	100	similar values $1.58^{+0.66}_{-0.59}/1.38^{+0.92}_{-0.51}$ $m_t$ for T4/CP5.
$m_t$	100	100	100	same value of $172.5 \pm 1$ GeV in all years
Tune	0	0	100	different settings for T4/CP5 tunes.
B hadron leptonic decays	100	100	100	same branching ratios in T4/CP5 tunes
Color reconnection	100	100	100	switching on ERD for T4 and CP5

Table 4: List of experimental uncertainties and their correlations among years.

Source	16/17	16/18	17/18	comments
Luminosity	21	29	30	Lumi POG recommendation
Pileup	85	85	85	the inelastic cross section is fully correlated (unc. 4.5%), the lumi about 30% (unc. 2.5%). The product should be about 85% correlated.
Jet energy scale	mult.	mult.	mult.	multiple sources with JME POG recommendation
Jet energy resolution	0	0	0	JME POG recommendation
$p_T^{\text{miss}}$	50?	50?	50?	$p_T^{\text{miss}}$ not related to jet energy corrections. Negligible uncertainty.
Leptons reco/ID	50	50	50	separate for $\mu/e$ . Using the same TNP methods might introduce correlations
Leptons triggers	50	50	50	separate for $\mu/e$ . Using the same TNP methods might introduce correlations
B-tagging	50?	50?	50?	introduce 3 nuisances that scale the loose and medium working points individually and simultaneously
L1 prefiring	0	0	0	only in 2016 and 2017 see Appendix B
Multijet/W background	0(100)	0(100)	0(100)	normalization: dominated by simulated statistics (shape: from same control region). Electron and muon channels uncorrelated. Affects only resolved categories (2m,1m1l)
Single top quark background	mult	mult	mult	evaluate dominant uncertainties for single top quark production: ME scales, jet energy scale, b-tagging. Affects only resolved categories (2m,1m1l)
ECal L1 prefire	0	0	0	statistical uncertainty in the L1 prefire correction (16 and 17 only)

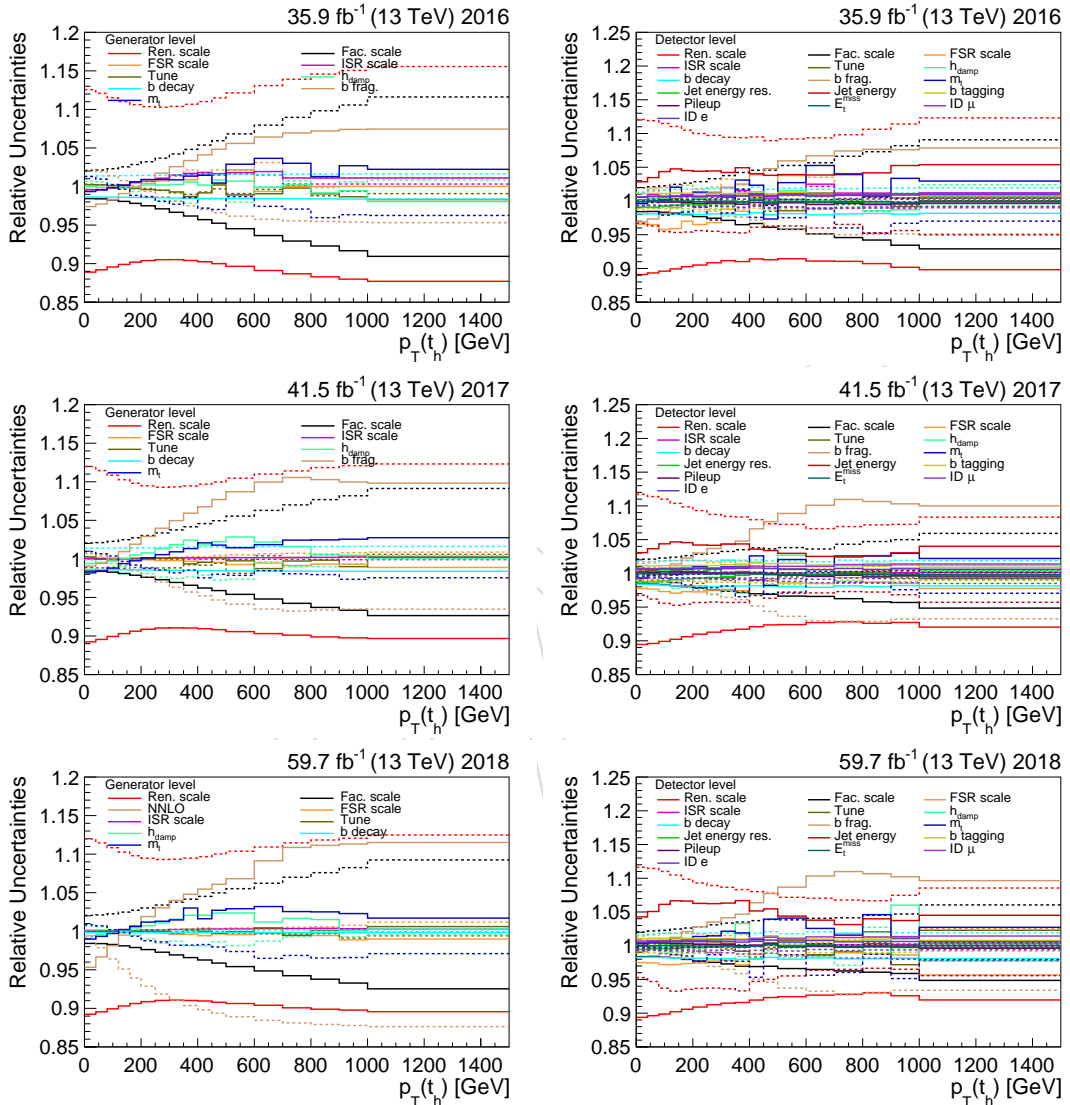


Figure 39: Effect of modelling uncertainties on the distribution of  $p_T(t_h)$  at generator (left) and detector (right) levels.

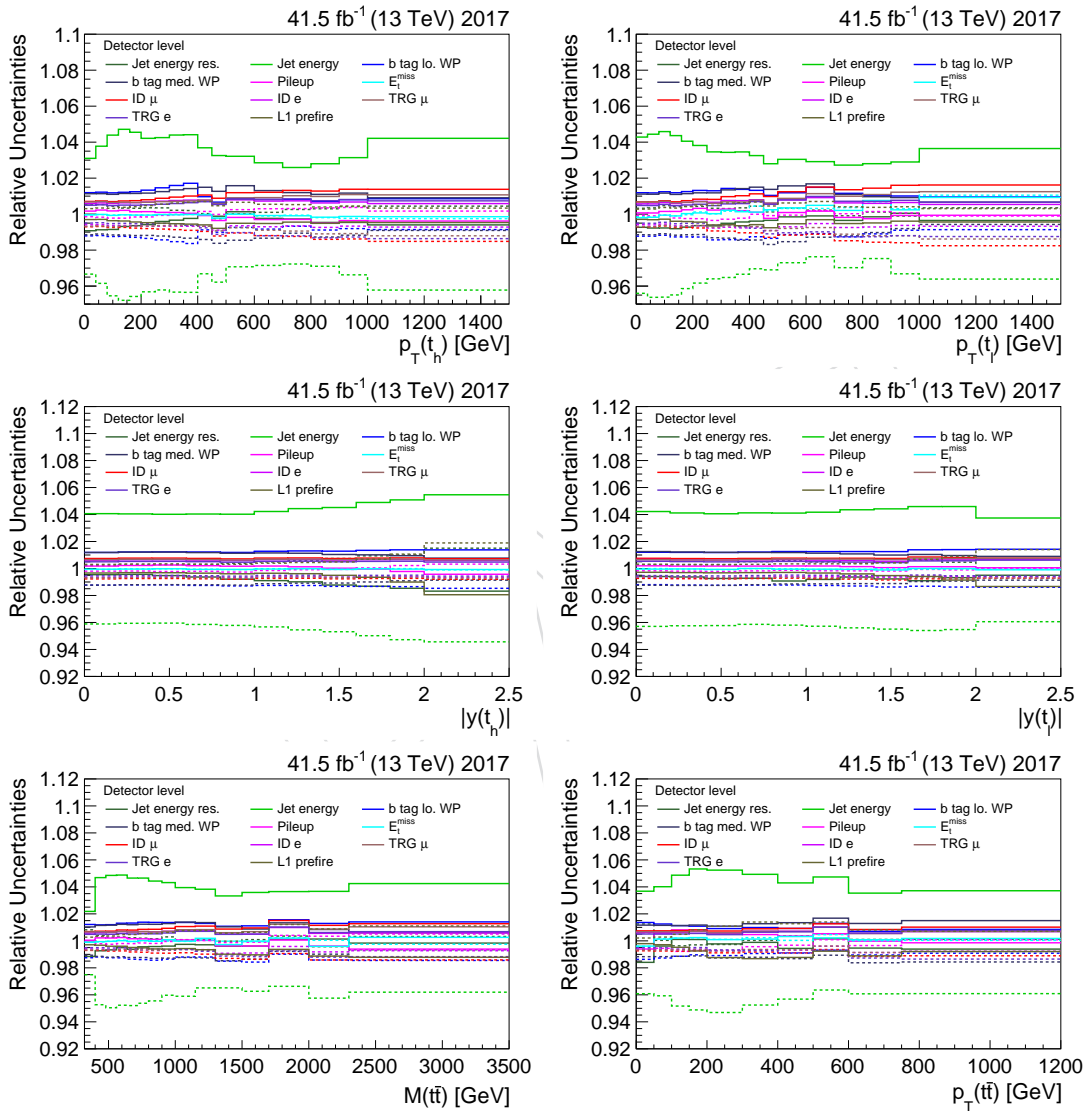


Figure 40: Effect of experimental uncertainties on various distributions at detector level.

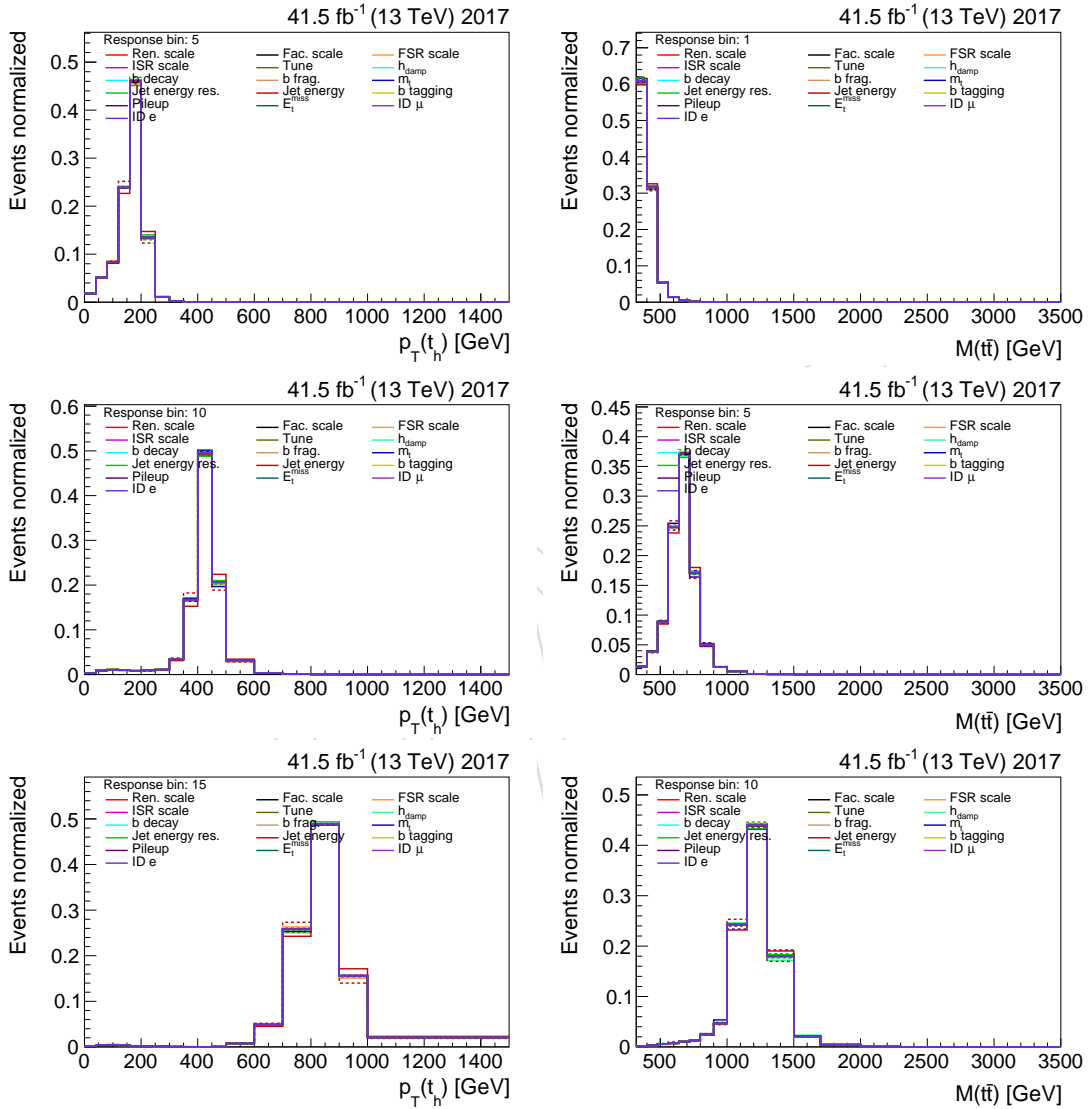


Figure 41: Effect of uncertainties on bin migrations. The distribution at detector level is shown for a few selected bins at generator level.

Table 5: Systematic uncertainties in the measurement of  $\sigma_{\text{tot}}$ .

Source	Uncertainty [pb] (%)
Jet energy	9.09(1.12)
Lepton	8.91(1.09)
b tagging	6.16(0.76)
Mistagging	3.93(0.48)
Pileup	1.11(0.14)
L1 prefire	0.87(0.11)
Background	5.93(0.73)
ISR scale	3.33(0.41)
PDF	2.76(0.34)
NNLO	2.22(0.27)
Scales $\mu_r / \mu_f$	1.31(0.16)
$h_{\text{damp}}$	1.18(0.14)
FSR scale	1.15(0.14)
CR model	0.93(0.11)
$m_t$	0.71(0.09)
Tune	0.56(0.07)
b decay	0.06(0.01)
Luminosity	14.28(1.75)
Sim. stat	7.08(0.87)
Sys	18.23(2.24)
Stat	0.17(0.02)
Luminosity	13.96(1.73)

$$\sigma_{\text{tot}} = 815 \pm 25 \text{ pb.}$$

(7)

<sup>497</sup> A detailed listing of the individual uncertainties is presented in Tab. 5.

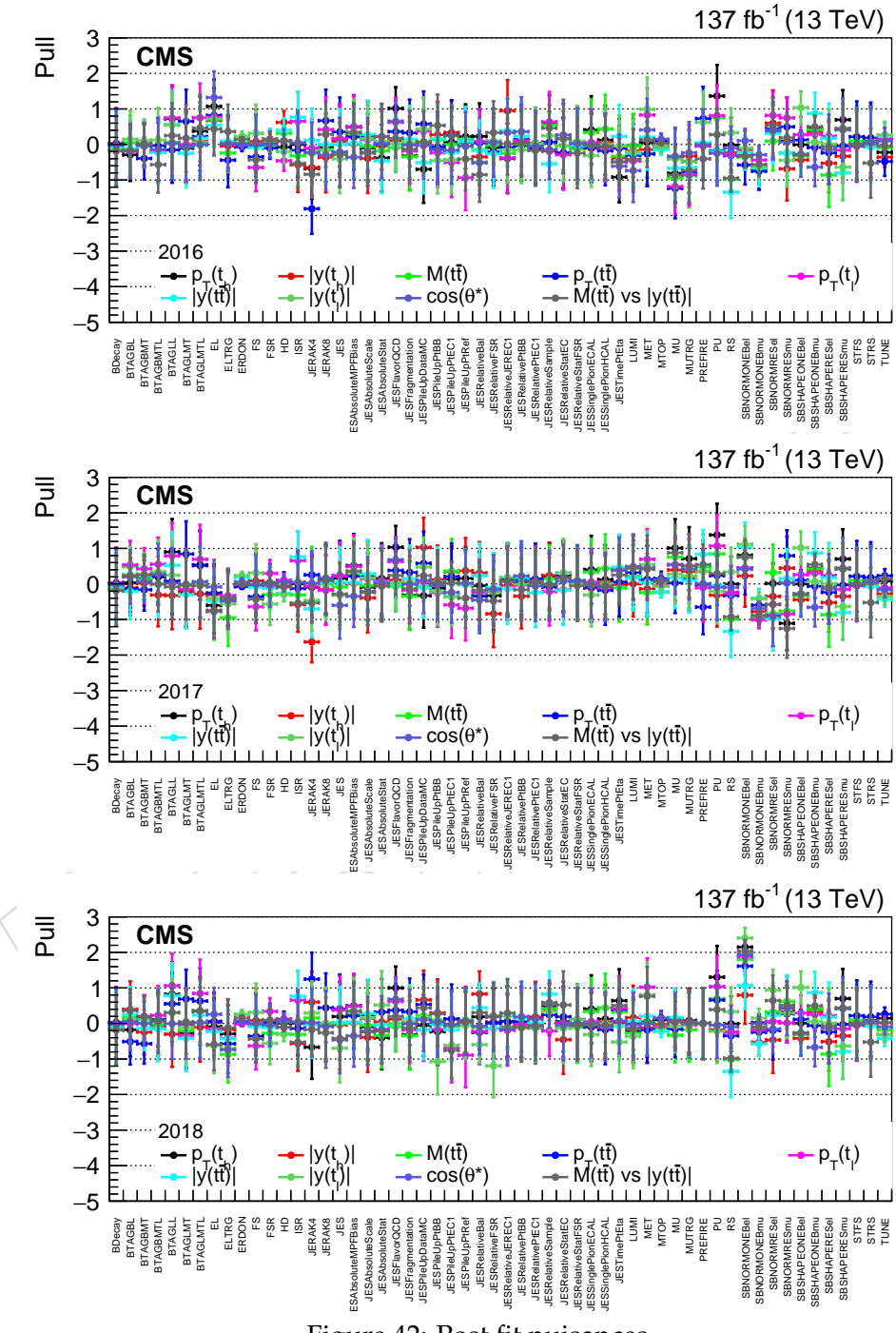


Figure 42: Post fit nuisances

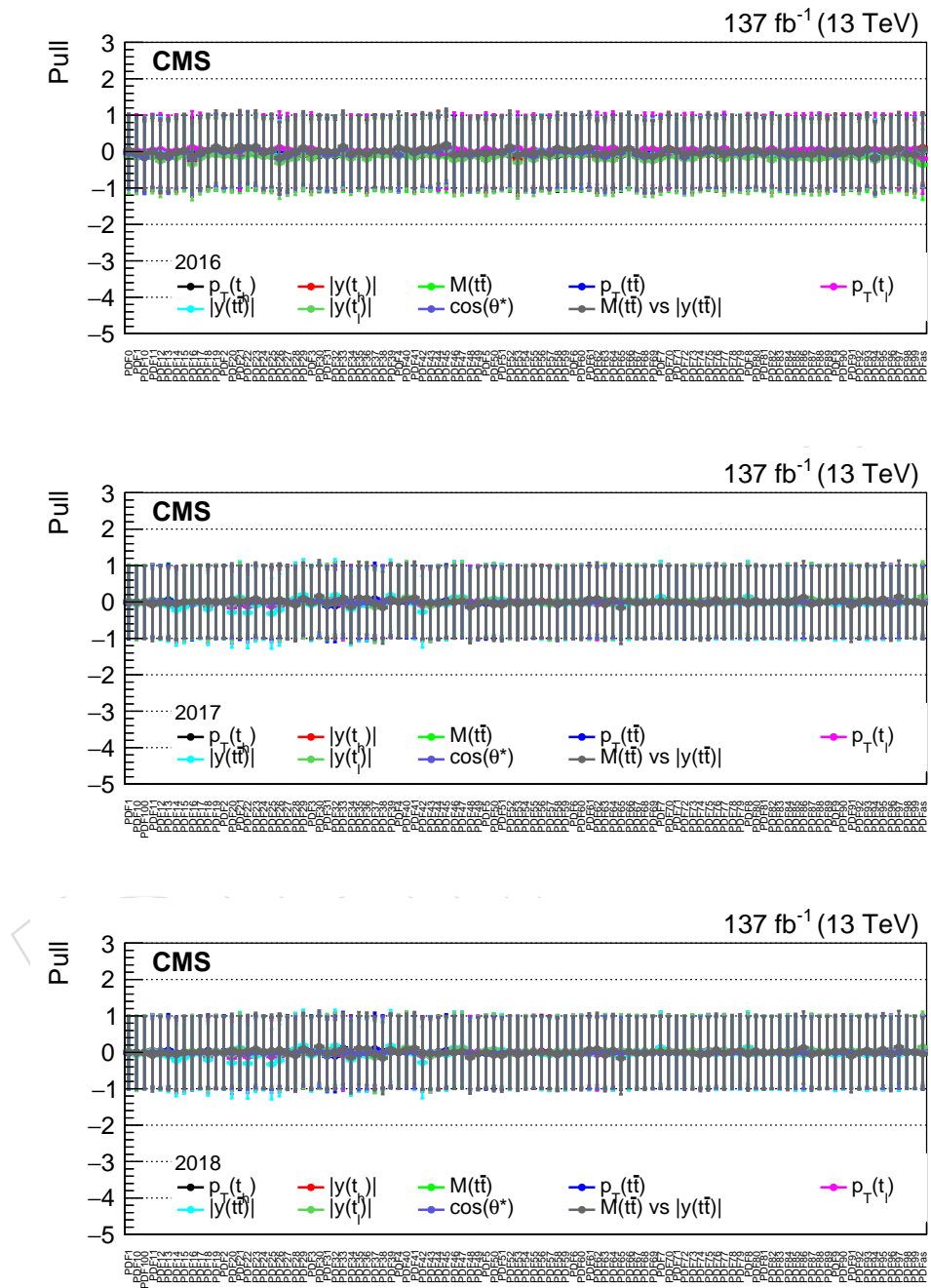


Figure 43: Post fit nuisances.

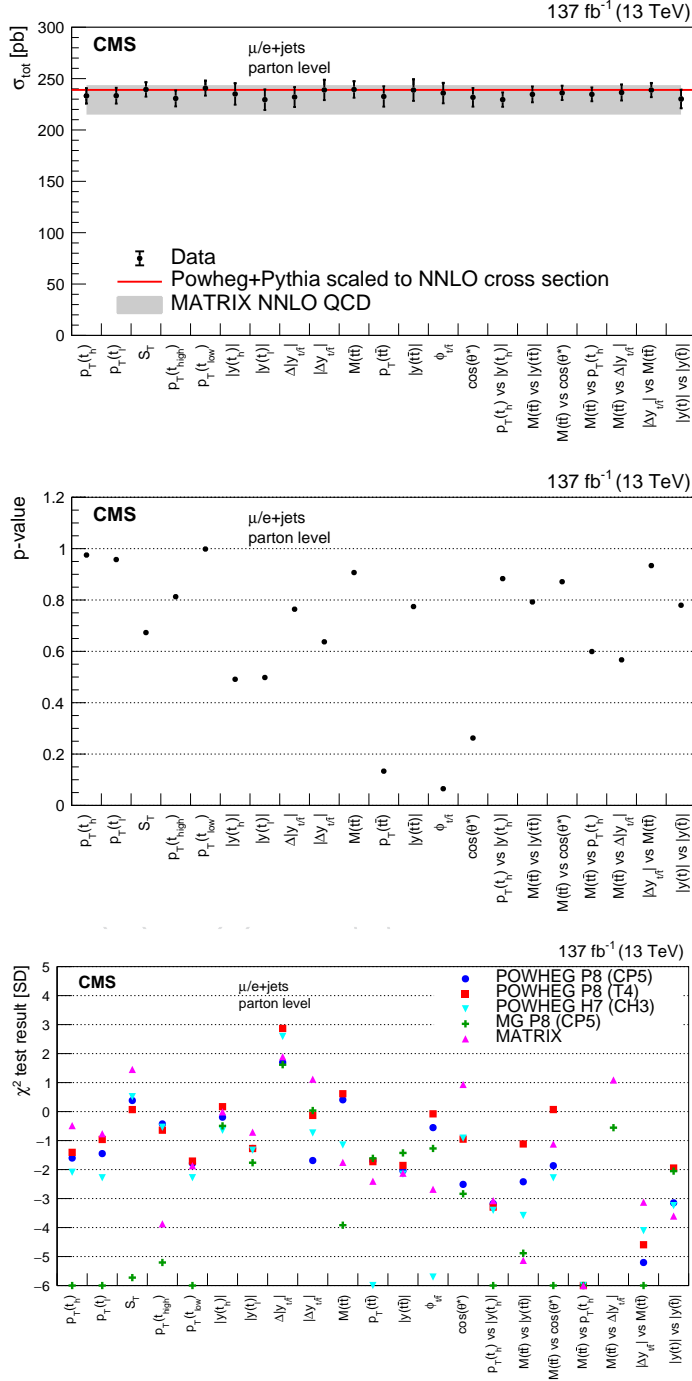


Figure 44: Upper: cross sections for  $|y(t)| < 2.5$  obtained by integrating all differential distributions. Middle: p-values after minimizing  $\chi^2$ . Lower: Results of  $\chi^2$  tests comparing the measurements with several SM predictions. The tests consider uncertainties in the measurements and the predictions.

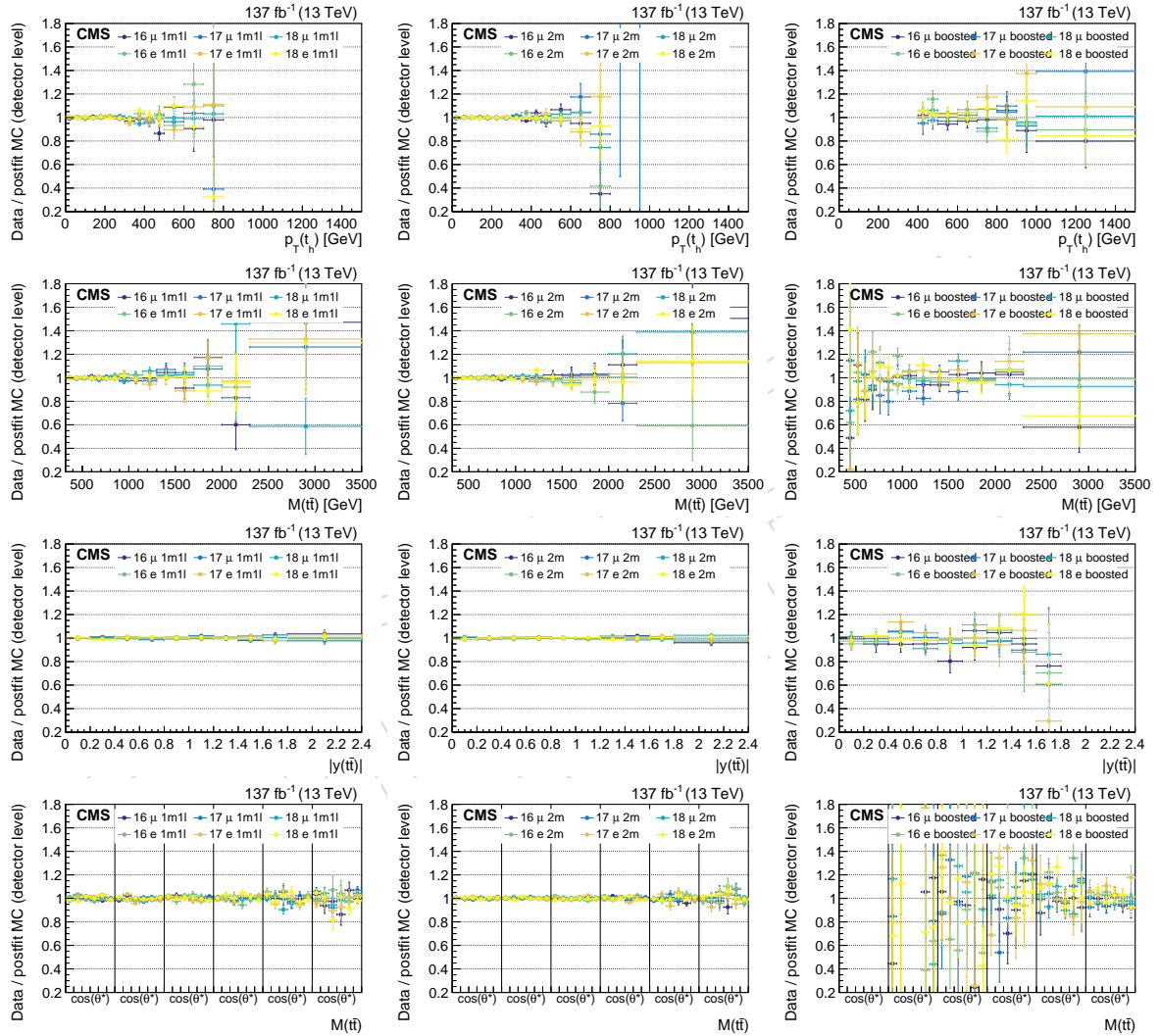


Figure 45: Post fit distribution compared to data.

## 498 11 Systematic Uncertainties

499 An overview of theoretical and experimental systematic uncertainties can be found in Tabs. 3  
500 and 4, respectively. In this Section we present more details:

501 Theoretical uncertainties:

- 502 • The effect of higher order contribution to the ME calculation is estimated by varying  
503 the renormalization and factorization scales by a factor of two. Distributions for  
504 these variations are obtained using event weights in the POWHEG+PYTHIA8 simu-  
505 lation. The renormalization and factorization scales are included as two separate  
506 uncertainties in the fit. Since the ME calculation is the same in all three years, these  
507 uncertainties are taken as fully correlated among the years.
- 508 • Since the renormalization and factorization scales variation barely describe the dif-  
509 ferences in the  $p_T$  spectrum between POWHEG (NLO) and MATRIX (NNLO) calcula-  
510 tion an additional uncertainty was introduced. A  $+1\sigma$  variation of this uncertainty  
511 corresponds to a reweighting of the  $p_T$  spectrum in the POWHEG simulation to the  
512 spectrum from MATRIX. This uncertainty is correlated among the three years.
- 513 • There are different PDFs in T4 (NNPDF30\_nlo\_as\_0118) and CP5 (NNPDF31\_nnlo\_hessian\_pdfs).  
514 In general, there are correlations between the PDF sets, but the parameterizations of  
515 PDF uncertainties cannot be directly compared. For the PDF uncertainties  $100 + 1 \alpha_s$   
516 nuisances are added to the fit for each year. The distributions are obtained using the  
517 corresponding event weights. Only 2017 and 2018 are fully correlated, 2016 is taken  
518 as uncorrelated.
- 519 • The uncertainty in the ISR parton shower is estimated by varying the shower scale  
520 by a factor of 2. The corresponding distributions are obtained using event weights  
521 in all years (including 2016). With  $\alpha_s = 0.1108/0.118$  for T4/CP5 the values are very  
522 similar and we assume that this uncertainty is fully correlated among the years.
- 523 • The uncertainty in the FSR parton shower is estimated by varying the shower scale  
524 by a factor of 2. The corresponding distributions are obtained using event weights  
525 in all years (including 2016). With  $0.1365/0.118$  for T4/CP5 for T4/CP5 the values  
526 are different and we assume that this uncertainty is uncorrelated among the years.
- 527 • With  $h_{\text{damp}}$  the matching between the ME calculation and the parton shower is con-  
528 trolled. The values used for the CP5 and T4 samples are  $1.58^{+0.66}_{-0.59}$  and  $1.38^{+0.92}_{-0.51} m_t$ ,  
529 respectively. Since the values are relatively close, the uncertainty is taken as fully  
530 correlated among the years. Separate samples produced with the different values of  
531  $h_{\text{damp}}$  are used to obtain the corresponding distributions.
- 532 • Separate samples produced with  $m_t = 171.5$  and  $m_t = 173.5$  are used to estimate  
533 the uncertainty due to the uncertainty in  $m_t$ . This 1 GeV variation is fully correlated  
534 among the years.
- 535 • The uncertainty in the hadronization is estimated using separate samples that rep-  
536 resent an envelope of the uncertainties in the tuning. This uncertainty is fully corre-  
537 lated between 2017 and 2018, but taken as uncorrelated with 2016.
- 538 • The fraction of leptonically decaying B hadrons is changed according to the known  
539 precision of the branching fraction using event based reweighting. This uncertainty  
540 is fully correlated among the years.
- 541 • The uncertainty in the color reconnection is assessed using an alternative model  
542 where the reconnection of colored particles from resonant decays is activated in

543 PYTHIA8, while this is deactivated in the default tune. The difference between these  
 544 two is taken as symmetric uncertainty. We assume that the amount of color recon-  
 545 nection is fully correlated among the years.

546 Experimental uncertainties:

- 547 • The uncertainties in the luminosity are 2.5%, 2.3%, and 2.5% for 2016, 2017, and 2018,  
 548 respectively. Their correlation can be found in Tab. 4. With these a combined overall  
 549 uncertainty in the luminosity of 1.8% is obtained.
- 550 • The uncertainty in the pileup estimation has two sources: the uncertainty in the  
 551 inelastic cross section (4.5%) and in the luminosity (see above). Since the former  
 552 is dominant and fully correlated among the years. The uncertainty in the pileup  
 553 estimation is highly correlated among the years (85%). The differences in the distri-  
 554 butions are obtained by reweighting the distribution of the number of pileup inter-  
 555 actions in the simulation.
- 556 • The jet energy scale is split into different sources. There are 20 different sources that  
 557 are relevant for jets within the tracker acceptance. We follow the POG recomme-  
 558 ndations about their year-by-year correlations. The sources affect the AK4 and AK8 jets  
 559 simultaneously. The differences in the distributions are obtained by rescaling the jet  
 560 momenta in the simulation.
- 561 • For AK4 and AK8 jets separate uncertainties in the resolution are introduced. The  
 562 uncertainties are uncorrelated among the years. The differences in the distributions  
 563 are obtained by rescaling the jet momenta in the simulation.
- 564 • The dominant uncertainty in the  $p_T^{\text{miss}}$  is due to the jet energy calibration. Therefore,  
 565 the  $p_T^{\text{miss}}$  is also recalculated whenever the jet momenta are rescaled. An additional  
 566 contribution to the uncertainty due to particles that do not belong the selected jets is  
 567 estimated. A 50% correlation of this uncertainty is taken.
- 568 • Uncertainty in the electron an muon reconstruction and trigger efficiencies are dis-  
 569 cussed in Appendix A. Four uncertainties are introduced in the fit (electron/muon,  
 570 reconstruction/trigger). Since the TnP method might introduce similar biases in all  
 571 years we a correlation of 50% is used among the years.
- 572 • Since the analysis uses the medium and loose WP, we introduce three variations of  
 573 the b-tagging uncertainty: varying the efficiencies of the loos an medium WP sepa-  
 574 rately and in addition a variation of the loose but not medium jets. The variations are  
 575 performed by recalculating an event probability using all jets and their true flavor.  
 576 We assume a 50% correlation among the years.

577 In addition, we estimate the effect of the limited statistics in the simulations by repeating the  
 578 whole fit 100 times with varied response matrices. From these results we calculate the covari-  
 579 ance matrix, which is added to the covariance matrix of the other uncertainties as obtained  
 580 from the fit with the original response matrices. The variations include the statistics in the de-  
 581 fault POWHEG+PYTHIA8 simulation and in the separate simulations used for the uncertainty  
 582 estimations of  $m_t$ ,  $h_{\text{damp}}$ , and PS tune. For the uncertainties estimated based on event weights  
 583 the correlations between the central bin contents and the reweighted bin contents are calcu-  
 584 lated. Usually these correlations are high (>98%) and taken into account when the reweighted  
 585 samples are varied. Only for the samples with rescaled jet momenta used in the estimation  
 586 of jet energy scale and resolution uncertainties the correlations with the central distribution is  
 587 hard to estimate. From the fluctuations in the ratio of these samples and the central sample we  
 588 assume a correlation of 90%. Overall the uncertainty due to limited statistics in the simulations

589 is of moderate size in most bins. It becomes a dominant systematic only in a few bins, but it is  
590 always small compared to statistical uncertainty in data.

591 An overview of the contributions of the systematic uncertainties in the various differential cross  
592 sections is shown in Appendix D.

## 593 12 Results

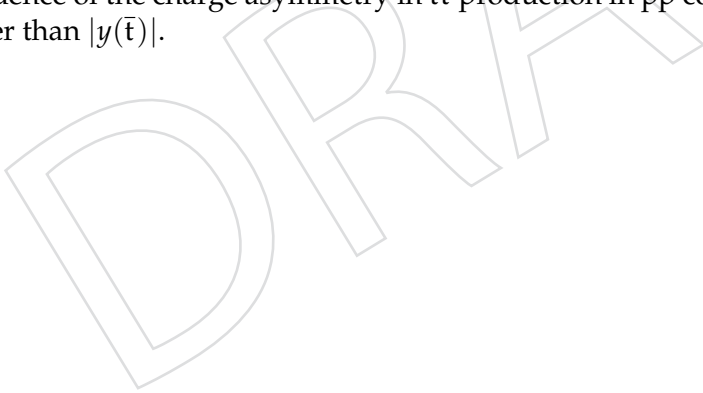
594 Differential cross sections are presented as function of  $p_T(t_h)$ ,  $p_T(t_\ell)$ ,  $p_T(t_{\text{hard}})$ ,  $p_T(t_{\text{soft}})$ , and the  
595 scalar sum of the top quark pair momenta  $S_T$  in Fig. 46. Compared to the POWHEG+PYTHIA8  
596 these spectra are softer at low  $p_T$ . For higher  $p_T$  values a constant deficit of about 20% is ob-  
597 served in data. The NNLO QCD calculation performed with MATRIX seems to describe the  
598 data significantly better.

599 Figure 47 shows the rapidities  $|y(t_h)|$ ,  $|y(t_\ell)|$ , and the differences  $\Delta|y_{t/\bar{t}}| = |y(t)| - |y(\bar{t})|$  and  
600  $|\Delta y_{t/\bar{t}}| = |y(t) - y(\bar{t})|$ .

601 In Fig. 48 the differential cross sections are shown as functions of kinematics of the  $t\bar{t}$  system  
602  $M(t\bar{t})$ ,  $p_T(t\bar{t})$ ,  $|y(t\bar{t})|$ , the angle between the top quarks in the transverse plane  $\Delta\phi_{t/\bar{t}}$ , and  
603  $\cos(\theta^*)$ , where  $\theta^*$  is the angle between  $t$  and the direction of flight of the  $t\bar{t}$  system calculated  
604 in the  $t\bar{t}$  rest-frame.

605 The double differential cross sections are shown in Figs. 49–54. Detailed information about the  
606 contribution of individual uncertainties is shown in Appendix D.

607 In Fig. 55 the double differential cross section as function of  $|y(t)|$  vs.  $|y(\bar{t})|$  is shown. This  
608 can be used to calculate the ratio of cross sections of  $t$  and  $\bar{t}$  as function of rapidity taking  
609 into account bin-by-bin correlations correctly. Differences in the rapidity of  $t$  and  $\bar{t}$  are a direct  
610 consequence of the charge asymmetry in  $t\bar{t}$  production in pp collisions, where in average  $|y(t)|$   
611 is higher than  $|y(\bar{t})|$ .



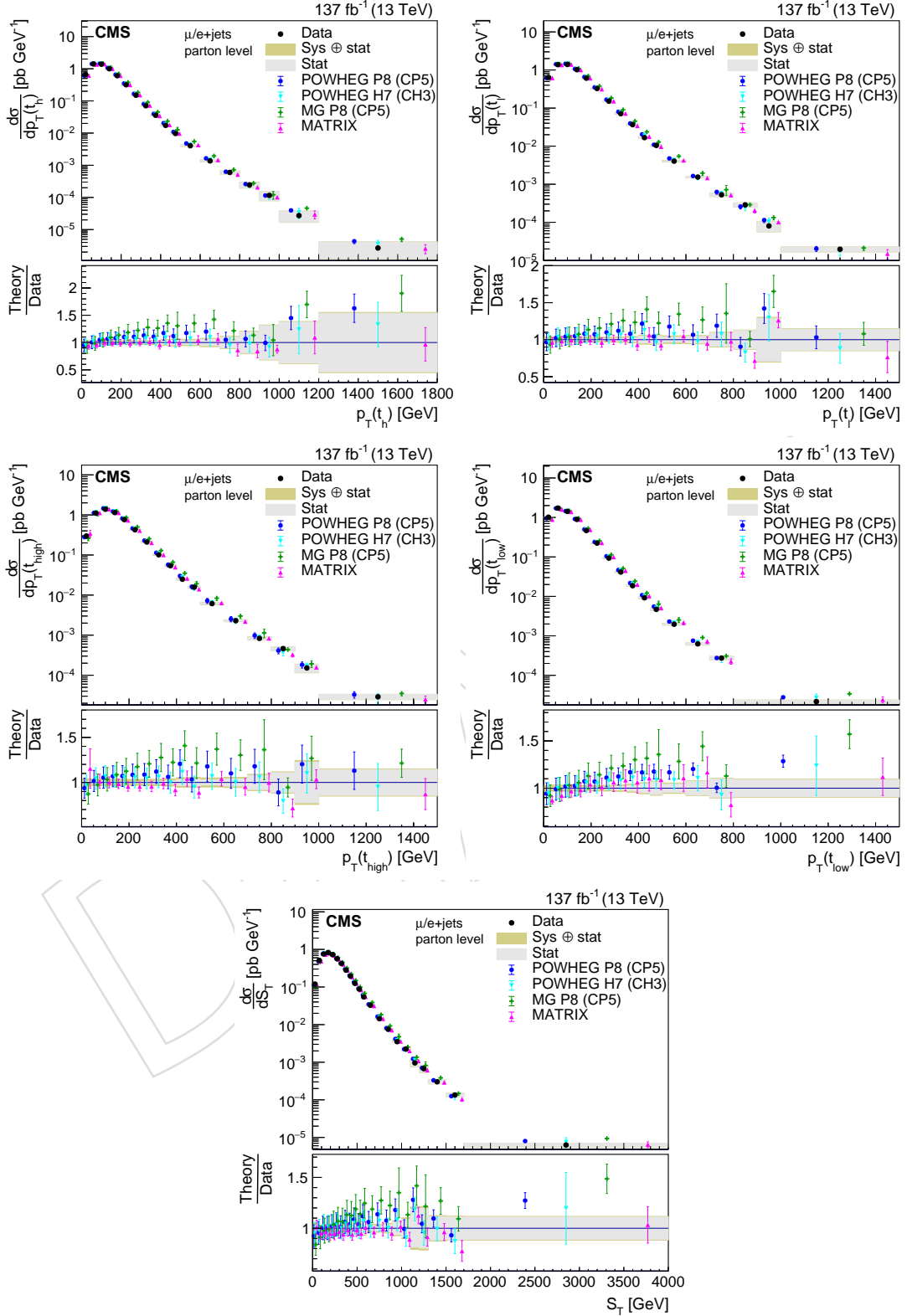


Figure 46: Differential cross section as function of  $p_T(t_h)$ ,  $p_T(t_\ell)$ ,  $p_T(t_{\text{hard}})$ ,  $p_T(t_{\text{soft}})$ , and  $S_T$

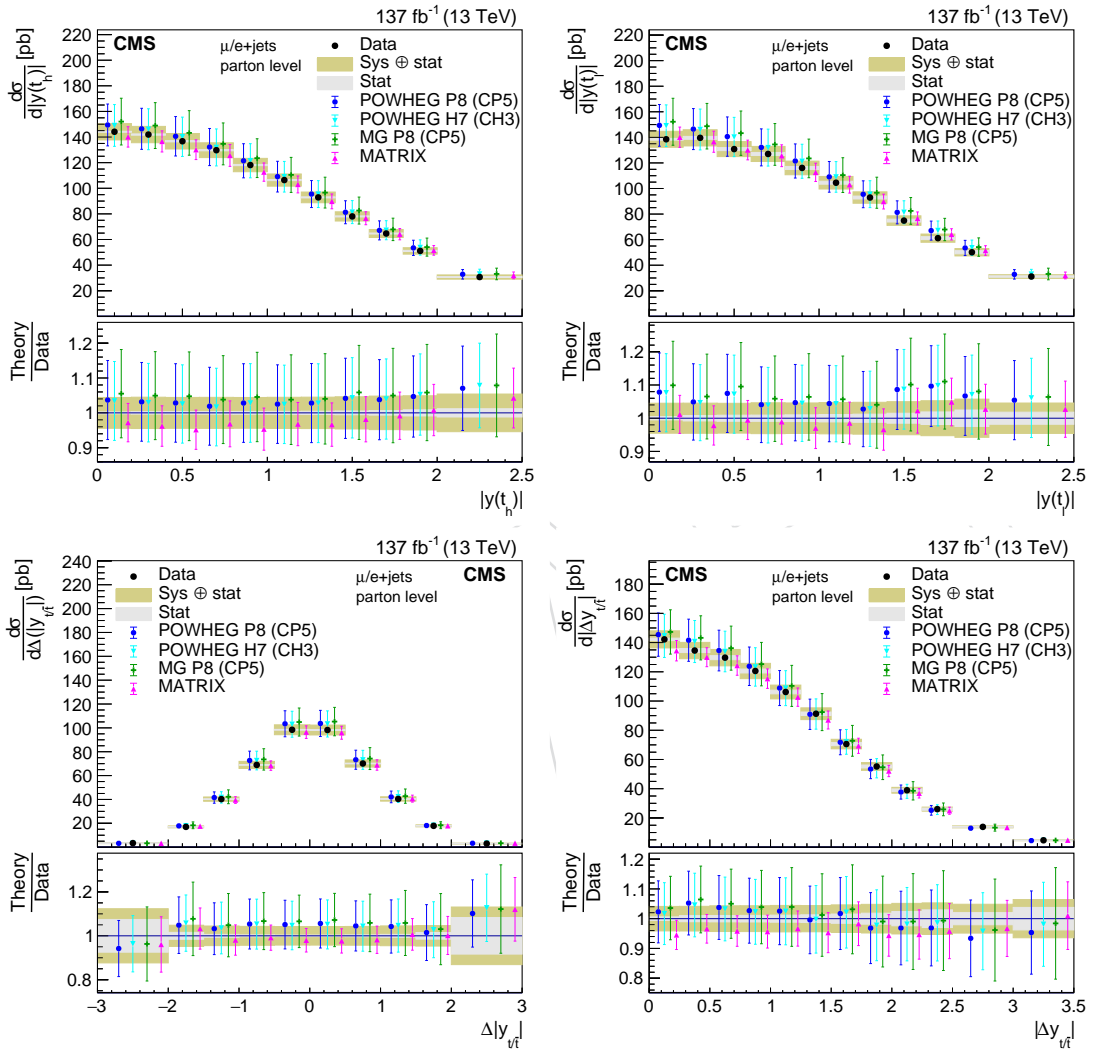


Figure 47: Differential cross section as function of  $|y(t_h)|$ ,  $|y(t_\ell)|$ , and the differences  $\Delta|y_{t/\bar{t}}|$  and  $|\Delta y_{t/\bar{t}}|$ .

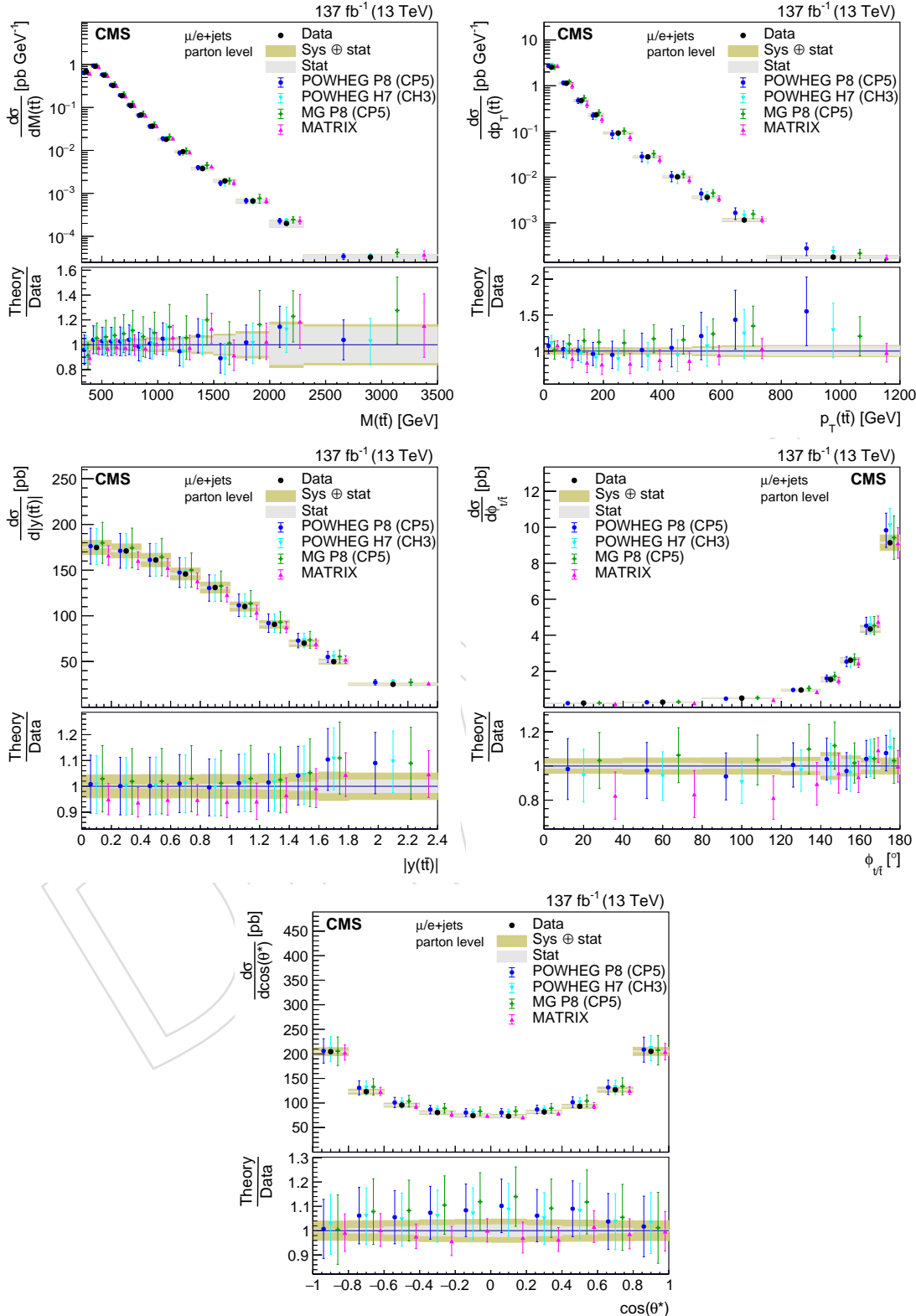


Figure 48: Differential cross sections as functions of quantities of the  $t\bar{t}$  system.

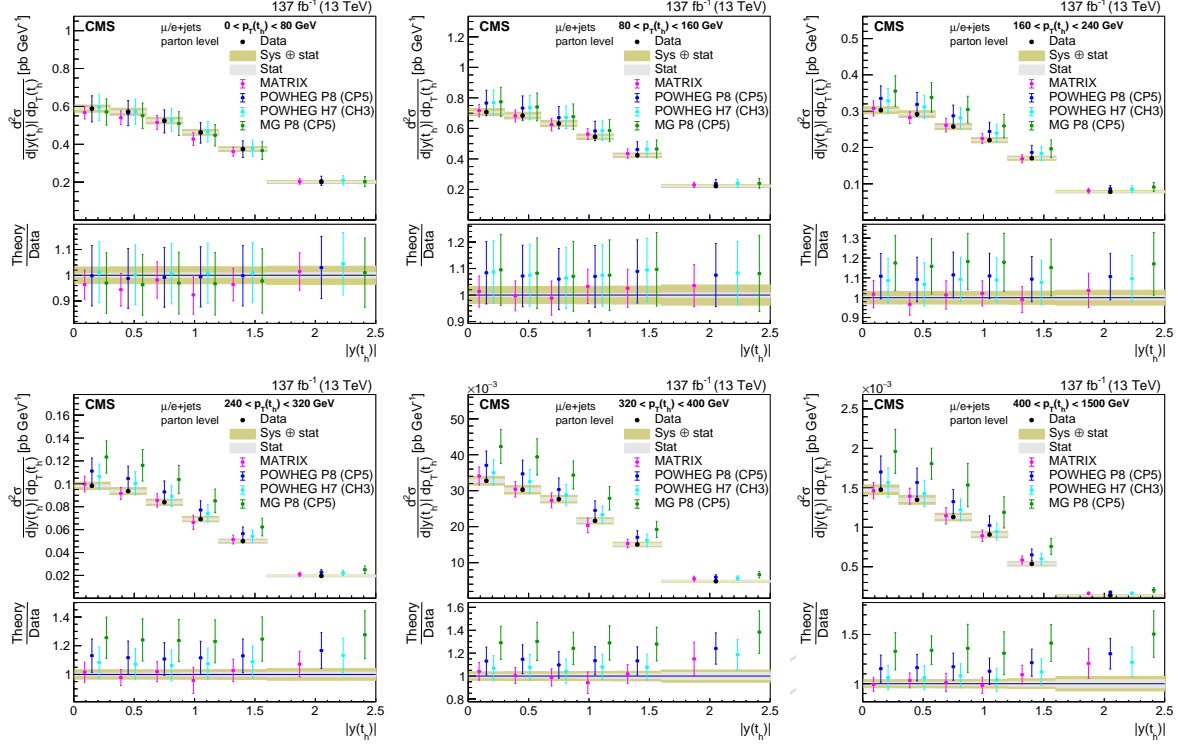


Figure 49: Double differential cross section as function of  $|y(t_h)|$  vs.  $p_T(t_h)$ .

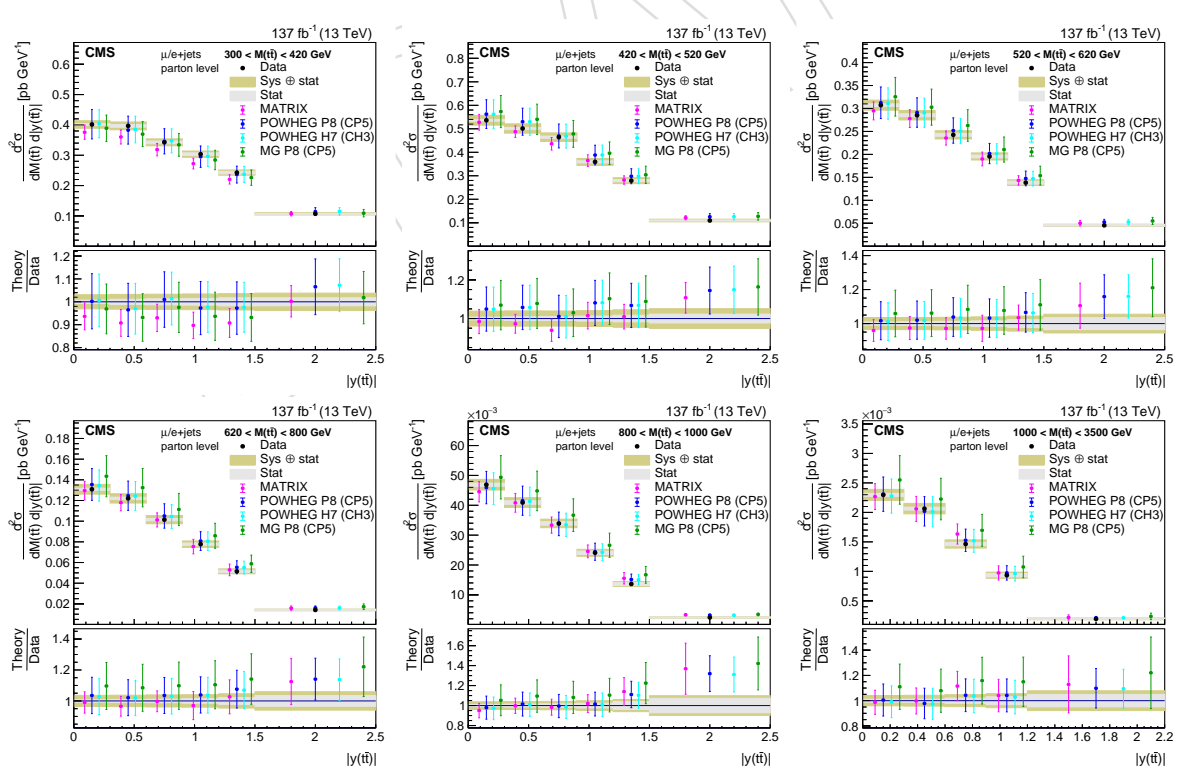


Figure 50: Double differential cross section as function of  $|y(t\bar{t})|$  vs.  $M(t\bar{t})$ .

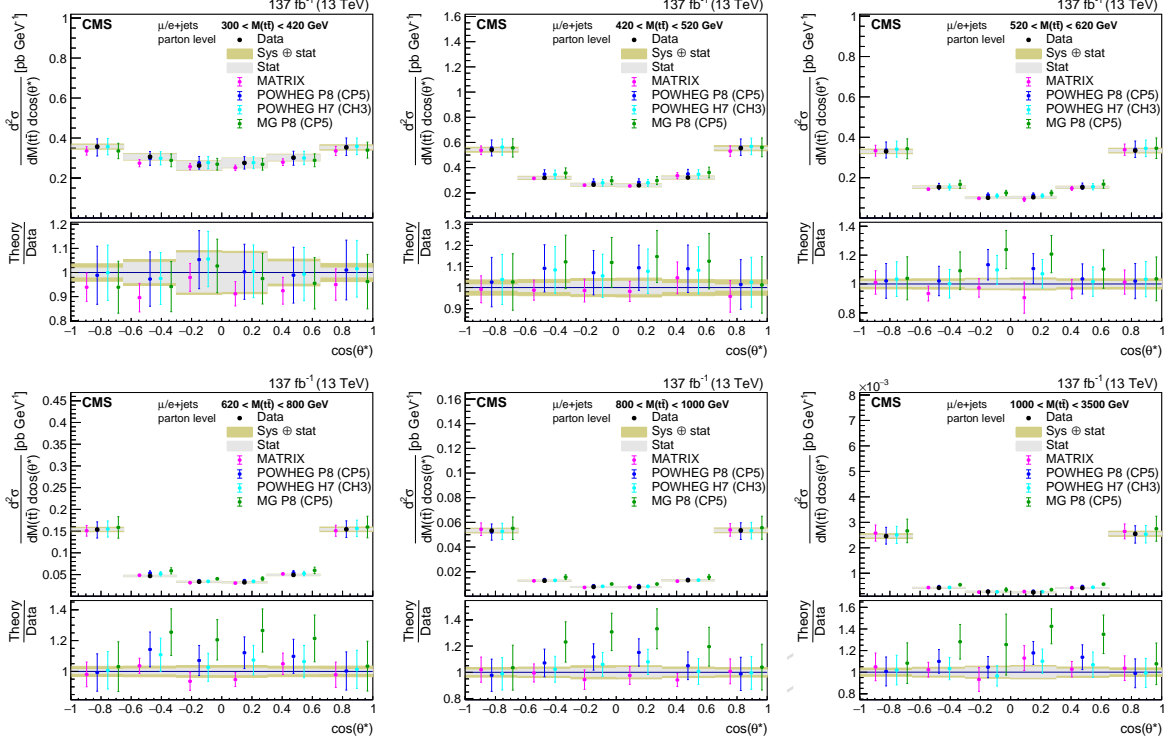


Figure 51: Double differential cross section as function of  $\cos(\theta^*)$  vs.  $M(t\bar{t})$ .

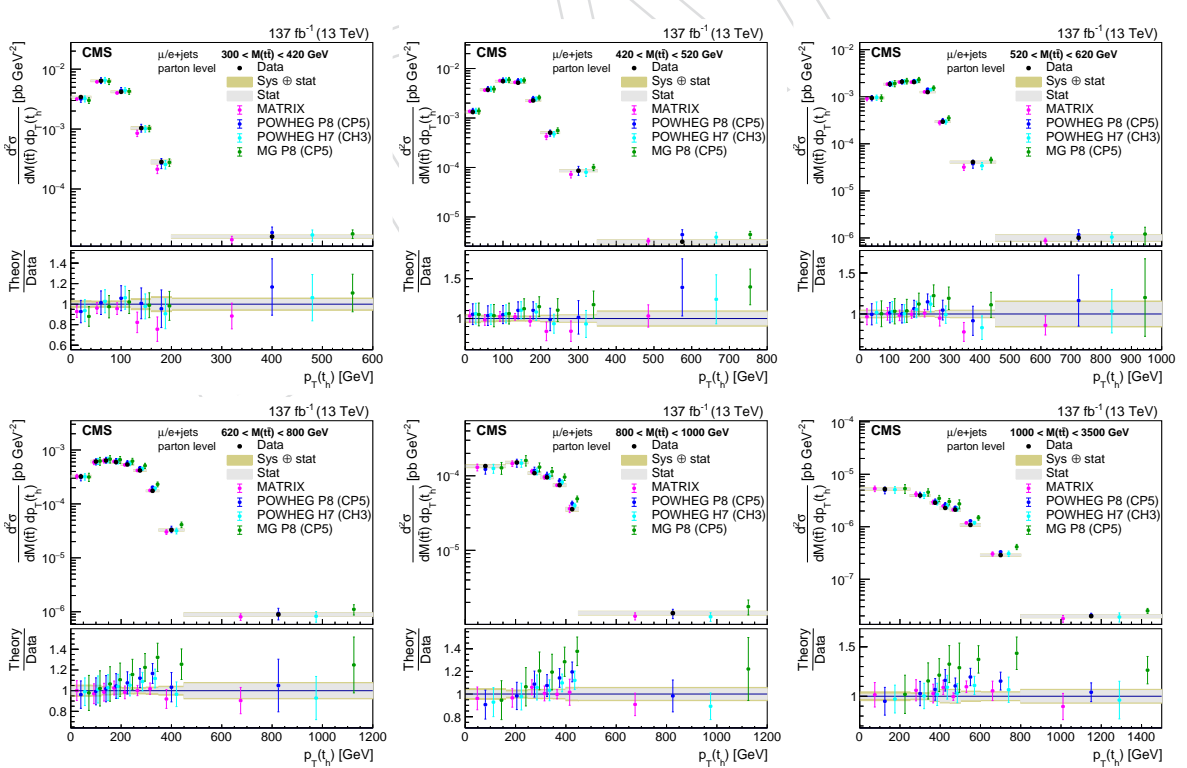


Figure 52: Double differential cross section as function of  $p_T(t_h)$  vs.  $M(t\bar{t})$ .

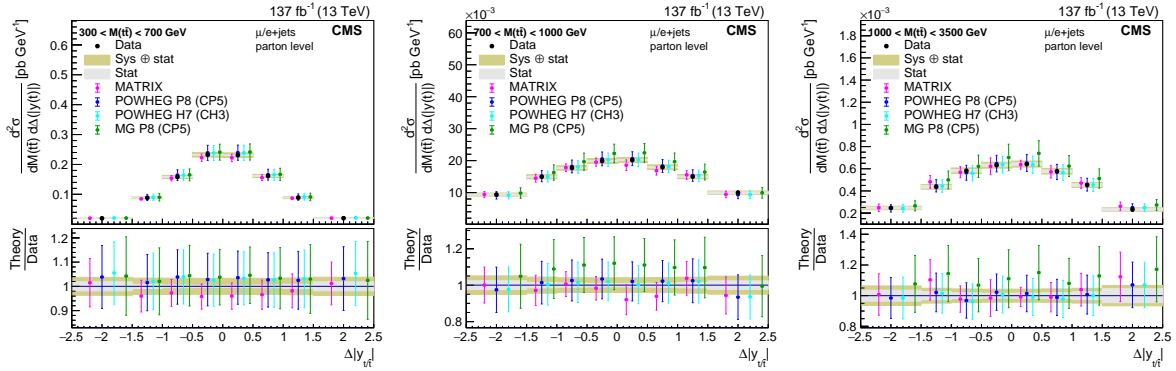


Figure 53: Double differential cross section as function of  $\Delta|y_{t/\bar{t}}|$  vs.  $M(t\bar{t})$ .

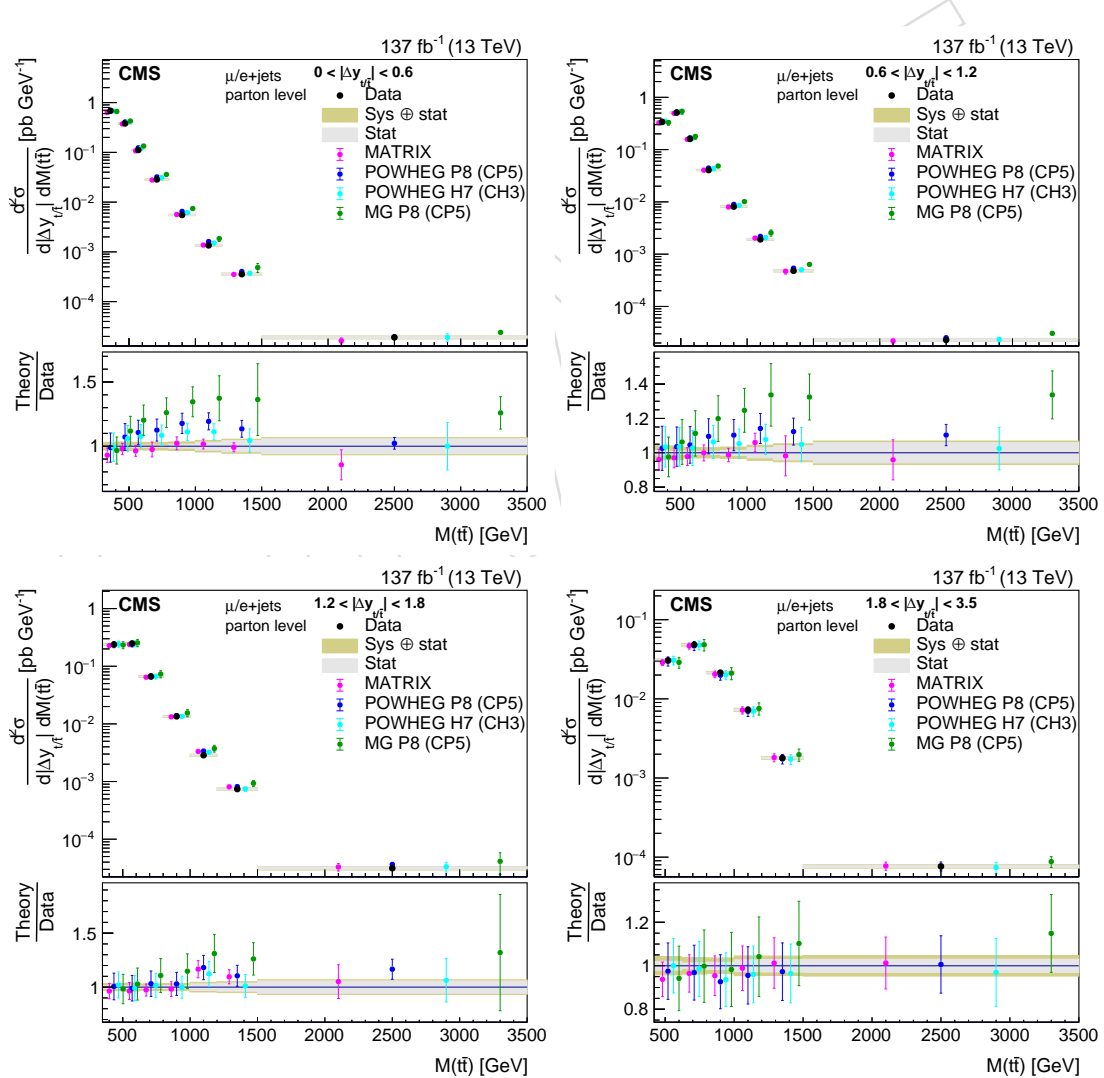


Figure 54: Double differential cross section as function of  $M(t\bar{t})$  vs.  $|\Delta y_{t/\bar{t}}|$ .

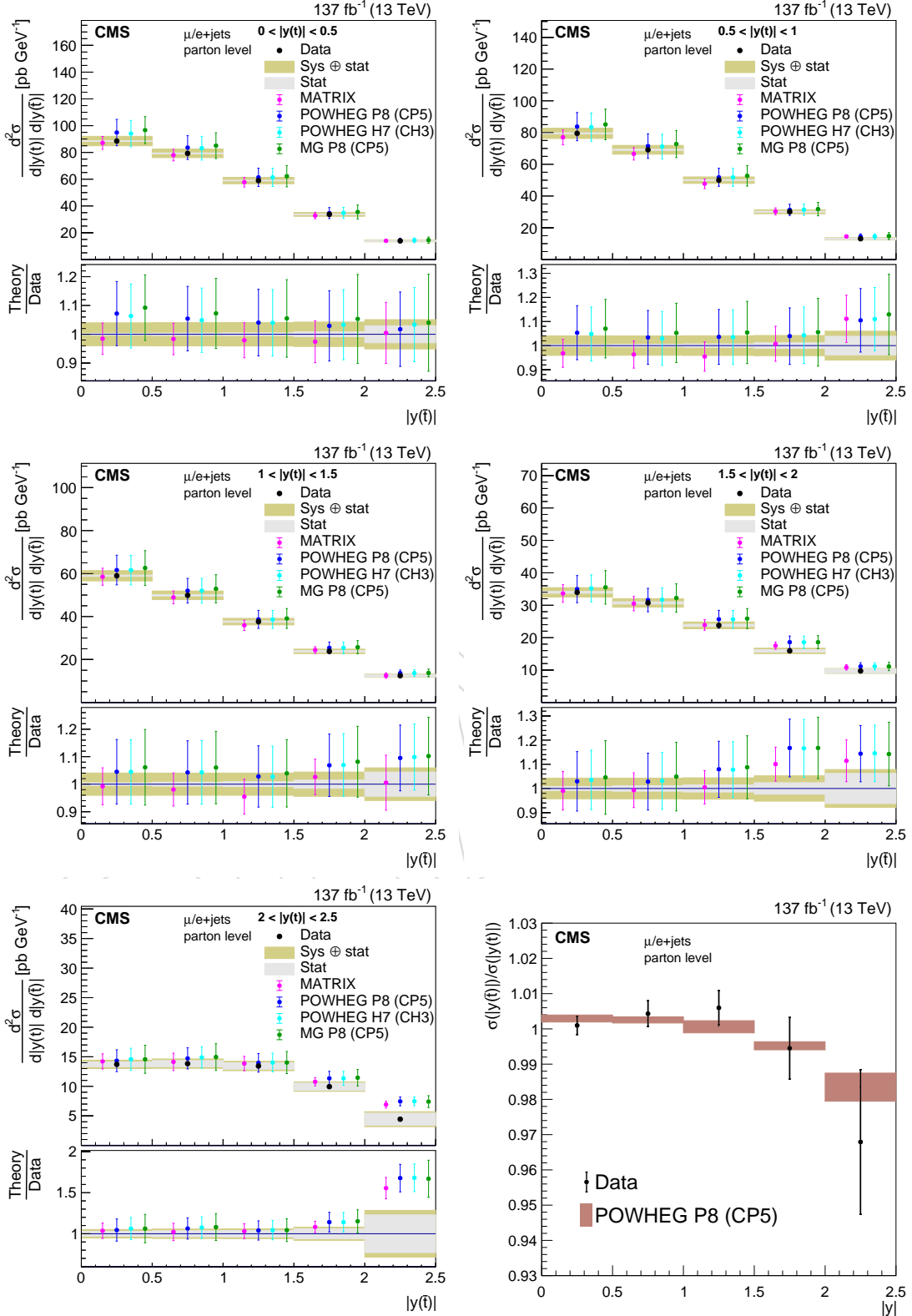


Figure 55: Double differential cross section as function of  $|y(t)|$  vs.  $|y(\bar{t})|$ . Bottom right: ratio of  $|y(\bar{t})|/|y(t)|$

## 612 13 Particle level analysis

### 613 13.1 Particle-level top quark definition

614 The definitions of particle-level objects constructed from quasi-stable simulated particles with  
 615 a mean lifetime greater than 30 ps, obtained from the predictions of  $t\bar{t}$  event generators before  
 616 any detector simulation, are summarized below. These particle-level objects are further used to  
 617 define the particle-level top quarks. Detailed studies on particle-level definitions can be found  
 618 in Ref. [19].

- 619 • All simulated electrons and muons, that do not originate from the decay of a hardron  
 620 in the final state, are corrected for effects of bremsstrahlung by adding the photon  
 621 momenta to the momentum of the closest lepton if their separation is  $\Delta R < 0.1$ . All  
 622 photons are considered for the momentum correction. In addition, we require the  
 623 corrected lepton to have  $p_T > 15 \text{ GeV}$  and  $|\eta| < 2.4$ .
- 624 • All neutrinos are selected including those stemming from decays of hadrons.
- 625 • Jets are clustered by the anti- $k_T$  jet algorithm [20, 21] with a distance parameter of  
 626 0.4. All quasi-stable particles with the exception of neutrinos are clustered. Jets with  
 627  $p_T > 25 \text{ GeV}$  and  $|\eta| < 2.4$  are selected if there is no ektron or muon, as defined  
 628 above, within  $\Delta R = 0.4$ .
- 629 • b jets at the particle level are defined as those jets that contain a b hadron. As a result  
 630 of the short lifetime of b hadrons, these are not quasi-stable particles and only their  
 631 decay products should be considered for the jet clustering. However, to allow their  
 632 association with a jet, the b hadrons are also included with their momenta scaled  
 633 down to a negligible value. This preserves the information of their directions, but  
 634 removes their impact on the jet clustering.
- 635 • Candidates of a boosted  $t_\ell$  are b jets that are rejected by the lepton cleaning, i.e.,  
 636 there is a selected lepton within the jet cone of  $\Delta R < 0.4$ . However, a  $p_T > 50 \text{ GeV}$   
 637 is required for the lepton. The candidate momentum is calculated as the sum of  
 638 the momenta of the jet, the lepton, and all selected neutrinos. It is ensured that the  
 639 lepton momentum is not counted twice if it is a constituent of the jet. Finally, a  
 640  $p_T > 400 \text{ GeV}$  and  $|\eta| < 2.4$  is required for the candidate.
- 641 • Candidates of a boosted  $t_h$  are jets defined exactly as the b jets above but clus-  
 642 tered and cleaned from leptons with a distance parameter of 0.8. In addition, the  
 643 invariant mass of all constituents  $M_{\text{jet}}$  is required to be greater than  $120 \text{ GeV}$  with  
 644  $p_T > 400 \text{ GeV}$  and  $|\eta| < 1.6$ .

645 Based on the invariant masses of these objects, we construct a pair of particle-level top quarks  
 646 in the  $e/\mu + \text{jets}$  final state. Events with exactly one electron or muon with  $p_T > 30 \text{ GeV}$  and  
 647  $|\eta| < 2.4$  are selected. Simulated events with an additional selected electron or muon are  
 648 rejected.

649 If one candidate for a boosted  $t_\ell$  and at least one candidate for a boosted  $t_h$  exist, the boosted  $t_h$   
 650 with  $M_{\text{jet}}$  closest to  $m_t$  is selected and the two form the pair of particle-level top quarks. If there  
 651 is a boosted  $t_\ell$  but no candidate of a boosted  $t_h$ , the event is rejected. A combination of a boosted  
 652  $t_\ell$  and a resolved reconstruction of a  $t_h$  is, in analogy to the detector-level reconstruction, not  
 653 considered.

654 If there is no boosted  $t_\ell$ , we take the sum of the four-momenta of all neutrinos as the neutrino  
 655 candidate momentum  $p_\nu$  from  $t_\ell$  decay and find the permutation of jets that minimizes the  
 656 quantity

$$[M(p_\nu + p_\ell + p_{b_\ell}) - m_t]^2 + [M(p_{j_{W1}} + p_{j_{W2}}) - m_W]^2 + [M(p_{j_{W1}} + p_{j_{W2}} + p_{b_h}) - m_t]^2, \quad (8)$$

657 where  $p_{j_{W1,2}}$  are the four-momenta of two light-flavor jet candidates, considered as the decay  
 658 products of the hadronically decaying W boson;  $p_{b_{\ell,h}}$  are the four-momenta of two b jet candi-  
 659 dates;  $p_\ell$  is the four-momentum of the lepton; and  $m_W = 80.4 \text{ GeV}$  [22] is the mass of the W  
 660 boson. All jets with  $p_T > 25 \text{ GeV}$  and  $|\eta| < 2.4$  are considered. At least four jets are required,  
 661 of which at least two must be b jets. The remaining jets with  $p_T > 30 \text{ GeV}$  and  $|\eta| < 2.4$  are  
 662 defined as additional jets.

663 Alternatively, we also evaluate the possibility of a selection with boosted  $t_h$  by minimizing

$$[M(p_\nu + p_\ell + p_{b_\ell}) - m_t]^2 + [M_{\text{jet}} - m_t]^2, \quad (9)$$

664 If both reconstruction methods, for the resolved and the boosted  $t_h$ , are successful, we select  
 665 the reconstruction for which  $M(t_h)$  is closer to  $m_t$ .

666 Events with a hadronically and a leptonically decaying particle-level top quark are not required  
 667 to be  $e/\mu$ +jets events at the parton level, e.g.,  $t\bar{t}$  dilepton events with additional jets can be  
 668 identified as  $e/\mu$ +jets event at the particle level if one lepton fails to pass the selection. As an  
 669 example, the comparison between the  $p_T(t_h)$  distributions at the particle and parton levels are  
 670 shown in Fig. 56 and demonstrates the direct relation between particle-level and parton-level  
 671 top quarks. Overall a good correspondence between the particle level and the parton level  
 672 is observed. This ensures that the observables are sensitive to the underlying physics of  $t\bar{t}$   
 673 production.

DRAFT

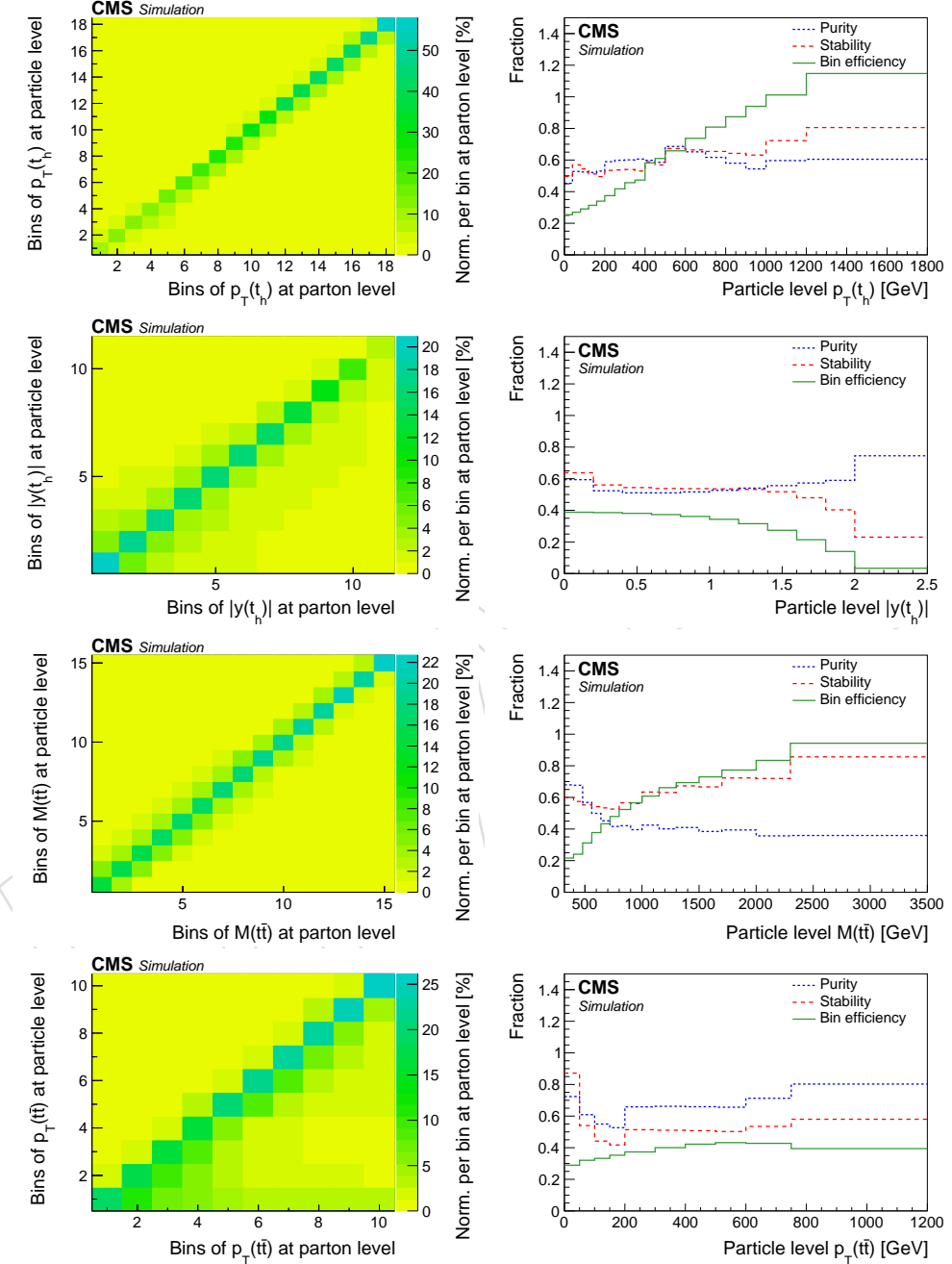


Figure 56: Relations between particle and parton-level.

674 **13.2 Differences in the particle-level analysis**

675 The event selection and reconstruction follows exactly the same strategy as in the parton-level  
 676 measurement. The only difference are modified probability distributions used in the recon-  
 677 struction of the resolved categories as shown in Fig. 57.

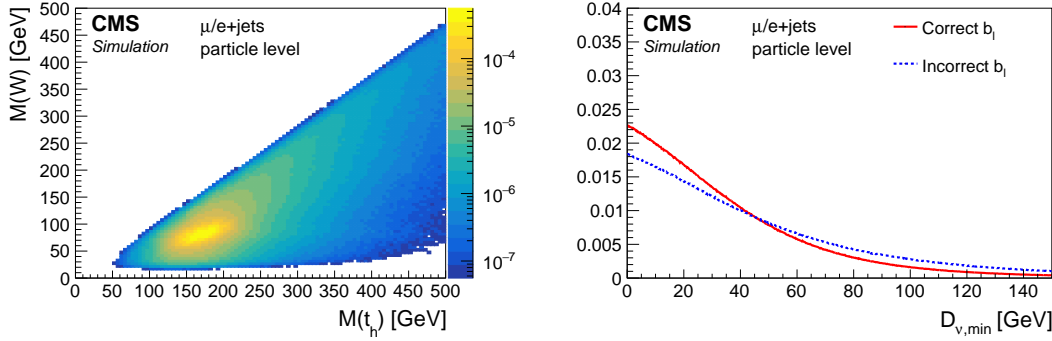


Figure 57: Normalized two-dimensional mass distribution of the correctly reconstructed hadronically decaying W bosons  $M(W)$  and the correctly reconstructed top quarks  $M(t_h)$  (left). Normalized distributions of the distance  $D_{v,\min}$  for correctly and incorrectly selected b jets from the leptonically decaying top quarks (right). The distributions are taken from the POWHEG+PYTHIA8 $t\bar{t}$  simulation.

678 In Figs. 58–62 comparisons of data and simulation are shown for the various categories.

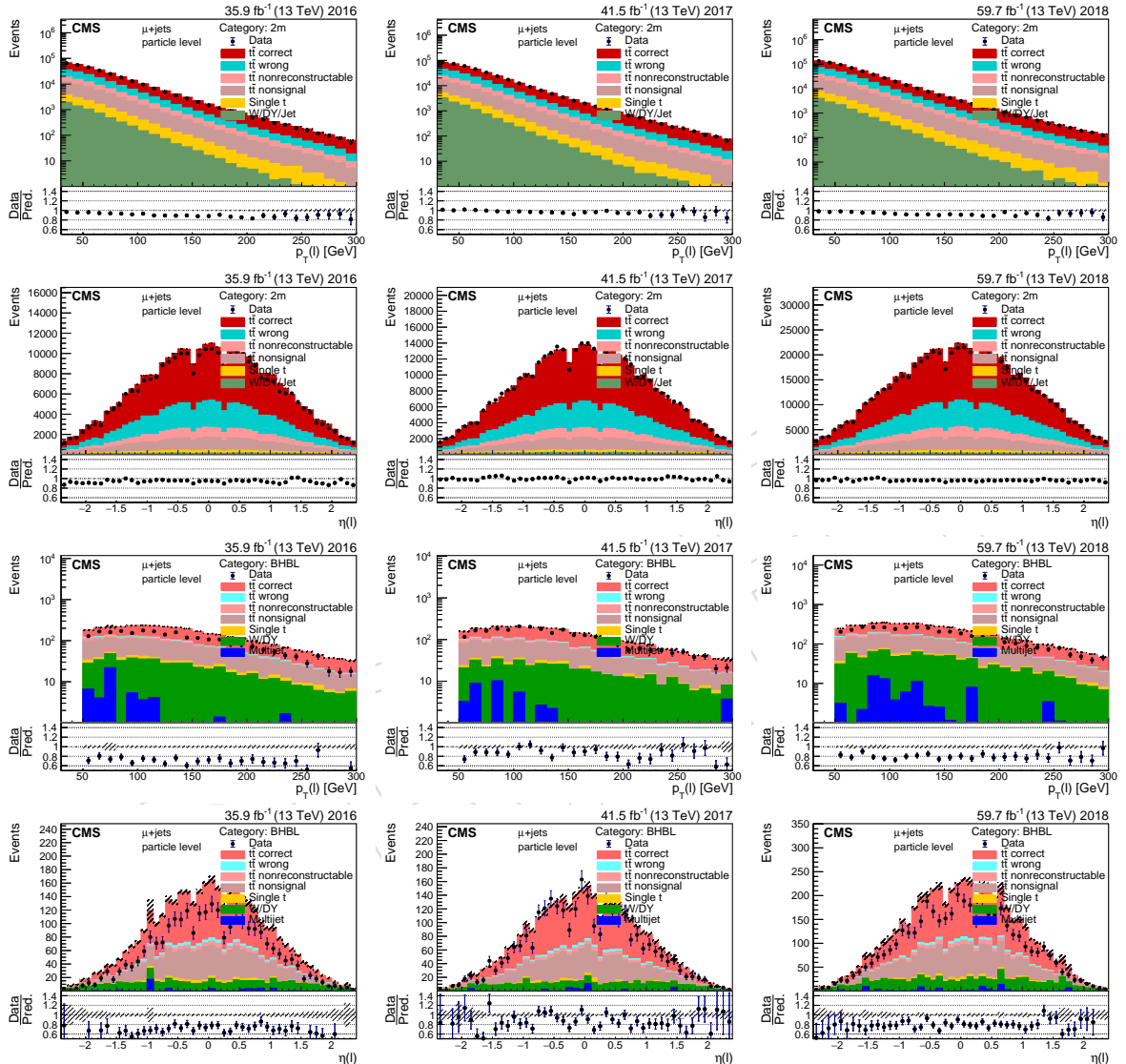


Figure 58: Data to simulation comparisons of the muon  $p_T$  and  $\eta$  for the three years. The upper two rows show the 2m category with isolated muons the lower two rows show the BHBL category with nonisolated muons. The hatched uncertainty shows the statistical uncertainties in the prediction.

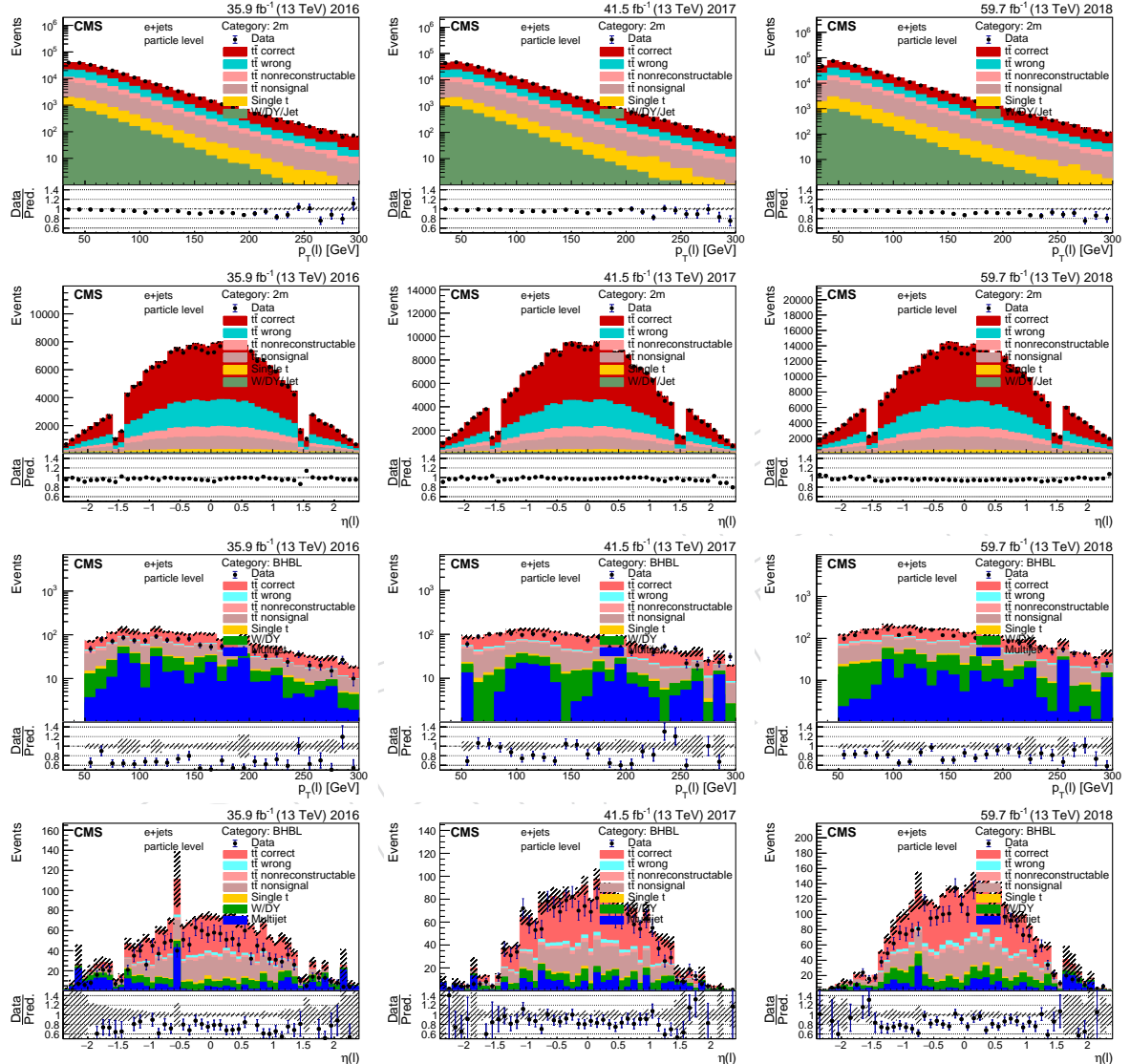


Figure 59: Data to simulation comparisons of the electron  $p_T$  and  $\eta$  for the three years. The upper two rows show the 2m category with isolated electrons the lower two rows show the BHBL category with nonisolated electrons. The hatched uncertainty shows the statistical uncertainty in the prediction.

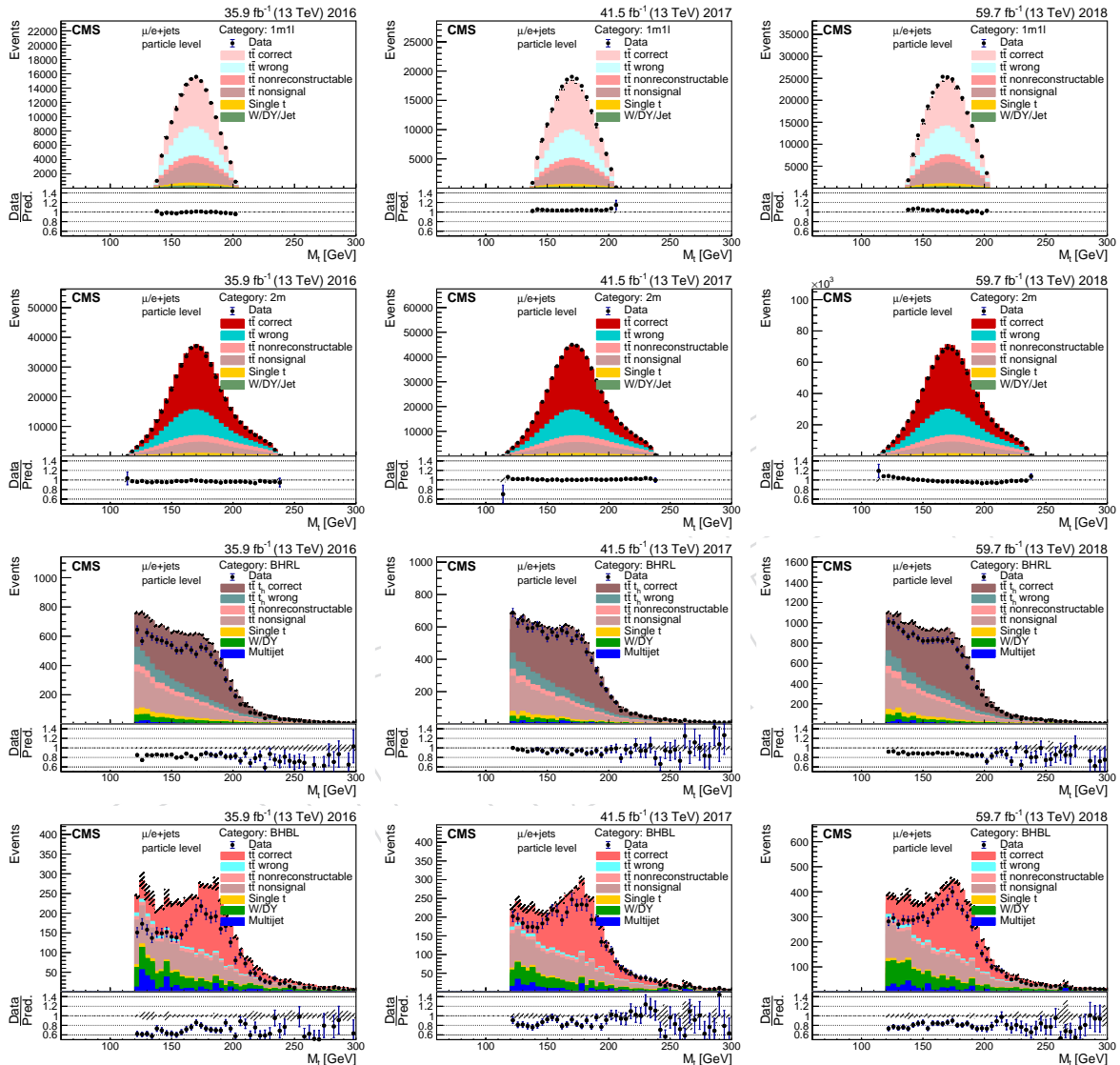


Figure 60: Data to simulation comparisons of the reconstructed  $m_t$  of the  $t_h$  for the three years. From top to bottom these are the categories: 1m1l, 1m, BHRL, BHBL. The hatched uncertainty shows the statistical uncertainties in the prediction.

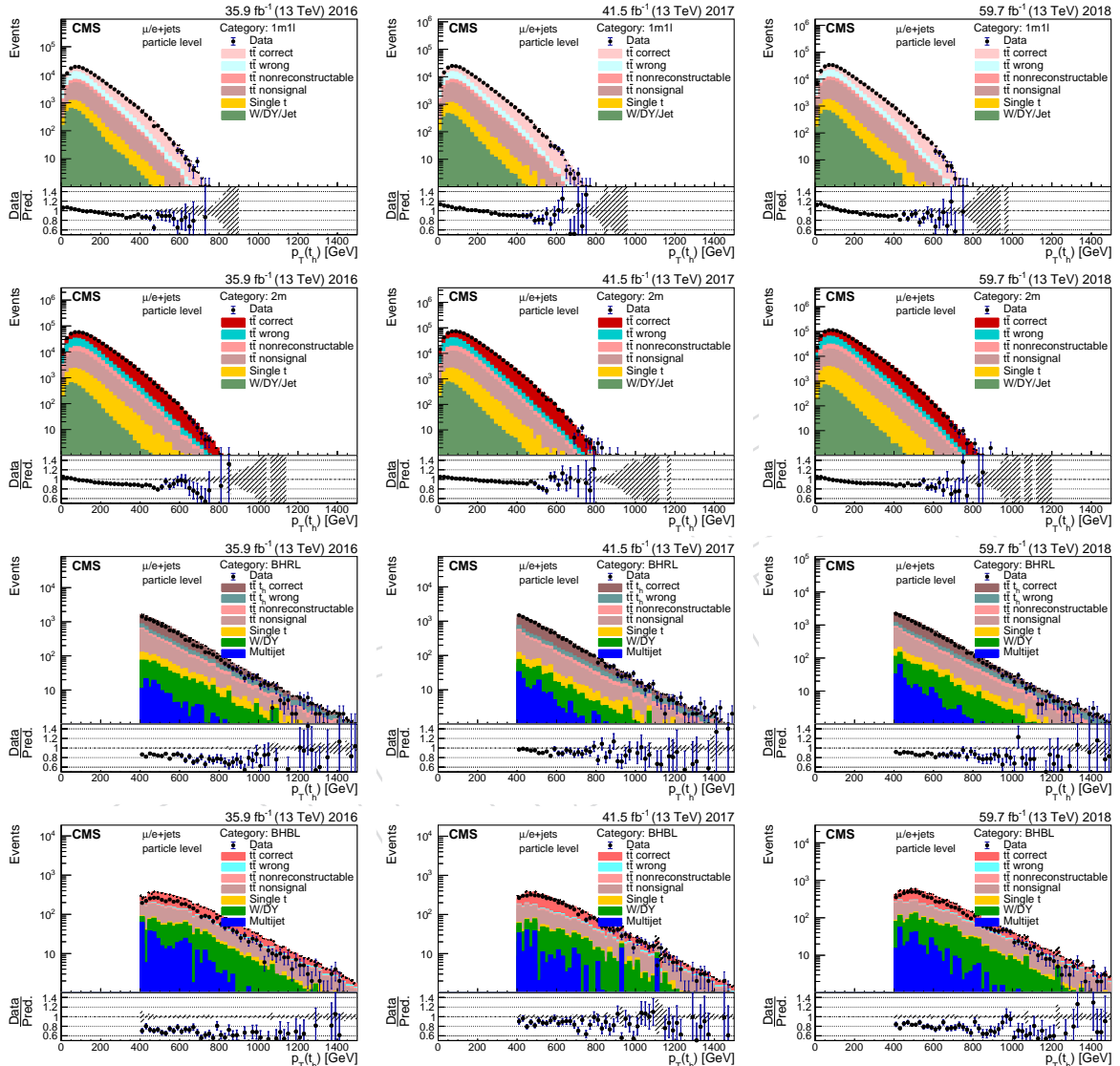


Figure 61: Data to simulation comparisons of the reconstructed  $p_T(t_h)$  for the three years. From top to bottom these are the categories: 1m1l, 1m, BHRL, BHBL. The hatched uncertainty shows the statistical uncertainties in the prediction.

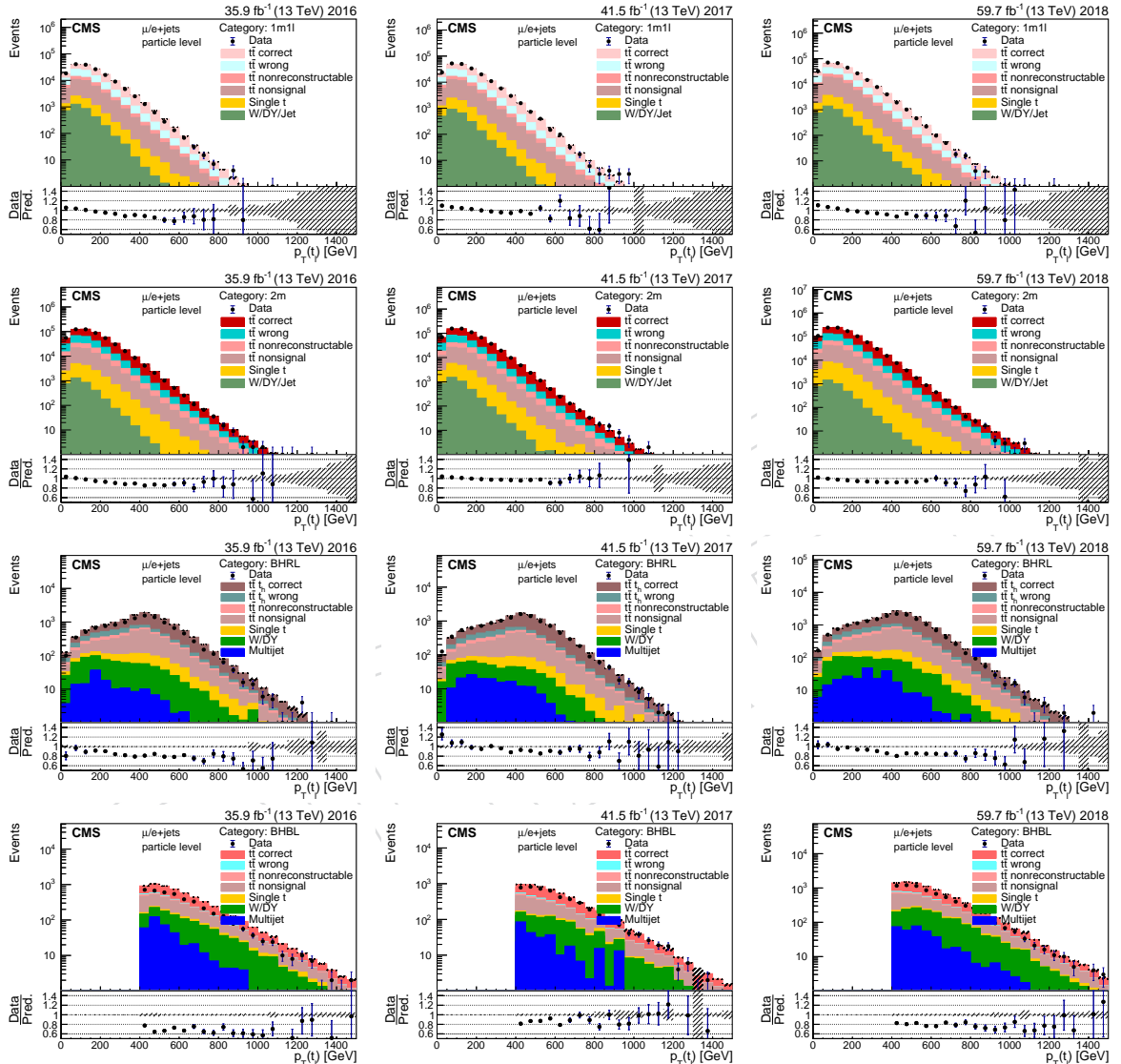


Figure 62: Data to simulation comparisons of the reconstructed  $p_T(t_\ell)$  for the three years. From top to bottom these are the categories: 1m1l, 1m, BHRL, BHBL. The hatched uncertainty shows the statistical uncertainties in the prediction.

Table 6: Systematic uncertainties in the measurement of  $\sigma_{\text{particle}}$ .

Source	Uncertainty [pb] (%)
Lepton	0.81(1.15)
Jet energy	0.70(0.99)
b tagging	0.59(0.84)
Mistagging	0.27(0.38)
L1 prefire	0.05(0.08)
Background	0.43(0.61)
Pileup	0.12(0.17)
FSR scale	0.24(0.34)
PDF	0.21(0.30)
Scales $\mu_r/\mu_f$	0.13(0.19)
CR model	0.10(0.15)
b decay	0.08(0.11)
$h_{\text{damp}}$	0.05(0.08)
Tune	0.04(0.06)
$m_t$	0.04(0.06)
NNLO	0.04(0.05)
ISR scale	0.01(0.02)
Sim. stat	0.81(1.15)
Sys	1.6(2.3)
Stat	0.05(0.07)
Luminosity	1.23(1.75)

### 679 13.3 Results at particle level

680 The same distributions measured as at parton level. In addition, new observables are added:  
 681 these is the transverse momentum of the lepton in the  $t\ell$  decay  $p_T(\ell)$ , the numbers of additional  
 682 jets ( $p_T(\text{jet}) > 30 \text{ GeV}$  and  $|\eta| < 2.4$ ), the scalar  $p_T$  sum of the additional jets  $H_T$ , and the  
 683 invariant mass of the top quarks and the additional jets  $M_{\text{evt}}$  (event mass). Detailed information  
 684 about the contribution of individual uncertainties is shown in Appendix E.

685 The pulls of the post fit nuisances are shown in Figs. 63 and 64, respectively. As in the parton-  
 686 level measurement almost all pulls are within  $1\sigma$  and mostly unconstrained. The p-values  
 687 indicating a decent goodness of the fits are calculated from the minimized  $\chi^2$  and the number  
 688 of degrees of freedom. They are shown in Fig. 65 together with the integrated cross sections,  
 689 which show compatible results for all measurements. One exception is the measurement as a  
 690 function of  $H_T$  where the integrated cross section is lower because  $H_T = 0$  for events with zero  
 691 additional jets and these events do not contribute. The most precise result is, as for the parton  
 692 level, the measurement of  $M(t\bar{t})$  vs.  $\cos(\theta^*)$  and is

$$\sigma_{\text{particle}} = 70.6 \pm 1.9 \text{ pb}. \quad (10)$$

693 In Tab. 6 the uncertainties are split into individual sources.

694 Figs. 66–79 show the results at particle level.

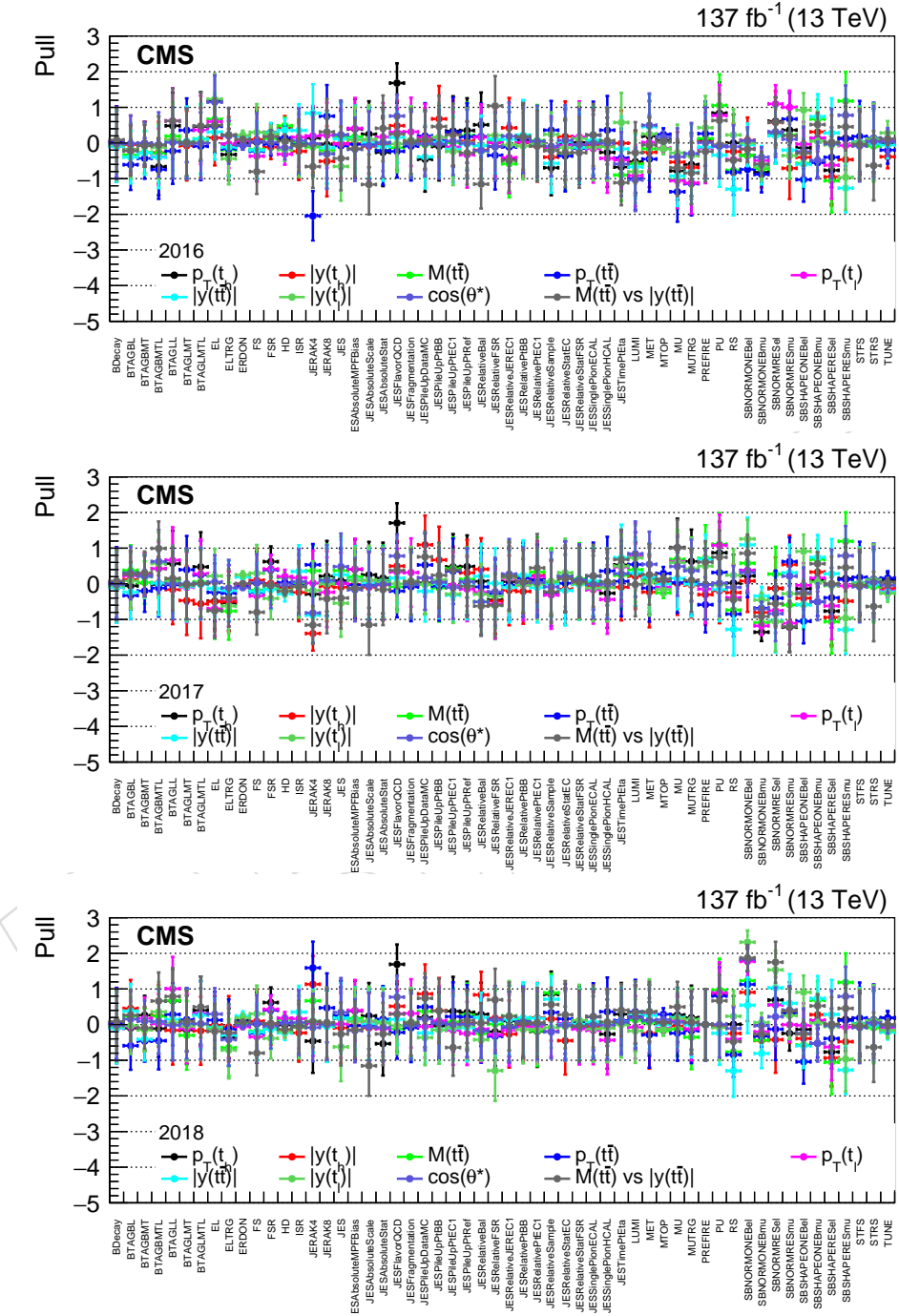


Figure 63: Post fit nuisances of the measurements at particle level.

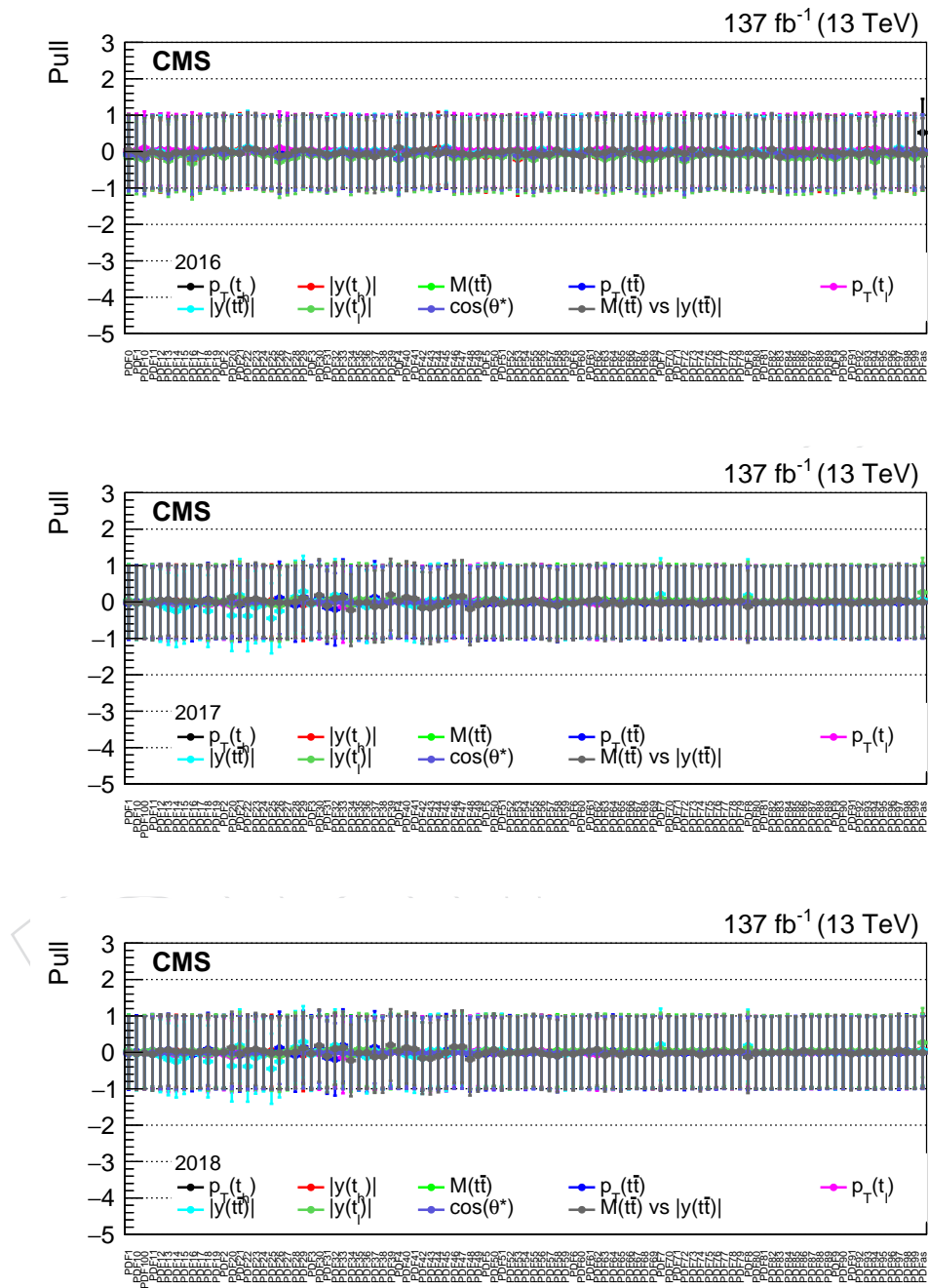


Figure 64: Post fit nuisances (PDF) of the measurements at particle level.

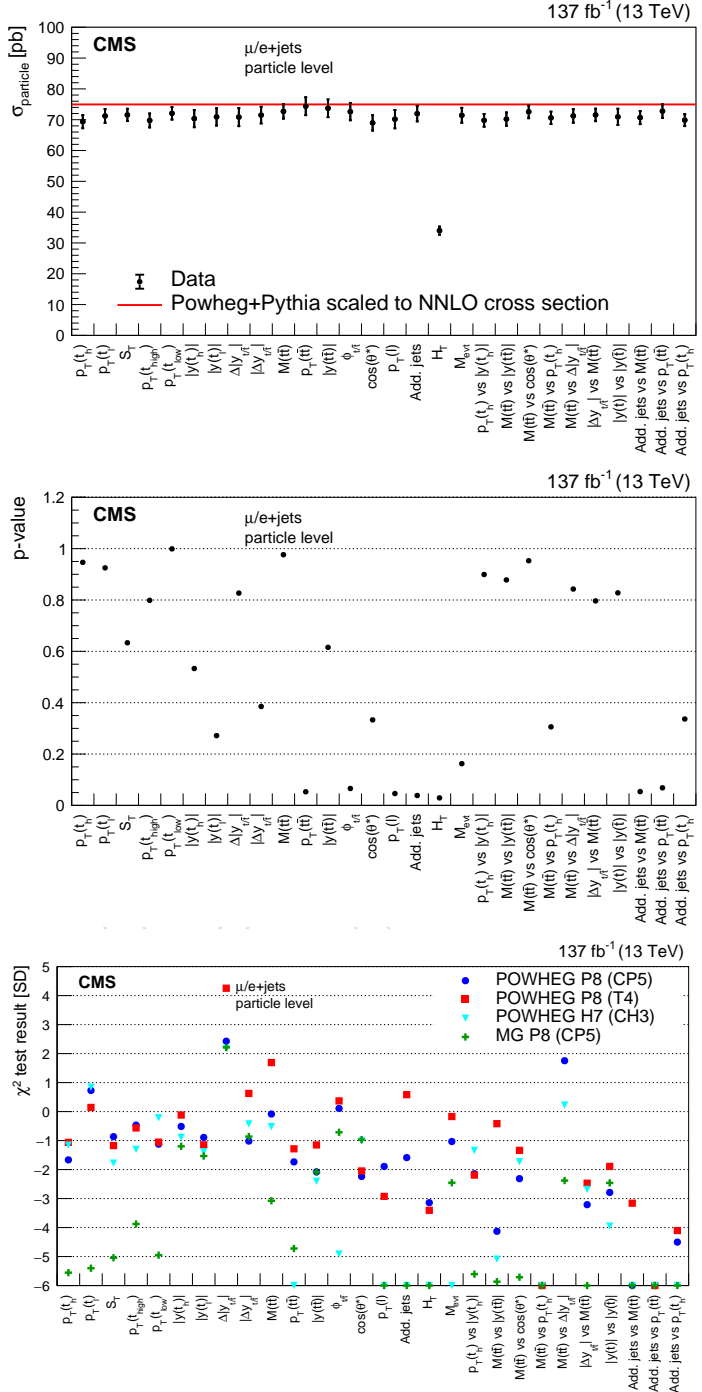


Figure 65: Upper: cross sections in the fiducial region defined by the particle level definition obtained by integrating the differential distributions. Middle: p-values after minimizing  $\chi^2$ . Lower: Results of  $\chi^2$  tests comparing the measurements to several SM predictions. The tests consider uncertainties in the measurements and the predictions.

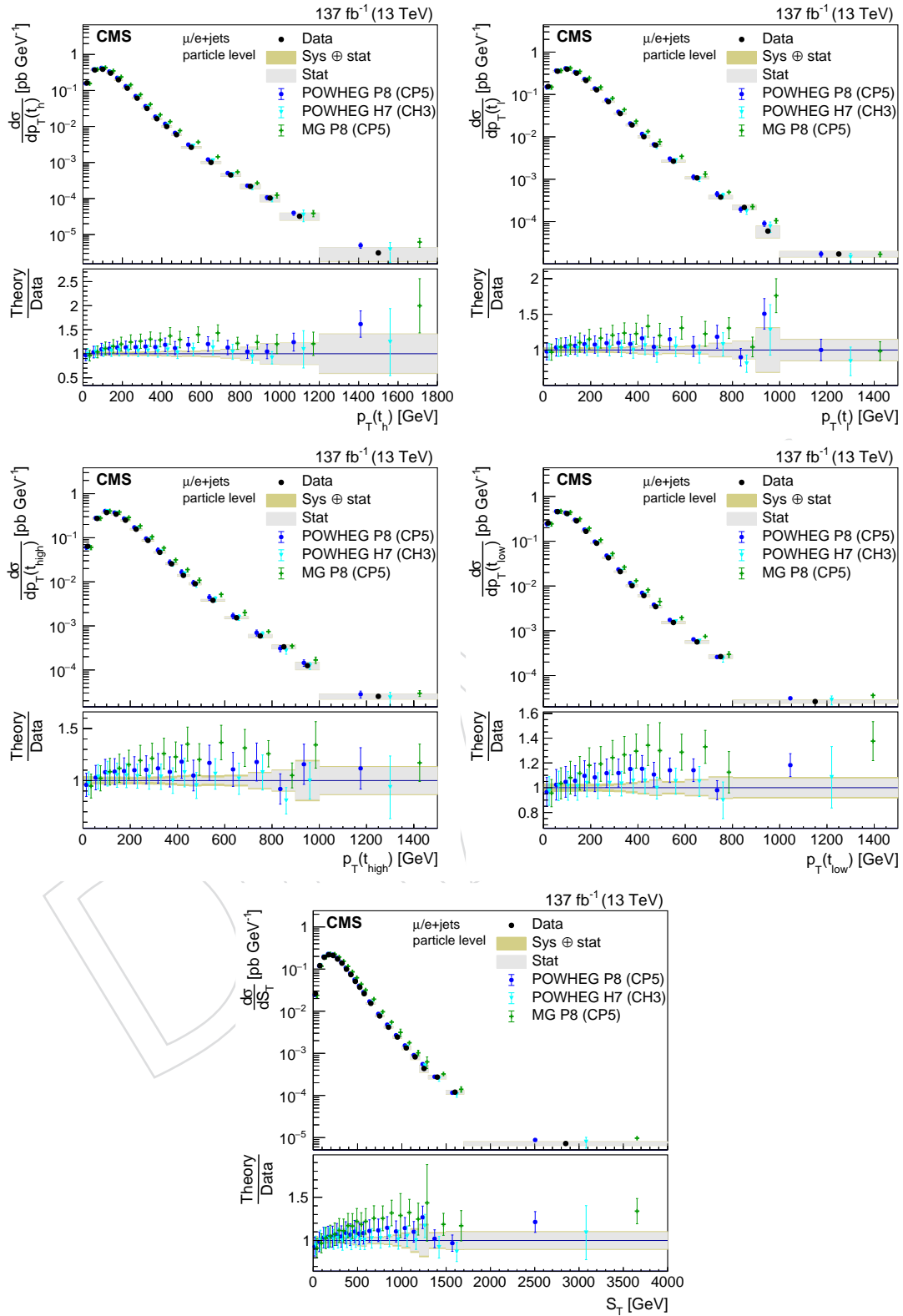


Figure 66: Differential cross section as function of  $p_T(t_h)$ ,  $p_T(t_\ell)$ ,  $p_T(t_{\text{hard}})$ ,  $p_T(t_{\text{soft}})$ , and  $S_T$

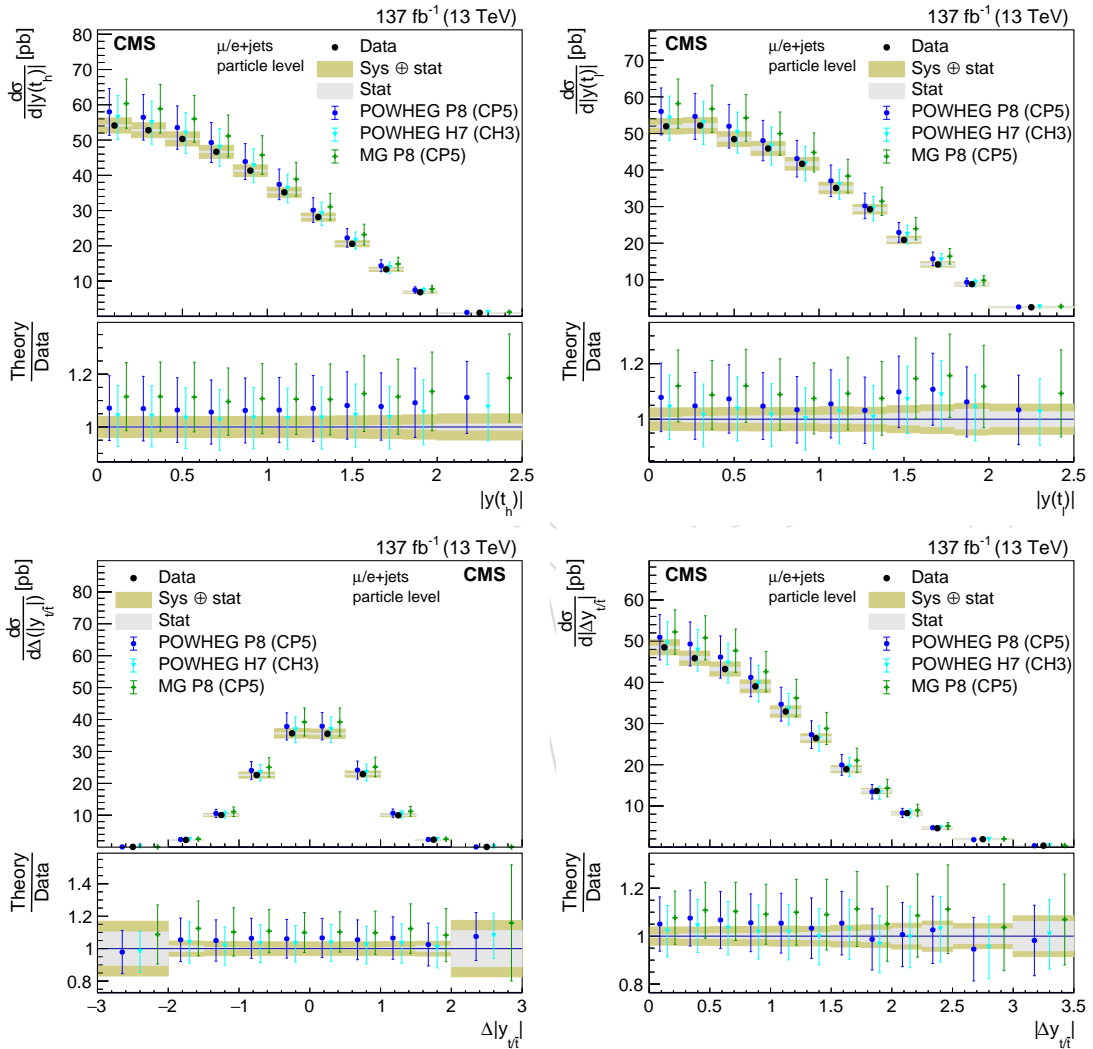


Figure 67: Differential cross section as function of  $|y(t_h)|$ ,  $|y(t_\ell)|$ , and the differences  $\Delta|y_{t/\bar{t}}|$  and  $|\Delta y_{t/\bar{t}}|$ .

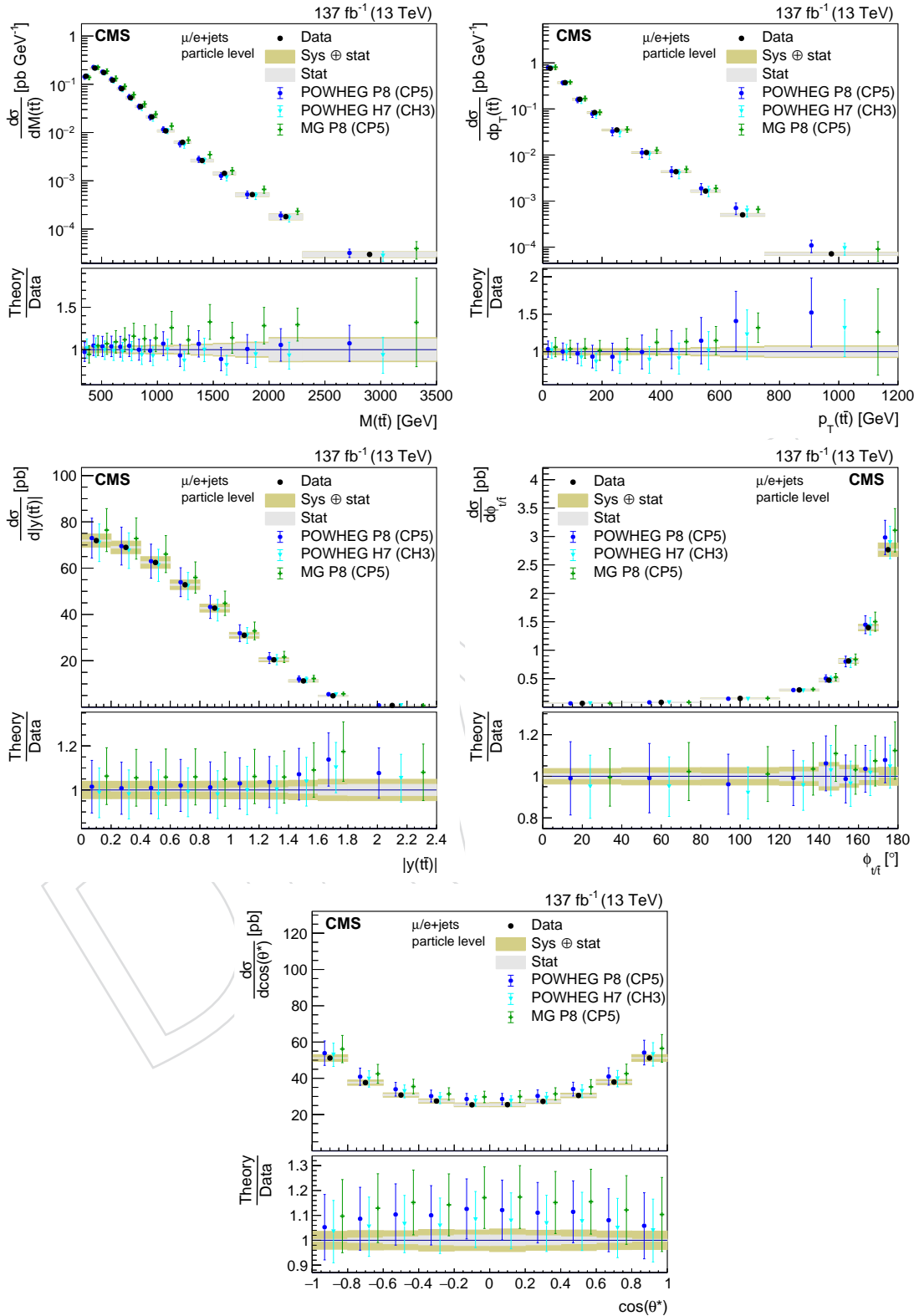


Figure 68: Differential cross sections as functions of quantities of the  $t\bar{t}$  system.

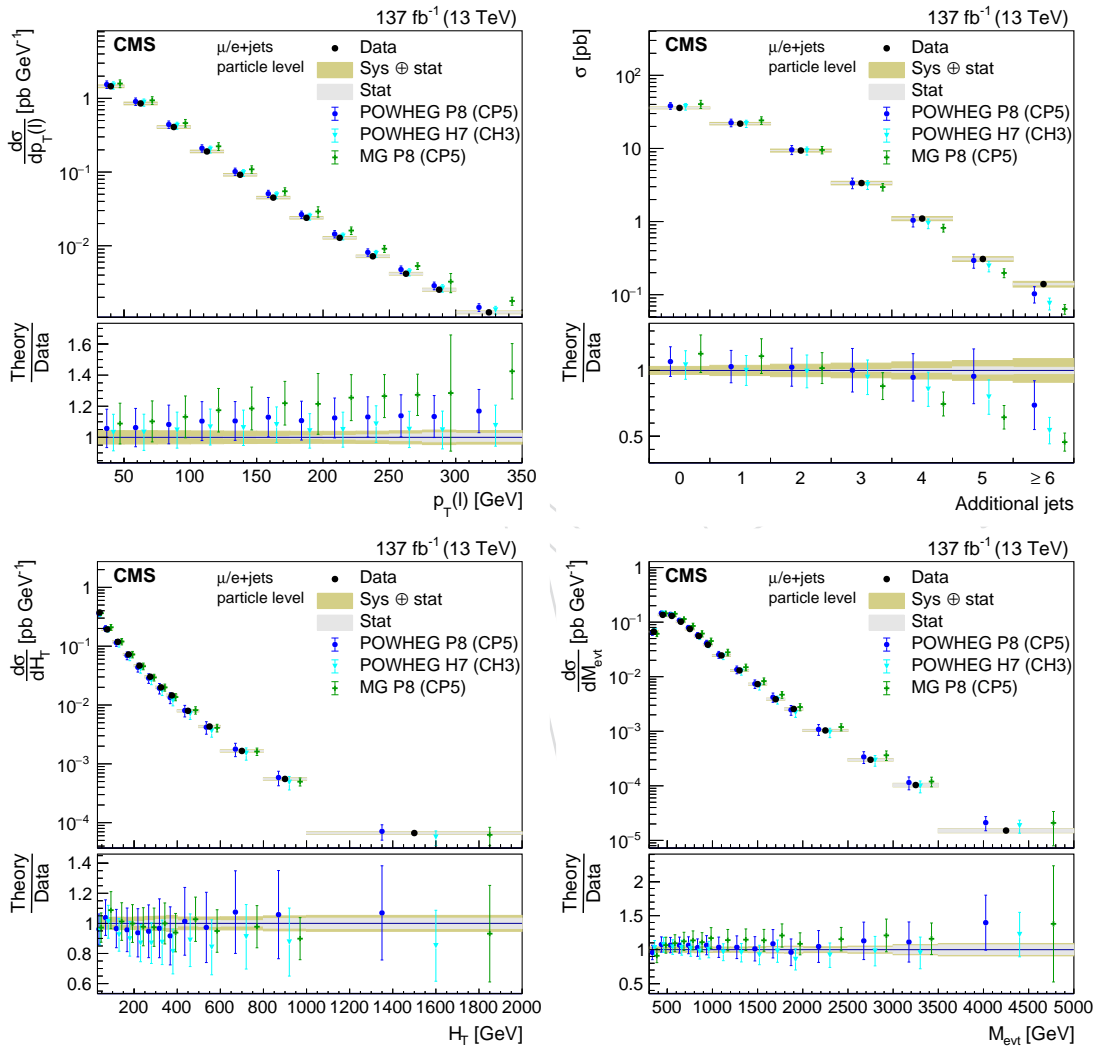
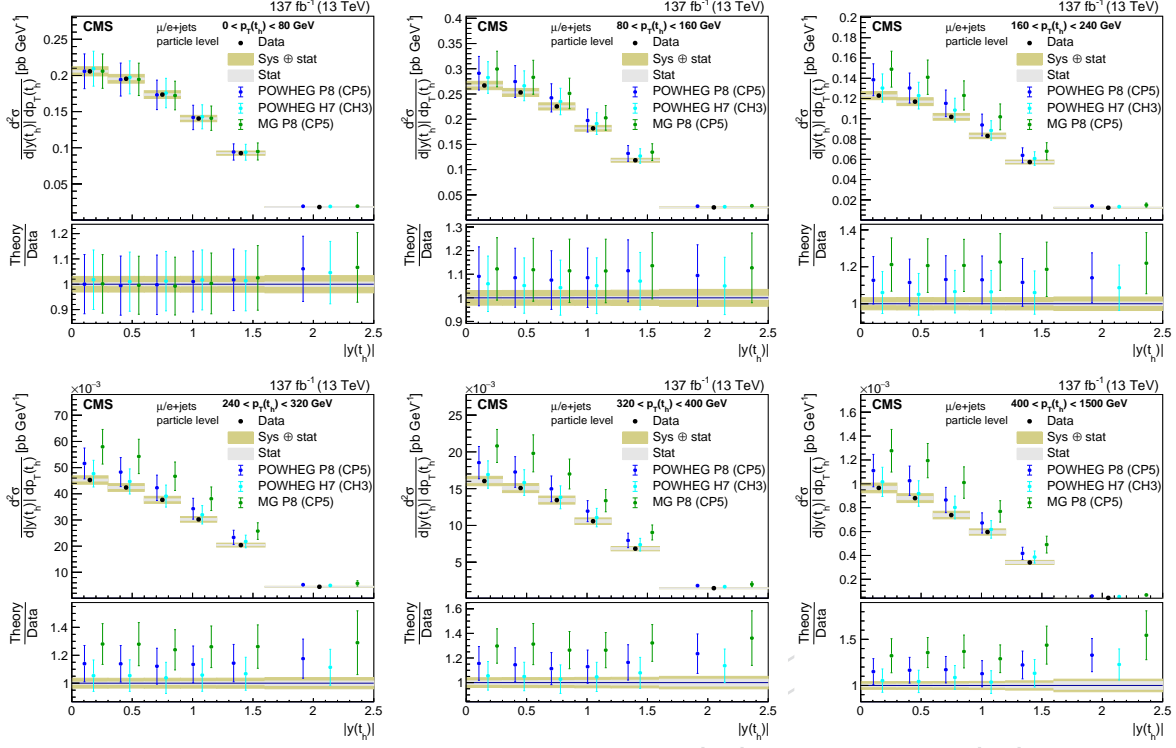
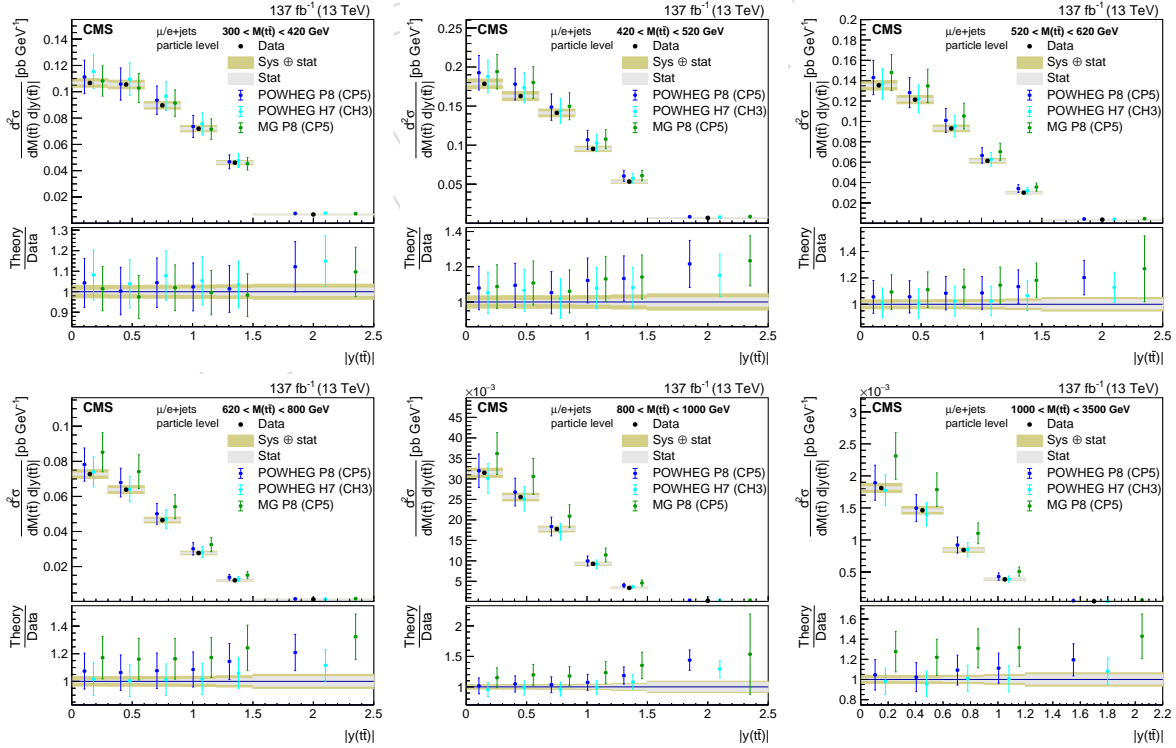


Figure 69: Differential cross sections as functions of  $p_T(\ell)$ , jet multiplicity,  $H_T$ , and  $M_{\text{evt}}$ .

Figure 70: Double differential cross section as function of  $|y(t_h)|$  vs.  $p_T(t_h)$ .Figure 71: Double differential cross section as function of  $|y(t\bar{t})|$  vs.  $M(t\bar{t})$ .

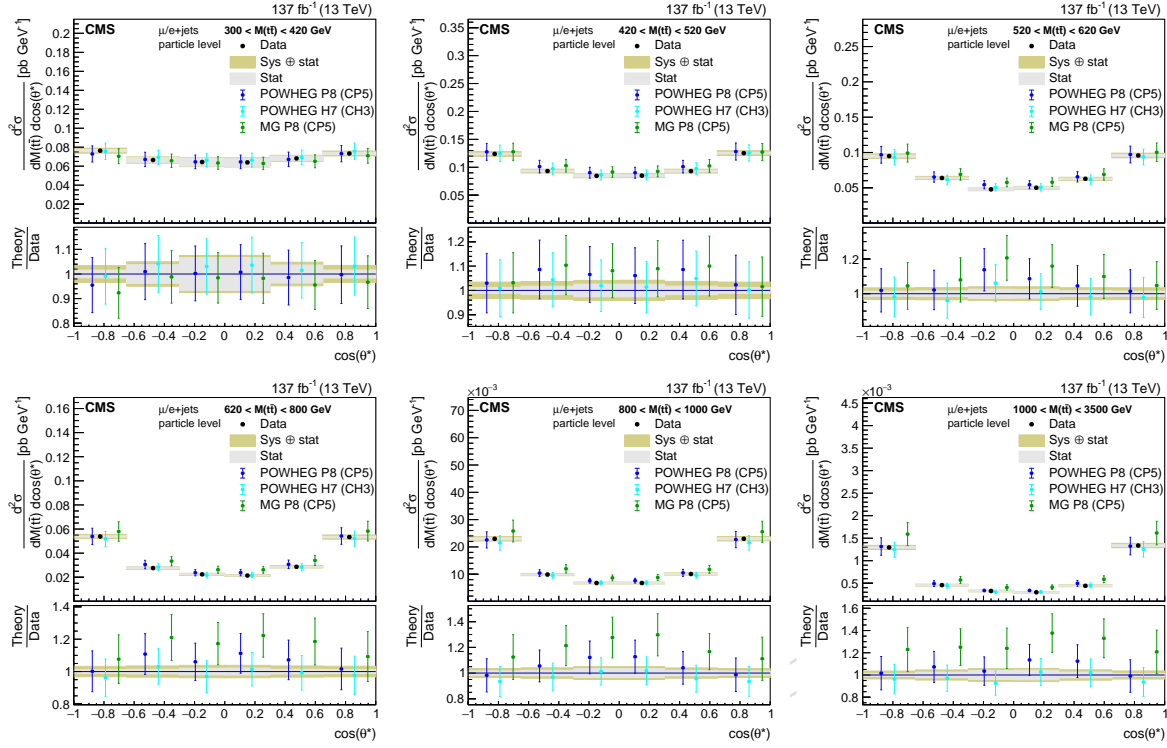


Figure 72: Double differential cross section as function of  $\cos(\theta^*)$  vs.  $M(t\bar{t})$ .

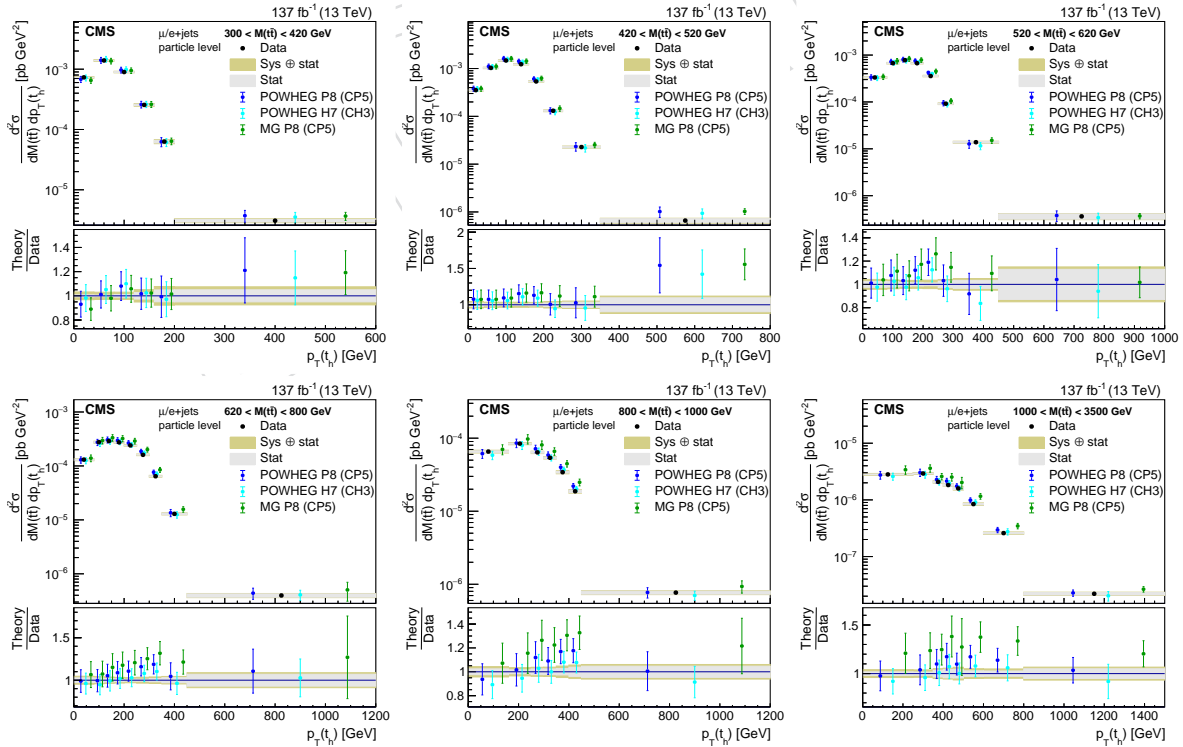
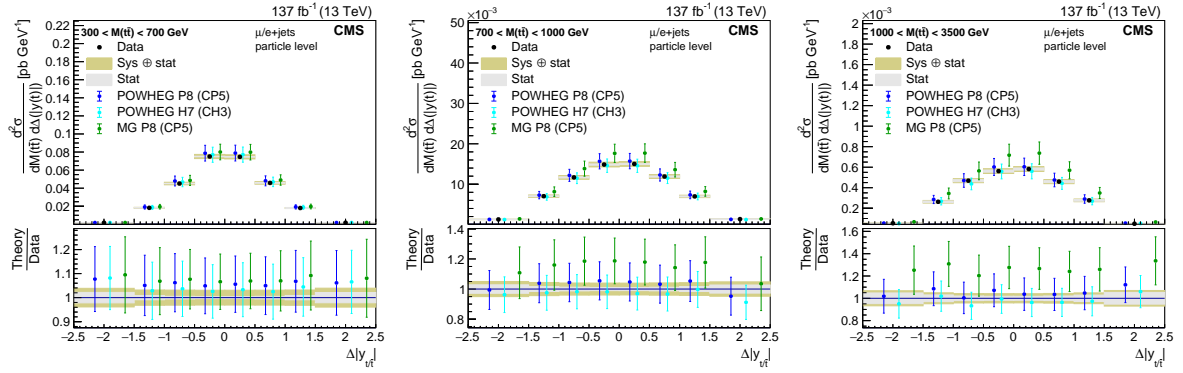
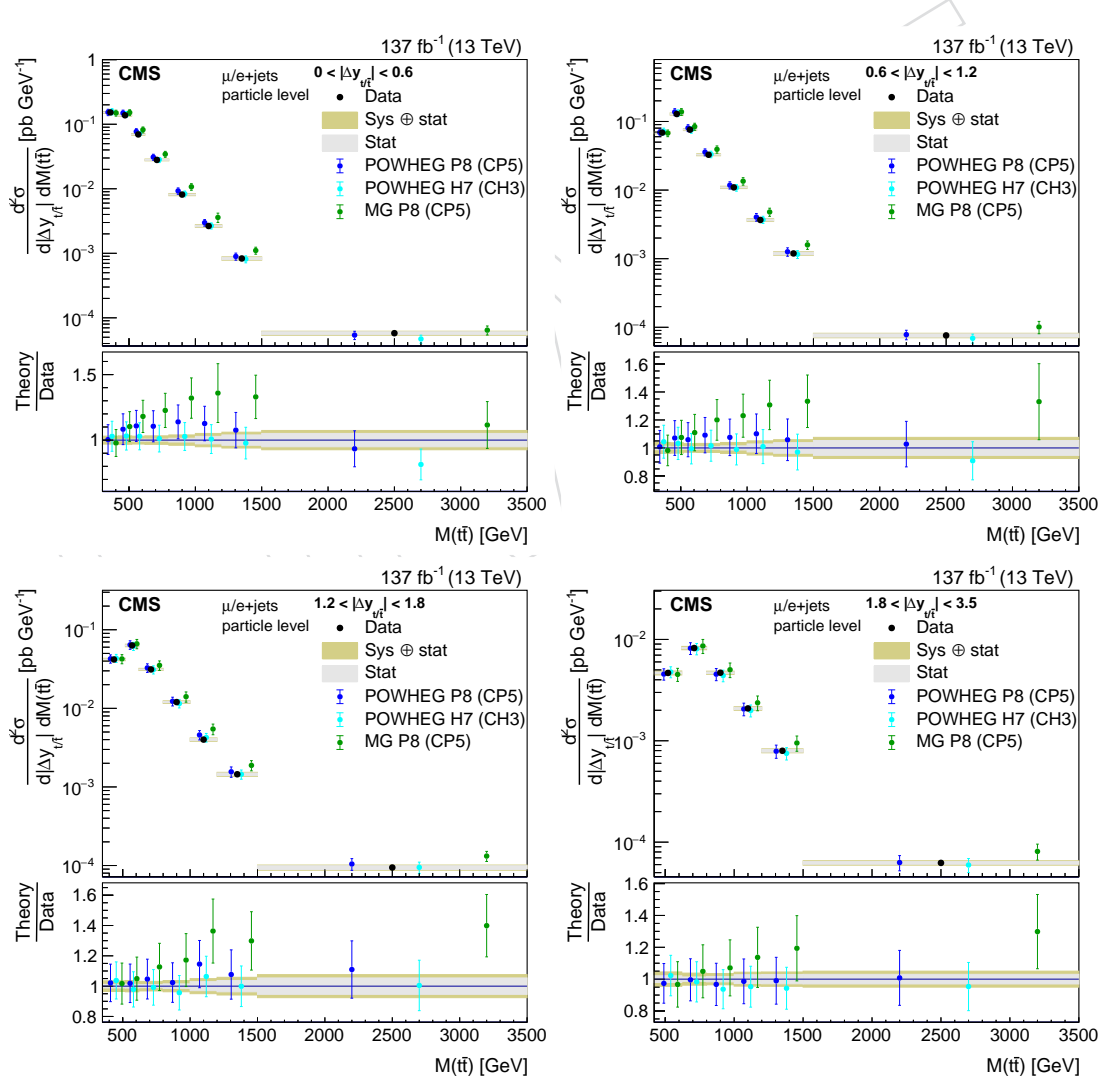


Figure 73: Double differential cross section as function of  $p_T(t_h)$  vs.  $M(t\bar{t})$ .

Figure 74: Double differential cross section as function of  $\Delta|y_{t/\bar{t}}|$  vs.  $M(t\bar{t})$ .Figure 75: Double differential cross section as function of  $M(t\bar{t})$  vs.  $|\Delta y_{t/\bar{t}}|$ .

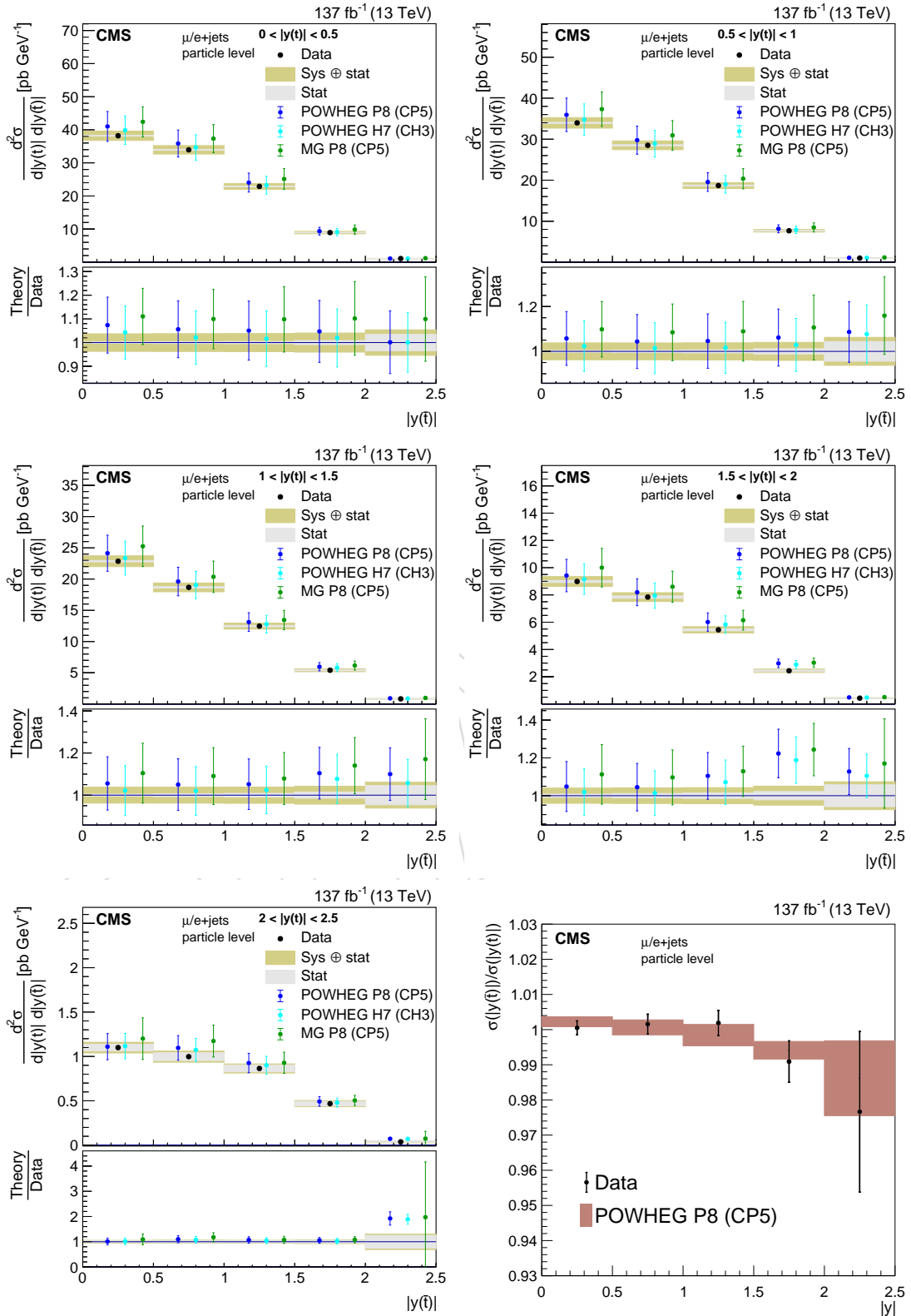


Figure 76: Double differential cross section as function of  $|y(t)|$  vs.  $|y(\bar{t})|$ . Bottom right: ratio of  $|y(\bar{t})|/|y(t)|$

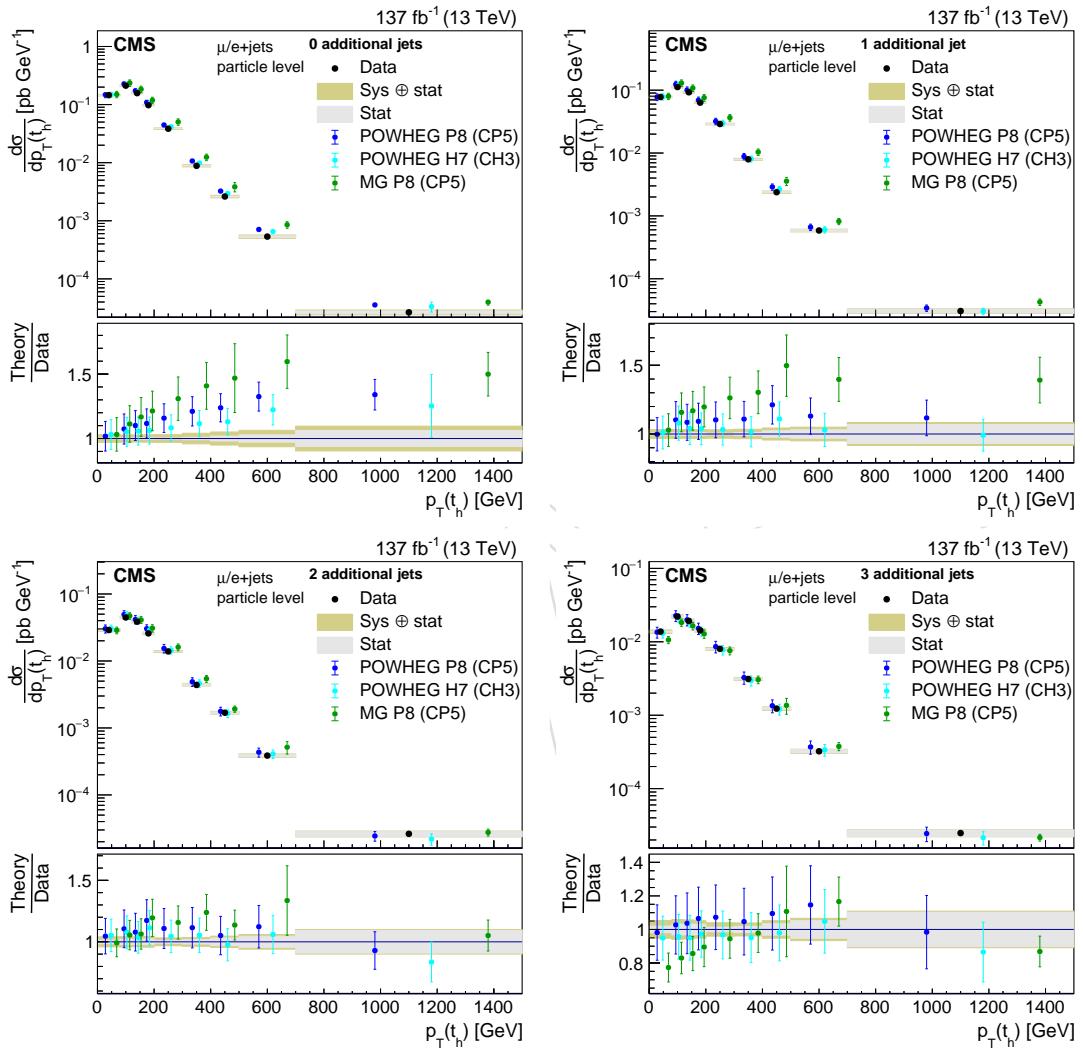


Figure 77: Differential cross section as function of  $p_T(t_h)$  in bins of jet multiplicity.

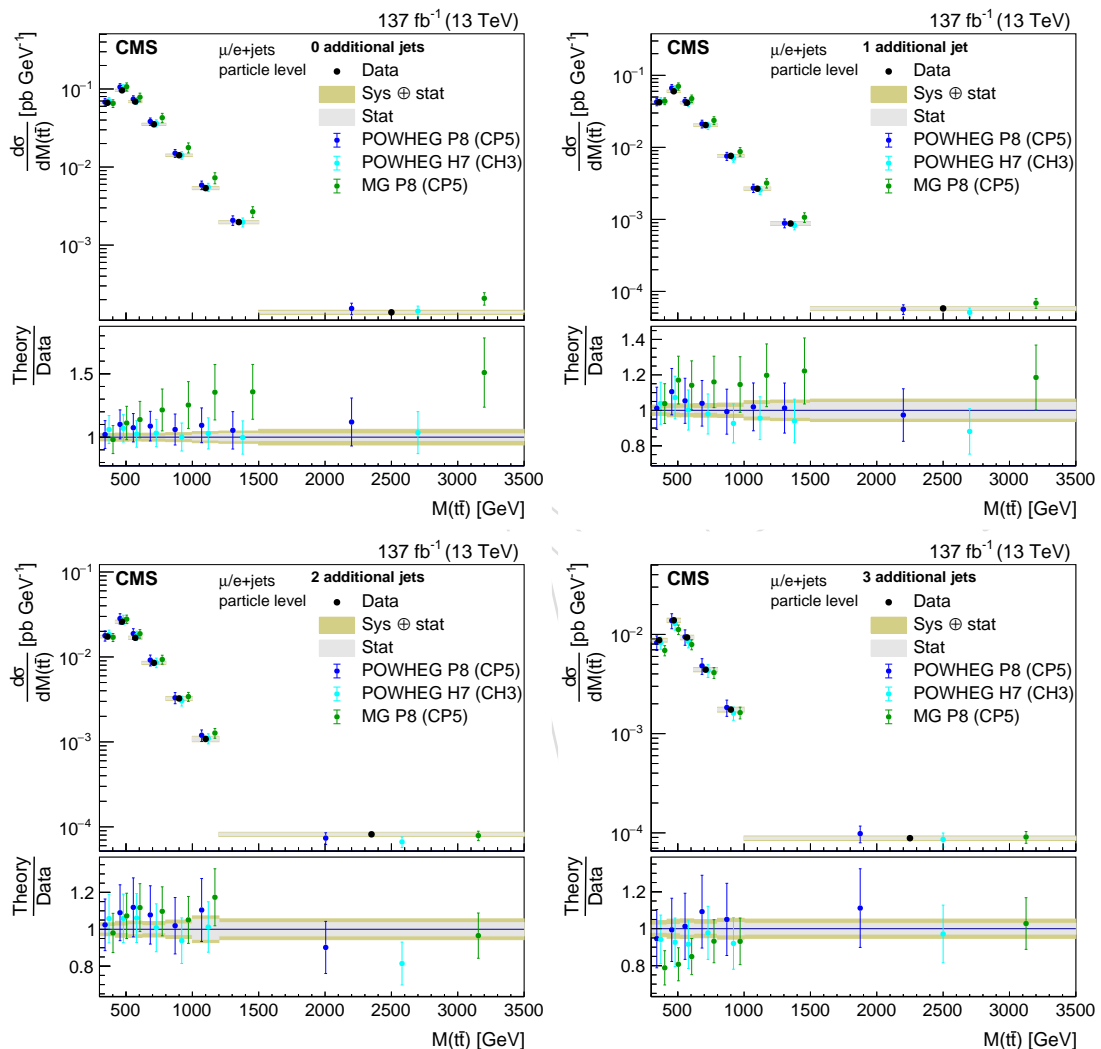


Figure 78: Differential cross section as function of  $M(t\bar{t})$  in bins of jet multiplicity.

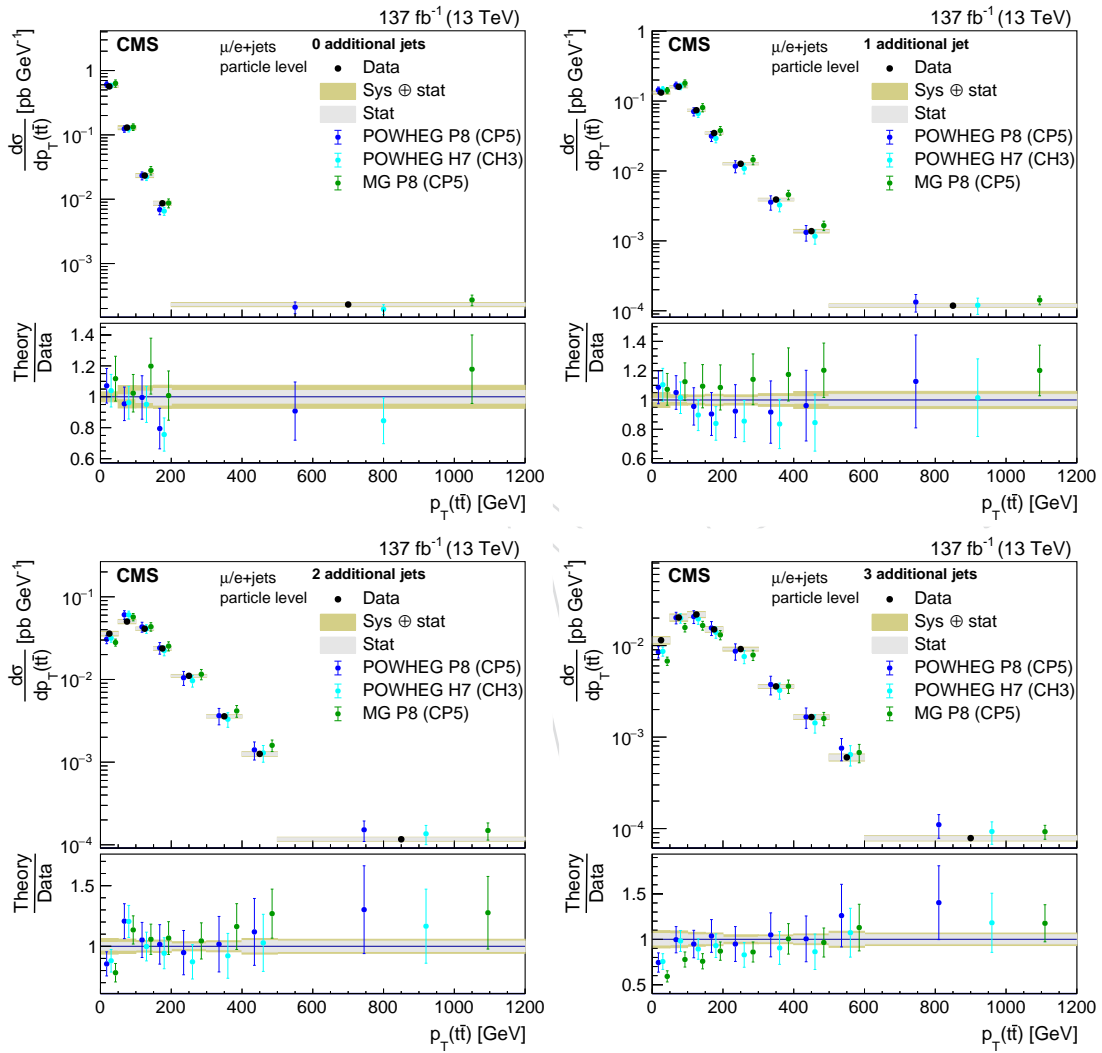


Figure 79: Differential cross section as function of  $p_T(t\bar{t})$  in bins of jet multiplicity.

**695 14 Summary**

696 We have presented a measurement of the differential and double differential  $t\bar{t}$  production  
697 cross sections as functions of many kinematic properties of the top quarks and the  $t\bar{t}$  system at  
698 parton and particle levels. In addition, the number of additional jets and kinematic variables  
699 in bins of jet multiplicities are measured at particle level. For the first time the cross section of  
700 the full spectra are obtained by combining resolved and boosted  $t\bar{t}$  topologies. The combina-  
701 tion of multiple reconstruction categories allow for constraints of systematic uncertainties and  
702 result in a significantly improved precision with respect to previous measurements. In general,  
703 most differential distributions are found to be compatible with the SM predictions. However,  
704 some tension is observed at high rapidities of the top quarks and the  $t\bar{t}$  system. The measured  
705 inclusive  $t\bar{t}$  production cross section is

$$\sigma_{\text{tot}} = 815 \pm 25 \text{ pb.} \quad (11)$$

706 and in good agreement with the SM expectation.

DRAFT

## 707 References

- 708 [1] CMS Collaboration, "Measurement of differential top-quark pair production cross  
709 sections in pp collisions at  $\sqrt{s} = 7 \text{ TeV}$ ", *Eur. Phys. J. C* **73** (2013) 2339,  
710 doi:[10.1140/epjc/s10052-013-2339-4](https://doi.org/10.1140/epjc/s10052-013-2339-4), arXiv:[1211.2220](https://arxiv.org/abs/1211.2220).
- 711 [2] ATLAS Collaboration, "Differential top-antitop cross-section measurements as a function  
712 of observables constructed from final-state particles using pp collisions at  $\sqrt{s} = 7 \text{ TeV}$  in  
713 the ATLAS detector", *JHEP* **06** (2015) 100, doi:[10.1007/JHEP06\(2015\)100](https://doi.org/10.1007/JHEP06(2015)100),  
714 arXiv:[1502.05923](https://arxiv.org/abs/1502.05923).
- 715 [3] CMS Collaboration, "Measurement of the differential cross section for top quark pair  
716 production in pp collisions at  $\sqrt{s} = 8 \text{ TeV}$ ", *Eur. Phys. J. C* **75** (2015) 542,  
717 doi:[10.1140/epjc/s10052-015-3709-x](https://doi.org/10.1140/epjc/s10052-015-3709-x), arXiv:[1505.04480](https://arxiv.org/abs/1505.04480).
- 718 [4] ATLAS Collaboration, "Measurements of top-quark pair differential cross-sections in the  
719 lepton+jets channel in pp collisions at  $\sqrt{s} = 8 \text{ TeV}$  using the ATLAS detector", *Eur. Phys.  
720 J. C* **76** (2016) 538, doi:[10.1140/epjc/s10052-016-4366-4](https://doi.org/10.1140/epjc/s10052-016-4366-4), arXiv:[1511.04716](https://arxiv.org/abs/1511.04716).
- 721 [5] ATLAS Collaboration, "Measurement of the differential cross-section of highly boosted  
722 top quarks as a function of their transverse momentum in  $\sqrt{s} = 8 \text{ TeV}$  proton-proton  
723 collisions using the ATLAS detector", *Phys. Rev. D* **93** (2016) 032009,  
724 doi:[10.1103/PhysRevD.93.032009](https://doi.org/10.1103/PhysRevD.93.032009), arXiv:[1510.03818](https://arxiv.org/abs/1510.03818).
- 725 [6] CMS Collaboration, "Measurement of the  $t\bar{t}$  production cross section in the all-jets final  
726 state in pp collisions at  $\sqrt{s} = 8 \text{ TeV}$ ", *Eur. Phys. J. C* **76** (2016) 128,  
727 doi:[10.1140/epjc/s10052-016-3956-5](https://doi.org/10.1140/epjc/s10052-016-3956-5), arXiv:[1509.06076](https://arxiv.org/abs/1509.06076).
- 728 [7] CMS Collaboration, "Measurement of the integrated and differential  $t\bar{t}$  production cross  
729 sections for high- $p_T$  top quarks in pp collisions at  $\sqrt{s} = 8 \text{ TeV}$ ", *Phys. Rev. D* **94** (2016)  
730 072002, doi:[10.1103/PhysRevD.94.072002](https://doi.org/10.1103/PhysRevD.94.072002), arXiv:[1605.00116](https://arxiv.org/abs/1605.00116).
- 731 [8] ATLAS Collaboration, "Measurement of top quark pair differential cross-sections in the  
732 dilepton channel in pp collisions at  $\sqrt{s} = 7$  and  $8 \text{ TeV}$  with ATLAS", *Phys. Rev. D* **94**  
733 (2016) 092003, doi:[10.1103/PhysRevD.94.092003](https://doi.org/10.1103/PhysRevD.94.092003), arXiv:[1607.07281](https://arxiv.org/abs/1607.07281).
- 734 [9] CMS Collaboration, "Measurement of double-differential cross sections for top quark  
735 pair production in pp collisions at  $\sqrt{s} = 8 \text{ TeV}$  and impact on parton distribution  
736 functions", *Eur. Phys. J. C* **77** (2017) 459, doi:[10.1140/epjc/s10052-017-4984-5](https://doi.org/10.1140/epjc/s10052-017-4984-5),  
737 arXiv:[1703.01630](https://arxiv.org/abs/1703.01630).
- 738 [10] ATLAS Collaboration, "Measurement of jet activity produced in top-quark events with  
739 an electron, a muon and two b-tagged jets in the final state in pp collisions at  
740  $\sqrt{s} = 13 \text{ TeV}$  with the ATLAS detector", *Eur. Phys. J. C* **77** (2017) 220,  
741 doi:[10.1140/epjc/s10052-017-4766-0](https://doi.org/10.1140/epjc/s10052-017-4766-0), arXiv:[1610.09978](https://arxiv.org/abs/1610.09978).
- 742 [11] ATLAS Collaboration, "Measurements of top-quark pair differential cross-sections in the  
743  $e\mu$  channel in pp collisions at  $\sqrt{s} = 13 \text{ TeV}$  using the ATLAS detector", *Eur. Phys. J. C* **77**  
744 (2017) 292, doi:[10.1140/epjc/s10052-017-4821-x](https://doi.org/10.1140/epjc/s10052-017-4821-x), arXiv:[1612.05220](https://arxiv.org/abs/1612.05220).
- 745 [12] CMS Collaboration, "Measurement of normalized differential  $t\bar{t}$  cross sections in the  
746 dilepton channel from pp collisions at  $\sqrt{s} = 13 \text{ TeV}$ . (2017). arXiv:[1708.07638](https://arxiv.org/abs/1708.07638).  
747 Submitted to *JHEP*.

- [13] CMS Collaboration, “Measurement of differential cross sections for top quark pair production using the lepton+jets final state in proton-proton collisions at 13 TeV”, *Phys. Rev. D* **95** (2017) 092001, doi:10.1103/PhysRevD.95.092001, arXiv:1610.04191.
- [14] CMS Collaboration, “Measurement of differential cross sections for the production of top quark pairs and of additional jets in lepton+jets events from pp collisions at 13 TeV”, *Phys. Rev. D* **97** (2018) 112003, doi:10.1103/PhysRevD.97.112003, arXiv:1803.08856.
- [15] ATLAS Collaboration, “Measurements of  $t\bar{t}$  differential cross-sections of highly boosted top quarks decaying to all-hadronic final states in pp collisions at  $\sqrt{s} = 13$  TeV using the ATLAS detector”, *Phys. Rev. D* **98** (2018) 012003, doi:10.1103/PhysRevD.98.012003, arXiv:1801.02052.
- [16] ATLAS Collaboration, “Measurements of top-quark pair differential and double-differential cross-sections in the  $\ell$ +jets channel with pp collisions at  $\sqrt{s} = 13$  TeV using the ATLAS detector”, *Eur. Phys. J. C* **79** (2019) 1028, doi:10.1140/epjc/s10052-019-7525-6, arXiv:1908.07305.
- [17] ATLAS Collaboration, “Measurement of the  $t\bar{t}$  production cross-section and lepton differential distributions in  $e\mu$  dilepton events from pp collisions at  $\sqrt{s} = 13$  TeV with the ATLAS detector”, *Submitted to Eur. Phys. J. C* (2019) arXiv:1910.08819.
- [18] B. A. Betchart, R. Demina, and A. Harel, “Analytic solutions for neutrino momenta in decay of top quarks”, *Nucl. Instrum. Meth. A* **736** (2014) 169, doi:10.1016/j.nima.2013.10.039, arXiv:1305.1878.
- [19] CMS Collaboration, “Object definitions for top quark analyses at the particle level”, CMS Note CERN-CMS-NOTE-2017-004, 2017.
- [20] M. Cacciari, G. P. Salam, and G. Soyez, “The anti- $k_t$  jet clustering algorithm”, *JHEP* **04** (2008) 063, doi:10.1088/1126-6708/2008/04/063, arXiv:0802.1189.
- [21] M. Cacciari, G. P. Salam, and G. Soyez, “FastJet user manual”, *Eur. Phys. J. C* **72** (2012) 1896, doi:10.1140/epjc/s10052-012-1896-2, arXiv:1111.6097.
- [22] Particle Data Group, C. Patrignani et al., “Review of particle physics”, *Chin. Phys. C* **40** (2016) 100001, doi:10.1088/1674-1137/40/10/100001.

## A Lepton efficiencies and correction factors

### A.1 Electrons

We use the tag and probe (T&P) method on the Z peak for a measurement of the electron reconstruction (Reco), selection (ID), and trigger (TRG) efficiencies. Electrons that fulfill all selection requirements and are matched to a trigger object are selected as tag. At least these tag electron triggered the event. The invariant mass of the tags and the probes are calculated for passing and failing probes separately. The background is subtracted using a fit of a template, taken from the simulation, for the signal and a Landau+Exponential distribution for the background. The signal templates are convolved with a Gaussian to allow for shifts of the peak position and a different resolution. The method is performed in bins of the probe  $p_T$ ,  $\eta$ , and the number of jets. Scale factors are calculated as a function of the lepton  $p_T$ - $\eta$  defined as the ratio of efficiencies measured in data and simulation. These scale factors are used as additional weights

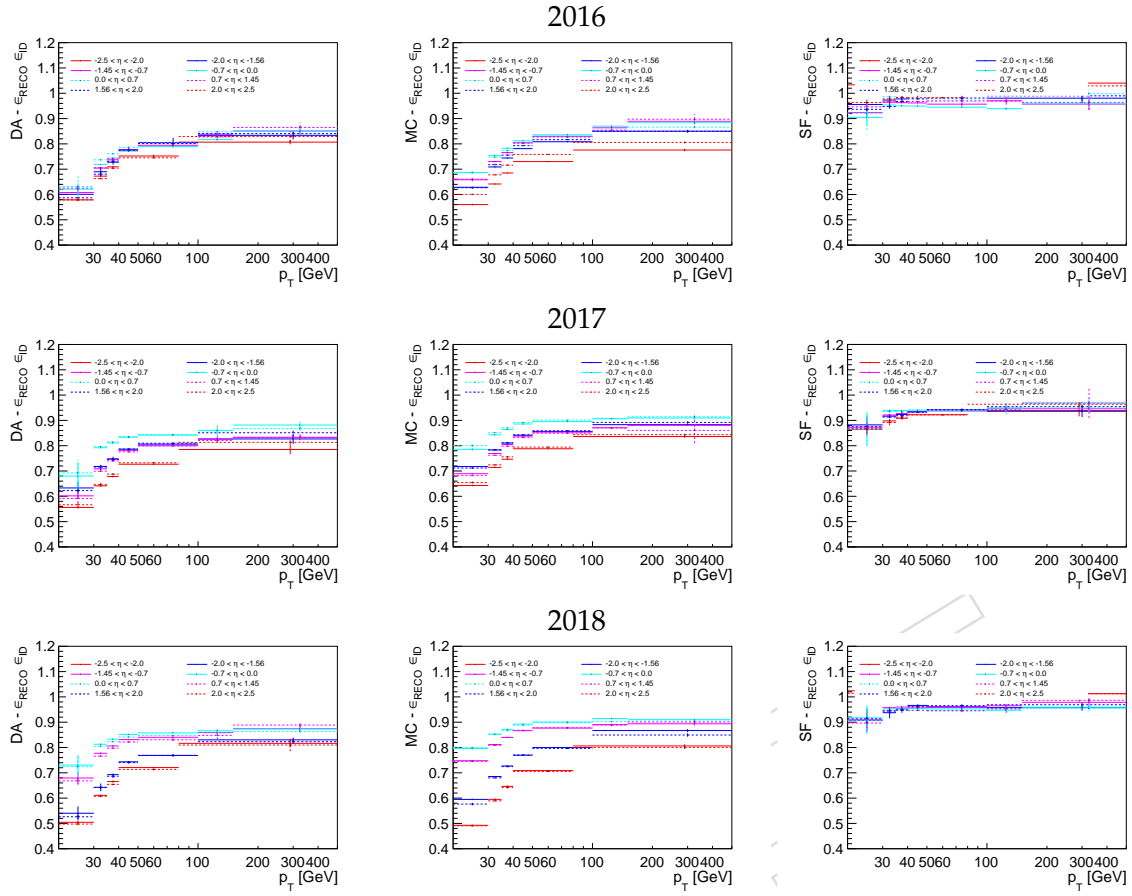


Figure 80: Efficiencies and scale factors of the electron reconstruction, and identification for 2016 to 2018 (upper to lower).

of the simulated events. The uncertainty is estimated from additional tests of changing the fit range, the tag selection, the minimum separation required between the tag and the probes. The probes and the passing probes are defined as follows:

- For the measurement of the reconstruction (RECO) efficiency we start from a photon object, which are clusters in the ECAL with less than 50% energy deposition in the HCAL behind the cluster. Such a probe becomes as passing probe if a GSF electron within a cone of  $\Delta R < 0.3$  pointing into the direction of this cluster is found.
- For the measurement of the identification (ID) efficiency we start with all reconstructed GSF electrons. These probes become passing if they fulfill all ID requirements except for the isolation. The identification efficiency with the isolation (ISO) requirement is measured separately.
- For electrons fulfilling all selection criteria including the isolation the efficiency of the isolated electron trigger is measured. Isolated electrons become a passing probe if they are matched to a trigger object of the isolated electron trigger.

The product of reconstruction and identification efficiencies with and without isolation requirement are shown in Figs. 80 and 81, respectively. The isolated electron trigger efficiency for isolated electrons is shown in Fig. 82.

Since the jet multiplicities in DY events is in average lower than in  $t\bar{t}$  events, we also evaluate the efficiencies and scale factors as function of jet multiplicity. This dependencies are shown in

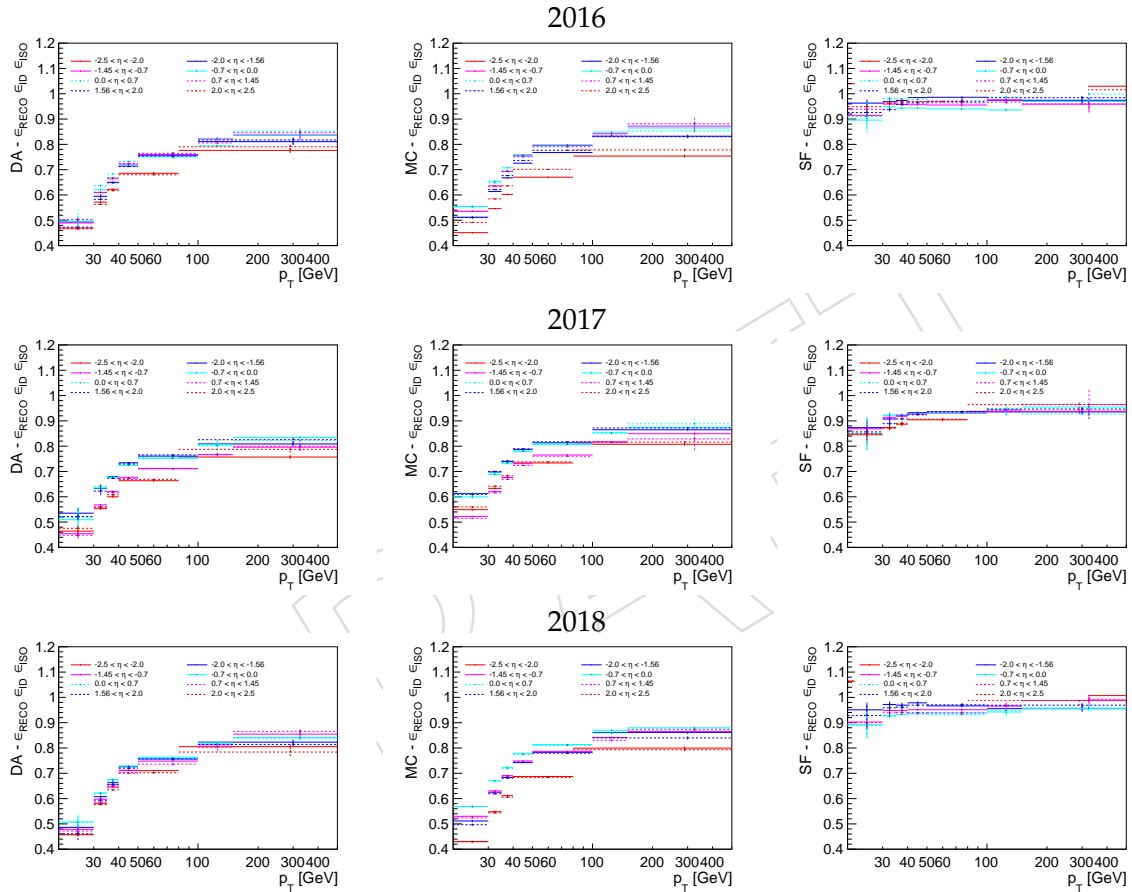


Figure 81: Efficiencies and scale factors of the electron reconstruction, identification, and isolation for 2016 to 2018 (upper to lower).

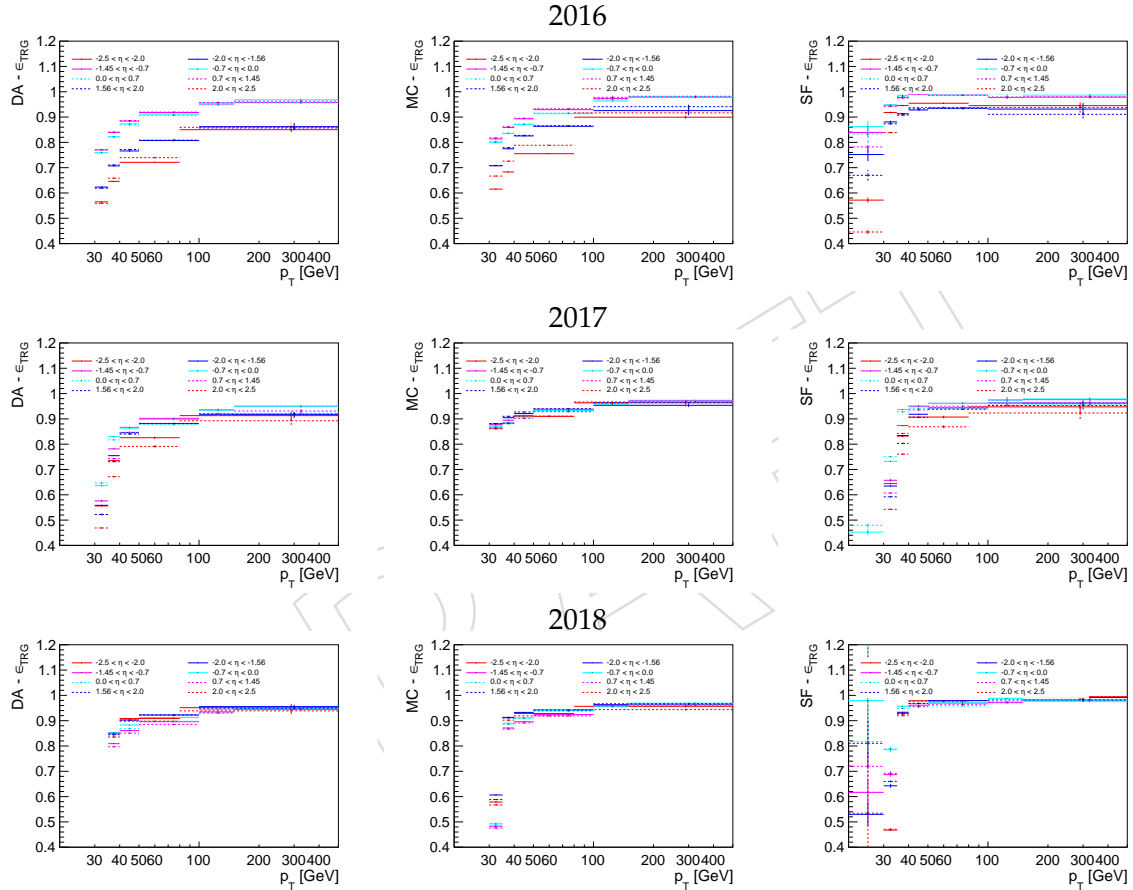


Figure 82: Efficiencies and scale factors of the isolated electron trigger for isolated electrons for 2016 to 2018 (upper to lower).

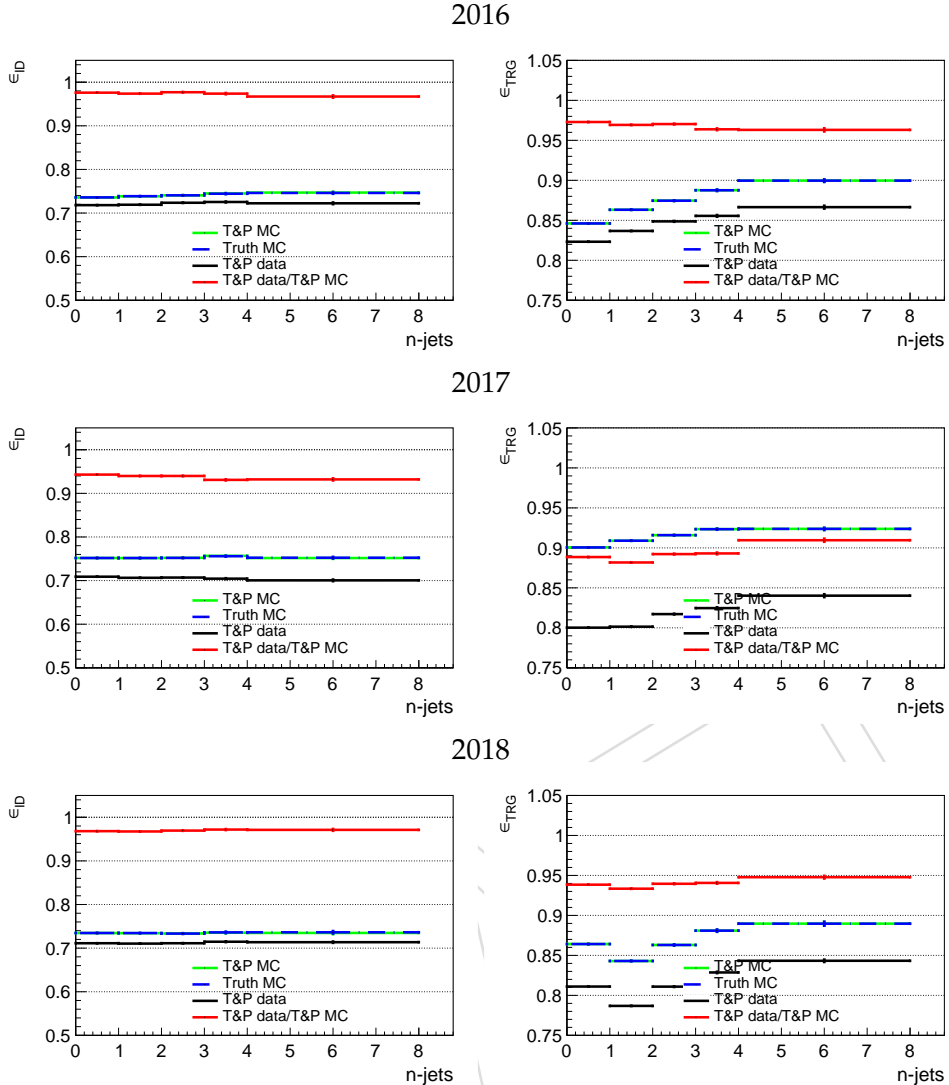


Figure 83: Efficiencies and scale factors as function of jet multiplicity for the electron ID and the isolated electron trigger for 2016 to 2018 (upper to lower).

808 Fig. 83. The scale factor of the electron does not depend on the jet multiplicity and no additional  
 809 correction uncertainty is taken into account. However, we observe a small dependency of the  
 810 trigger efficiency scale factor. Therefore, we add an additional 1% uncertainty to take into  
 811 account the effects of higher jet multiplicities in  $t\bar{t}$  events.

## 812 A.2 Muons

813 For muons the same method is used as for the electrons except for different criteria on the  
 814 passing and failing probes.

- 815 • We measure the reconstruction efficiency in the silicon tracker (TRK) starting with a  
 816 track in the muon system. If a corresponding track in the silicon tracker is found, it  
 817 becomes a passing probe. The two tracks have to fulfill the associated requirements  
 818 in the muon identification.
- 819 • We measure the reconstruction efficiency in the muon system and the selection effi-  
 820 ciency starting with a track in the silicon tracker. If a corresponding selected muon is  
 821 found that fulfills all selection criteria, it becomes a passing probe. The identification

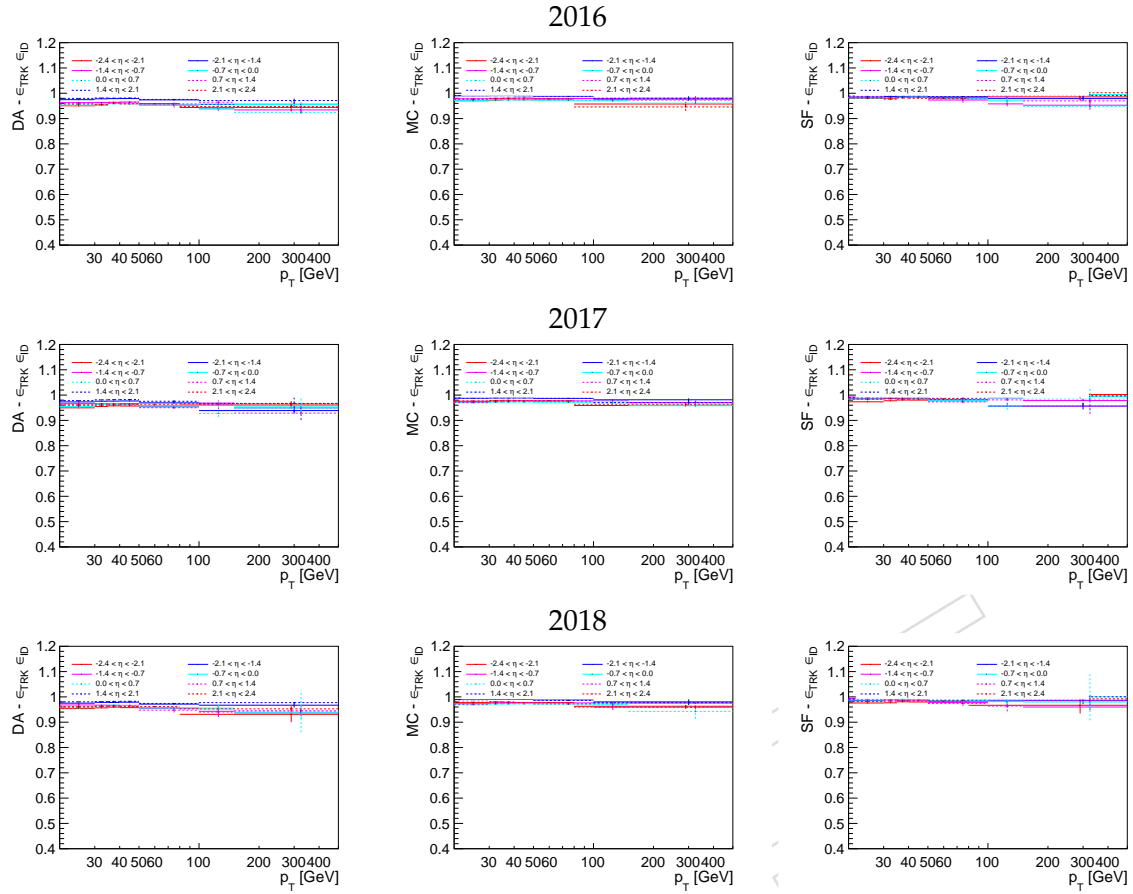


Figure 84: Efficiencies and scale factors of the muon reconstruction and identification for 2016 to 2018 (upper to lower).

- efficiency is measured with and without the isolation requirement.
- For isolated muons that fulfill all selection criteria the trigger efficiency of the iso OR noniso muon triggers are measured. Such selected muon becomes a passing probe if a trigger object of one of the triggers can be spatially matched.

The product of reconstruction and identification efficiencies with and without isolation requirement are shown in Figs. 84 and 85, respectively. The trigger efficiency for isolated muons is shown in Fig. 86. The measurement of trigger efficiencies for nonisolated muons is described in Section A.3.

In Fig. 87 the efficiencies and scale factors as function of jet multiplicity are shown. The scale factors of the muon ID seem to be constant as a function of the jet multiplicity with the exception of the  $n\text{-jet} \geq 4$  bin in 2017. Since there is no general trend, we assume this is glitch in the measurement and do not apply any further correction or uncertainty. However, we observe a small dependency of the trigger efficiency scale factors. Therefore, we add an additional 0.5% uncertainty to take into account the effects of higher jet multiplicities in  $t\bar{t}$  events.

### A.3 Trigger efficiencies

The lepton efficiencies for nonisolated lepton triggers are measured in  $t\bar{t}$  dilepton events. Events with a single isolated muon that triggered the isolated muon trigger are used in this measurement.

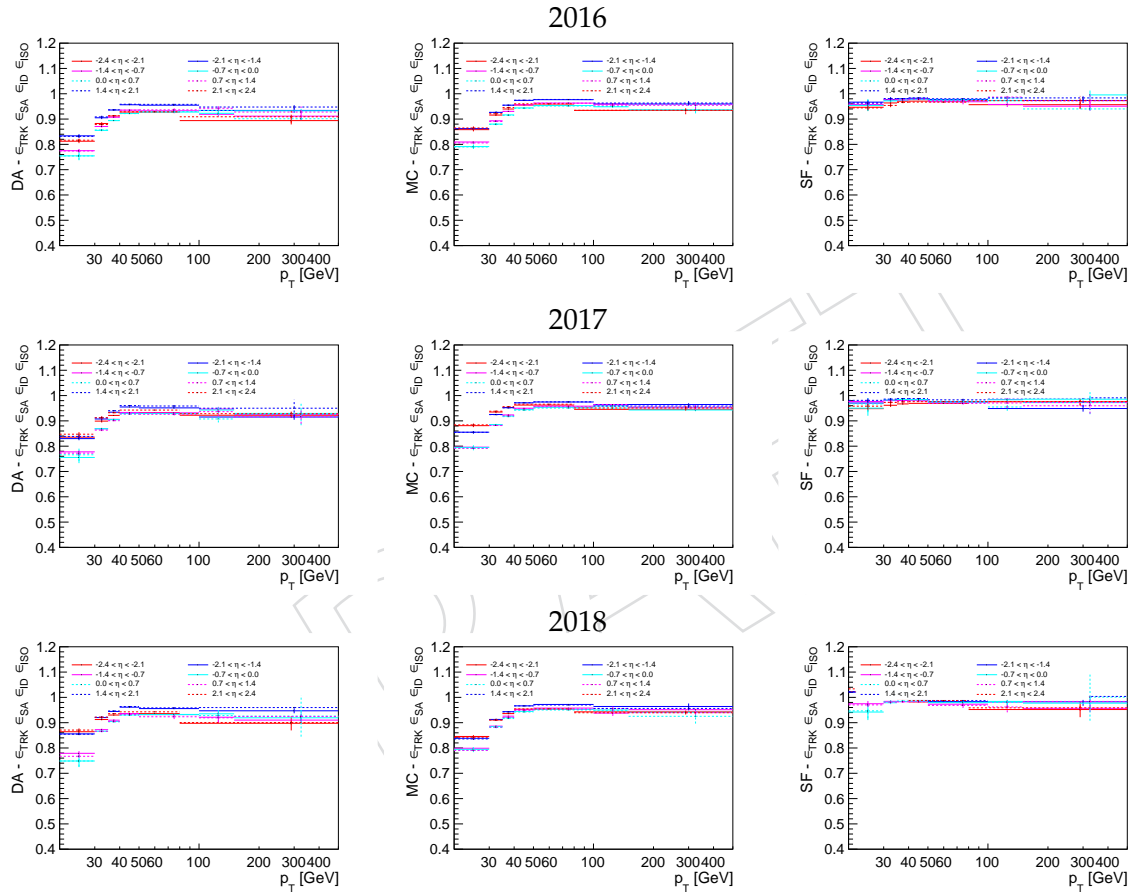


Figure 85: Efficiencies and scale factors of the muon reconstruction, identification, and isolation for 2016 to 2018 (upper to lower).

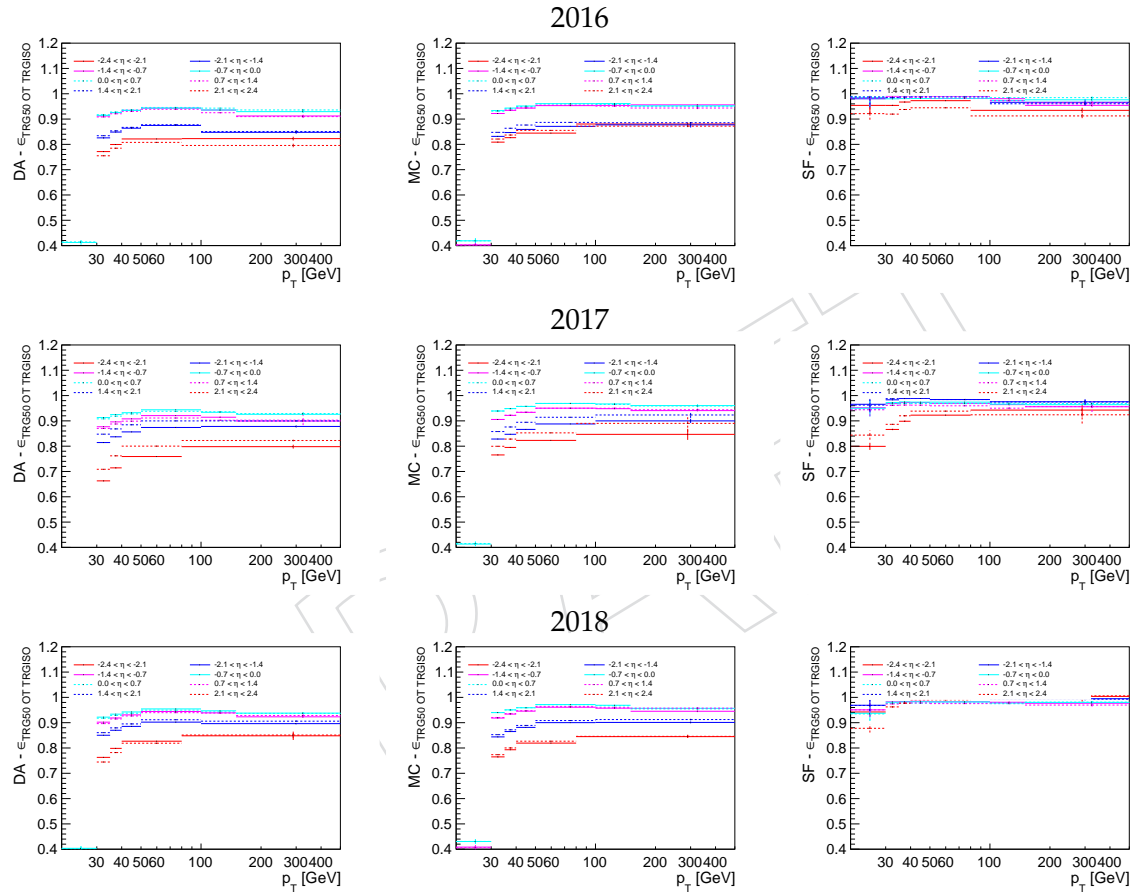


Figure 86: Efficiencies and scale factors of the isolated OR nonisolated muon triggers for 2016 to 2018 (upper to lower).

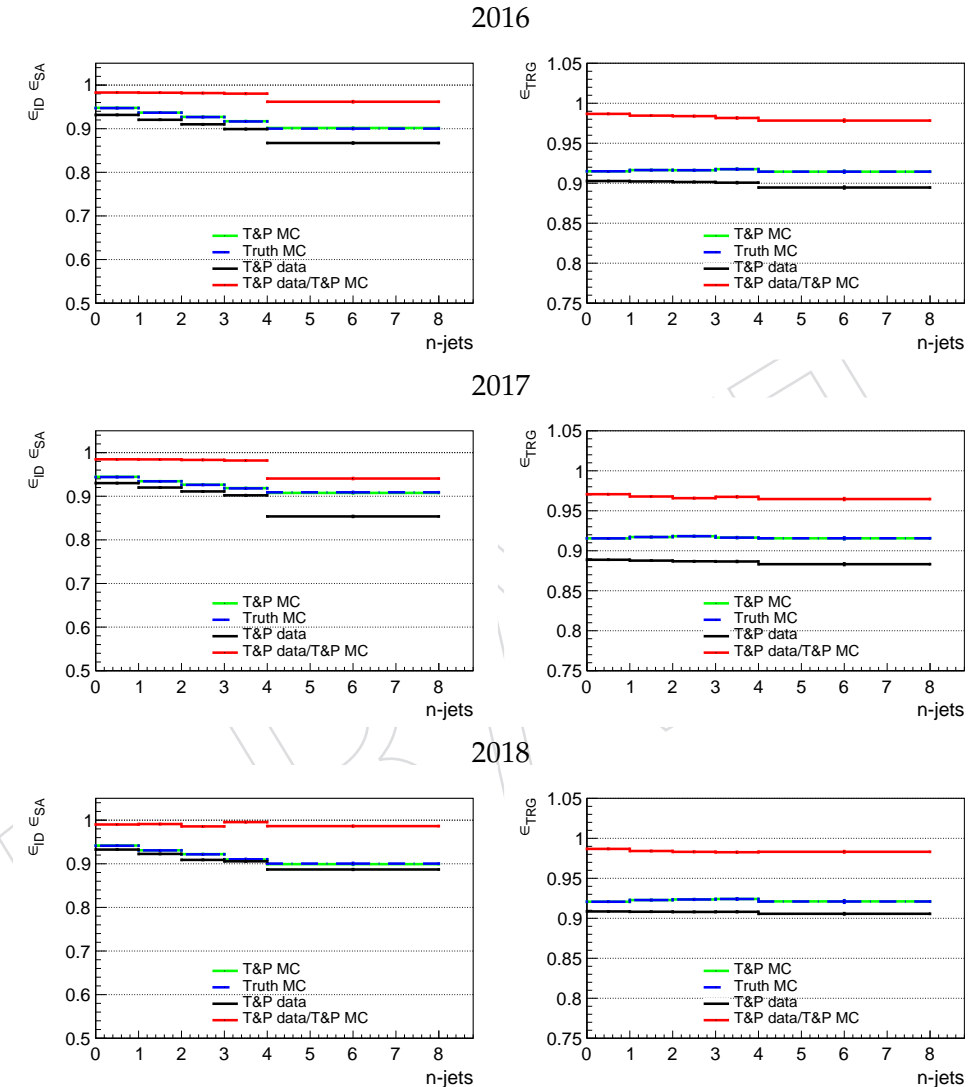


Figure 87: Efficiencies and scale factors as function of jet multiplicity for the muon ID and the isolated muon trigger for 2016 to 2018 (upper to lower).

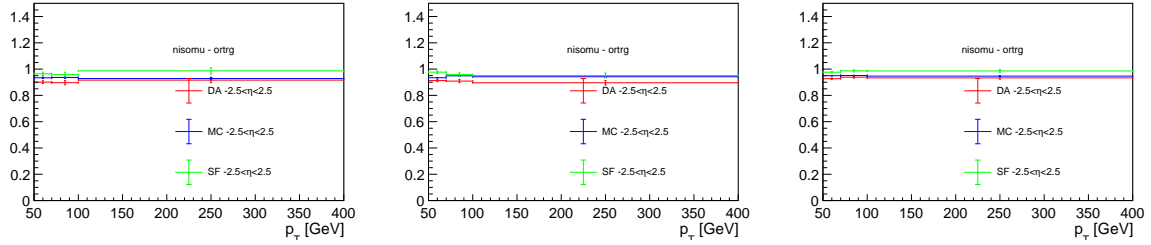


Figure 88: noniso or iso muon trigger efficiency and scale factors for nonisolated muons for 2016 to 2018 (left to right).

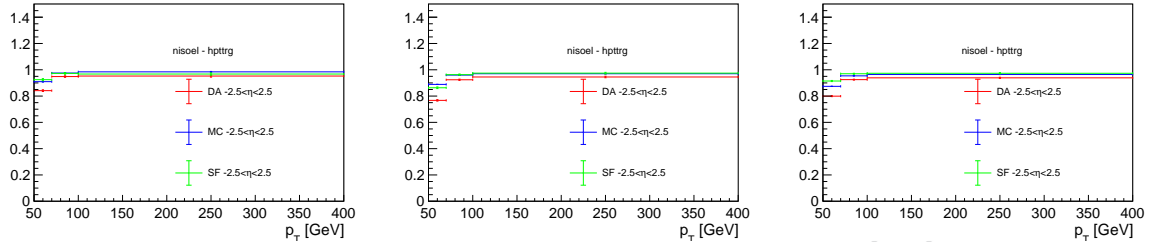


Figure 89: noniso electron trigger efficiency and scale factors for nonisolated electrons for 2016 to 2018 (left to right).

#### 840 • noniso or iso muon trigger for noniso muons

841 The pre-selection is extended by the requirement of two b jets to obtain a  $t\bar{t}$  dimuon  
842 sample. The efficiency for the nonisolated muons with  $p_T > 50$  GeV to trigger the  
843 noniso or the iso muon trigger is determined. The results are shown in Fig. 88.

#### 844 • noniso trigger for noniso electrons

845 The efficiency for the nonisolated electrons with  $p_T > 50$  GeV to trigger the noniso  
846 or the iso electron trigger is determined. The results are shown in Fig. 89. The trig-  
847 ger filter object used for the noniso electron trigger is independent from jet that is  
848 required for the full trigger.

#### 849 • iso electron trigger for noniso electrons

850 The efficiency for the nonisolated electrons with  $p_T > 50$  GeV to trigger the iso elec-  
851 tron trigger is determined. The results are shown in Fig. 90. This efficiency only  
852 affects events in which the noniso electron trigger cannot fire because of the missing  
853 jet with  $p_T > 165$  GeV.

#### 854 • noniso electron trigger for iso electrons

855 The efficiency for isolated electrons to trigger the noniso electron trigger is deter-  
856 mined. The results are shown in Fig. 91.

#### 857 • jet filter in noniso electron trigger

858 The pre-selection is extended by the requirement of electron that passes the electron  
859 filter of the noniso electron trigger. The efficiency of a jet to pass the  $p_T > 165$  GeV  
860 filter is determined. The results are shown in Fig. 92.

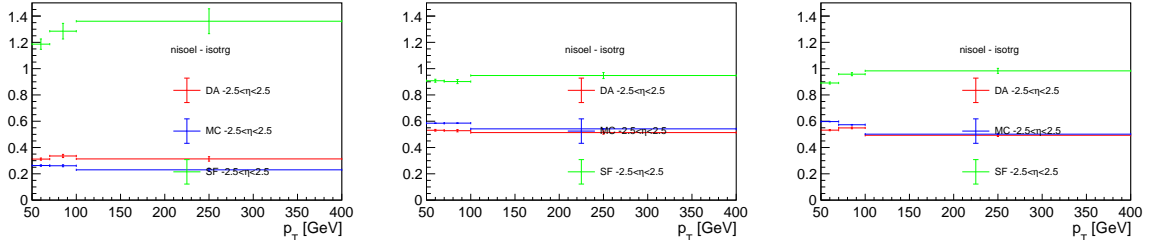


Figure 90: iso electron trigger efficiency and scale factors for nonisolated electrons for 2016 to 2018 (left to right).

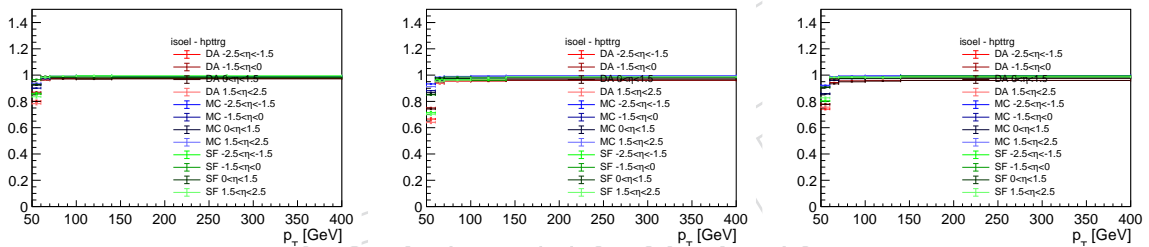


Figure 91: noniso electron trigger efficiency and scale factors for isolated electrons for 2016 to 2018 (left to right).

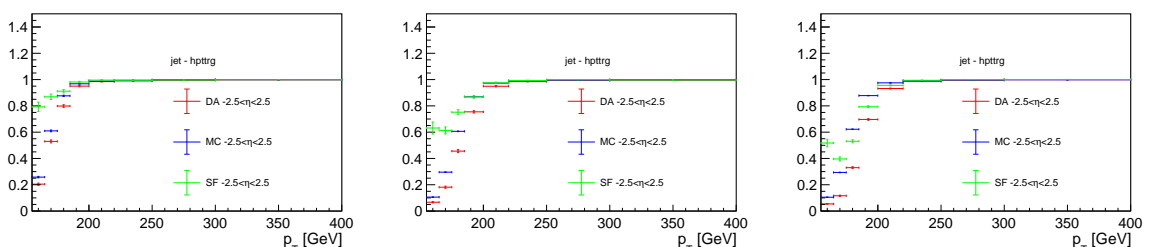


Figure 92: efficiency and scale factors for the jet  $p_T > 165$  GeV filter in the noniso electron trigger for 2016 to 2018 (left to right).

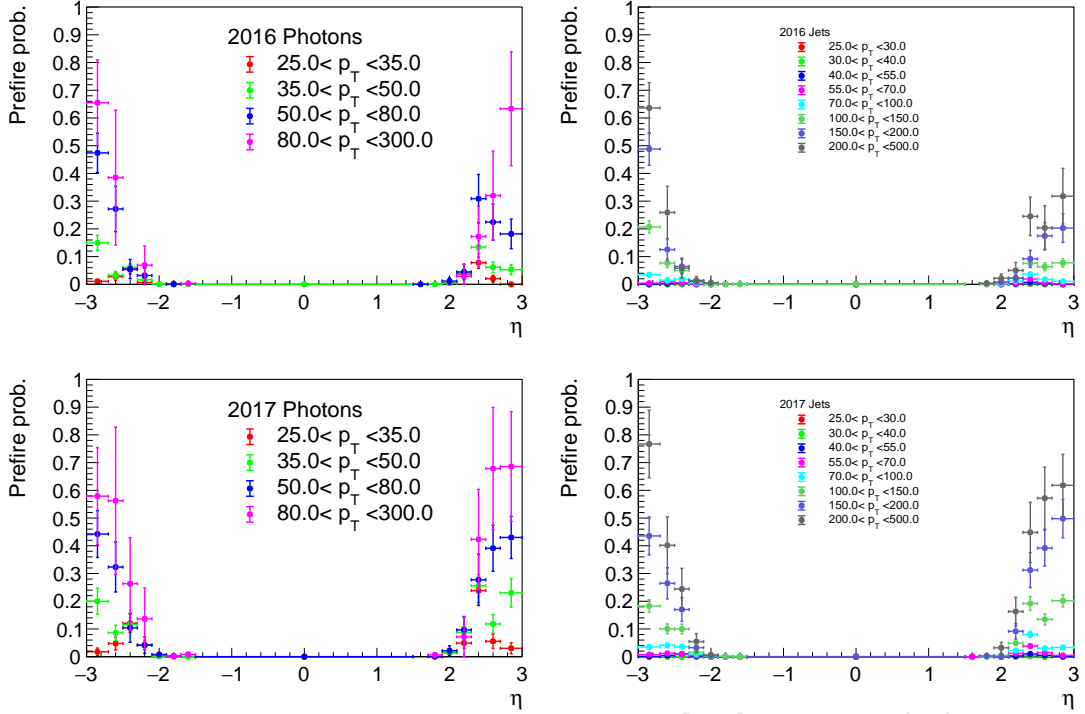


Figure 93: Prefire probabilities for photon/electron objects (left) and jets (right).

## 861 B L1 Prefire corrections

862 During the data taking in 2016 and 2017 the timing of the ECal for  $|\eta| > 2.1$  in the L1 trigger  
 863 degraded leading to an increasing fraction of ECal energy deposits assigned to the bunch  
 864 crossing (BX) before to the correct one. These energy deposits are missing in the correct bunch  
 865 crossing (BX0) leading to a reduced efficiency of the EG L1 triggers. Moreover, if these energy  
 866 deposits cause the L1 trigger to fire in BX-1, the L1 trigger is blocked for the next two BXs, and  
 867 the event of interest is not recorded.

868 The inefficiency in the data taking due to this L1 prefiring is studied using unprefireable events.  
 869 These are events recorded three BXs after any other L1 trigger, which had blocked the two BXs  
 870 in between. For the trigger, we require the standard muon triggers or a standard electron trigger  
 871 restricted to the barrel. In these events, we select photons and electrons using the photon  
 872 objects with a loose WP and no electron/pixel seed veto with  $p_T > 25$  and  $|\eta| < 3$ . In addi-  
 873 tion, we select PFAK4 jets with  $p_T > 25$  and  $|\eta| < 3$ . These are cleaned from the selected  
 874 photons/electron objects and the standard muons. The photon/electron objects and the jets  
 875 are matched to L1 EG objects either in the correct or the previous BX. Based on the  $p_T$  of the  
 876 L1 EG object, its isolation flag, and  $\eta$  (below or above 2.1), we can calculate a prescale based  
 877 probability that the object fired averaged over a year. Weighting each photon/electron object  
 878 or jet with its probability to fire a L1\_Single(Iso)EG(er2p1) trigger, a map (Fig. 93) is calculated  
 879 showing the probability for a photon/electron object or a jet to prefire the event.

880 To correct the simulation we apply the same photon/electron object and jet selections and cal-  
 881 culate based on the maps the probability that non of the objects prefire the event. Using these  
 882 probabilities as event weights, a corrected simulation is obtained. The effect on some of the  
 883 relevant distributions is shown in Fig. 94.

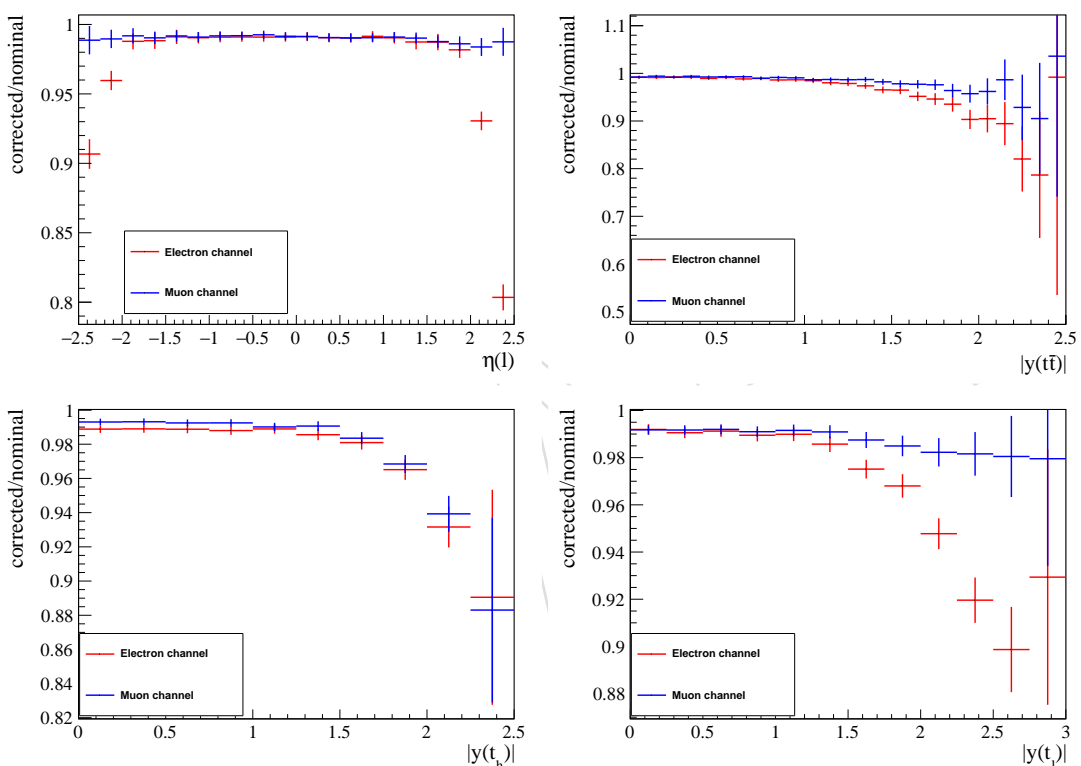


Figure 94: Effect

884 **C Tables of simulated samples**

MC	$\sigma$ [pb]	weights	L fb <sup>-1</sup>
TT_TuneCUETP8M2T4_13TeV-powheg-pythia8	832	153790053	185
TT_TuneCUETP8M2T4_PSweights_13TeV-powheg-pythia8	832	77456400	93.1
TT_AK8HT650_TuneCUETP8M2T4_13TeV-powheg-pythia8	1.92	16097567	8.38e+03
TT_AK8HT650_TuneCUETP8M2T4Down_13TeV-powheg-pythia8	1.92	9291647	4.83e+03
TT_AK8HT650_TuneCUETP8M2T4Up_13TeV-powheg-pythia8	1.92	9346657	4.86e+03
TT_AK8HT650_TuneCUETP8M2T4_erdON_13TeV-powheg-pythia8	1.92	9704727	5.05e+03
TT_AK8HT650_TuneCUETP8M2T4_mtop1715_13TeV-powheg-pythia8	1.92	8808382	4.58e+03
TT_AK8HT650_TuneCUETP8M2T4_mtop1735_13TeV-powheg-pythia8	1.92	8783797	4.57e+03
TT_AK8HT650_hdampDown_TuneCUETP8M2T4_13TeV-powheg-pythia8	1.92	9276548	4.83e+03
TT_AK8HT650_hdampUp_TuneCUETP8M2T4_13TeV-powheg-pythia8	1.92	9007864	4.69e+03
TT_TuneCUETP8M2T4_mtop1715_13TeV-powheg-pythia8	832	19607502	23.6
TT_TuneCUETP8M2T4_mtop1735_13TeV-powheg-pythia8	832	19420550	23.3
TT_TuneCUETP8M2T4down_13TeV-powheg-pythia8	832	58220060	70
TT_TuneCUETP8M2T4up_13TeV-powheg-pythia8	832	58672604	70.5
TT_hdampDOWN_TuneCUETP8M2T4_13TeV-powheg-pythia8	832	58353717	70.1
TT_hdampUP_TuneCUETP8M2T4_13TeV-powheg-pythia8	832	58689096	70.5
TT_TuneCUETP8M2T4_erdON_13TeV-powheg-pythia8	832	46225872	55.6
DYJetsToLL_M-50_TuneCUETP8M1_13TeV-amcatnloFXFX-pythia8	6.02e+03	80924255	13.4
WJetsToLNu_TuneCUETP8M1_13TeV-madgraphMLM-pythia8	6.15e+04	86916455	1.41
WW_TuneCUETP8M1_13TeV-pythia8	119	7982180	67.2
WZ_TuneCUETP8M1_13TeV-pythia8	50	3997571	80
ZZ_TuneCUETP8M1_13TeV-pythia8	27.3	1988098	72.9
QCD_Pt-30to50_MuEnrichedPt5_TuneCUETP8M1_13TeV-pythia8	1.66e+06	29809492	0.0179
QCD_Pt-50to80_MuEnrichedPt5_TuneCUETP8M1_13TeV-pythia8	4.52e+05	19662175	0.0435
QCD_Pt-80to120_MuEnrichedPt5_TuneCUETP8M1_13TeV_pythia8	1.06e+05	23560662	0.221
QCD_Pt-120to170_MuEnrichedPt5_TuneCUETP8M1_13TeV_pythia8	2.57e+04	19809962	0.771
QCD_Pt-170to300_MuEnrichedPt5_TuneCUETP8M1_13TeV_pythia8	8.68e+03	37139904	4.28
QCD_Pt-300to470_MuEnrichedPt5_TuneCUETP8M1_13TeV_pythia8	801	49005976	61.2
QCD_Pt-470to600_MuEnrichedPt5_TuneCUETP8M1_13TeV_pythia8	79.4	19489276	246
QCD_Pt-600to800_MuEnrichedPt5_TuneCUETP8M1_13TeV_pythia8	25.3	19909529	787
QCD_Pt-800to1000_MuEnrichedPt5_TuneCUETP8M1_13TeV_pythia8	4.72	19940747	4.22e+03
QCD_Pt-1000toInf_MuEnrichedPt5_TuneCUETP8M1_13TeV_pythia8	1.61	13577827	8.42e+03
QCD_Pt-30to50_EMEnriched_TuneCUETP8M1_13TeV_pythia8	6.95e+06	11508842	0.00166
QCD_Pt-50to80_EMEnriched_TuneCUETP8M1_13TeV_pythia8	2.16e+06	45789059	0.0212
QCD_Pt-80to120_EMEnriched_TuneCUETP8M1_13TeV_pythia8	4.17e+05	77800204	0.186
QCD_Pt-120to170_EMEnriched_TuneCUETP8M1_13TeV_pythia8	7.58e+04	36015016	0.475
QCD_Pt-170to300_EMEnriched_TuneCUETP8M1_13TeV_pythia8	1.88e+04	11540163	0.613
QCD_Pt-300toInf_EMEnriched_TuneCUETP8M1_13TeV_pythia8	1.22e+03	7380341	6.04
ST_s-channel_4f_leptonDecays_13TeV-amcatnlo-pythia8_TuneCUETP8M1	3.45	622990	181
ST_t-channel_antitop_4f_inclusiveDecays_13TeV-powhegV2-madspin-pythia8_TuneCUETP8M1	81	38811017	479
ST_t-channel_top_4f_inclusiveDecays_13TeV-powhegV2-madspin-pythia8_TuneCUETP8M1	136	67105876	493
ST_tW_antitop_5f_NoFullyHadronicDecays_13TeV-powheg_TuneCUETP8M1	19.3	3256407	169
ST_tW_top_5f_NoFullyHadronicDecays_13TeV-powheg_TuneCUETP8M1	19.3	3256650	169
WJetsToLNu_HT-70To100_TuneCUETP8M1_13TeV-madgraphMLM-pythia8	—	10020533	—
WJetsToLNu_HT-100To200_TuneCUETP8M1_13TeV-madgraphMLM-pythia8	1.64e+03	9945478	6.05
WJetsToLNu_HT-200To400_TuneCUETP8M1_13TeV-madgraphMLM-pythia8	440	38984322	88.7
WJetsToLNu_HT-400To600_TuneCUETP8M1_13TeV-madgraphMLM-pythia8	59.6	7759701	130

WJetsToLNu_HT-600To800_TuneCUETP8M1_13TeV-madgraphMLM-pythia8	14.7	18687480	1.27e+03
WJetsToLNu_HT-800To1200_TuneCUETP8M1_13TeV-madgraphMLM-pythia8	6.71	7830536	1.17e+03
WJetsToLNu_HT-1200To2500_TuneCUETP8M1_13TeV-madgraphMLM-pythia8	1.62	6872441	4.23e+03
WJetsToLNu_HT-2500ToInf_TuneCUETP8M1_13TeV-madgraphMLM-pythia8	0.0392	2637821	6.73e+04
GJets_HT-100To200_TuneCUETP8M1_13TeV-madgraphMLM-pythia8	9.25e+03	10104155	1.09
GJets_HT-200To400_TuneCUETP8M1_13TeV-madgraphMLM-pythia8	2.32e+03	20527506	8.84
GJets_HT-400To600_TuneCUETP8M1_13TeV-madgraphMLM-pythia8	275	5060070	18.4
GJets_HT-600ToInf_TuneCUETP8M1_13TeV-madgraphMLM-pythia8	93.2	5080857	54.5
QCD_HT200to300_TuneCUETP8M1_13TeV-madgraphMLM-pythia8	1.71e+06	57580393	0.0337
QCD_HT300to500_TuneCUETP8M1_13TeV-madgraphMLM-pythia8	3.48e+05	54552852	0.157
QCD_HT500to700_TuneCUETP8M1_13TeV-madgraphMLM-pythia8	3.21e+04	62622029	1.95
QCD_HT700to1000_TuneCUETP8M1_13TeV-madgraphMLM-pythia8	6.83e+03	15629253	2.29
QCD_HT1000to1500_TuneCUETP8M1_13TeV-madgraphMLM-pythia8	1.21e+03	15210939	12.6
QCD_HT1500to2000_TuneCUETP8M1_13TeV-madgraphMLM-pythia8	120	11839357	98.7
QCD_HT2000toInf_TuneCUETP8M1_13TeV-madgraphMLM-pythia8	25.2	6019541	238
TT_TuneEE5C_13TeV-powheg-herwigpp	832	9628901	11.6
TTJets_TuneCUETP8M2T4_13TeV-amcatnloFXFX-pythia8	832	30124664	36.2

Table 7: MC samples 2016

MC	$\sigma$ [pb]	weights	$L \text{ fb}^{-1}$
TTTo2L2Nu_TuneCP5_PSweights_13TeV-powheg-pythia8	87.4	68595608	785
TTTo2L2Nu_TuneCP5down_PSweights_13TeV-powheg-pythia8	87.4	5455842	62.4
TTTo2L2Nu_TuneCP5up_PSweights_13TeV-powheg-pythia8	87.4	5455706	62.4
TTTo2L2Nu_hdampDOWN_TuneCP5_PSweights_13TeV-powheg-pythia8	87.4	5385951	61.6
TTTo2L2Nu_hdampUP_TuneCP5_PSweights_13TeV-powheg-pythia8	87.4	8662531	99.1
TTTo2L2Nu_mtop171p5_TuneCP5_PSweights_13TeV-powheg-pythia8	87.4	5906280	67.6
TTTo2L2Nu_mtop173p5_TuneCP5_PSweights_13TeV-powheg-pythia8	87.4	5951656	68.1
TTTo2L2Nu_TuneCP5_erdON_13TeV-powheg-pythia8	87.4	5050286	57.8
TTToHadronic_TuneCP5_PSweights_13TeV-powheg-pythia8	380	129119166	340
TTToHadronic_TuneCP5down_PSweights_13TeV-powheg-pythia8	380	27032802	71.1
TTToHadronic_TuneCP5up_PSweights_13TeV-powheg-pythia8	380	26889896	70.7
TTToHadronic_hdampDOWN_TuneCP5_PSweights_13TeV-powheg-pythia8	380	26671068	70.2
TTToHadronic_hdampUP_TuneCP5_PSweights_13TeV-powheg-pythia8	380	27137584	71.4
TTToHadronic_mtop171p5_TuneCP5_PSweights_13TeV-powheg-pythia8	380	23788202	62.6
TTToHadronic_mtop173p5_TuneCP5_PSweights_13TeV-powheg-pythia8	380	24178268	63.6
TTToHadronic_TuneCP5_erdON_13TeV-powheg-pythia8	380	26277890	69.1
TTToSemiLeptonic_TuneCP5_PSweights_13TeV-powheg-pythia8	364	305195316	838
TTToSemiLeptonic_TuneCP5down_PSweights_13TeV-powheg-pythia8	364	26651751	73.1
TTToSemiLeptonic_TuneCP5up_PSweights_13TeV-powheg-pythia8	364	19959204	54.8
TTToSemiLeptonic_hdampDOWN_TuneCP5_PSweights_13TeV-powheg-pythia8	364	25931501	71.2
TTToSemiLeptonic_hdampUP_TuneCP5_PSweights_13TeV-powheg-pythia8	364	23868910	65.5
TTToSemiLeptonic_mtop171p5_TuneCP5_PSweights_13TeV-powheg-pythia8	364	24797544	68.1
TTToSemiLeptonic_mtop173p5_TuneCP5_PSweights_13TeV-powheg-pythia8	364	22347764	61.3
TTToSemiLeptonic_TuneCP5_erdON_13TeV-powheg-pythia8	364	9043828	24.8
TT_AK8HT650_TuneCP5_PSweights_13TeV-powheg-pythia8	1.92	23793804	1.24e+04
TT_AK8HT650_TuneCP5Down_PSweights_13TeV-powheg-pythia8	1.92	13102239	6.82e+03
TT_AK8HT650_TuneCP5Up_PSweights_13TeV-powheg-pythia8	1.92	13376952	6.96e+03
TT_AK8HT650_TuneCP5_PSweights_mtop1715_13TeV-powheg-pythia8	1.92	13617582	7.09e+03
TT_AK8HT650_TuneCP5_PSweights_mtop1735_13TeV-powheg-pythia8	1.92	13282302	6.91e+03

TT_AK8HT650_hdampUp_TuneCP5_PSweights_13TeV-powheg-pythia8	1.92	13626998	7.09e+03
TT_AK8HT650_hdampDown_TuneCP5_PSweights_13TeV-powheg-pythia8	1.92	14080439	7.33e+03
DYJetsToLL_M-50.TuneCP5_13TeV-amcatnloFXFX-pythia8	6.02e+03	243610331	40.4
WJetsToLNu_TuneCP5_13TeV-madgraphMLM-pythia8	6.15e+04	23219346	0.377
WW_TuneCP5_13TeV-pythia8	119	7765828	65.4
WZ_TuneCP5_13TeV-pythia8	50	3928572	78.6
ZZ_TuneCP5_13TeV-pythia8	27.3	1949729	71.5
QCD_Pt-100toInf_MuEnrichedPt5_TuneCP5_13TeV_pythia8	1.61	11464561	7.11e+03
QCD_Pt-50to80_EMEEnriched_TuneCP5_13TeV_pythia8	1.99e+06	10266407	0.00516
QCD_Pt-120to170_EMEEnriched_TuneCP5_13TeV_pythia8	6.65e+04	8757280	0.132
QCD_Pt-120to170_MuEnrichedPt5_TuneCP5_13TeV_pythia8	2.57e+04	20774448	0.808
QCD_Pt-170to300_EMEEnriched_TuneCP5_13TeV_pythia8	1.65e+04	3521136	0.214
QCD_Pt-170to300_MuEnrichedPt5_TuneCP5_13TeV_pythia8	8.68e+03	46169787	5.32
QCD_Pt-300to470_MuEnrichedPt5_TuneCP5_13TeV_pythia8	801	17620133	22
QCD_Pt-300toInf_EMEEnriched_TuneCP5_13TeV_pythia8	1.1e+03	2898041	2.64
QCD_Pt-30to50_EMEEnriched_TuneCP5_13TeV_pythia8	6.4e+06	14619762	0.00229
QCD_Pt-30to50_MuEnrichedPt5_TuneCP5_13TeV_pythia8	1.66e+06	29029754	0.0175
QCD_Pt-470to600_MuEnrichedPt5_TuneCP5_13TeV_pythia8	79.4	24243142	305
QCD_Pt-50to80_MuEnrichedPt5_TuneCP5_13TeV_pythia8	4.52e+05	24068188	0.0532
QCD_Pt-600to800_MuEnrichedPt5_TuneCP5_13TeV_pythia8	25.3	16391846	648
QCD_Pt-800to1000_MuEnrichedPt5_TuneCP5_13TeV_pythia8	4.72	15694643	3.32e+03
QCD_Pt-80to120_EMEEnriched_TuneCP5_13TeV_pythia8	3.66e+05	8414100	0.023
QCD_Pt-80to120_MuEnrichedPt5_TuneCP5_13TeV_pythia8	1.06e+05	23248523	0.218
ST_s-channel_4f_leptonDecays_TuneCP5_PSweights_13TeV-amcatnlo_pythia8	3.45	6179680	1.79e+03
ST_t-channel_antitop_4f_inclusiveDecays_TuneCP5_13TeV-powhegV2-madspin_pythia8	81	3939941	48.7
ST_t-channel_top_4f_inclusiveDecays_TuneCP5_13TeV-powhegV2-madspin_pythia8	136	5865760	43.1
ST_tW_antitop_5f_NoFullyHadronicDecays_TuneCP5_PSweights_13TeV-powheg_pythia8	19.3	5347721	277
ST_tW_top_5f_NoFullyHadronicDecays_TuneCP5_PSweights_13TeV-powheg_pythia8	19.3	4666798	242
WJetsToLNu_HT-70To100_TuneCP5_13TeV-madgraphMLM_pythia8	—	22049427	—
WJetsToLNu_HT-100To200_TuneCP5_13TeV-madgraphMLM_pythia8	1.62e+03	35804623	22.1
WJetsToLNu_HT-1200To2500_TuneCP5_13TeV-madgraphMLM_pythia8	1.25	19991892	1.6e+04
WJetsToLNu_HT-200To400_TuneCP5_13TeV-madgraphMLM_pythia8	474	21192211	44.7
WJetsToLNu_HT-2500ToInf_TuneCP5_13TeV-madgraphMLM_pythia8	0.0093	20629585	2.22e+06
WJetsToLNu_HT-400To600_TuneCP5_13TeV-madgraphMLM_pythia8	66.8	14250114	213
WJetsToLNu_HT-600To800_TuneCP5_13TeV-madgraphMLM_pythia8	15	21582309	1.44e+03
WJetsToLNu_HT-800To1200_TuneCP5_13TeV-madgraphMLM_pythia8	6.24	20272990	3.25e+03
CJets_HT-100To200_TuneCP5_13TeV-madgraphMLM_pythia8	8.64e+03	9956909	1.15
GJets_HT-200To400_TuneCP5_13TeV-madgraphMLM_pythia8	2.18e+03	18523977	8.48
CJets_HT-400To600_TuneCP5_13TeV-madgraphMLM_pythia8	254	4733459	18.6
GJets_HT-600ToInf_TuneCP5_13TeV-madgraphMLM_pythia8	85.3	535335	6.28
QCD_HT200to300_TuneCP5_13TeV-madgraph_pythia8	1.55e+06	58622224	0.0379
QCD_HT300to500_TuneCP5_13TeV-madgraph_pythia8	3.23e+05	60204502	0.187
QCD_HT500to700_TuneCP5_13TeV-madgraph_pythia8	3e+04	54460980	1.82
QCD_HT700to1000_TuneCP5_13TeV-madgraph_pythia8	6.33e+03	47518055	7.5
QCD_HT1000to1500_TuneCP5_13TeV-madgraph_pythia8	1.09e+03	16485029	15.2
QCD_HT1500to2000_TuneCP5_13TeV-madgraph_pythia8	99.1	11508604	116
QCD_HT2000toInf_TuneCP5_13TeV-madgraph_pythia8	20.2	5825566	288

Table 8: MC samples 2017

MC	$\sigma$ [pb]	weights	L $\text{fb}^{-1}$
TTToSemiLeptonic.TuneCP5_13TeV-powheg-pythia8	364	296988758	815
TTTo2L2Nu.TuneCP5_13TeV-powheg-pythia8	87.4	63791484	730
TTToHadronic.TuneCP5_13TeV-powheg-pythia8	380	330640220	870
TTToSemiLeptonic.TuneCP5_erdON_13TeV-powheg-pythia8	364	25847240	70.9
TTToSemiLeptonic.TuneCP5down_13TeV-powheg-pythia8	364	19666756	54
TTToSemiLeptonic.TuneCP5up_13TeV-powheg-pythia8	364	26729924	73.4
TTToSemiLeptonic.hdampDOWN.TuneCP5_13TeV-powheg-pythia8	364	32542624	89.3
TTToSemiLeptonic.hdampUP.TuneCP5_13TeV-powheg-pythia8	364	26841790	73.7
TTToSemiLeptonic.mtop171p5.TuneCP5_13TeV-powheg-pythia8	364	24781190	68
TTToSemiLeptonic.mtop173p5.TuneCP5_13TeV-powheg-pythia8	364	23699522	65
TTTo2L2Nu.TuneCP5_erdON_13TeV-powheg-pythia8	87.4	3707776	42.4
TTTo2L2Nu.TuneCP5down_13TeV-powheg-pythia8	87.4	4914480	56.2
TTTo2L2Nu.TuneCP5up_13TeV-powheg-pythia8	87.4	5401744	61.8
TTTo2L2Nu.hdampDOWN.TuneCP5_13TeV-powheg-pythia8	87.4	5368300	61.4
TTTo2L2Nu.hdampUP.TuneCP5_13TeV-powheg-pythia8	87.4	5236080	59.9
TTTo2L2Nu.mtop171p5.TuneCP5_13TeV-powheg-pythia8	87.4	5848484	66.9
TTTo2L2Nu.mtop173p5.TuneCP5_13TeV-powheg-pythia8	87.4	5686136	65.1
TTToHadronic.TuneCP5_erdON_13TeV-powheg-pythia8	380	22855432	60.1
TTToHadronic.TuneCP5down_13TeV-powheg-pythia8	380	26459542	69.6
TTToHadronic.TuneCP5up_13TeV-powheg-pythia8	380	30508060	80.2
TTToHadronic.hdampDOWN.TuneCP5_13TeV-powheg-pythia8	380	25988142	68.4
TTToHadronic.hdampUP.TuneCP5_13TeV-powheg-pythia8	380	24851988	65.4
TTToHadronic.mtop171p5.TuneCP5_13TeV-powheg-pythia8	380	24576792	64.6
TTToHadronic.mtop173p5.TuneCP5_13TeV-powheg-pythia8	380	24654910	64.8
TT_AK8HT650.LHEJetPt350.TuneCP5Up_13TeV-powheg-pythia8	1.92	9608581	5e+03
TT_AK8HT650.LHEJetPt350.TuneCP5_erdON_13TeV-powheg-pythia8	1.92	9389853	4.89e+03
TT_AK8HT650.TuneCP5_mtop1715_13TeV-powheg-pythia8	1.92	12483751	6.5e+03
TT_AK8HT650.TuneCP5_mtop1735_13TeV-powheg-pythia8	1.92	11206188	5.83e+03
TT_AK8HT650.LHEJetPt350.hdampUp.TuneCP5_13TeV-powheg-pythia8	1.92	9091004	4.73e+03
TT_AK8HT650.hdampDown.TuneCP5_13TeV-powheg-pythia8	1.92	12658799	6.59e+03
DYJetsToLL_M-50.TuneCP5_13TeV-amcatnloFXFX-pythia8	6.02e+03	112531450	18.7
WJetsToLNu.TuneCP5_13TeV-madgraphMLM-pythia8	6.15e+04	23219346	0.377
WW.TuneCP5_PSweights_13TeV-pythia8	119	7958000	67
WZ.TuneCP5_PSweights_13TeV-pythia8	50	3893000	77.9
ZZ.TuneCP5_13TeV-pythia8	27.3	1979000	72.5
QCD_HT50to100.TuneCP5_13TeV-madgraphMLM-pythia8	—	38753686	—
QCD_HT100to200.TuneCP5_13TeV-madgraphMLM-pythia8	2.37e+07	93952968	0.00396
QCD_HT200to300.TuneCP5_13TeV-madgraphMLM-pythia8	1.55e+06	54251666	0.0351
QCD_HT300to500.TuneCP5_13TeV-madgraphMLM-pythia8	3.23e+05	54600685	0.169
QCD_HT500to700.TuneCP5_13TeV-madgraphMLM-pythia8	3e+04	55056202	1.84
QCD_HT700to1000.TuneCP5_13TeV-madgraphMLM-pythia8	6.33e+03	44369073	7
QCD_HT1000to1500.TuneCP5_13TeV-madgraphMLM-pythia8	1.09e+03	15407797	14.2
QCD_HT1500to2000.TuneCP5_13TeV-madgraphMLM-pythia8	99.1	10887751	110
QCD_HT2000toInf.TuneCP5_13TeV-madgraphMLM-pythia8	20.2	5414545	268
QCD_Pt-30to50.EMEnriched.TuneCP5_13TeV_pythia8	6.4e+06	15086084	0.00236
QCD_Pt-50to80.EMEnriched.TuneCP5_13TeV_pythia8	1.99e+06	10798233	0.00543
QCD_Pt-80to120.EMEnriched.TuneCP5_13TeV_pythia8	3.66e+05	9648791	0.0263
QCD_Pt-120to170.EMEnriched.TuneCP5_13TeV_pythia8	6.65e+04	9964143	0.15

QCD_Pt-170to300_EMEEnriched_TuneCP5_13TeV_pythia8	1.65e+04	3712174	0.225
QCD_Pt-300toInf_EMEEnriched_TuneCP5_13TeV_pythia8	1.1e+03	2901355	2.64
QCD_Pt-30to50_MuEnrichedPt5_TuneCP5_13TeV_pythia8	1.66e+06	29884616	0.018
QCD_Pt-50to80_MuEnrichedPt5_TuneCP5_13TeV_pythia8	4.52e+05	20268872	0.0448
QCD_Pt-80to120_MuEnrichedPt5_TuneCP5_13TeV_pythia8	1.06e+05	25039361	0.235
QCD_Pt-120to170_MuEnrichedPt5_TuneCP5_13TeV_pythia8	2.57e+04	20682254	0.805
QCD_Pt-170to300_MuEnrichedPt5_TuneCP5_13TeV_pythia8	8.68e+03	35978539	4.14
QCD_Pt-300to470_MuEnrichedPt5_TuneCP5_13TeV_pythia8	801	29488563	36.8
QCD_Pt-470to600_MuEnrichedPt5_TuneCP5_13TeV_pythia8	79.4	20495750	258
QCD_Pt-600to800_MuEnrichedPt5_TuneCP5_13TeV_pythia8	25.3	16618977	657
QCD_Pt-800to1000_MuEnrichedPt5_TuneCP5_13TeV_pythia8	4.72	16749914	3.55e+03
QCD_Pt-1000toInf_MuEnrichedPt5_TuneCP5_13TeV_pythia8	1.61	10719790	6.65e+03
ST_s-channel_4f_leptonDecays_TuneCP5_13TeV-madgraph-pythia8	3.45	12447484	3.61e+03
ST_t-channel_antitop_4f_InclusiveDecays_TuneCP5_13TeV-powheg-madspin-pythia8	81	74227130	917
ST_t-channel_top_4f_InclusiveDecays_TuneCP5_13TeV-powheg-madspin-pythia8	136	143932590	1.06e+03
ST_tW_antitop_5f_NoFullyHadronicDecays_TuneCP5_13TeV-powheg-pythia8	19.3	5796514	300
ST_tW_top_5f_NoFullyHadronicDecays_TuneCP5_13TeV-powheg-pythia8	19.3	7602101	394
WJetsToLNu_HT-70To100_TuneCP5_13TeV-madgraphMLM-pythia8	1.53e+03	28060302	18.3
WJetsToLNu_HT-100To200_TuneCP5_13TeV-madgraphMLM-pythia8	1.62e+03	29488310	18.2
WJetsToLNu_HT-200To400_TuneCP5_13TeV-madgraphMLM-pythia8	474	25423155	53.6
WJetsToLNu_HT-400To600_TuneCP5_13TeV-madgraphMLM-pythia8	66.8	5915969	88.6
WJetsToLNu_HT-600To800_TuneCP5_13TeV-madgraphMLM-pythia8	15	19699782	1.32e+03
WJetsToLNu_HT-800To1200_TuneCP5_13TeV-madgraphMLM-pythia8	6.24	8362227	1.34e+03
WJetsToLNu_HT-1200To2500_TuneCP5_13TeV-madgraphMLM-pythia8	1.25	7571583	6.06e+03
WJetsToLNu_HT-2500ToInf_TuneCP5_13TeV-madgraphMLM-pythia8	0.0093	3191612	3.43e+05
GJetsHT-100To200_TuneCP5_13TeV-madgraphMLM-pythia8	8.64e+03	9796870	1.13
GJetsHT-200To400_TuneCP5_13TeV-madgraphMLM-pythia8	2.18e+03	19055655	8.72
GJetsHT-400To600_TuneCP5_13TeV-madgraphMLM-pythia8	254	4652345	18.3
GJetsHT-600ToInf_TuneCP5_13TeV-madgraphMLM-pythia8	85.3	4971983	58.3

Table 9: MC samples 2018

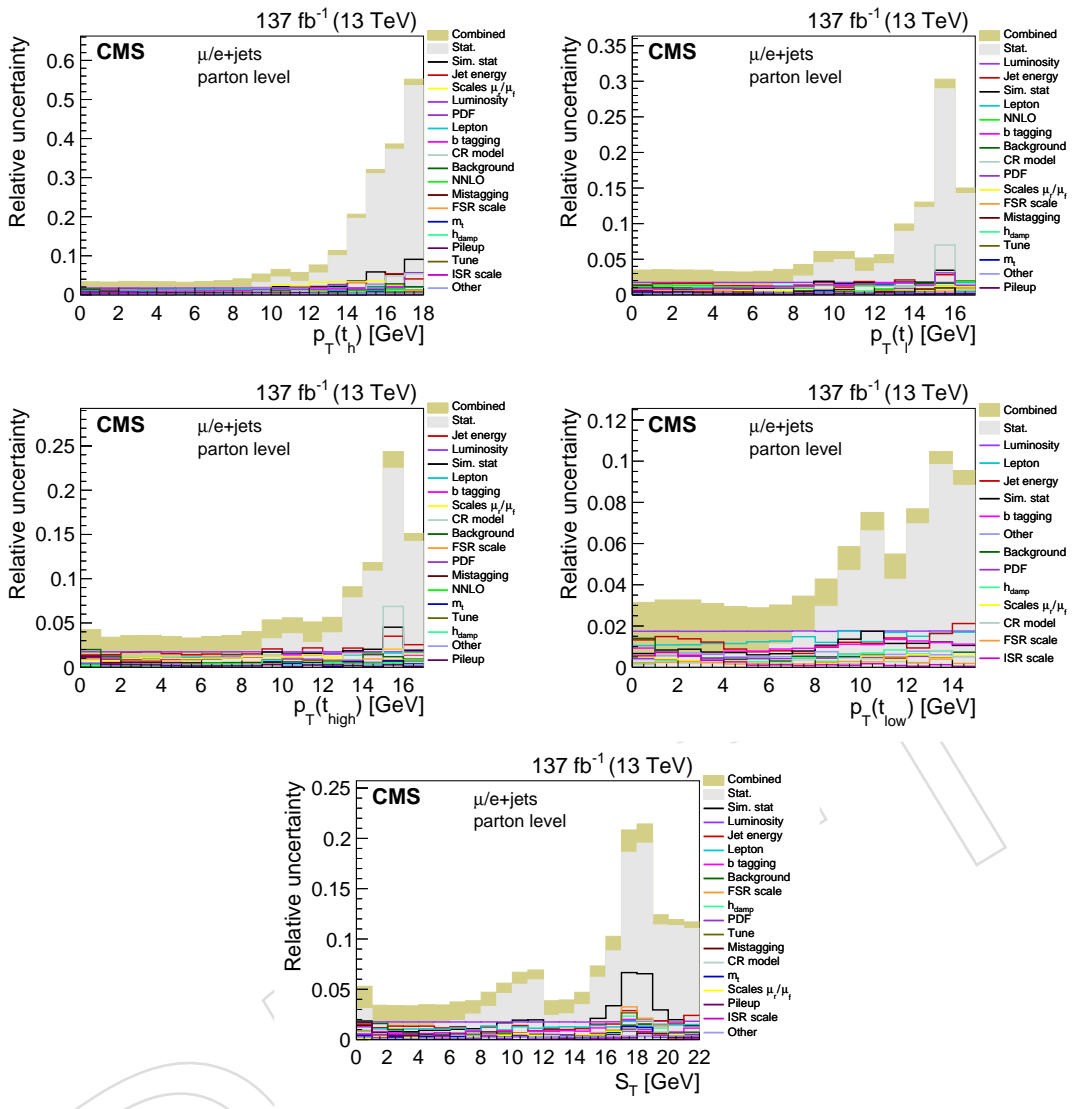


Figure 95

## 885 D Detailed plots of uncertainties at parton level

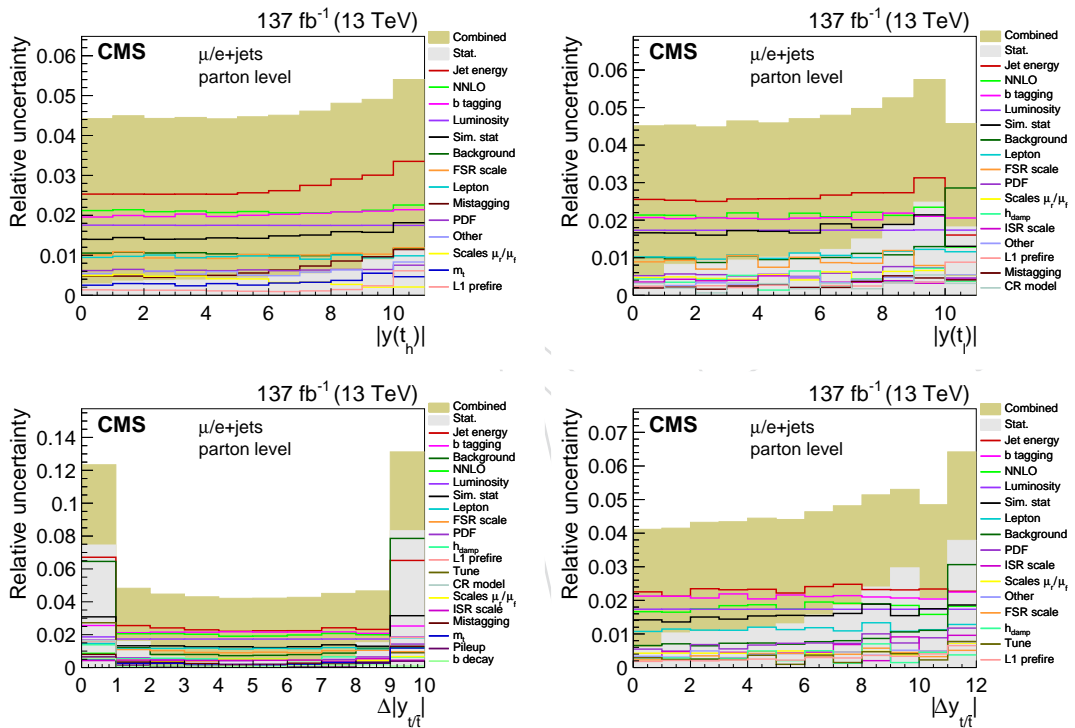


Figure 96

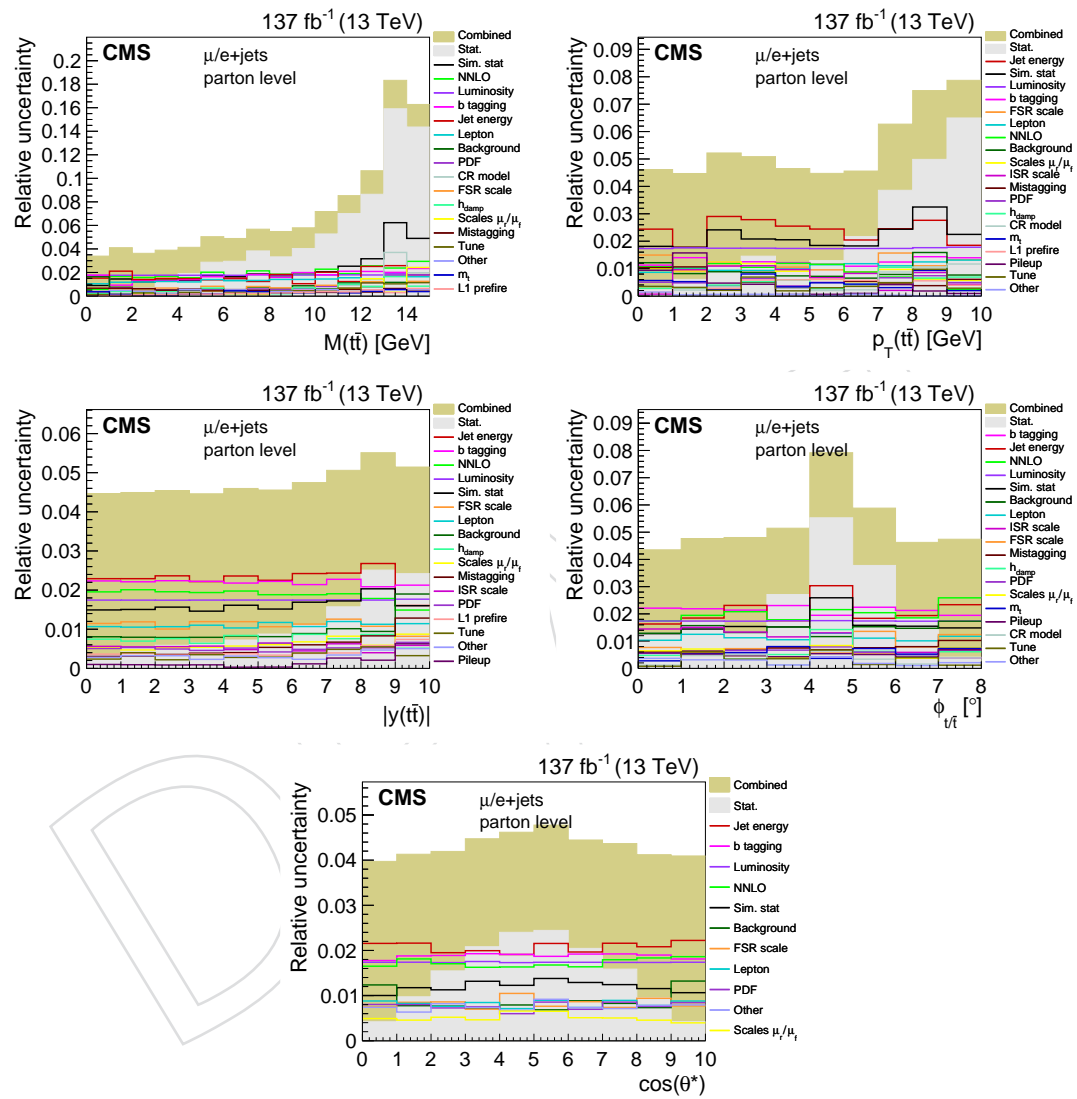


Figure 97

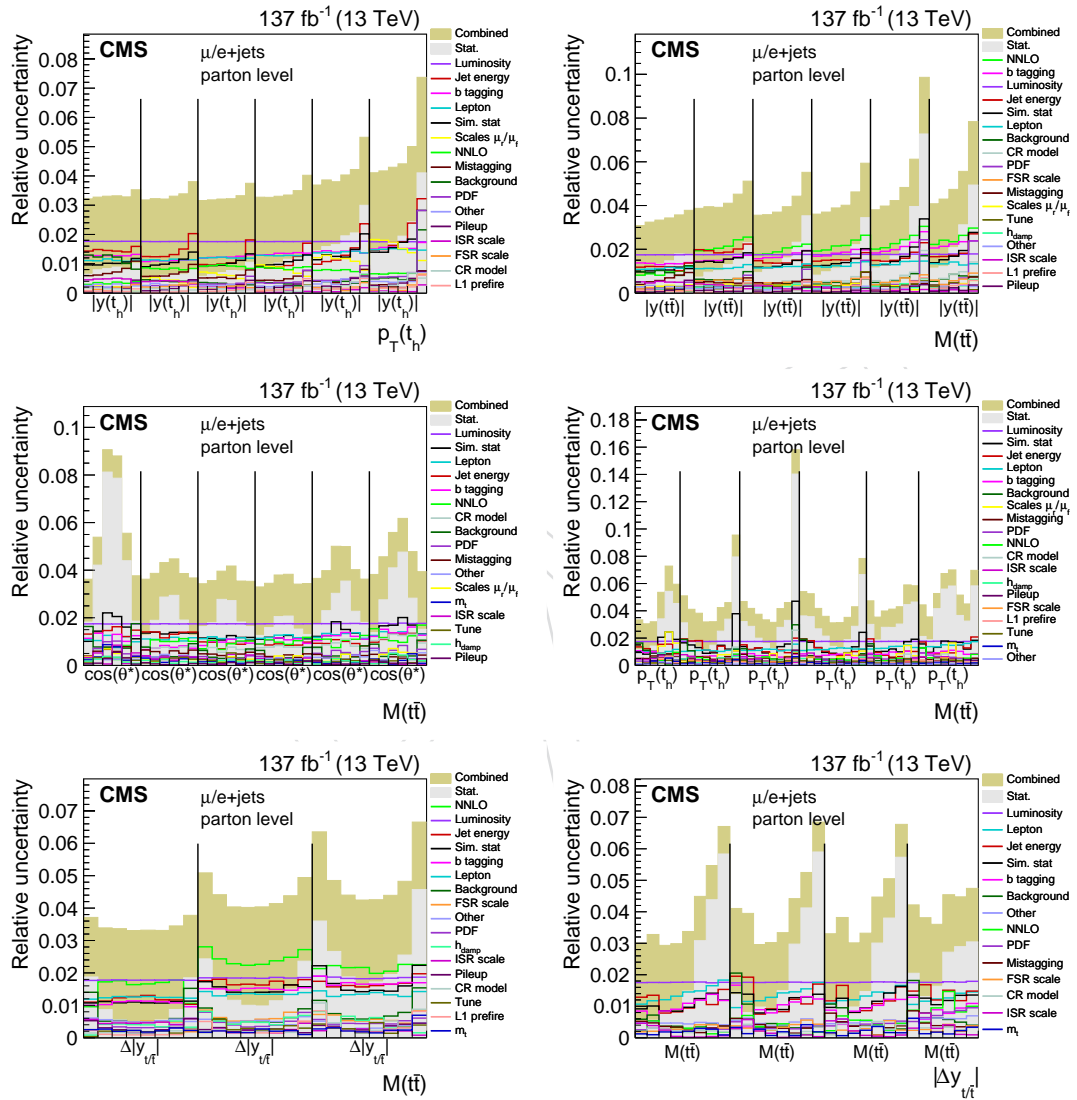


Figure 98

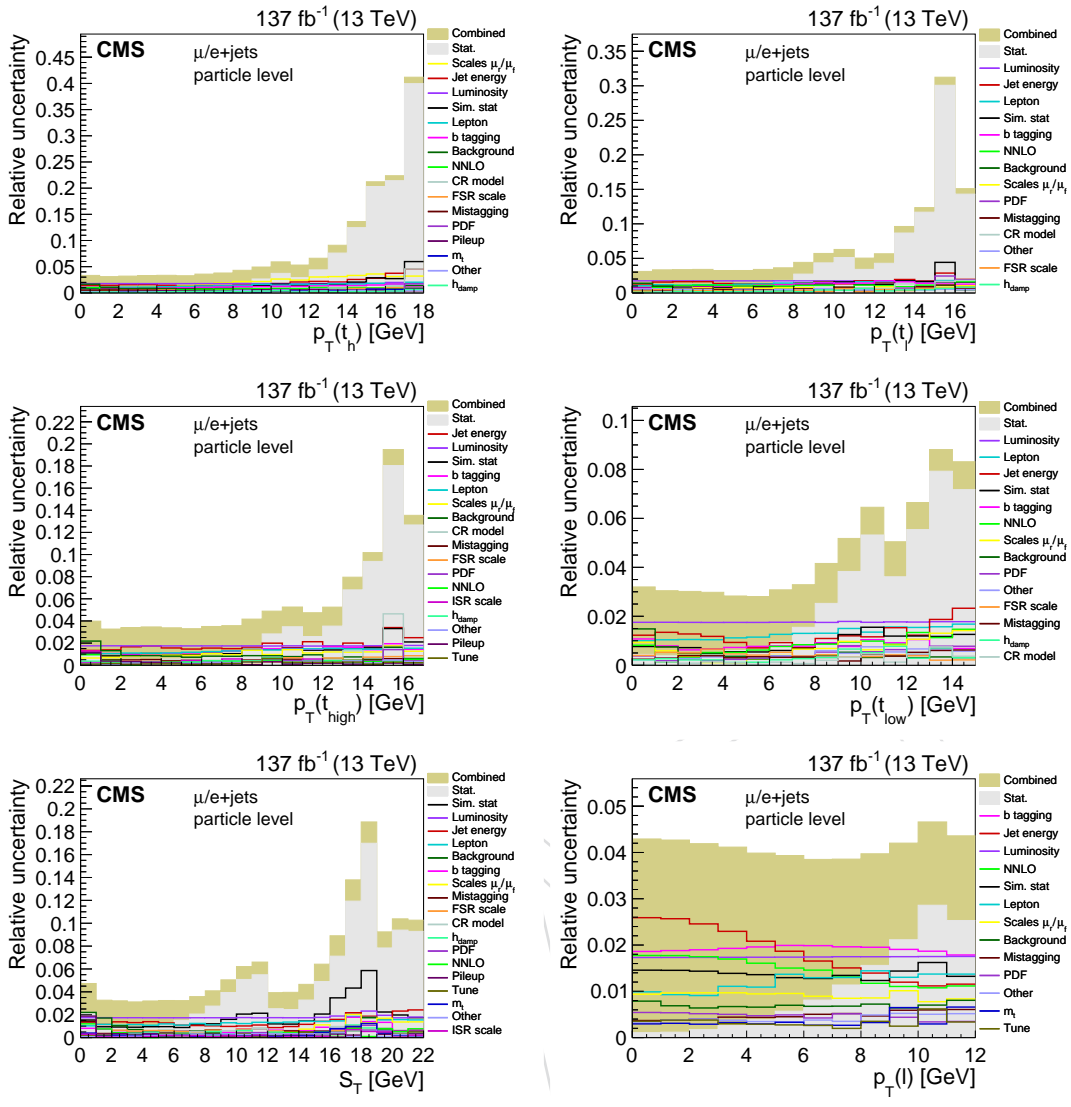


Figure 99

## E Detailed plots of uncertainties at particle level

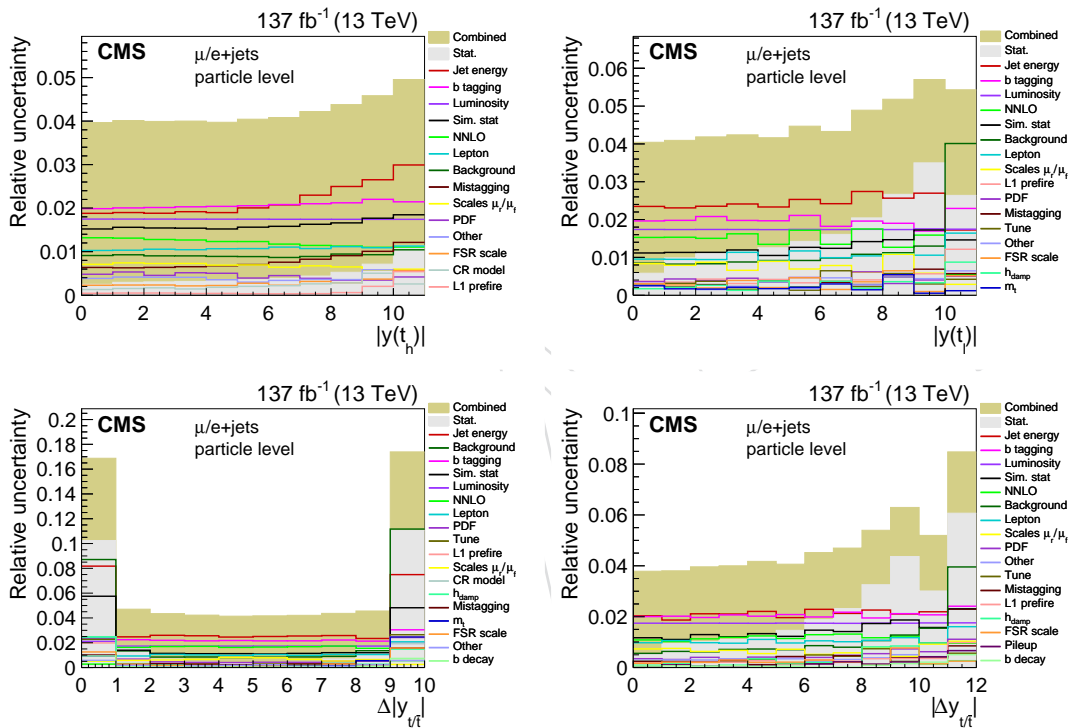


Figure 100

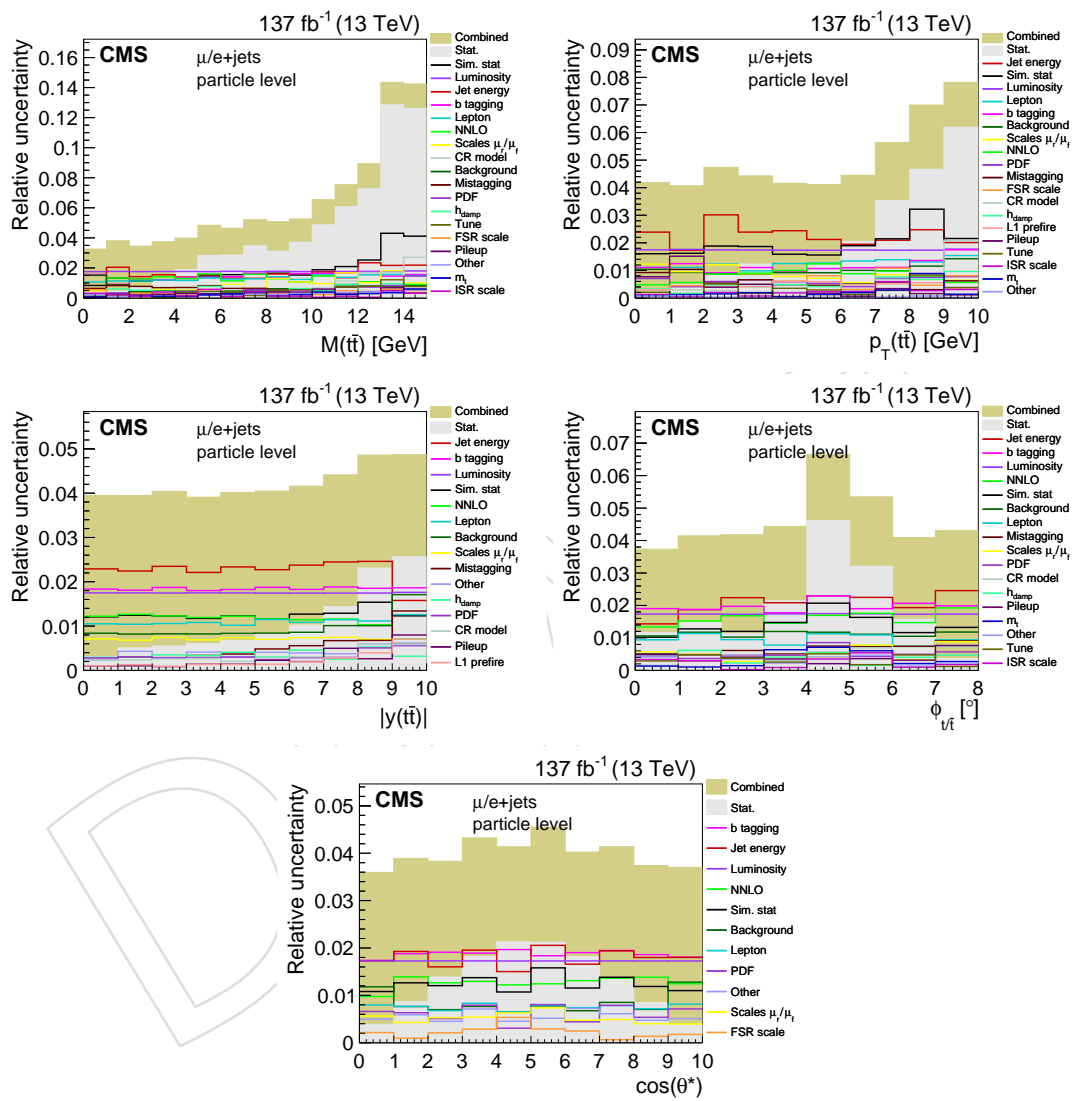


Figure 101

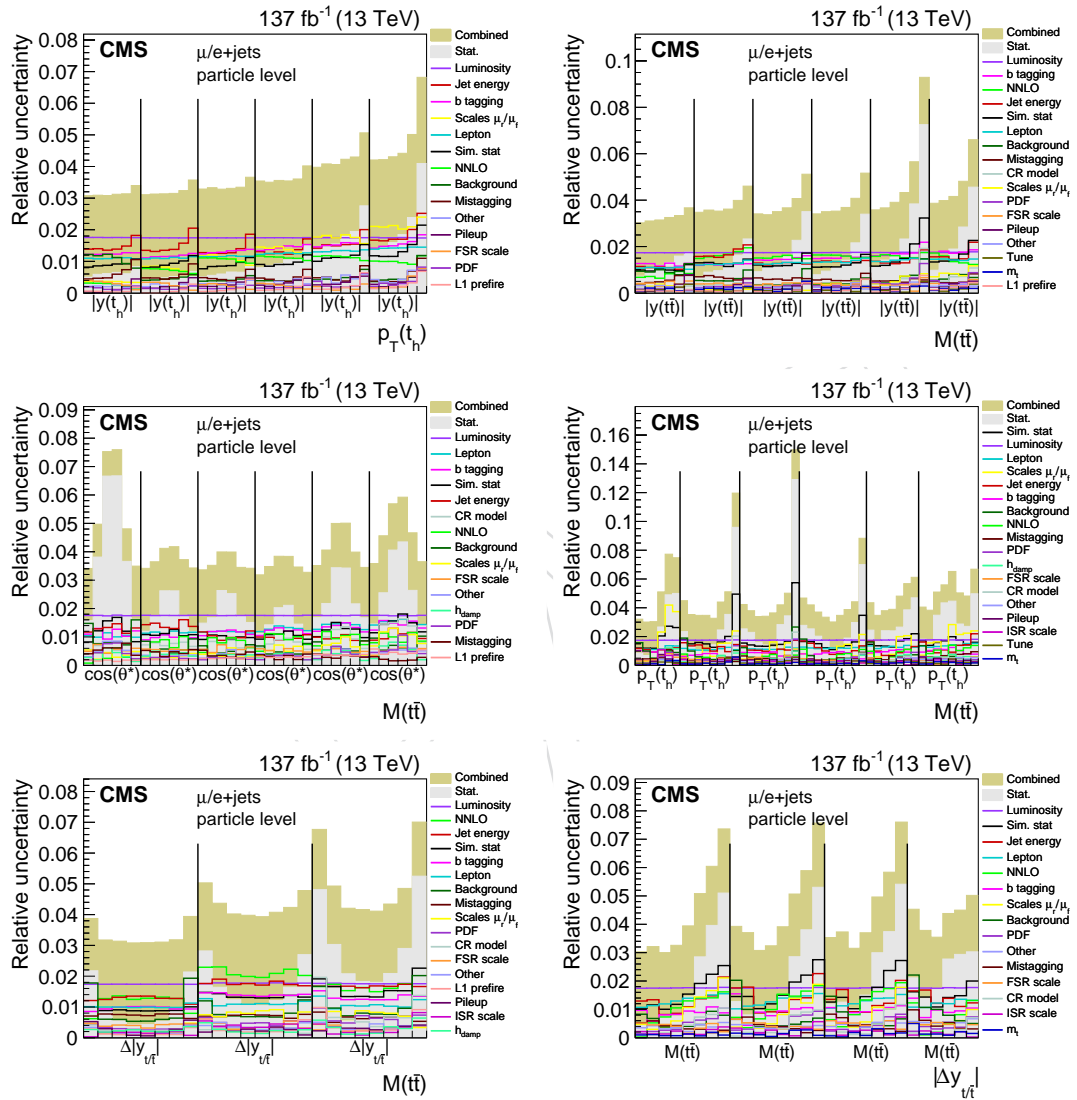


Figure 102

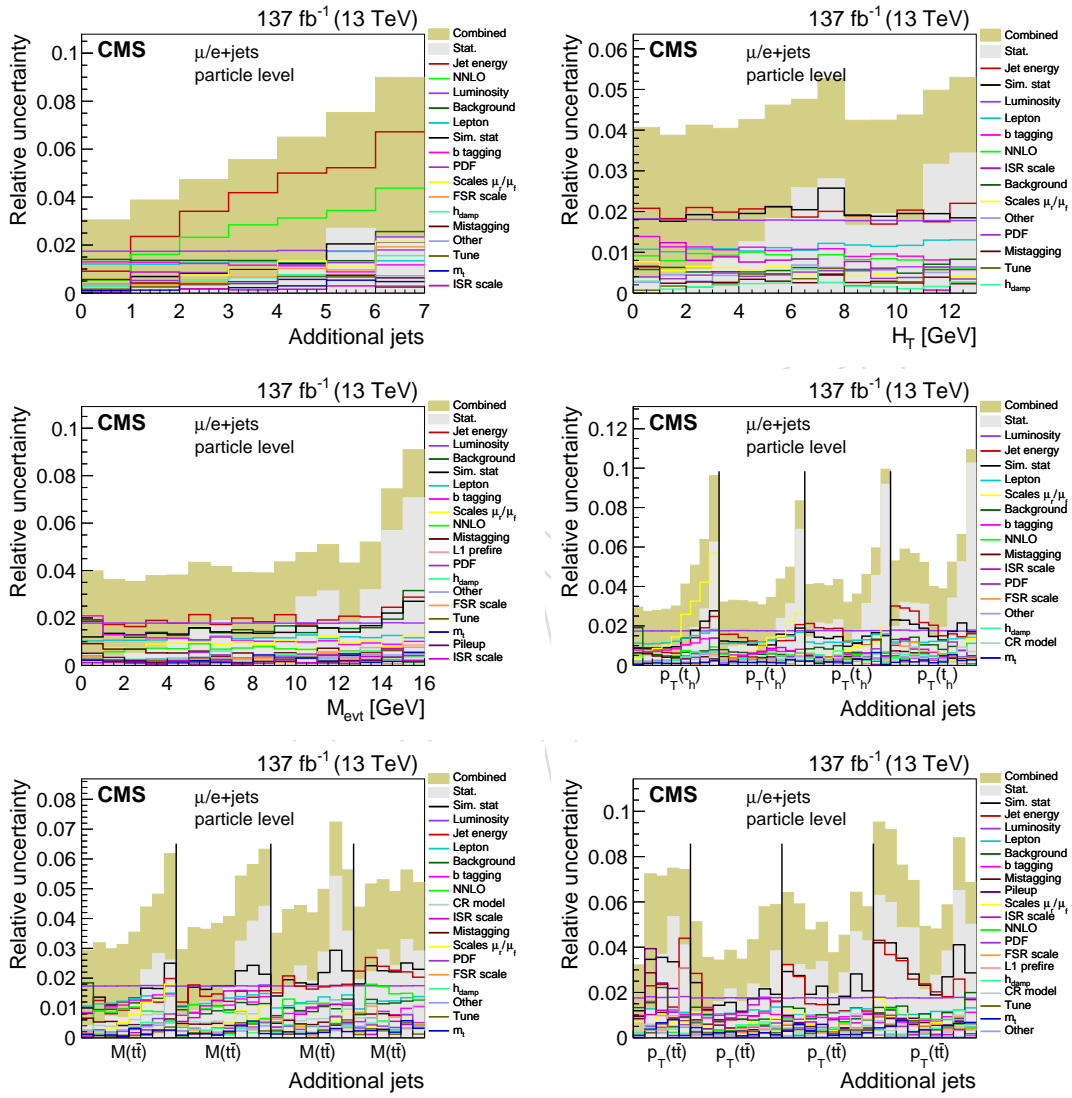


Figure 103

---

887 **F Properties of migration matrices in the parton-level measure-**

888 **ment**

DRAFT

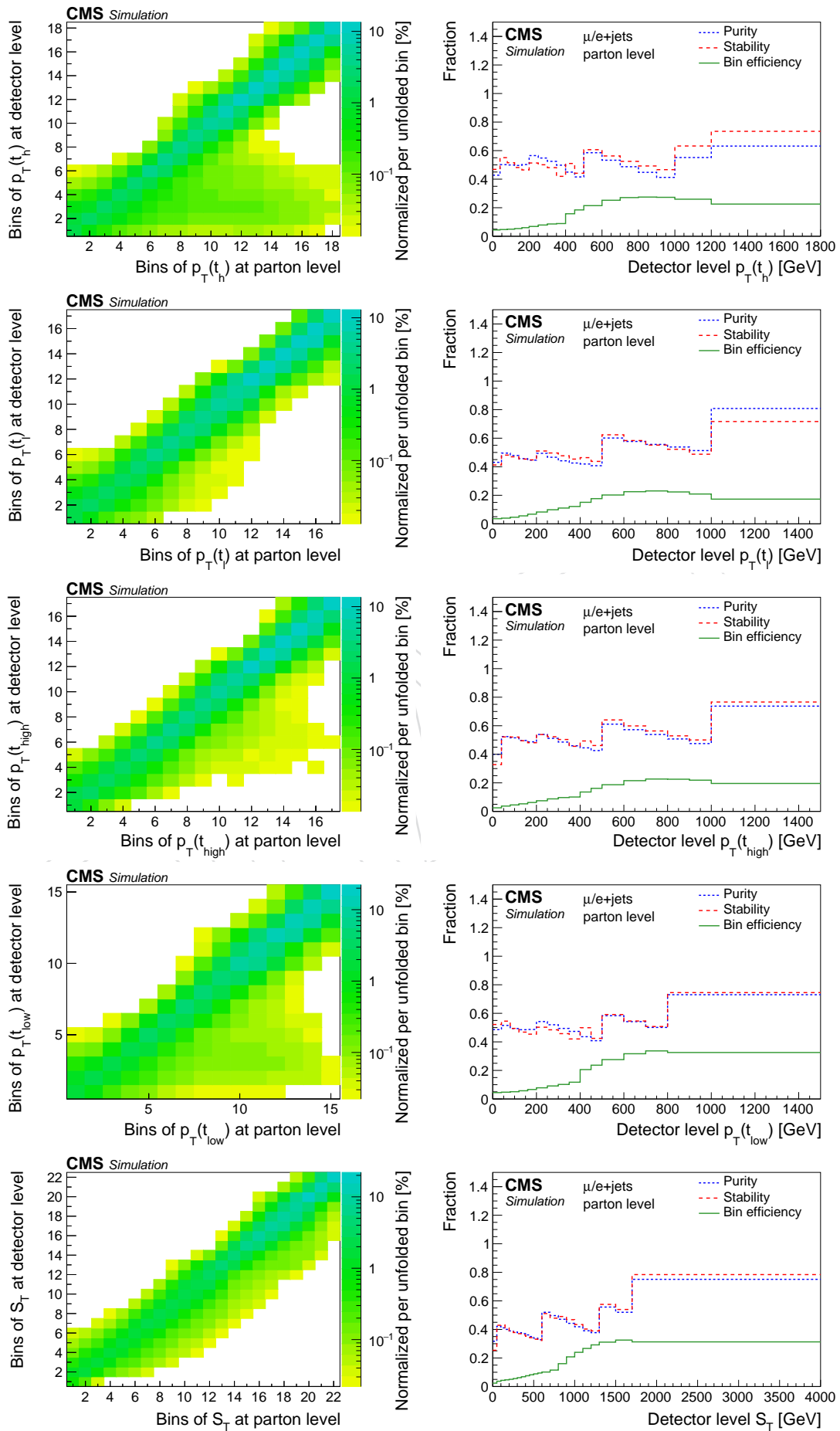


Figure 104

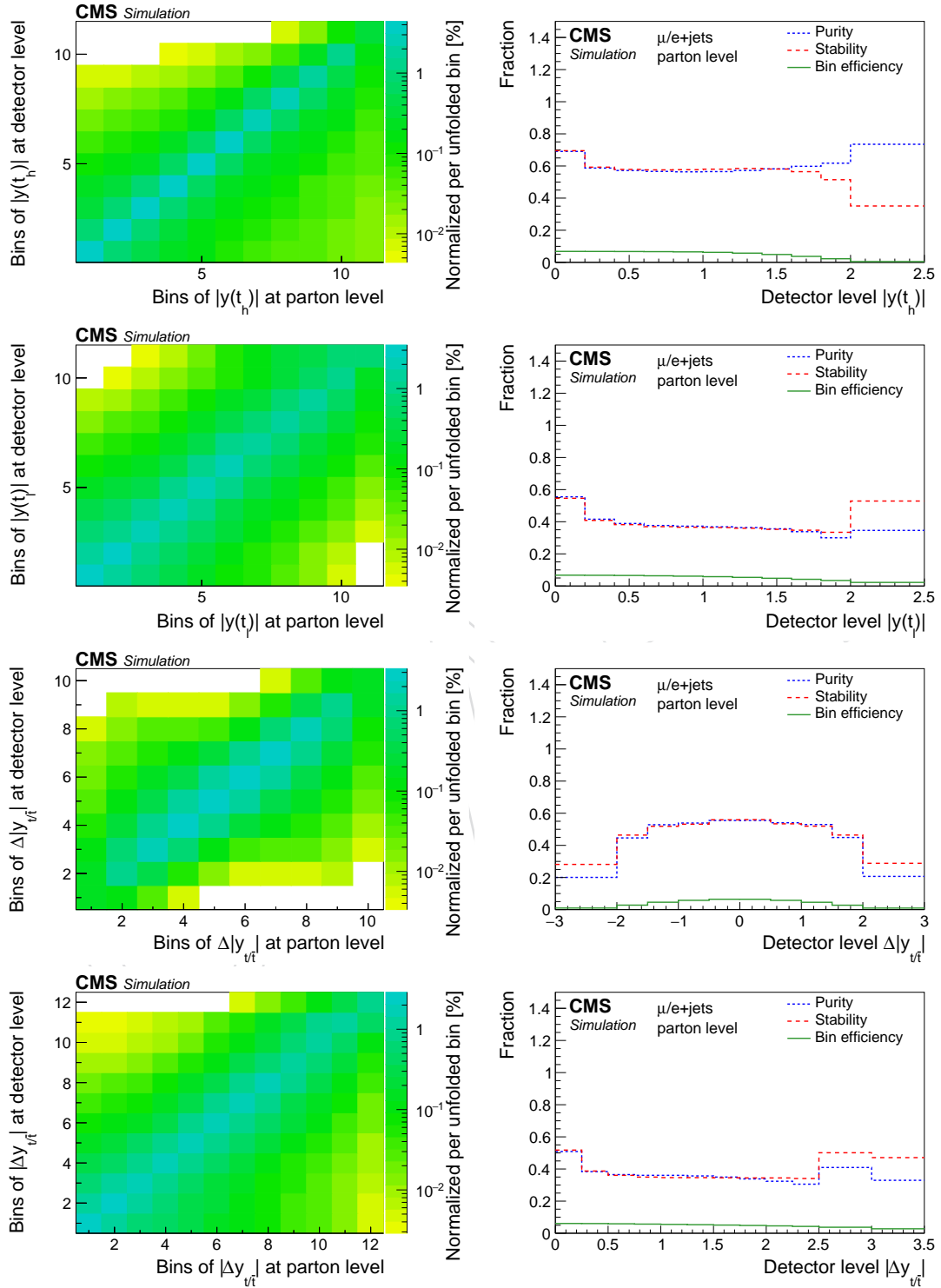


Figure 105

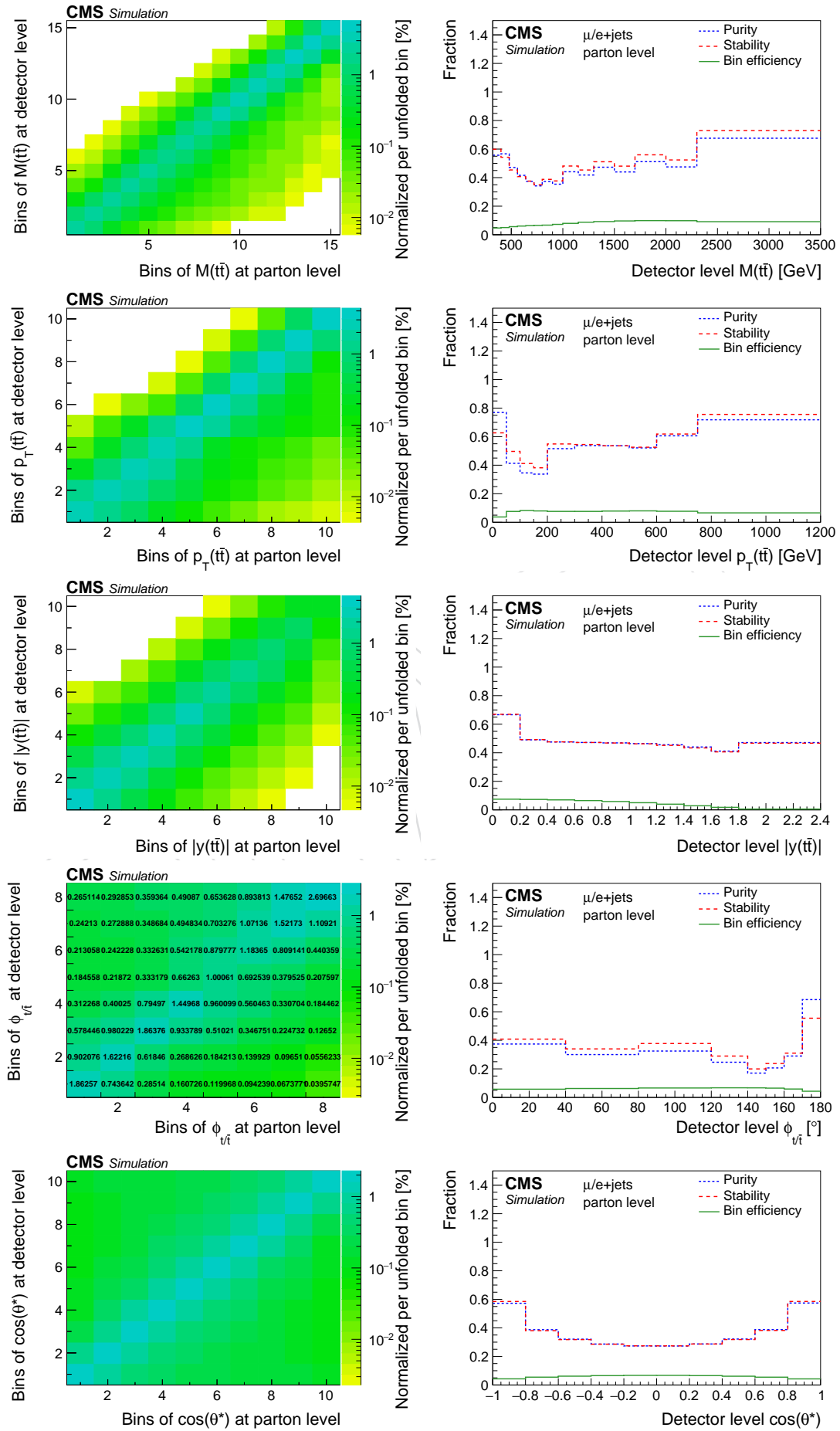


Figure 106

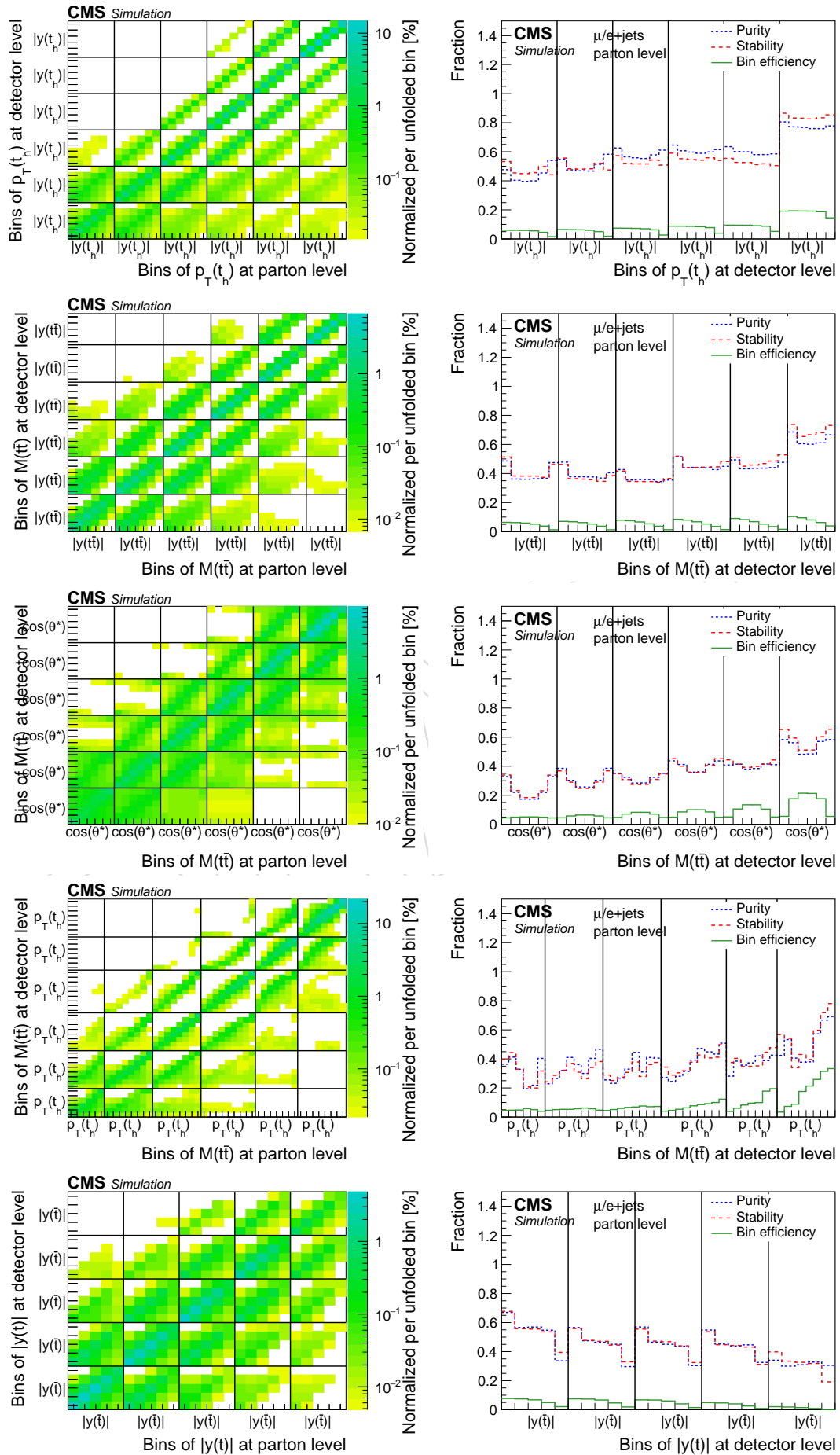


Figure 107

889 **G Properties of migration matrices in the particle-level measure-**

890 **ment**

DRAFT

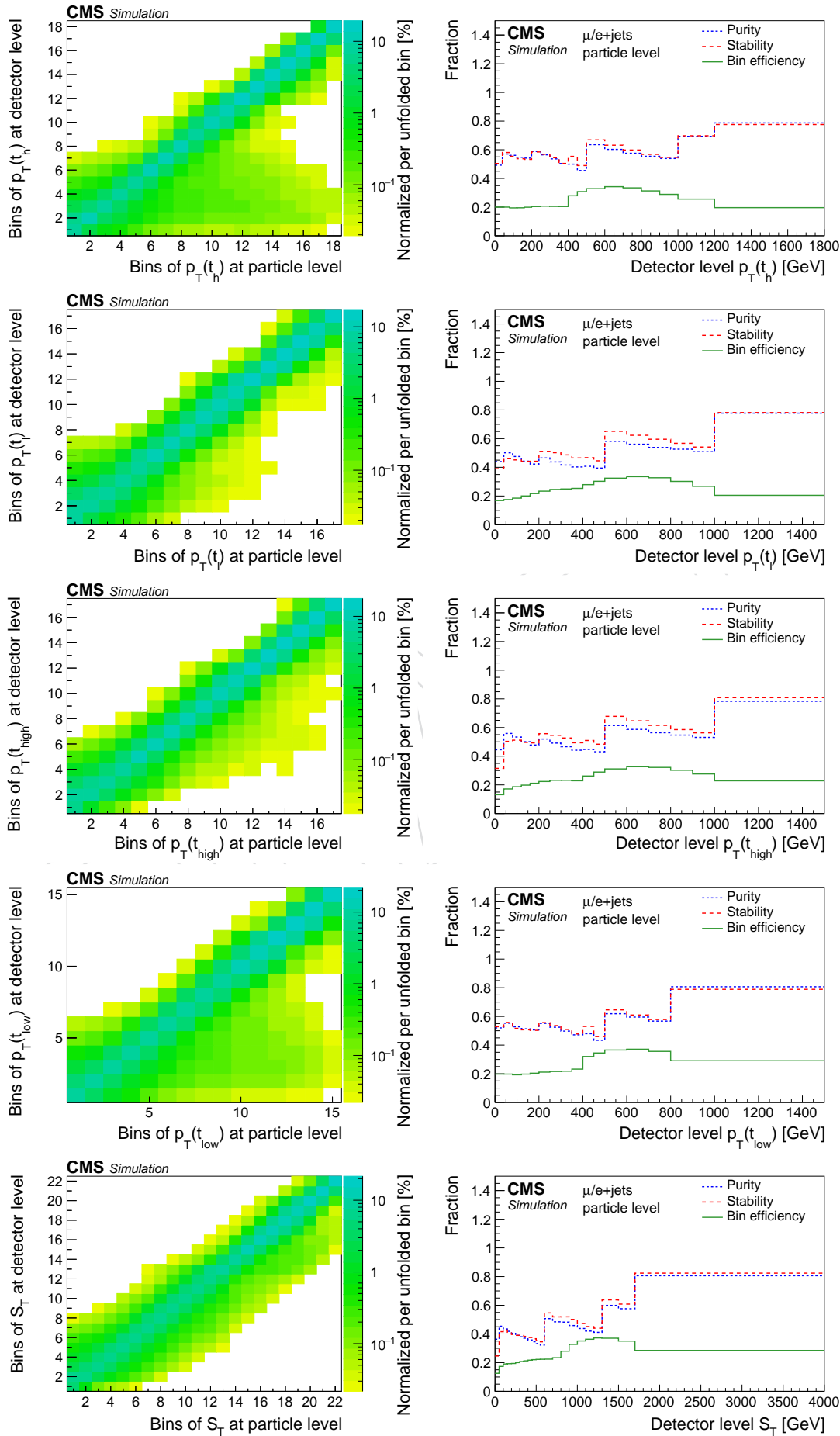


Figure 108

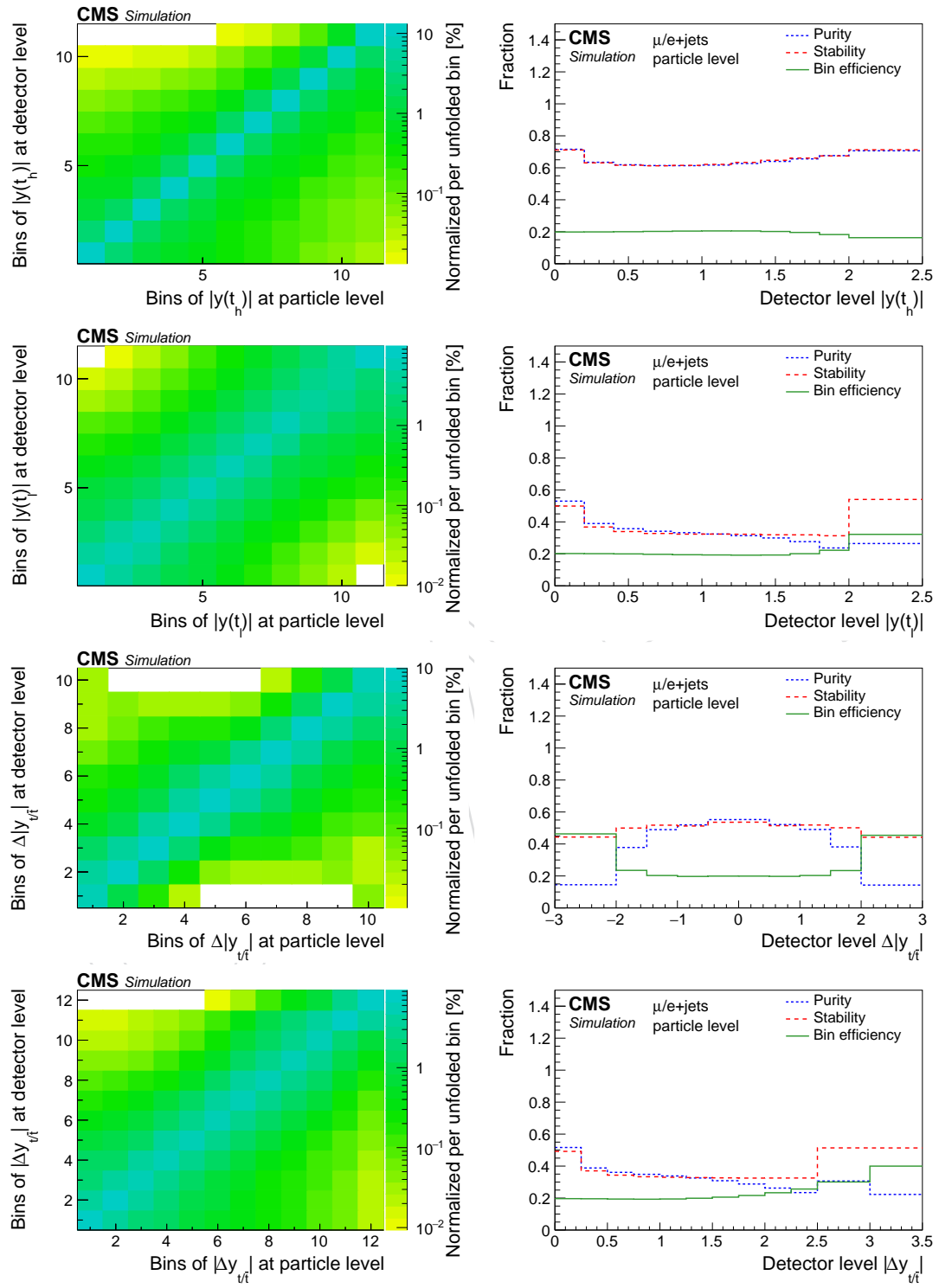


Figure 109

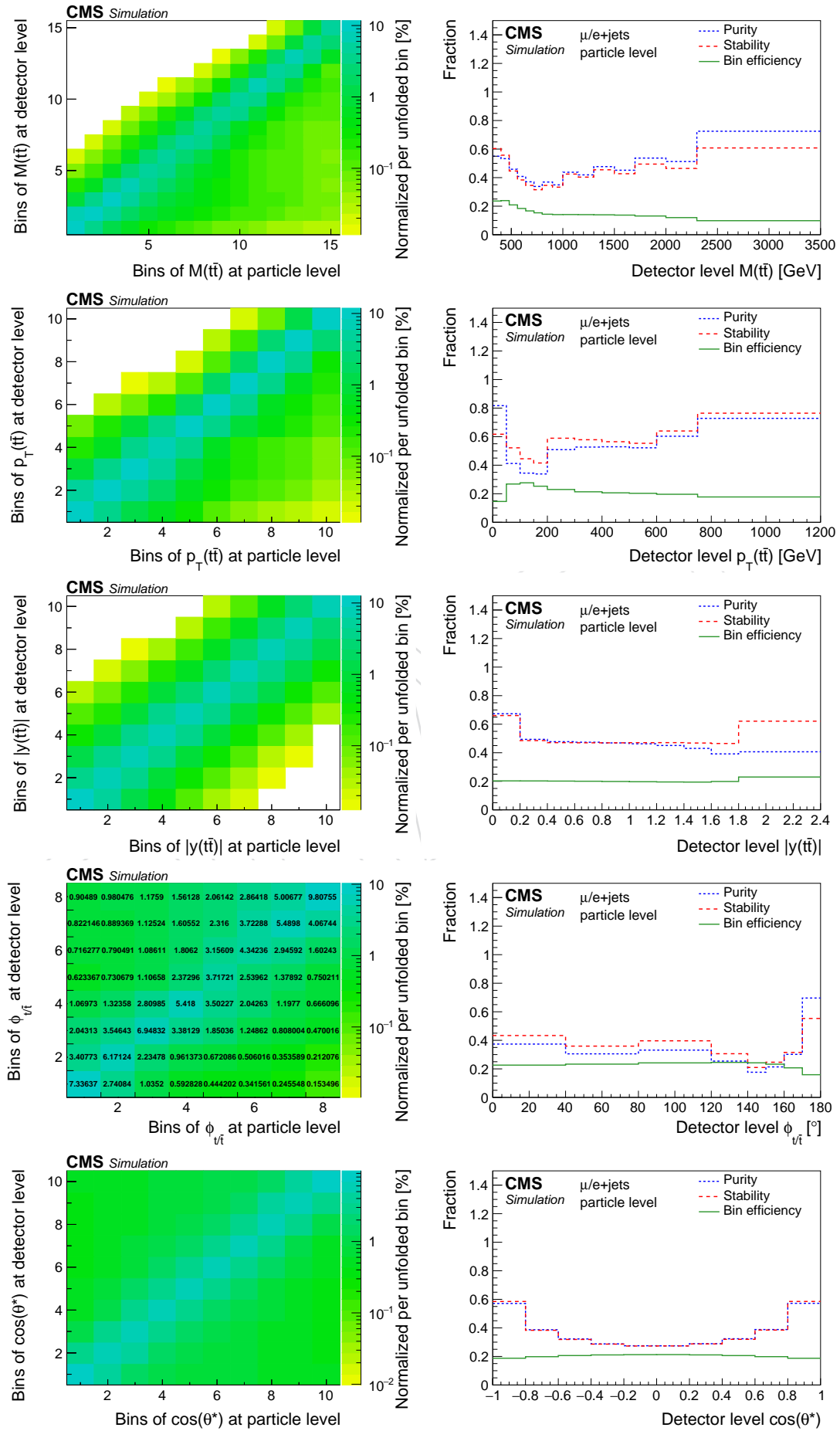


Figure 110

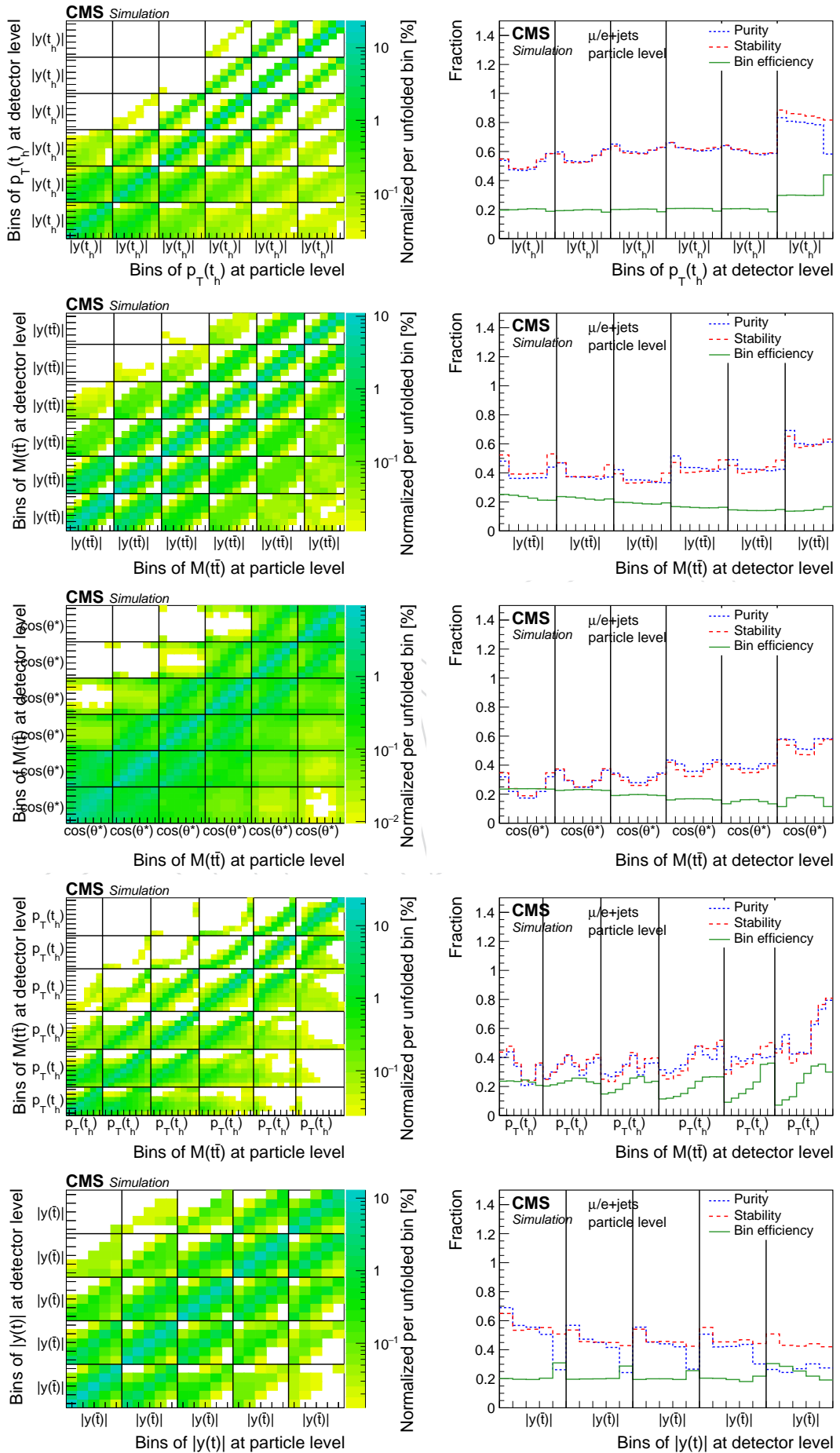


Figure 111

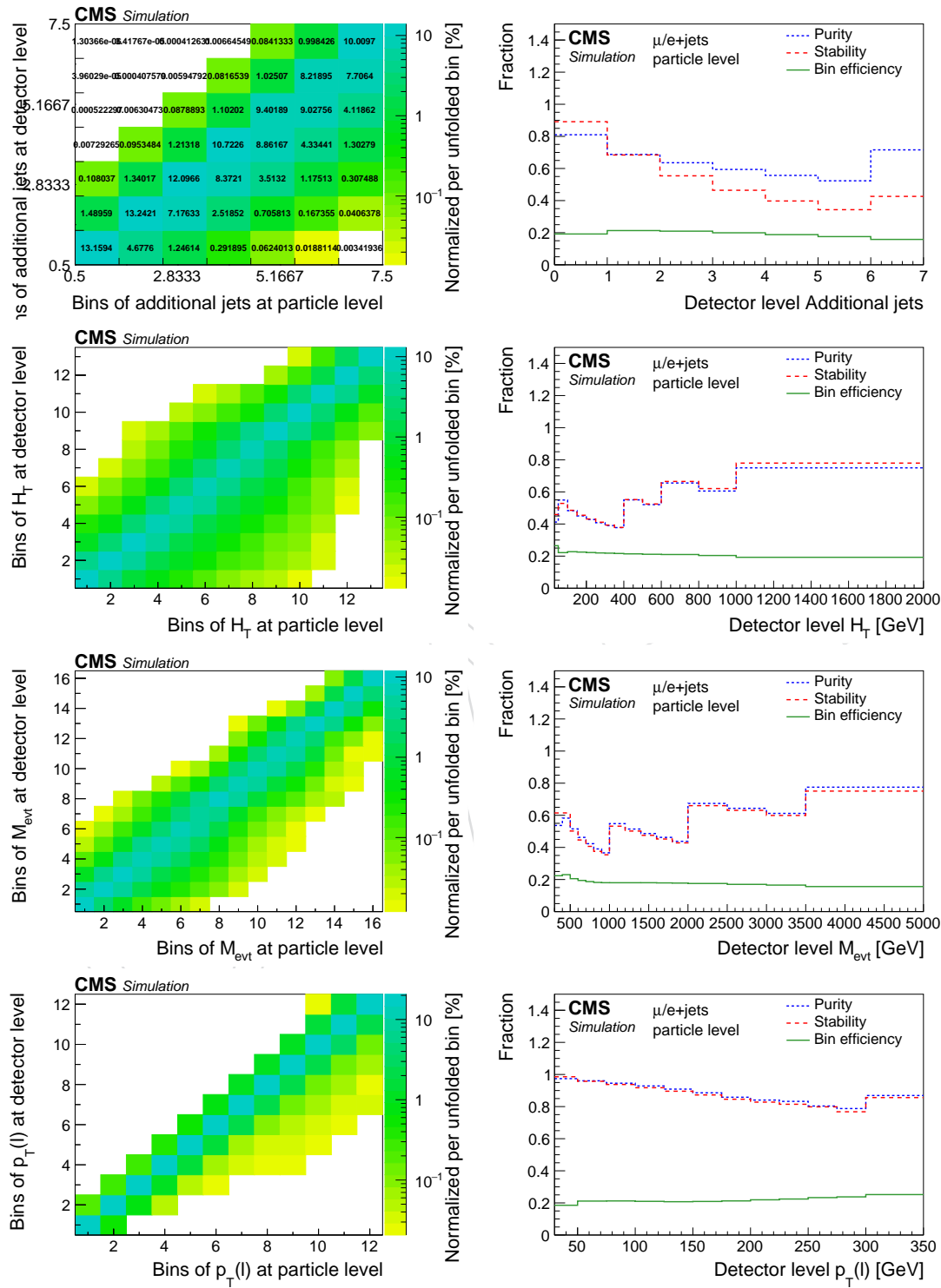


Figure 112

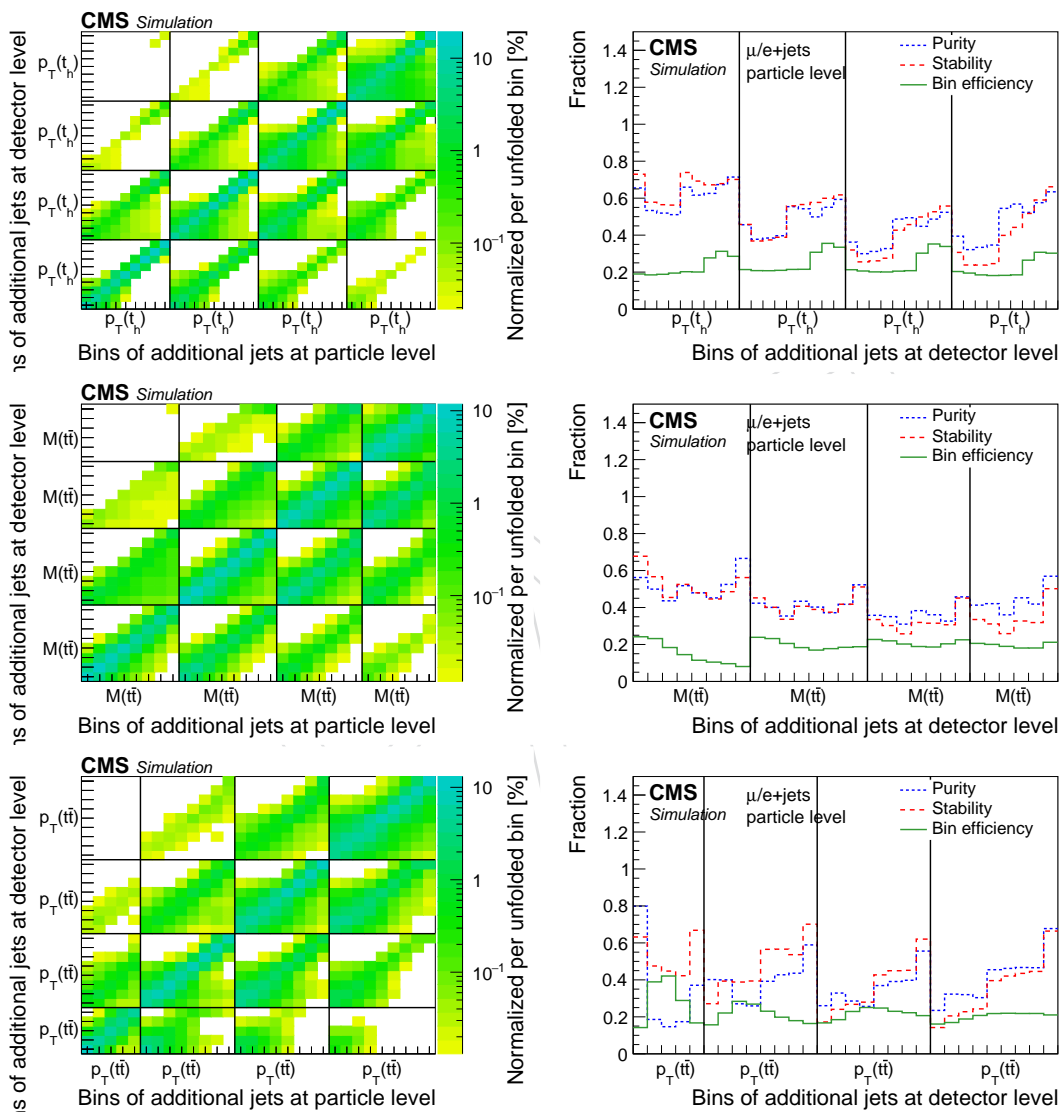


Figure 113

---

891 **H NN inputs for all years**

DRAFT

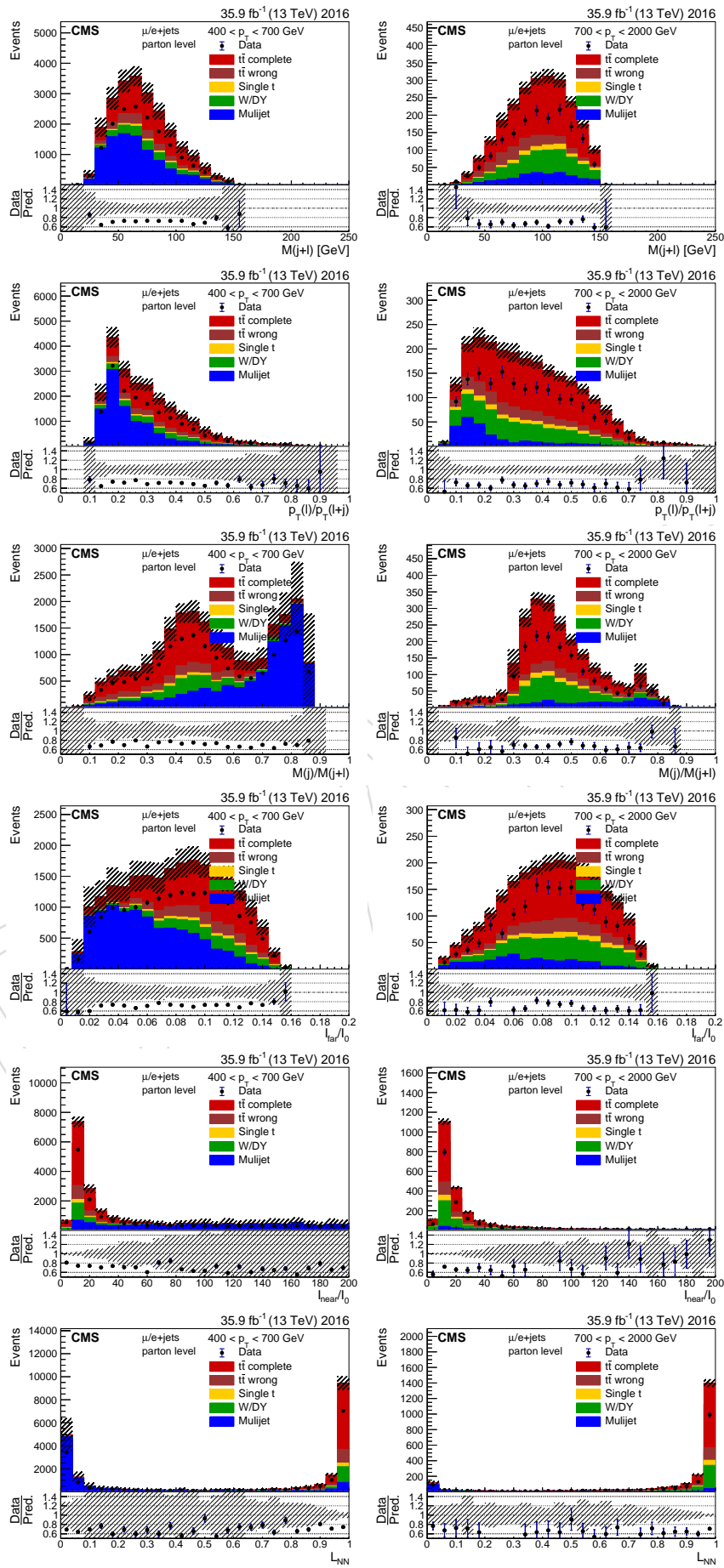


Figure 114: Distribution of variables used as input to the NN for the identification of a boosted  $t\ell$ .

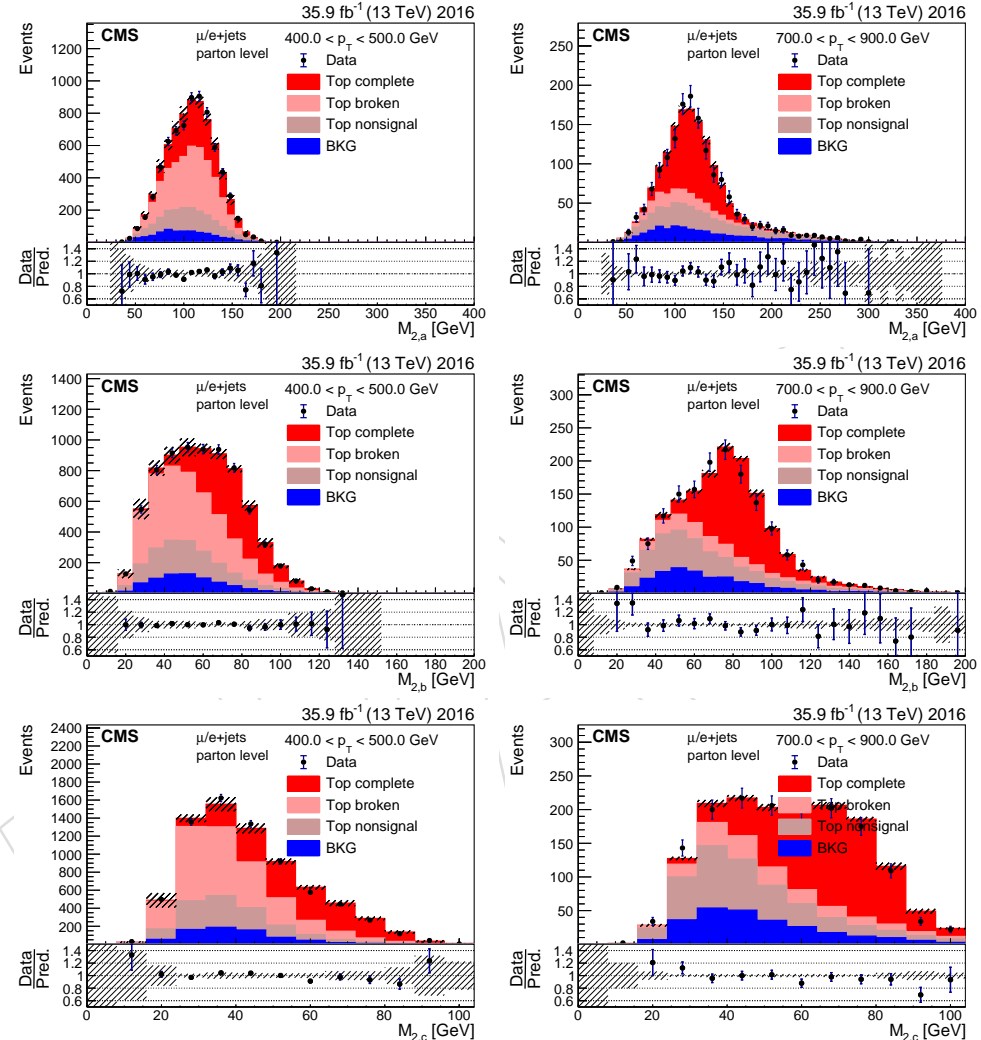


Figure 115: Variables used in the identification of boosted top quarks. The plots are shown for events with an reconstructed  $t_\ell$ . The normalization of the various components is obtained from a fit of  $H_{NN}$  used to extract the signal contribution (complete and broken top candidates.)

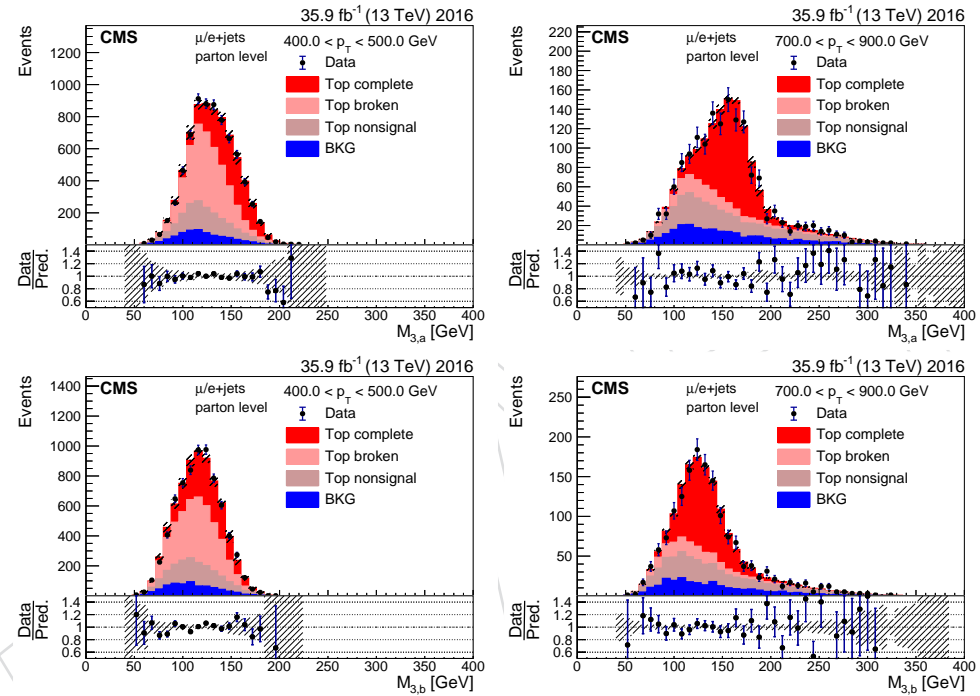


Figure 116: Variables used in the identification of boosted top quarks. The plots are shown for events with an reconstructed  $t_\ell$ . The normalization of the various components is obtained from a fit of  $H_{NN}$  used to extract the signal contribution (complete and broken top candidates.)

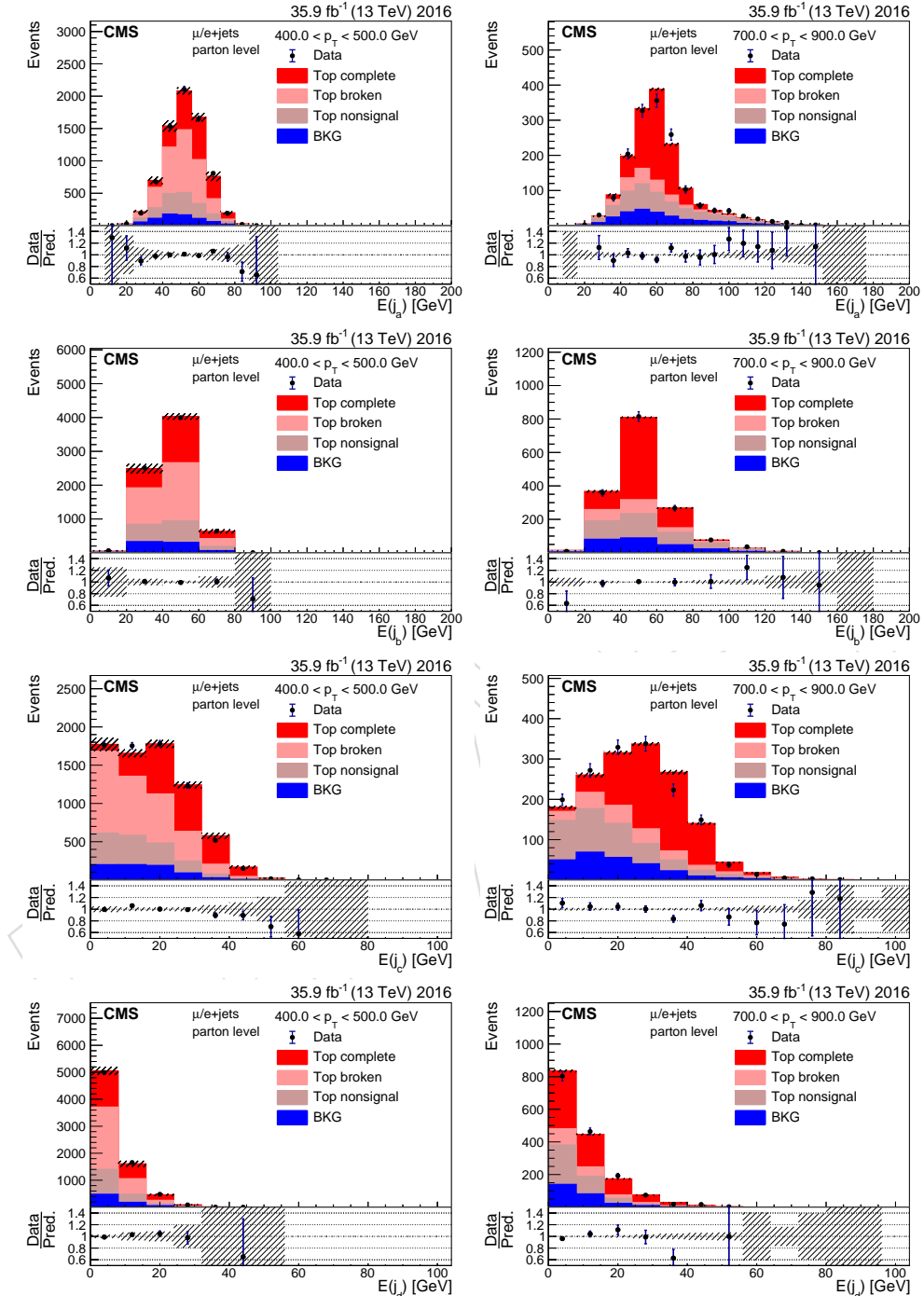


Figure 117: Variables used in the identification of boosted top quarks. The plots are shown for events with a reconstructed  $t_\ell$ . The normalization of the various components is obtained from a fit of  $H_{NN}$  used to extract the signal contribution (complete and broken top candidates.)

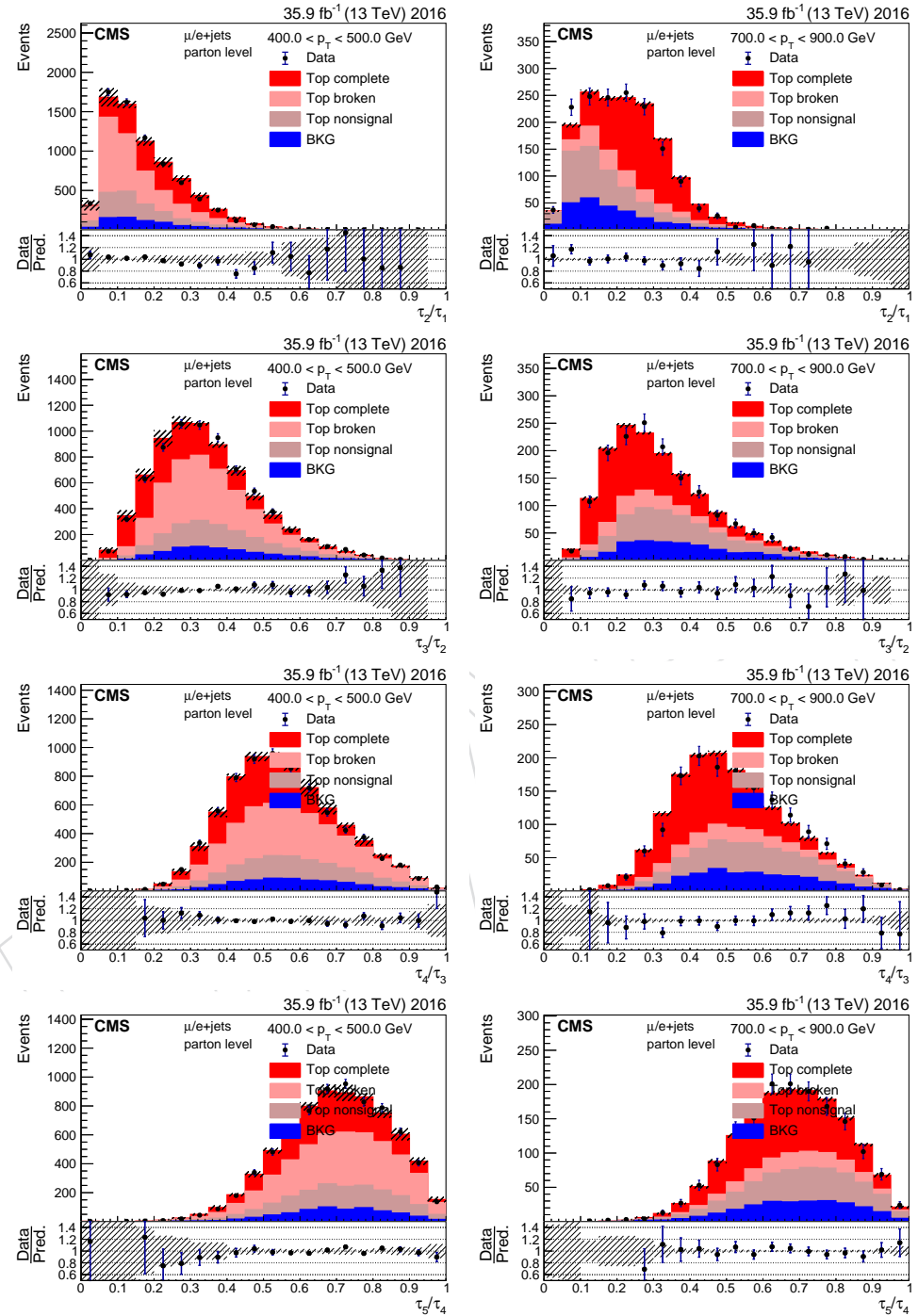


Figure 118: Variables used in the identification of boosted top quarks. The plots are shown for events with a reconstructed  $t_\ell$ . The normalization of the various components is obtained from a fit of  $H_{NN}$  used to extract the signal contribution (complete and broken top candidates.)

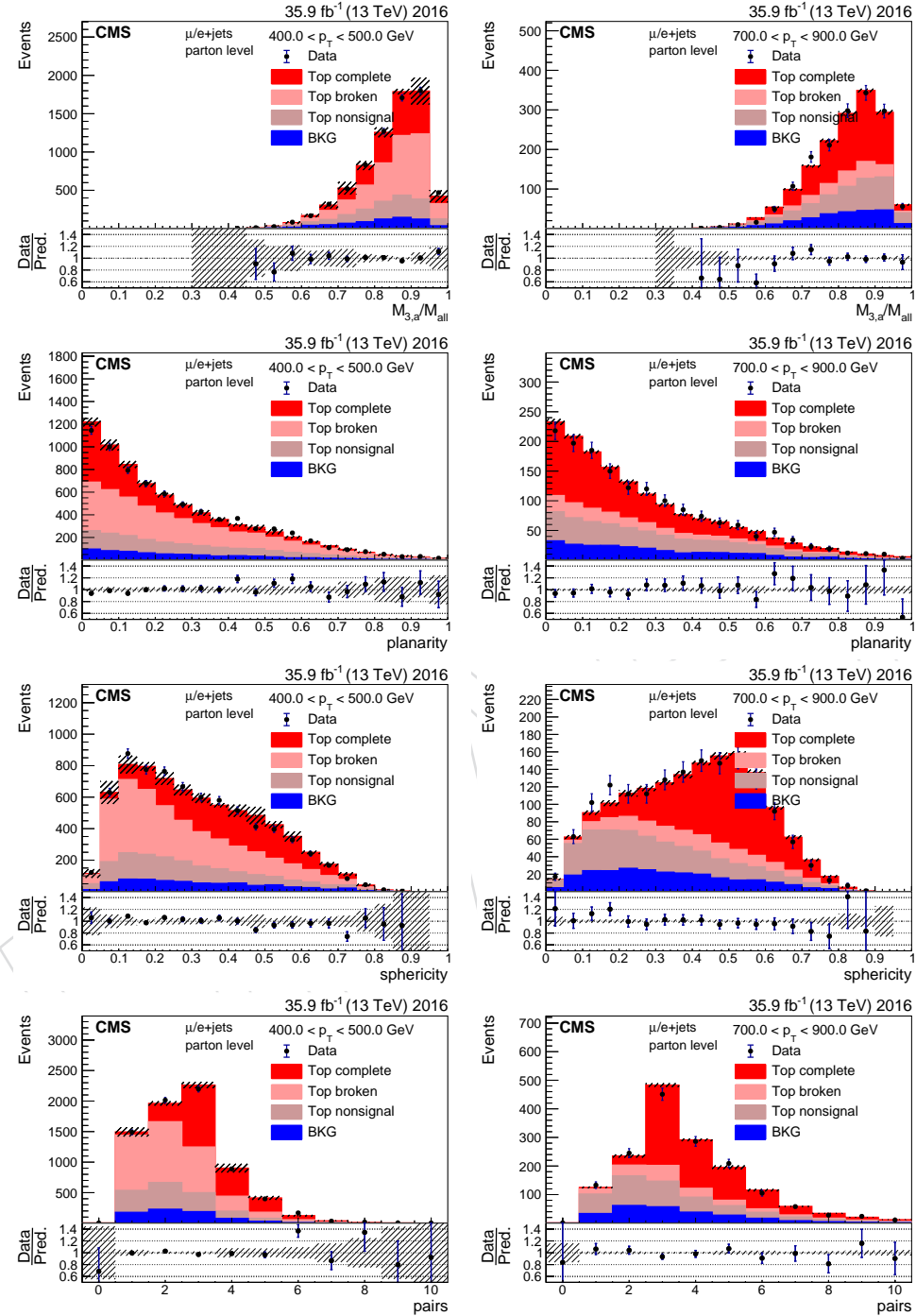


Figure 119: Variables used in the identification of boosted top quarks. The plots are shown for events with a reconstructed  $t_\ell$ . The normalization of the various components is obtained from a fit of  $H_{NN}$  used to extract the signal contribution (complete and broken top candidates.)

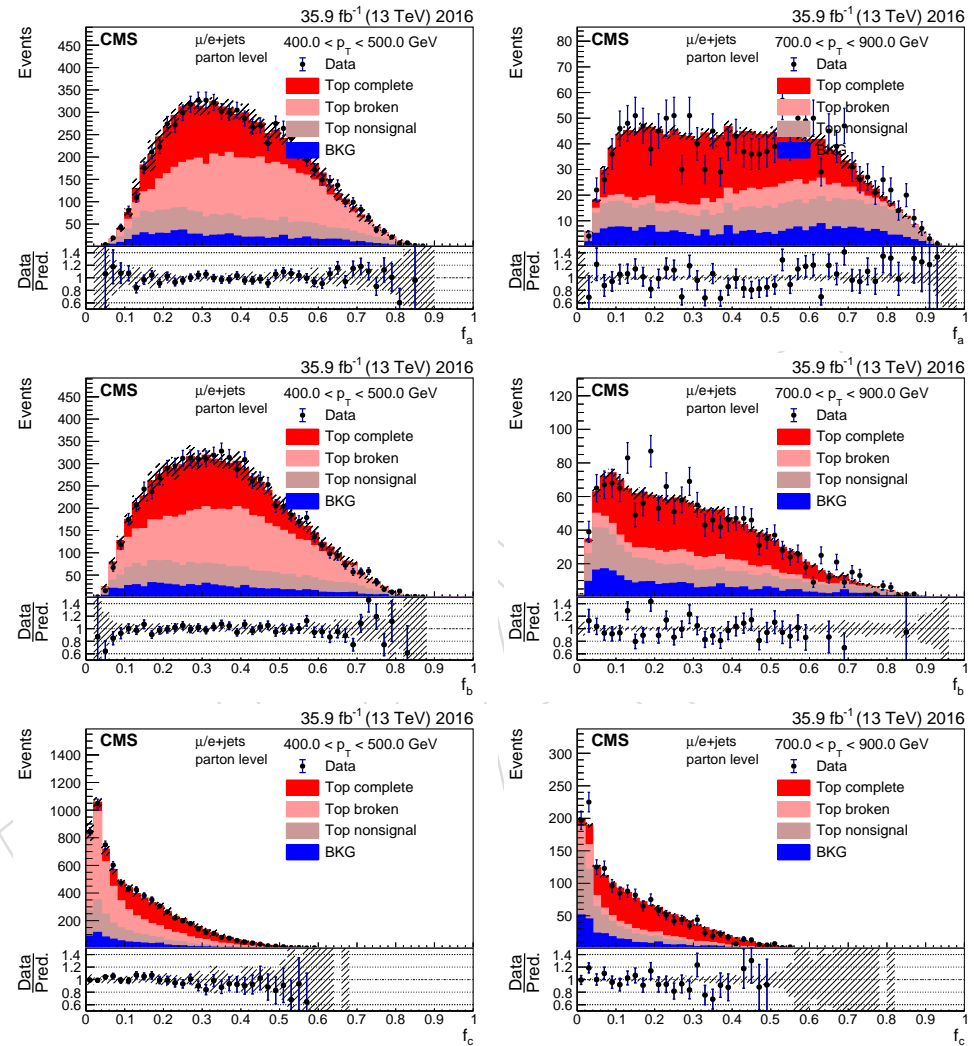


Figure 120: Variables used in the identification of boosted top quarks. The plots are shown for events with a reconstructed  $t_\ell$ . The normalization of the various components is obtained from a fit of  $H_{NN}$  used to extract the signal contribution (complete and broken top candidates.)

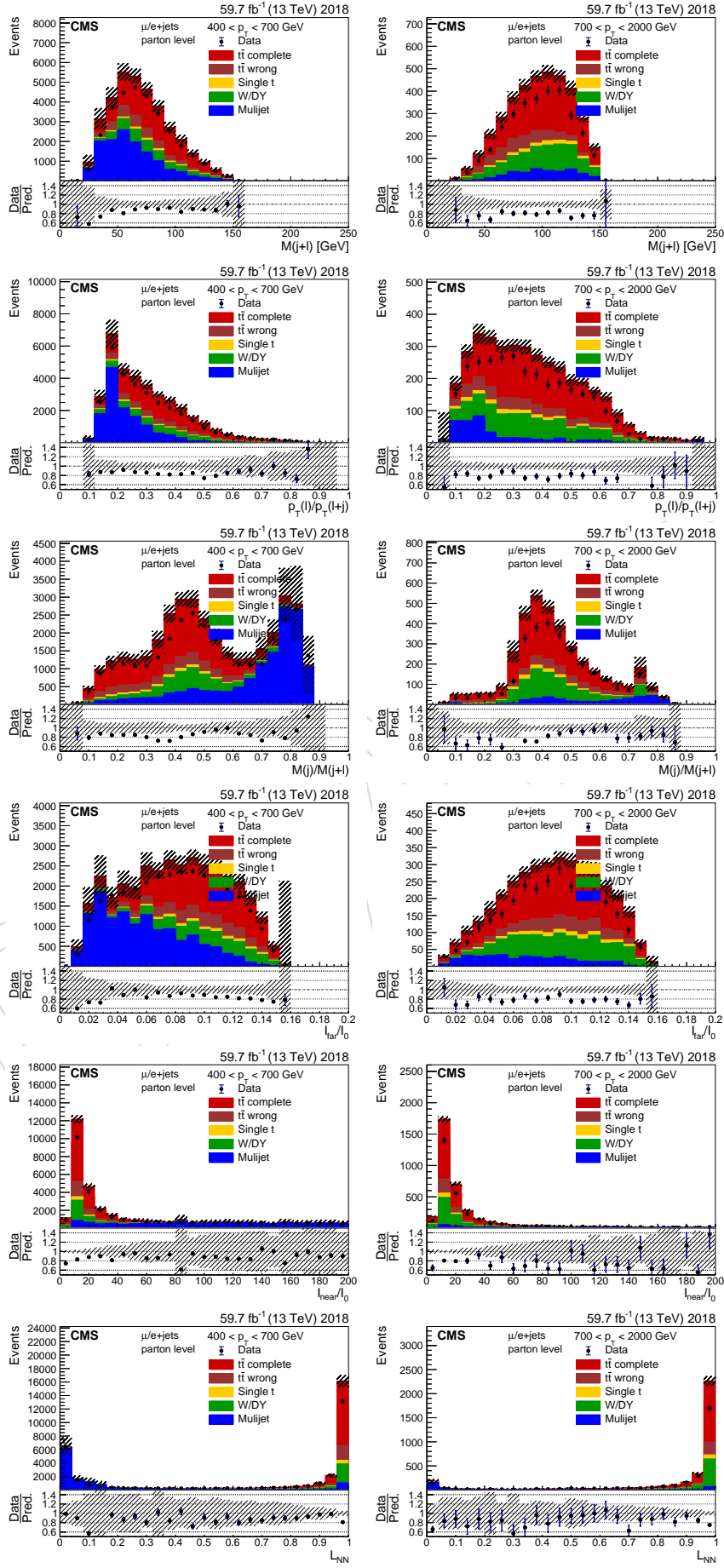


Figure 121: Distribution of variables used as input to the NN for the identification of a boosted  $t\bar{t}\ell$ .

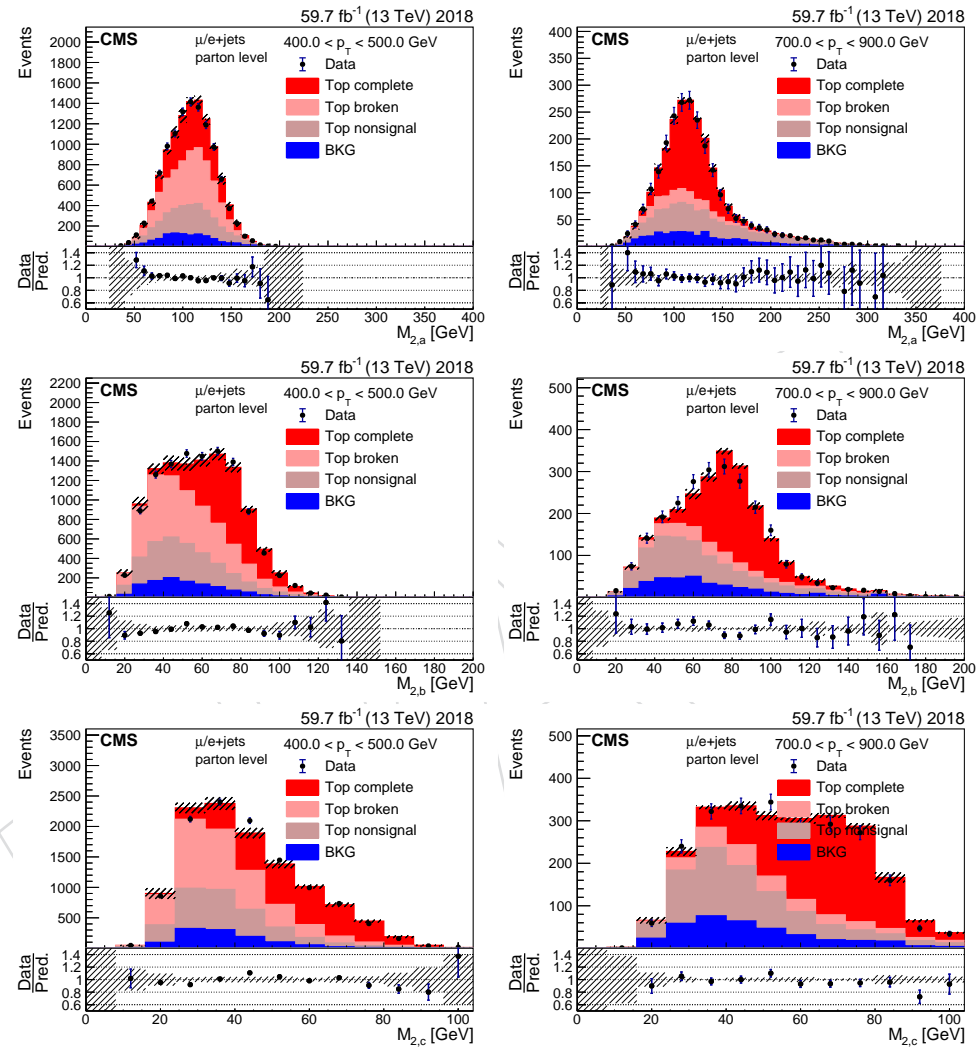


Figure 122: Variables used in the identification of boosted top quarks. The plots are shown for events with an reconstructed  $t_\ell$ . The normalization of the various components is obtained from a fit of  $H_{NN}$  used to extract the signal contribution (complete and broken top candidates.)

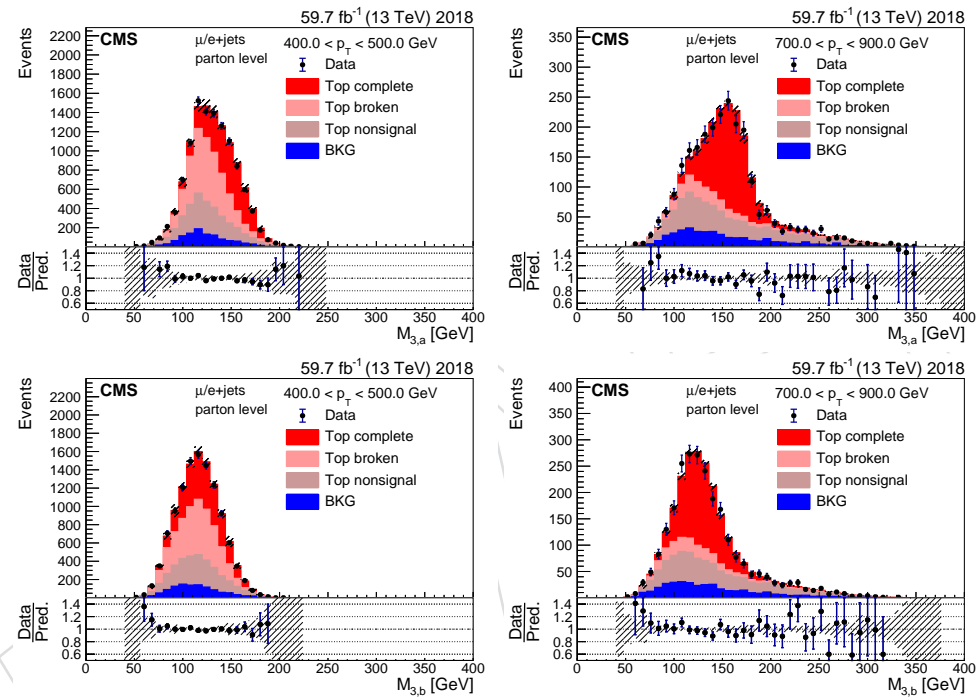


Figure 123: Variables used in the identification of boosted top quarks. The plots are shown for events with an reconstructed  $t_\ell$ . The normalization of the various components is obtained from a fit of  $H_{NN}$  used to extract the signal contribution (complete and broken top candidates.)

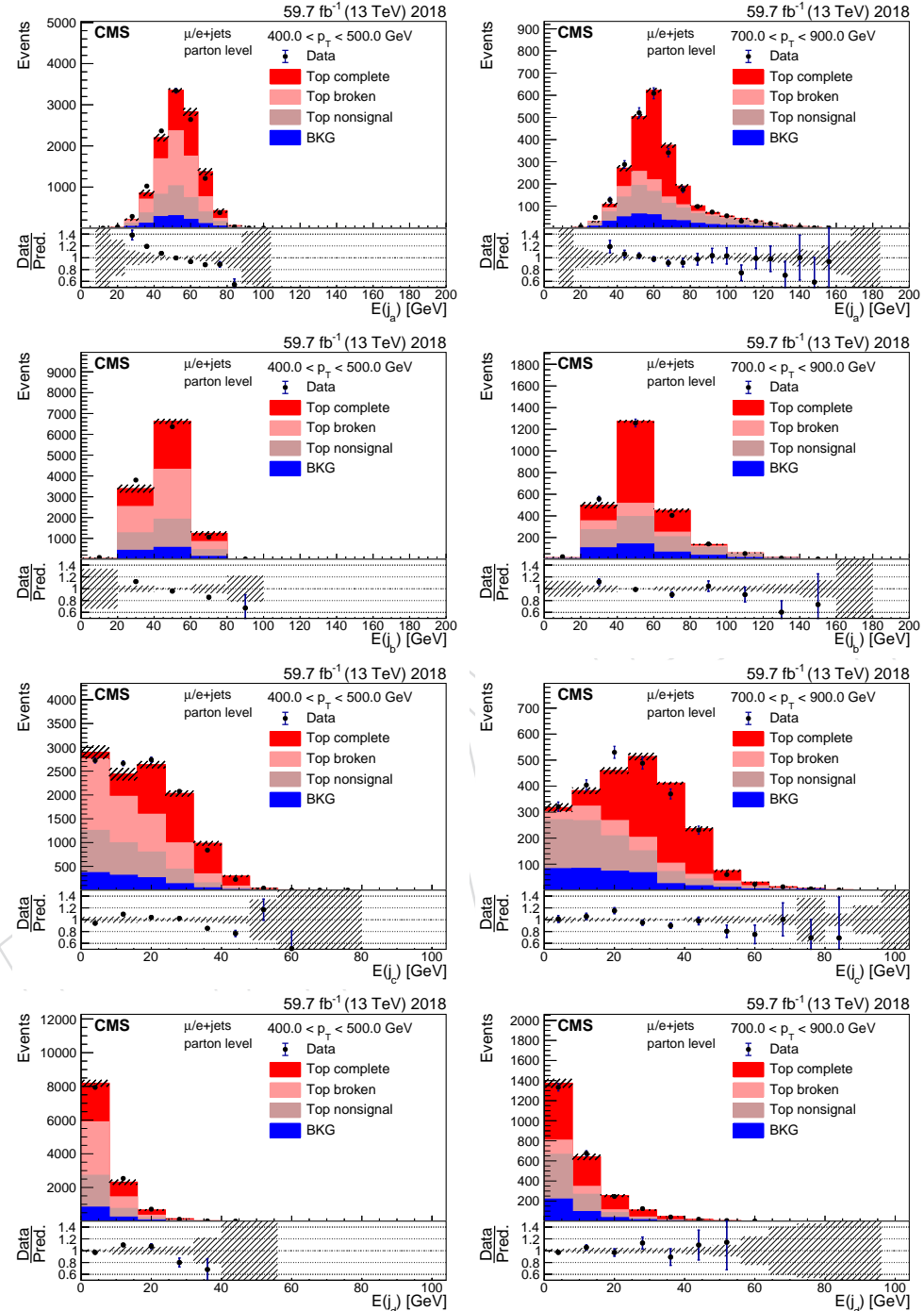


Figure 124: Variables used in the identification of boosted top quarks. The plots are shown for events with a reconstructed  $t_\ell$ . The normalization of the various components is obtained from a fit of  $H_{NN}$  used to extract the signal contribution (complete and broken top candidates.)

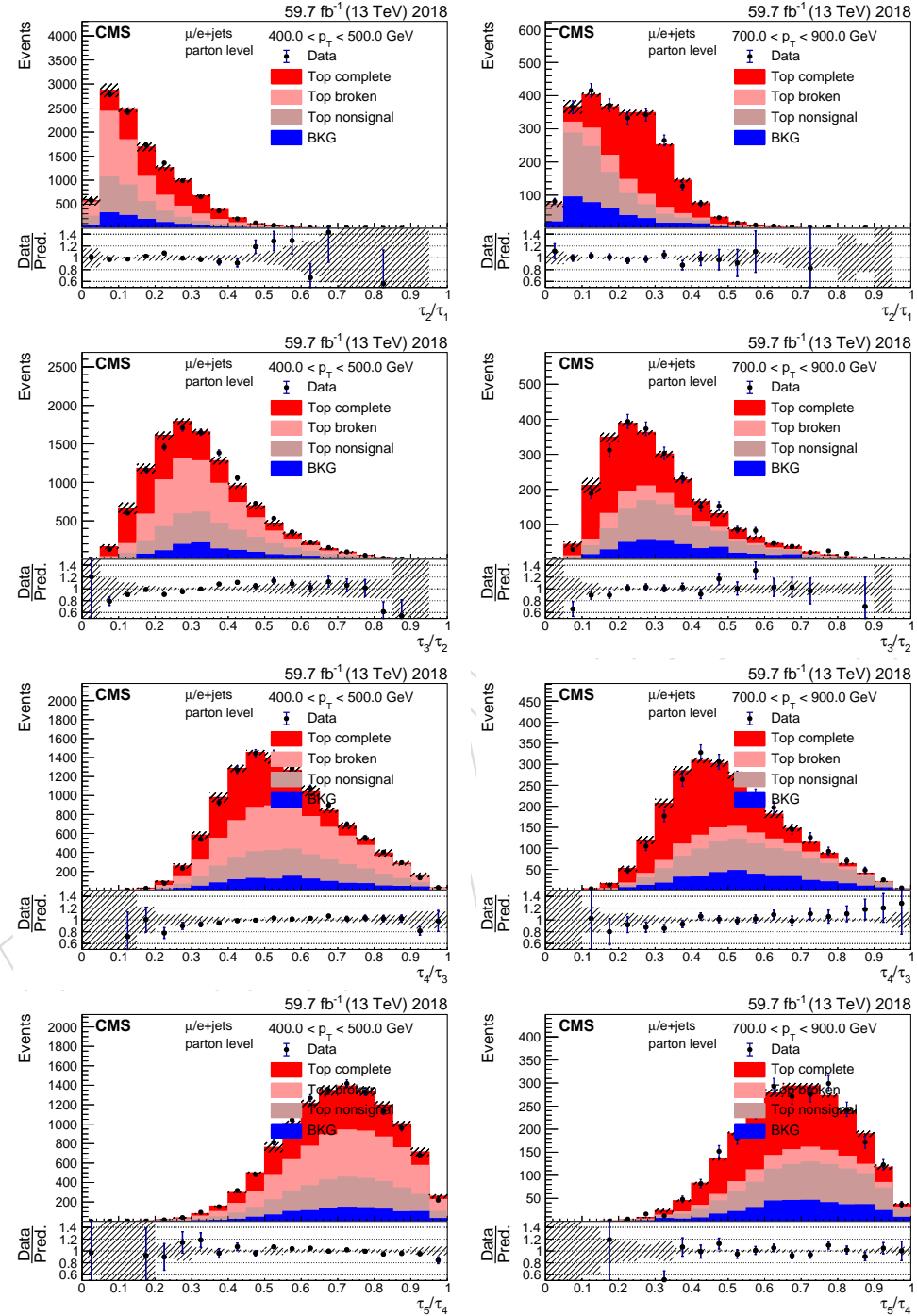


Figure 125: Variables used in the identification of boosted top quarks. The plots are shown for events with a reconstructed  $\tau_\ell$ . The normalization of the various components is obtained from a fit of  $H_{NN}$  used to extract the signal contribution (complete and broken top candidates.)

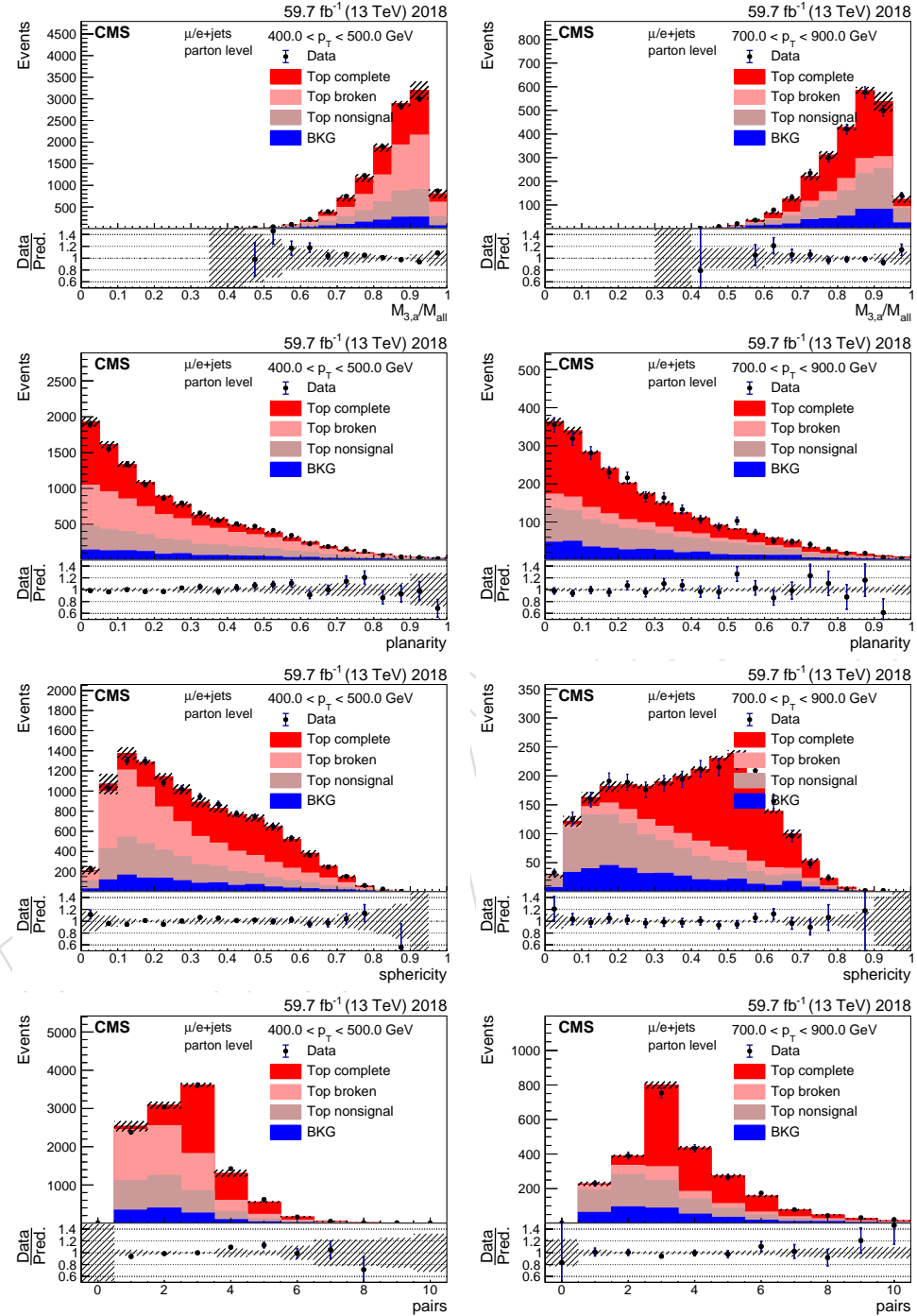


Figure 126: Variables used in the identification of boosted top quarks. The plots are shown for events with a reconstructed  $t_\ell$ . The normalization of the various components is obtained from a fit of  $H_{NN}$  used to extract the signal contribution (complete and broken top candidates.)

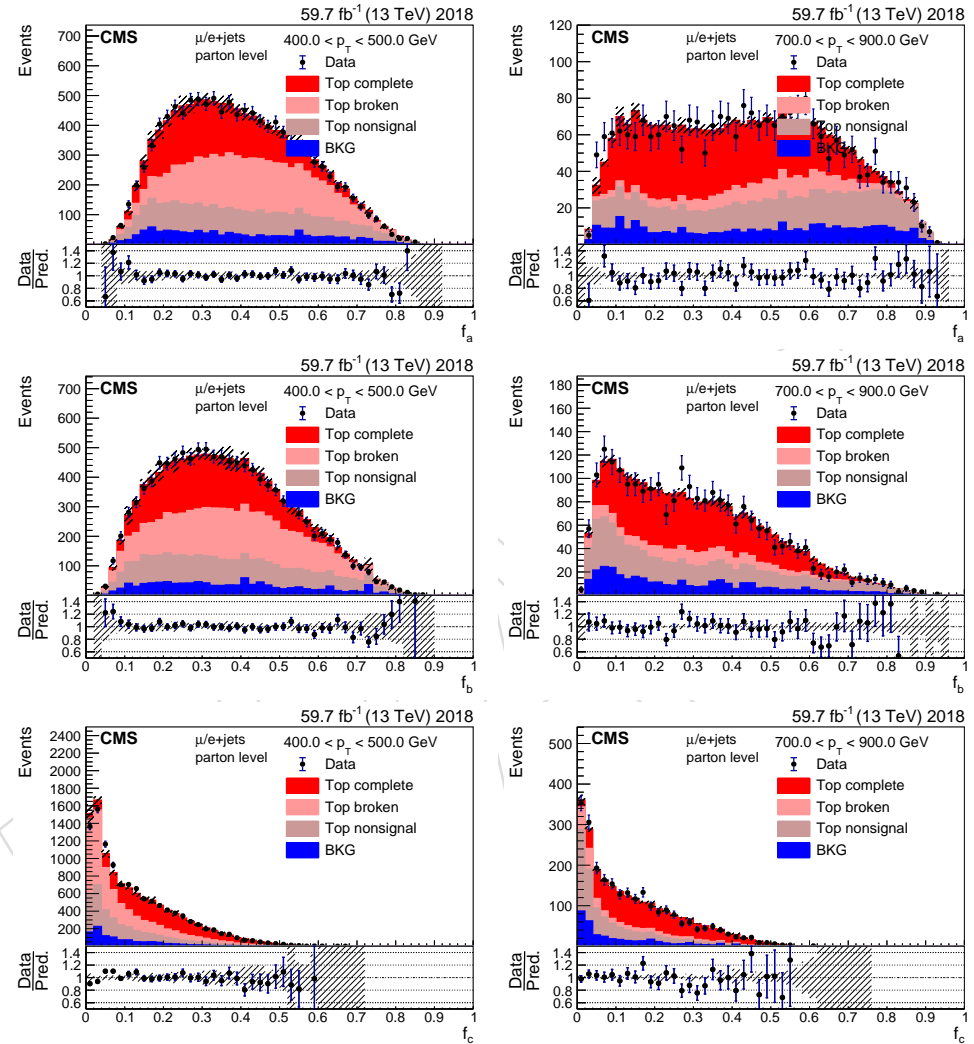


Figure 127: Variables used in the identification of boosted top quarks. The plots are shown for events with a reconstructed  $t_\ell$ . The normalization of the various components is obtained from a fit of  $H_{NN}$  used to extract the signal contribution (complete and broken top candidates.)

**I Cross sections from individual years and channels**

As an additional check to prove the stability of the results, we extract the differential cross sections using data from individual years and the muon and electron channels separately. These are compared in Figs. 128 and 129. The individual measurements are found to overlap mostly within their uncertainties, though their uncertainties are not fully uncorrelated. There are no signs of large deviations in a single channel. The high p-values of the combined fits however are a good indicator that the measurements are fully compatible.

DRAFT

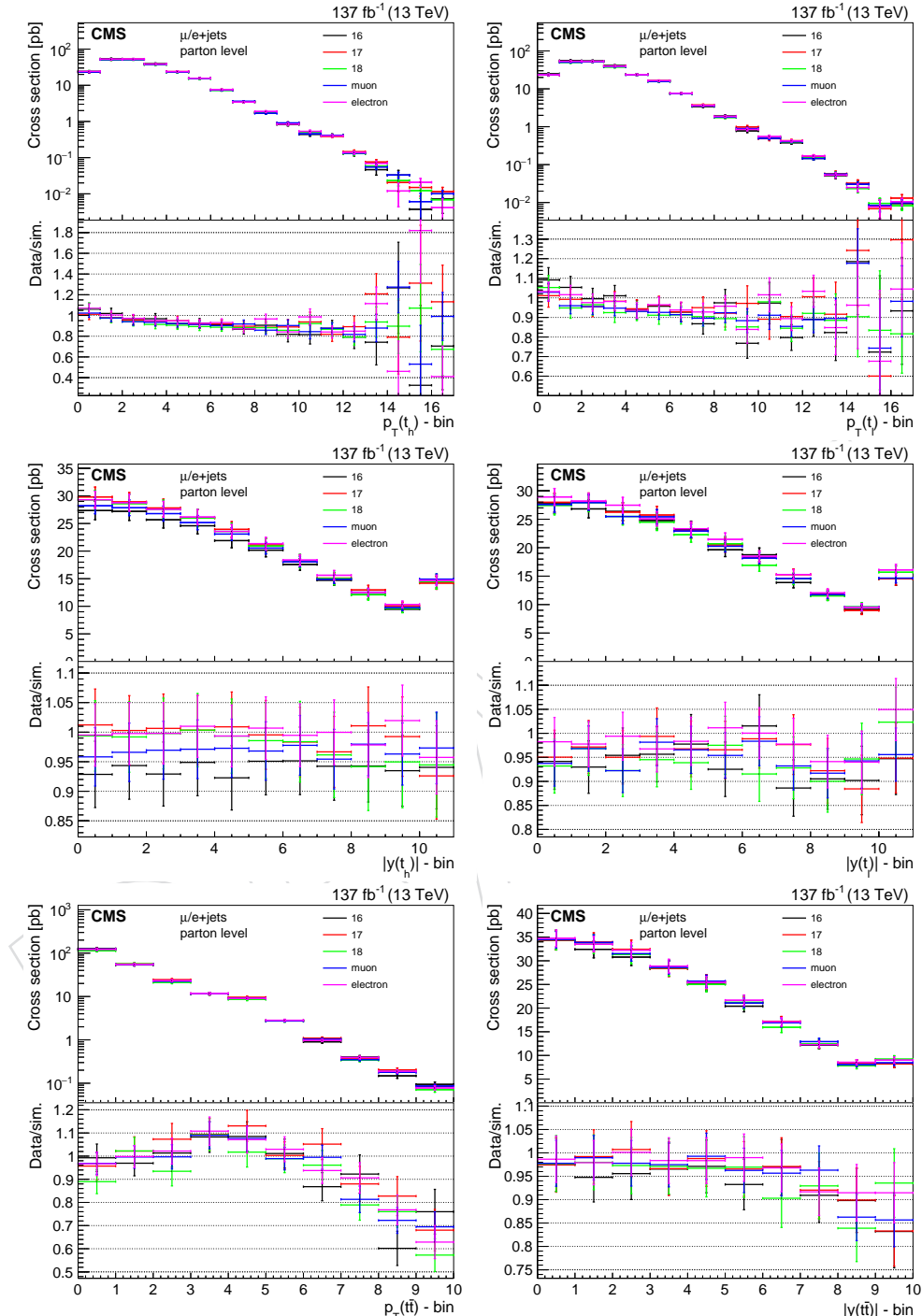


Figure 128: Comparisons of the differential cross sections measured using data from individual years and the muon and electron channels separately. The lower panels show the ratio to the POWHEG+PYTHIA8 simulation.

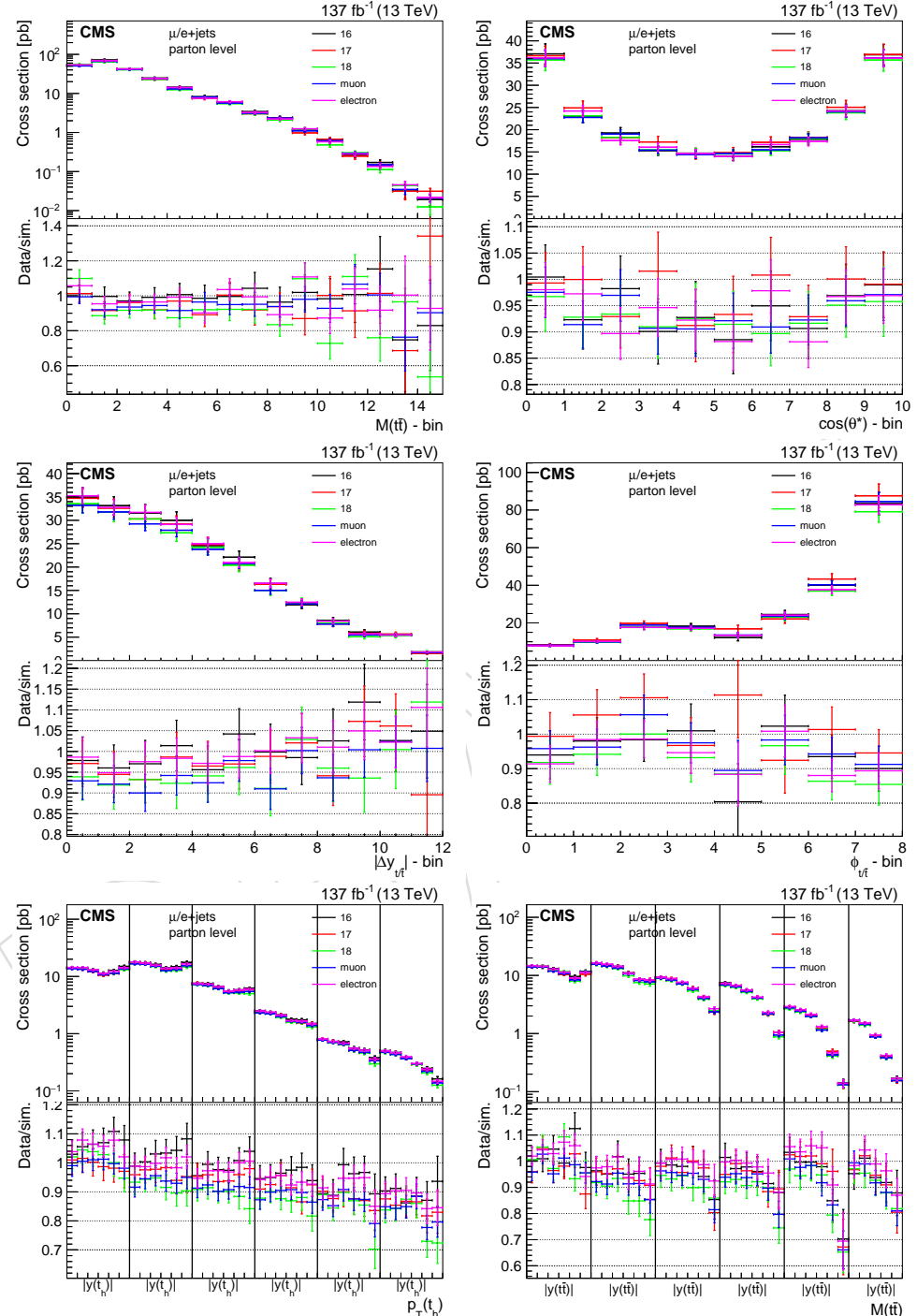


Figure 129: Comparisons of the differential cross sections measured using data from individual years and the muon and electron channels separately. The lower panels show the ratio to the POWHEG+PYTHIA8 simulation.

---

899 **J Plots of template fits**

DRAFT

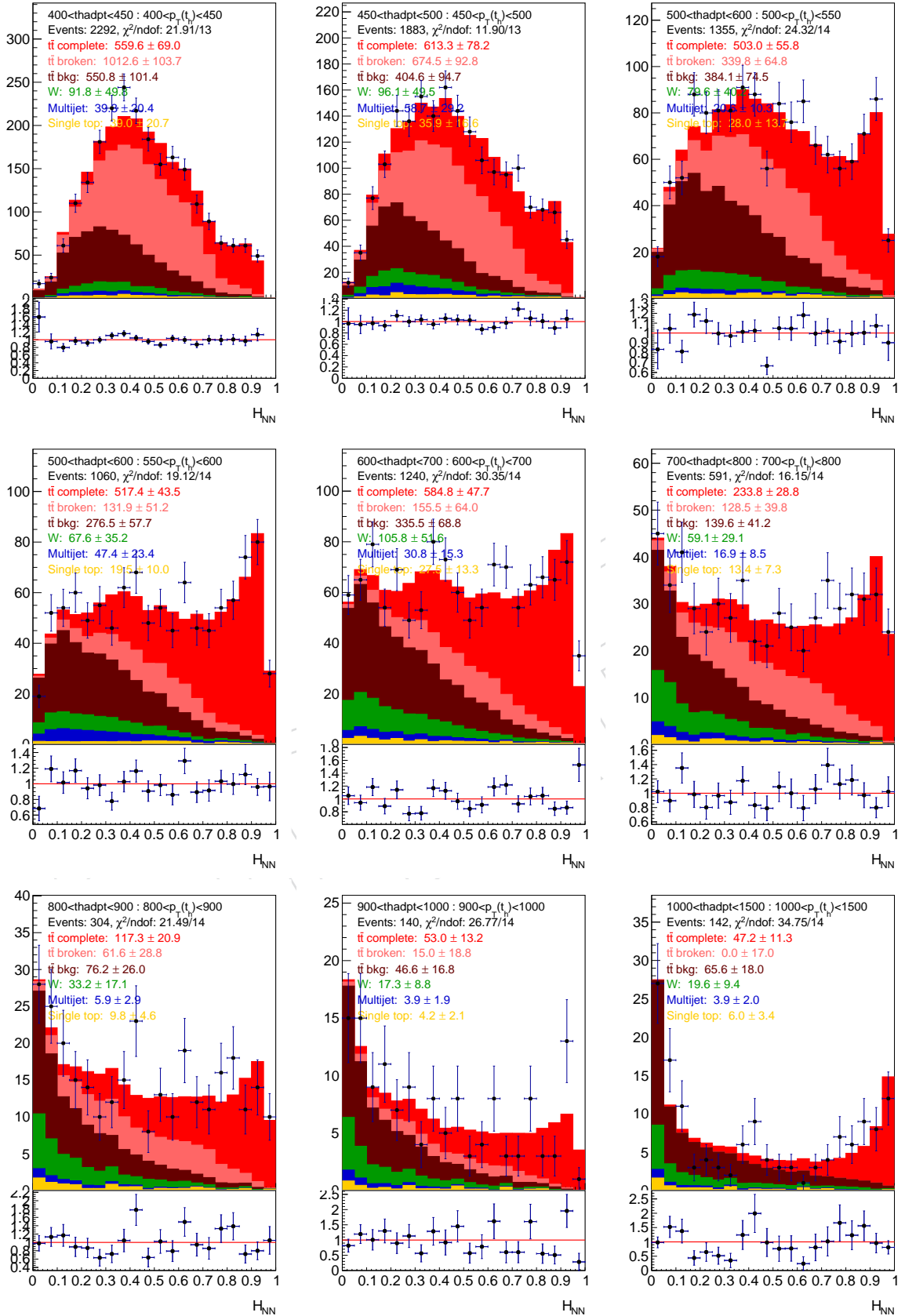


Figure 130: Fit in bins of  $p_T(t_h)$  in the muon channel for 2016 data. Signal  $t\bar{t}$  complete/broken (red/light red), background  $t\bar{t}$  (brown),  $W/Z$  boson (green), multijet (green), single top (yellow).

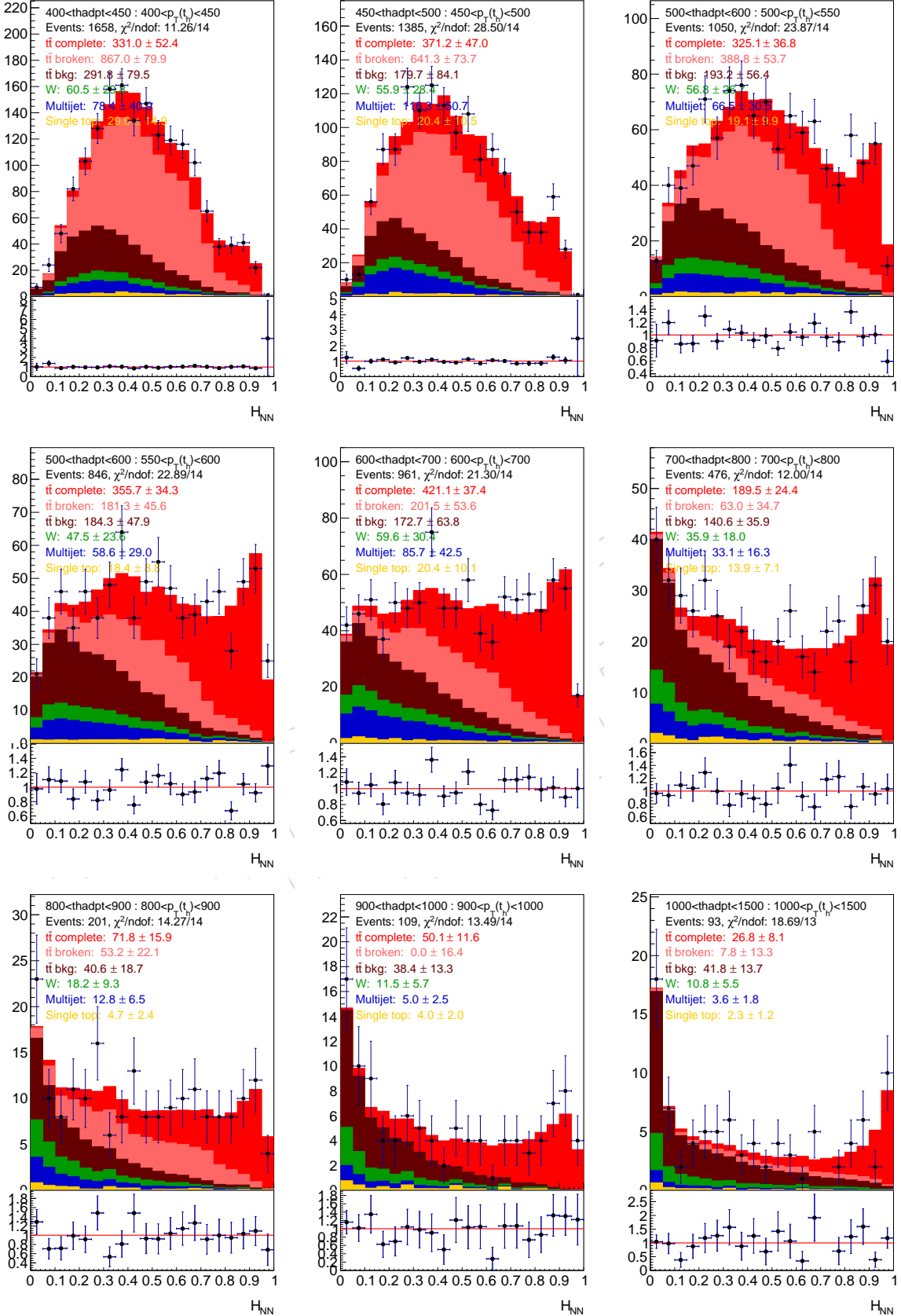


Figure 131: Fit in bins of  $p_T(t_h)$  in the electron channel for 2016 data. Signal  $t\bar{t}$  complete/broken (red/light red), background  $t\bar{t}$  (brown),  $W/Z$  boson (green), multijet (green), single top (yellow).

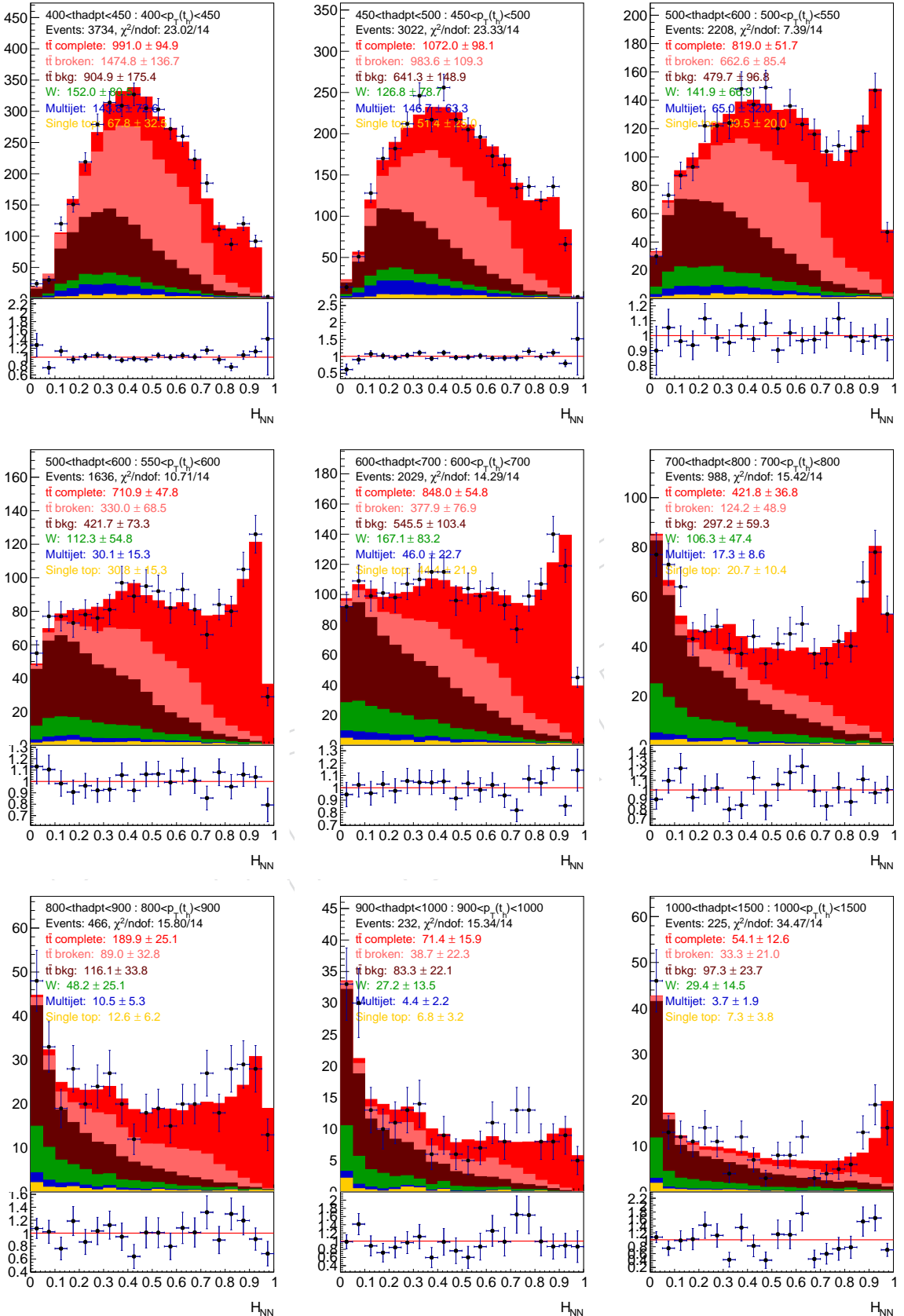


Figure 132: Fit in bins of  $p_T(t_h)$  in the muon channel for 2018 data. Signal  $t\bar{t}$  complete/broken (red/light red), background  $t\bar{t}$  (brown),  $W/Z$  boson (green), multijet (green), single top (yellow).

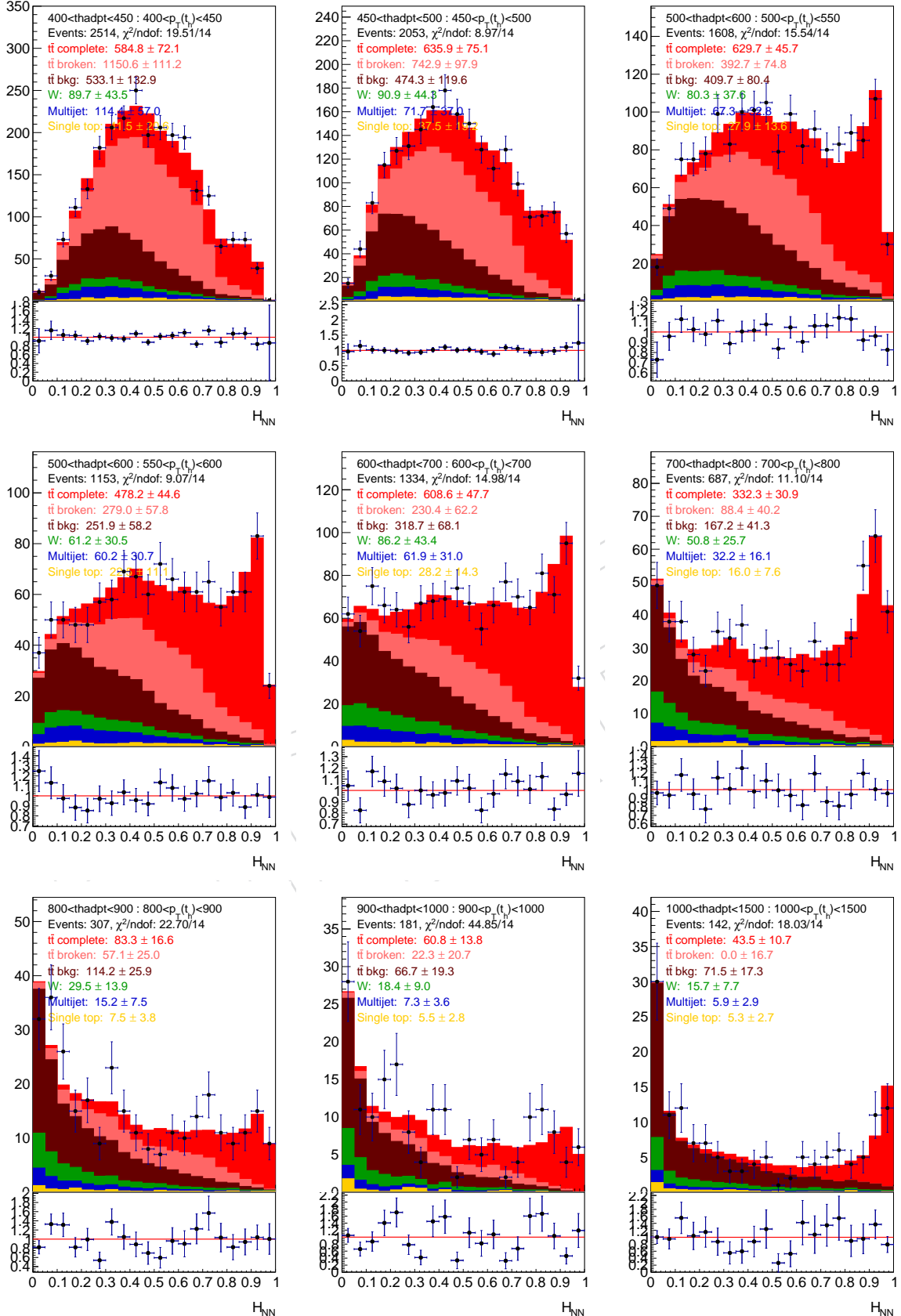


Figure 133: Fit in bins of  $p_T(t_h)$  in the electron channel for 2018 data. Signal  $t\bar{t}$  complete/broken (red/light red), background  $t\bar{t}$  (brown), W/Z boson (green), multijet (green), single top (yellow).

## 900 K Test of bias with modified simulations

901 We perform the cross section fits followed by the regularization using the default simulation at  
902 detector level instead of using the signal yields in data. With this input distributions the ob-  
903 tained cross sections are expected to be exactly the differential cross sections in the simulation.  
904 This is confirmed in Fig. 134. With this consistency test technical problems with the setup of  
905 the fit could be discovered. This tests can only be performed in the combination of 2017 and  
906 2018 simulations since the unfolded distributions in the 2016 simulation is different (CP5 tune  
907 vs. T4).

908 In the next step we do not extract the cross sections from the default simulation, but from  
909 modified simulations. These are obtained by reweighting the default simulation as functions  
910 of  $p_T(t)$ ,  $M(t\bar{t})$ , or  $|y(t_h)|$ . For each test in one of this distributions a Sine like modulation  
911 with an amplitude of 20% is introduced. Afterwards, the cross section extraction is performed  
912 to test if the modified spectra can be obtained correctly. The results are shown in Figs. 135–  
913 137. In general, we expect the unfolded results to follow the modified spectra (red line). The  
914 modification with respect to the default simulation that is still used to obtain the response  
915 matrices, can be seen from the blue lines. The injected modifications are rather extreme and  
916 the agreements between real data and simulation are better than in this tests. Nevertheless, the  
917 observed bias is usually small and within the uncertainty band of the measurement. The results  
918 include the regularization (of course, the prior is taken from the default simulation). However,  
919 the observed biases are similar before the regularization is performed. The main contribution  
920 of the bias is introduces by response matrices that depend on certain assumptions based on the  
921 default simulation, but these are no longer correct for the reweighted simulations.

DRAFT

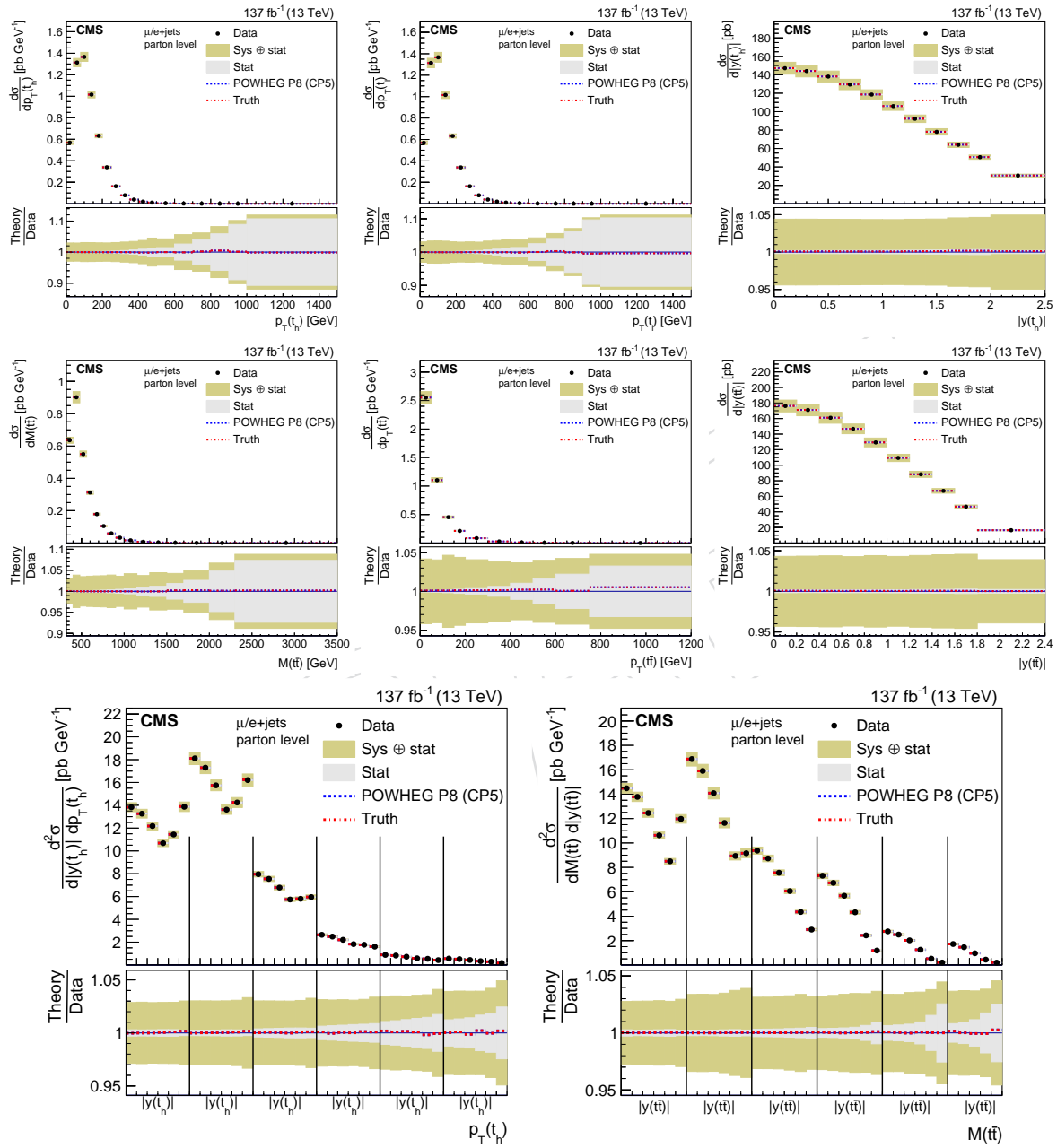
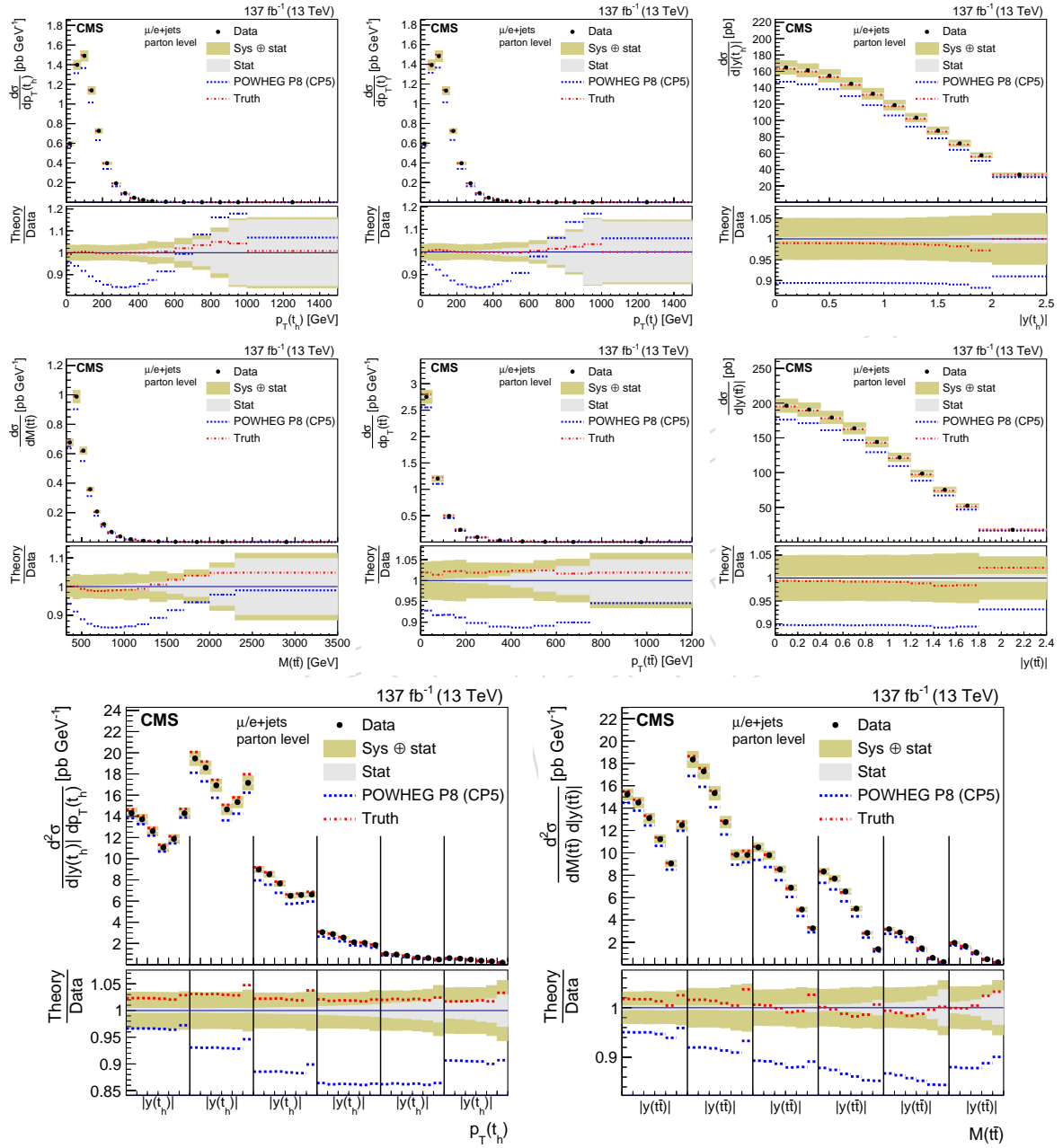
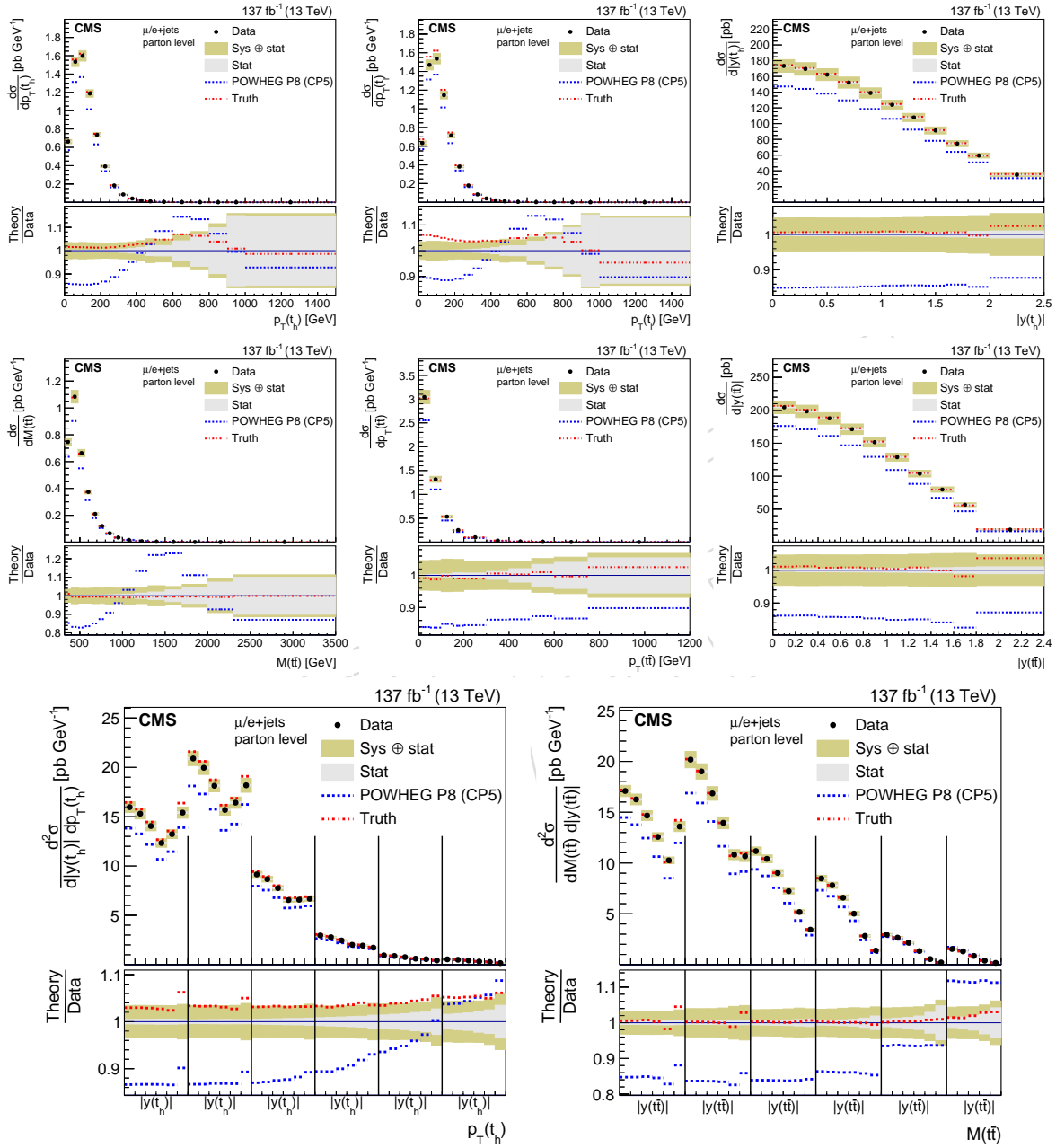
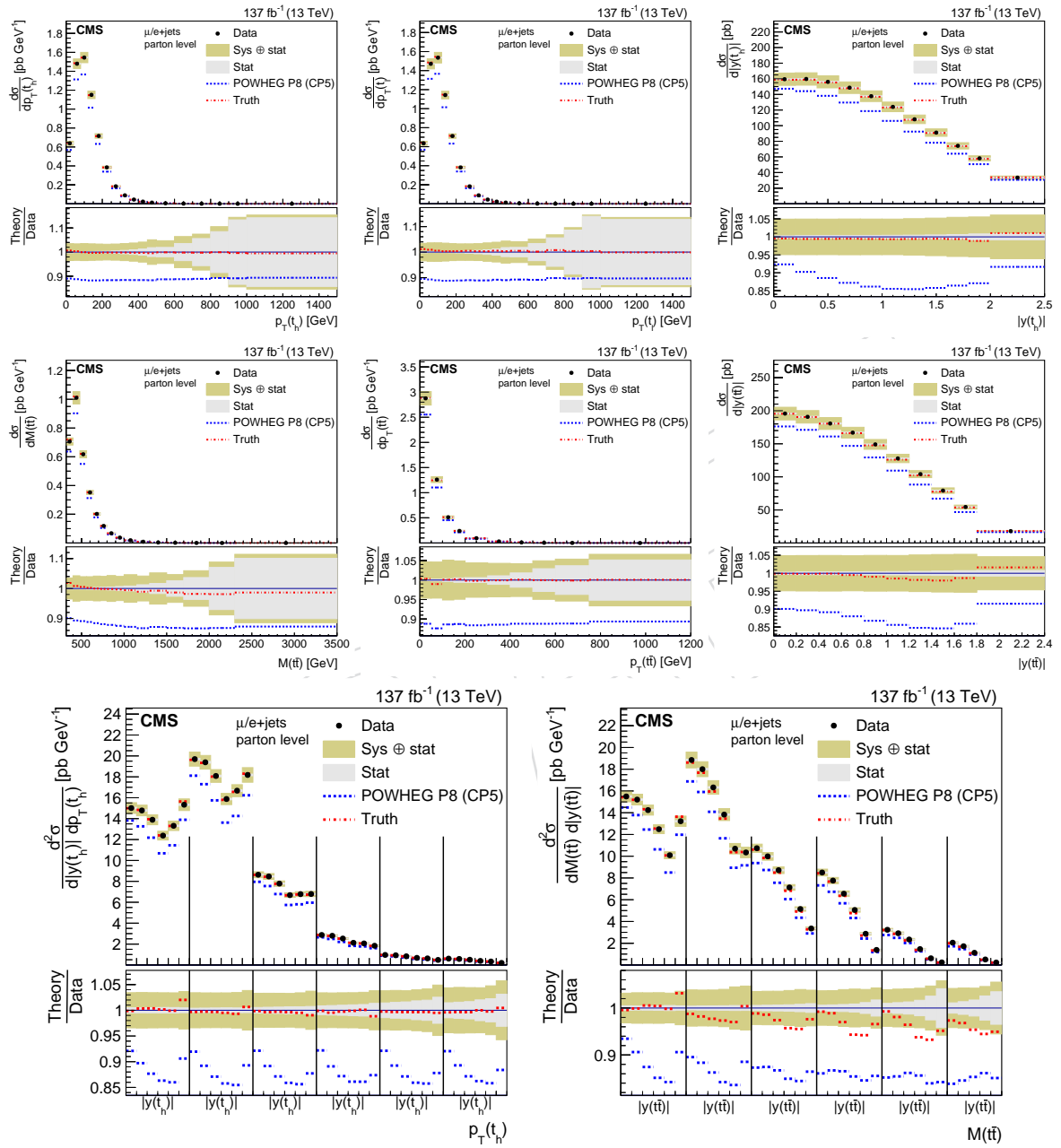


Figure 134: Test with default Simulation.

Figure 135: Test with reweighted  $p_T(t)$ .

Figure 136: Test with reweighted  $M(t\bar{t})$ .

Figure 137: Test with reweighted  $|y(t_h)|$ .

922 **L Comparison with TOP-17-002**

DRAFT

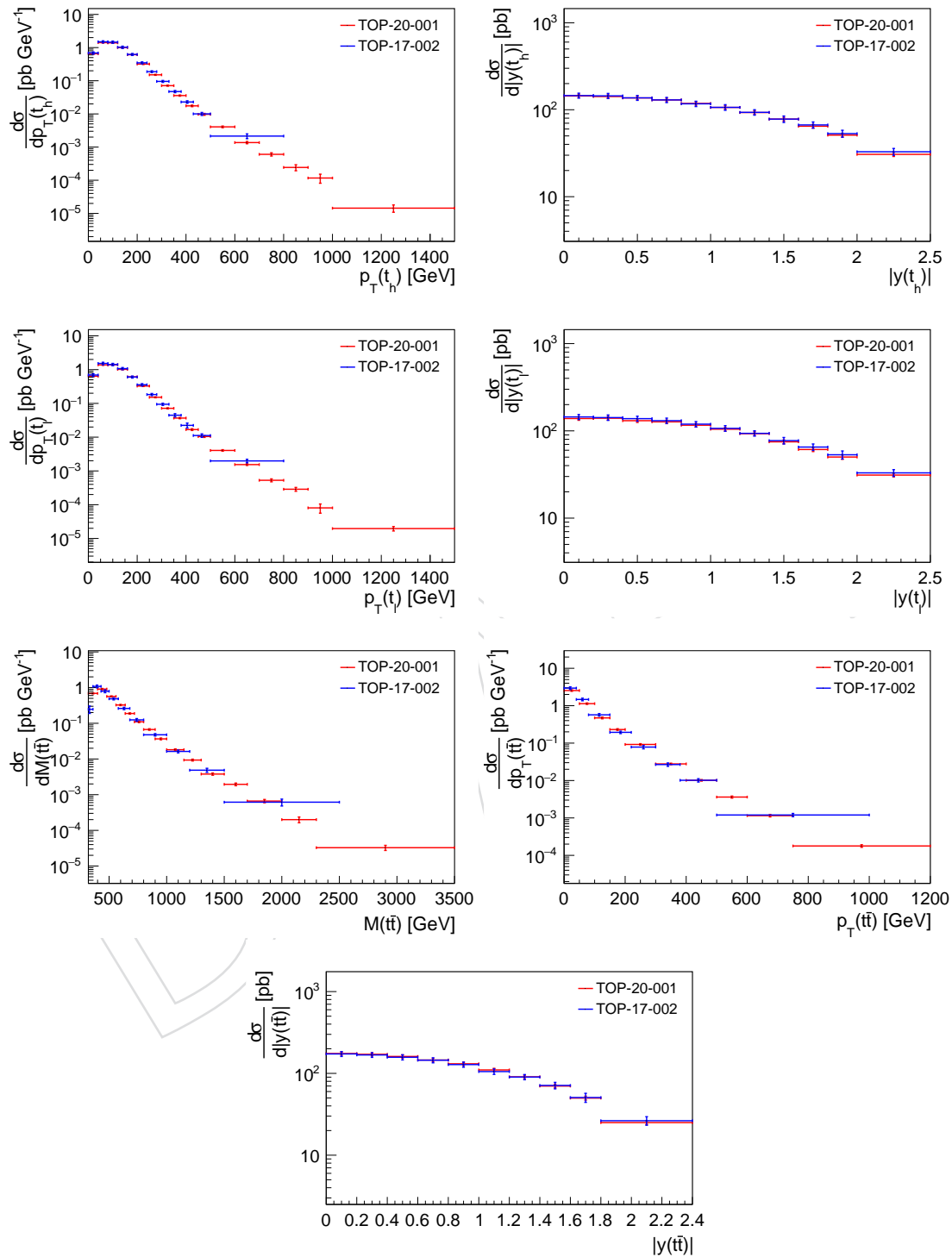


Figure 138: Comparisons of TOP-17-002 and TOP-20-001